Molecules exposed to Intense, Ultrashort Laser Fields

D I S S E R T A T I O N

zur Erlangung des akademischen Grades
doctor rerum naturalium
(Dr. rer. nat.)
im Fach Physik

eingereicht an der
Mathematisch-Naturwissenschaftlichen Fakultät
der Humboldt-Universität zu Berlin

von

M. Sc. Johann Jakob Förster

Präsidentin der Humboldt-Universität zu Berlin:
Prof. Dr.-Ing. Dr. Sabine Kunst

Dekan der Mathematisch-Naturwissenschaftlichen Fakultät:
Prof. Dr. Elmar Kulke

Gutachter/innen:	1. Prof. Dr. Alejandro Saenz
	2. Prof. Dr. Stefanie Gräfe
	3. Prof. Dr. Mikhail Ivanov
Tag der mündlichen Prüfung:	16.03.2018

Abstract

In this thesis the ionization behavior of small molecules (especially H_2 and NH_3) exposed to intense, ultrashort laser fields is investigated theoretically. The focus lies on the influence of nuclear dynamics on this ionization behavior. The matrix algorithm is introduced, compared to the B-spline method, and thereupon used for the numerical description of the molecular vibration of H_2 and NH_3. The ionization behavior of the H_2 molecule is first examined within the frozen-nuclei approximation. A previously reported pronounced breakdown of the fixed-nuclei approximation can be explained already within this level of approximation. Furthermore, the transition from the multiphoton to the quasistatic ionization regime is studied for 800 nm laser pulses. The simple FC-ADK approximation is investigated. It is observed that this approximation agrees surprisingly well to the numerical solution of the time-dependent Schrödinger equation. Furthermore, a novel approach for the correlated description of the electronic-vibrational motion of the H_2 molecule is developed. First, a simple two-dimensional model for H_2^+ is examined in detail. Afterwards, the implemented approach is generalized for the solution of the seven-dimensional problem for H_2. The influence of vibrational dynamics during the laser field on the ionization behavior is investigated using this novel method. A pronounced difference on the previously discussed breakdown of the fixed-nuclei approximation is observed. The vibrational dynamics also lead to a notable change for a recently experimentally observed isotope effect in the ionization of the molecular isotopes H_2 vs. D_2.

The ionization behavior of the NH_3 molecule is studied in the second part of this thesis. First, a recent experiment in which the high-harmonic spectra of the isotopes NH_3 vs. ND_3 are compared is investigated theoretically within a simple model. A predicted autocorrelation maximum can be explained by a "wave-packet race". Furthermore, a pronounced geometry dependence of the ionization yield is observed in order to quantitatively explain the experiment. Also for the NH_3 molecule, the FC-ADK approximation also compares quantitatively surprisingly well to the numerical solution of the time-dependent Schrödinger equation. The possibility to exploit the geometry dependence of the ionization yield in order to create and measure vibrational wave packets in the neutral NH_3 molecule via *Lochfraß* is explored. The expected vibrational dynamics and the optimal laser parameters to observe this effect are demonstrated. Furthermore, the possibility to shoot a "movie" of a tunneling wave packet in the double-well potential along the vibrational coordinate is investigated. Indeed, extremely short laser fields should allow to create a real time movie of the quantum-mechanical tunneling process. Finally, an existing program is extended in order to study the orientation dependence of the ionization yield of the NH_3 molecule. Furthermore, elliptically polarized laser fields are implemented. The obtained geometry-dependent ionization yields are demonstrated and found to behave similarly to the orbital shape of the NH_3 molecule.

Zusammenfassung

In dieser Dissertation wird das Ionisierungsverhalten kleiner Moleküle (insbesondere H_2 und NH_3) in intensiven, ultrakurzen Laserfeldern theoretisch untersucht. Das Hauptaugenmerk liegt dabei auf dem Einfluss der Kerndynamik. Die Matrixmethode wird zur numerischen Beschreibung der Molekülschwingung von H_2 sowie von NH_3 eingeführt, mit der B-Spline-Methode verglichen und zur Lösung des Schwingungsproblems im weiteren Verlauf der Arbeit verwendet. Zunächst wird das Ionisierungsverhalten des H_2-Moleküls bei eingefrorener Kernschwingung untersucht. Bereits im Rahmen dieser Näherung kann im Mehrphotonenregime ein zuvor beobachteter Zusammenbruch der Näherung im Gleichgewichtsabstand festgehaltener Kerne erklärt werden. Weiterhin wird der Übergang vom Mehrphotonenzum quasistatischen Ionisierungsregime für 800-nm-Laserfelder untersucht. Die einfache FC-ADK-Näherung wird untersucht. Es wird beobachtet, dass diese Näherung überraschend gut mit der numerischen Lösung der Schrödingergleichung übereinstimmt. Im weiteren Verlauf wird eine neuartige Methode zur Beschreibung der korrelierten Schwingungs- und Elektronendynamik des H_2-Moleküls entwickelt. Zunächst wird ein zweidimensionales H_2^+-Modell im Detail untersucht, bevor die Methode zur Lösung dieses siebendimensionalen Problems weiterentwickelt wird. Mit dieser neuartigen Methode wird schließlich der Einfluss der Kernbewegung während des Laserfeldes auf das Ionisierungsverhalten untersucht. Es wird ein sichtbarer Einfluss auf den zuvor diskutierten Zusammenbruch der Näherung festgehaltener Kerne beobachtet. Dies gilt ebenfalls für einen vor kurzem experimentell beobachteten Isotopeneffekt in der Ionisierung der Moleküle H_2 vs. D_2 untersucht.

Im zweiten Teil der Arbeit wird das Ionisierungsverhalten des NH_3-Moleküls untersucht. Zunächst wird ein aktuelles Experiment, welches die Spektren hoher Harmonischer der Isotope NH_3 vs. ND_3 vergleicht, modelliert und theoretisch untersucht. Für ein vorhergesagtes Autokorrelationsmaximum kann eine einfache Erklärung im Rahmen eines „Wellenpaket-Wettrennens“ gefunden werden. Zur vollständigen Erklärung des Experiments wird eine starke Kerngeometrieabhängigkeit des Ionisierungsverhaltens beobachtet. Auch für das NH_3-Molekül stimmt die einfache FC-ADK-Näherung gut mit der numerischen Lösung der Schrödingergleichung überein. Die Möglichkeit, die Kerngeometrieabhängigkeit zur Erzeugung und Messung von Schwingungswellenpaketen im neutralen NH_3-Molekül mittels *Lochfraß* auszunutzen, wird untersucht. Das erwartete Schwingungsverhalten und die dafür optimalen Laserparameter werden aufgezeigt. Zusätzlich wird die Möglichkeit des „Filmens“ eines tunnelnden Kernwellenpakets im Doppelmuldenpotential entlang der Schwingungskoordinate untersucht. In der Tat sollte die Verwendung extrem kurzer Laserfelder das Drehen eines Echtzeit-Filmes dieses quantenmechanischen Tunnelprozesses ermöglichen. Abschließend wird das vorhandene Programm für die Beschreibung der Winkelabhängigkeit der Ionisierungswahrscheinlichkeit von NH_3 sowie elliptisch polarisierter Laserfelder weiterentwickelt. Die erhaltenen Winkelabhängigkeiten, welche der Orbitalgeometrie des NH_3-Moleküls ähneln, werden untersucht.

List of publications

[1] J. Förster, A. Saenz, and U. Wolff. Matrix algorithm for solving Schrödinger equations with position-dependent mass or complex optical potentials. *Phys. Rev. E*, 86:016701, 2012.

[2] J. Förster and A. Saenz. Theoretical study of the inversion motion of the ammonia cation with subfemtosecond resolution for high-harmonic spectroscopy. *ChemPhysChem*, 14:1438, 2013.

[3] J. Förster, Y. V. Vanne, and A. Saenz. Ionization behavior of molecular hydrogen in intense laser fields: Influence of molecular vibration and alignment. *Phys. Rev. A*, 90:053424, 2014.

[4] J. Förster, E. Plésiat, Á. Magaña, and A. Saenz. Imaging of the umbrella motion and tunneling in ammonia molecules by strong-field ionization. *Phys. Rev. A*, 94:043405, 2016.

In preparation:

- J. Förster and A. Saenz. Fully correlated electronic and vibrational motions: the (1+1)-dimensional H_2^+ model. *In preparation*, based on Section 4.3.
- J. Förster and A. Saenz. Fully correlated electronic and vibrational motions of molecular hydrogen. *In preparation*, based on Section 4.4.
- J. Förster, P. Decleva, and A. Saenz. Orientation-Dependent Ionization of Ammonia Molecules and Elliptically Polarized Fields. *In preparation*, based on Section 4.7.

Publications not discussed within this thesis:

[5] J. P. Farrell, S. Petretti, J. Förster, B. K. McFarland, L. S. Spector, Y. V. Vanne, P. Decleva, P. H. Bucksbaum, A. Saenz, and M. Gühr. Strong field ionization to multiple electronic states in water. *Phys. Rev. Lett.*, 107:083001, 2011.

[6] S. Sala, J. Förster, and A. Saenz. Ultracold-atom quantum simulator for attosecond science. *Phys. Rev. A*, 95:011403(R), 2017.

Contents

1 Introduction

Thanks to the rapid development of intense, ultrashort laser field sources during the last decades field durations of a few femtoseconds and peak intensities of $10^{10} - 10^{21}$ W/cm^2 at wavelengths around 800 nm are nowadays accessible[1] [7–9]. These laser fields offer prospects to image and manipulate molecules on their sub-femtosecond and sub-ångström scales. Exposing molecules to intense, ultrashort laser fields thus not only allows to study molecular structure, but especially time-dependent processes. The understanding of this laser-molecule interaction is thus the prerequisite for producing a real-time "movie" of the electronic and nuclear dynamics launched in molecules. The multitude of possible laser field parameters (laser field duration, intensity, shape of the laser field, wavelength, ...) offers furthermore many possibilities to control time-dependent processes with the long-term goal of controlling chemical reactions. Promising approaches to achieve these goals have been developed and demonstrated for small molecules during the last years.

First, the electronic dynamics launched in molecules when exposed to intense, ultrashort laser fields is considered. In addition to electronic excitations especially the ionization process, i.e. the removal of one (or more) electrons is of interest[2]. The dependence of the ionization yield on the orientation of the laser polarization of a linearly polarized laser field relative to the molecule carries information about the molecular structure (orbital tomography, [10, 11]). Furthermore, ionization is the first step in Corkum's three-step model [12, 13] for high-harmonics generation (HHG), see Figure 1.1. The frequency ω_{HHG} of the emitted high harmonics is a (typically odd) multiple of the frequency ω of the incoming laser field, e.g. $\omega_{\mathrm{HHG}} = 15, 17, \ldots \omega$. HHG can be used to generate attosecond laser fields [7, 13] and orbital tomography [13, 14]. Additionally extracting time-dependent information from HHG allows to image correlated electron-nuclear dynamics as in [15, 16]. Instead of recombination also rescattering may occur as the third step in the three-step model. This leads to laser-induced electron diffraction [10, 17, 18] and the information from the rescattered electron also allows for time-resolved imaging.

[1] Free electron lasers like the Linac Coherent Light Source in Stanford (USA) or the recently built European X-Ray Free-Electron Laser in Hamburg (Germany) allow to create ultrashort, intense laser fields of much shorter wavelengths. These laser fields potentially allow for imaging molecular structures and dynamics, e.g. via X-Ray diffraction. This thesis focuses on long wavelengths around 800 nm.

[2] Within this thesis only the removal of a single electron (single ionization) is considered. The probability to remove two (double ionization) or more electrons is typically orders of magnitude smaller than the single ionization yield for long wavelength laser fields. The main reason is the exponential dependence of the ionization yield on the binding energy and the significant larger binding energy of the double ionization process compared to single ionization.

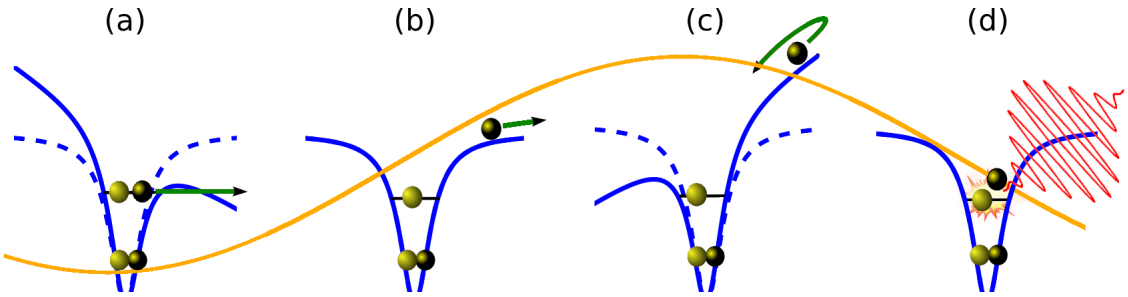

Figure 1.1: Corkum's three-step model for high-harmonic generation. **a)** Step 1: Tunneling ionization. The laser field (orange) tilts the binding potential (dashed blue line) such that an electron (sphere) can escape through the tilted potential (full blue line). **b) and c)** Step 2: Propagation of the electron in the laser field. Due to the time-dependence of the laser field the electron is accelerated back towards the atom or molecule. **d)** Step 3: Recombination of the electron with the ionized atom or molecule. The exceeding energy absorbed from the laser field is emitted by a high harmonic. Instead of recombination elastic or inelastic scattering may occur. Figure taken from [6] (modified to emphasize HHG).

When comparing the behavior of atoms to molecules exposed to intense, ultrashort laser fields pronounced differences are observed due to the nuclear motion (rotation and vibrations) of molecules. When directly comparing the high-harmonic spectra of two isotopes of a molecule **p**robing **a**ttosecond dynamics by **c**hirp **e**ncoded **r**ecollision (*PACER*) allows to image the relative nuclear dynamics launched in the corresponding molecule cations[3] [2, 5, 19–22]. Seemingly surprisingly, the relative nuclear dynamics in water molecules (D_2O^+/H_2O^+) showed a significant contribution of HOMO-1 electron ionization[4] was observed even for unaligned molecules [5]. Before, it was assumed that the HOMO electron alone dominates HHG.

Clearly, also the ionization process is strongly influenced by the nuclear geometry and dynamics of molecules. Within a simple model the breakdown of the Franck–Condon approximation was first predicted for diatomic molecules exposed to intense laser fields [23] and experimentally confirmed thereafter [24]. The prediction in [23] was based on the exponential dependence of the strong-field ionization rates on the binding energy of the ejected electron [25–27] (vertical ionization potential of the initial state). Already small changes in the binding energy lead to a very pronounced (exponential) dependence of the electronic transition amplitude on nuclear geometry. This exponential dependence was later further confirmed by direct solutions of the time-dependent Schrödinger equation for the H_2 molecule

[3] Due to the larger masses the heavier isotope exhibits a slower nuclear motion than the lighter one.

[4] The HOMO (Highest Occupied Molecular Orbital) is the energetically highest occupied orbital. The HOMO-1 is the energetically next lower orbital.

[28, 29]. The breakdown of the Franck–Condon approximation also influences the HHG spectra ratio in *PACER* [2, 21]. Based on the mechanism that leads to the breakdown of the Franck–Condon approximation, *Lochfraß* was theoretically proposed [30] as method to prepare and image a nuclear wave packet in real time by measuring total ionization yields. Indeed, the predicted nuclear vibration on the sub-ångström scale has been measured in experiments on the diatomic molecules D_2 [31] and I_2 [32, 33] with sub-femtosecond resolution. The vibration of the D_2 molecule is the fastest vibration which has been measured in real time so far. Due to the unexpectedly long life time and stability of the vibration it may be used as a molecular clock (10,000 times faster than the cesium clock) [31]. Furthermore, the principle behind *Lochfraß* was recently used to align molecules[5] [34, 35].

Measuring the fragments (electrons, ions) of a molecule after exposure to an intense, ultrashort laser field allows for deep insights inside the physics of strong laser fields. Popular techniques to measure these fragments are the reaction microscope or cold target recoil-ion momentum spectroscopy (COLTRIMS) [36] as well as velocity map imaging [37]. This allowed, e.g., to observe the first theoretically predicted interatomic Coulombic decay mechanism [38] experimentally [39]. The interpretation, i.e. the theoretical description, of the experimentally observed coupled electron-nuclear dynamics (and the clean separation of different effects) is, however, still very challenging even for very small molecules. Even for the simplest molecule, H_2^+, a recent comparison [40] noted room for improvement for both experiment and theory.

The dynamics of molecules exposed to intense, ultrashort laser fields is sensitive on the exact time-dependence of the laser field (pulse shape). This offers prospects to control chemical reactions. For example, the dynamics can be controlled by varying the carrier-envelope phase [40–44]. This allows, e.g. to control at which core an electron remains after dissociation of a molecule [40, 42, 43] and even controlled breaking of chemical bonds [44]. Additionally, circularly polarized, ultrashort laser fields may be used to induce ring currents [45].

For the theoretical description of the interaction of molecules with intense, ultrashort laser fields the direct solution of the time-dependent Schrödinger equation (TDSE) gains increasing importance. The validity regime of many common approximations is no longer known for the nowadays accessible ultrashort laser fields and should thus be checked using the TDSE. However, since this direct solution of the TDSE is computationally extremely demanding, the development of efficient methods and finding reliable approximations constitutes a great challenge. In most cases the electronic problem describing the molecule in the laser field is solved for a fixed nuclear geometry. Eventually, the nuclear motion is then treated separately (in the Born-Oppenheimer sense). Alternatively, nuclear motion (including rotation) can be included using classical mechanics [46, 47]. Even for the smallest molecules, often low-dimensional models are used for the solution of the electronic problem.

[5] In contrast to alignment using a static electric field, this generates a rotational wave packet leading to field-free alignment.

The single-active-electron approximation is furthermore almost always applied for atoms and molecules with more than two electrons. In fact, the six-dimensional treatment of two-electron systems like He or H_2 is today still state of the art [3, 48–52]. In order to check the validity of the single active electron approximation the study of molecular hydrogen H_2 is of special interest. A configuration-interaction method has been previously developed which allows to solve the TDSE for fixed nuclear geometries in full dimensionality [48, 53]. Other previously developed methods include the solution of the TDSE of polyatomic molecules like N_2, O_2, CO_2, H_2O within the single-determinant approximation [5, 11, 54] as well as the solution of the time-dependent Dirac equation for highly charged one-electron ions [55] in full dimensionality, respectively. For all these methods the TDSE is expanded using bound and properly discretized continuum states obtained from solving the time-independent Schrödinger equation (TISE) in a B spline basis set first. A clear restriction of the previously mentioned methods describing molecules is the neglect of nuclear dynamics by freezing the nuclear motion.

In this thesis the influence of nuclear motion (especially vibration) on the ionization behavior of molecules is investigated. Basic theoretical concepts are introduced in Chapter 2. Different computational methods to solve the TISE and TDSE are presented in Chapter 3. These concepts and methods form the basis for the seven studies presented in Chapter 4. In the first part of Chapter 4 primarily molecular hydrogen is studied. The second part focuses on the ammonia molecule. A final summary and outlook for the whole thesis is found in Chapter 5.

2 Basic Theoretical Concepts: Molecules and their Interaction with Laser Fields

This chapter covers the basic elements of the non-relativistic quantum mechanical treatment of molecules and their interaction with intense, ultrashort laser fields. Unless noted otherwise, atomic units ($\hbar = e = m_e = 4\pi\,\epsilon_0 = 1$ a.u.) are used throughout this thesis (except for laser field parameters where the common units W/cm^2, fs and so on are used). The Hamiltonian for the description of molecules is given in Section 2.1 in Cartesian coordinates and the terms Born-Oppenheimer approximation and nonadiabatic couplings are introduced. In Section 2.2 the description of the nuclear motion of diatomic molecules is discussed. Section 2.3 introduces the inversion motion of the ammonia molecule. Time scales of nuclear motion of small molecules are briefly estimated in Section 2.4. The basic description of the interaction of a molecule with a laser field is introduced in Section 2.5. Different pictures for the ionization of molecules in different regimes are presented in Section 2.6. Finally, the time dependence of the intense, ultrashort laser fields employed here is introduced and discussed in Section 2.7.

2.1 The Hamiltonian for the Description of Molecules

The Hamiltonian $\hat{\mathrm{H}}_{\mathrm{mol}}$ describing a molecule consisting of N_{nuc} nuclei and n_{e} electrons interacting via Coulomb interactions reads in Cartesian coordinates

$$\begin{aligned}\hat{\mathrm{H}}_{\mathrm{mol}} &= \sum_{k=1}^{N_{\mathrm{nuc}}} \frac{\hat{\vec{\mathrm{P}}}_k^{\,2}}{2\,M_k} + \sum_{i=1}^{n_{\mathrm{e}}} \frac{\hat{\vec{\mathrm{p}}}_i^{\,2}}{2} - \sum_{i=1}^{n_{\mathrm{e}}}\sum_{k=1}^{N_{\mathrm{nuc}}} \frac{Z_k}{\left|\vec{r}_i - \vec{R}_k\right|} \\ &\quad + \frac{1}{2}\sum_{\substack{k=1\\k\neq l}}^{N_{\mathrm{nuc}}}\sum_{l=1}^{N_{\mathrm{nuc}}} \frac{Z_k\,Z_l}{\left|\vec{R}_k - \vec{R}_l\right|} + \frac{1}{2}\sum_{\substack{i=1\\i\neq j}}^{n_{\mathrm{e}}}\sum_{j=1}^{n_{\mathrm{e}}} \frac{1}{|\,\vec{r}_i - \vec{r}_j\,|} \\ &= \hat{\mathrm{T}}_{\mathrm{nuc}} + \hat{\mathrm{T}}_{\mathrm{e}} + V_{\mathrm{en}} + V_{\mathrm{nn}} + V_{\mathrm{ee}} = \hat{\mathrm{T}}_{\mathrm{nuc}} + \hat{\mathrm{H}}_{\mathrm{e}} \end{aligned} \tag{2.1}$$

with positions $\vec{r}_i$ (momenta $\hat{\vec{\mathrm{p}}}_i$) of electron i and positions $\vec{R}_k$ (momenta $\hat{\vec{\mathrm{P}}}_k$, masses M_k, charges Z_k) of nucleus k. Spin interactions and any other relativistic effects are neglected in this equation.

In the following, the sets of coordinates are abbreviated as $\underline{\mathbf{r}} = \{\vec{r}_1, \vec{r}_2, ..., \vec{r}_{n_{\mathrm{e}}}\}$ and $\underline{\mathbf{R}} = \{\vec{R}_1, \vec{R}_2, ..., \vec{R}_{N_{\mathrm{nuc}}}\}$. In order to learn about the structural properties of a

molecule the goal is to solve the time-independent Schrödinger equation[1]

$$\hat{\mathrm{H}}_{\mathrm{mol}}\,\psi(\underline{\mathbf{r}},\underline{\mathbf{R}}) \;=\; E\,\psi(\underline{\mathbf{r}},\underline{\mathbf{R}}) \quad . \tag{2.2}$$

Even for the comparably small hydrogen molecule H_2, this problem is already 12-dimensional ($3n_{\mathrm{e}} = 3N_{\mathrm{nuc}} = 6$). An ansatz to simplify this problem arises from the huge mass difference between electrons and nuclei ($M_k \gg m_e$) which is expected to lead to a much slower nuclear motion compared to the electronic one. Thus, electrons may follow changes of the nuclear geometry adiabatically. The starting point is the solution of the electronic Schrödinger equation

$$\hat{\mathrm{H}}_{\mathrm{e}}\,\Phi_n(\underline{\mathbf{r}};\underline{\mathbf{R}}) \;=\; \mathcal{E}_n(\underline{\mathbf{R}})\,\Phi_n(\underline{\mathbf{r}};\underline{\mathbf{R}}) \tag{2.3}$$

for different, fixed nuclear geometries $\underline{\mathbf{R}}$ (the nuclear geometry $\underline{\mathbf{R}}$ is separated by ";" in the argument of the wave function Φ_n to denote that it is a parameter). This is the first step of the Born-Oppenheimer approximation (however, the set of eigenstates $\Phi_n(\underline{\mathbf{r}};\underline{\mathbf{R}})$ can also be used as a basis to solve the full problem Eq. (2.2) as discussed later in this section). Within the Born-Oppenheimer approximation, the action of the nuclear momentum operator on the electronic wave function is neglected, $\hat{\mathrm{P}}_k\,\Phi_n(\underline{\mathbf{r}};\underline{\mathbf{R}}) = 0$. The *Born-Oppenheimer ansatz*

$$\psi^{\mathrm{BO}}_{n\nu}(\underline{\mathbf{r}},\underline{\mathbf{R}}) \;=\; \chi_{n\nu}(\underline{\mathbf{R}})\,\Phi_n(\underline{\mathbf{r}};\underline{\mathbf{R}}) \tag{2.4}$$

separates the total wave function ψ into a single product of an electronic wave function Φ obtained from the solution of Eq. (2.3) and a nuclear wave function χ. Inserting this ansatz into Eq. (2.2) leads to the *Born-Oppenheimer equation*

$$\Big(\hat{\mathrm{T}}_{\mathrm{k}} \;+\; \mathcal{E}_n(\underline{\mathbf{R}})\Big)\,\chi_{n\nu}(\underline{\mathbf{R}}) \;=\; E_{n\nu}\,\chi_{n\nu}(\underline{\mathbf{R}}) \tag{2.5}$$

to obtain the nuclear eigenfunctions $\chi_{n\nu}(\underline{\mathbf{R}})$ with quantum number ν for the nuclear problem. Thus, the solution of the electronic problem Eq. (2.3) yields the *Born-Oppenheimer potential-energy surface* $\mathcal{E}_n(\underline{\mathbf{R}})$ in which the nuclear problem is solved. Due to the neglect of the action of the momentum operator on the electronic wave function, $\hat{\mathrm{P}}_k\,\Phi_n(\underline{\mathbf{r}};\underline{\mathbf{R}}) = 0$, there are no electronic transitions driven by the nuclear motion and the total wave function ψ indeed factorizes into the simple product in Eq. (2.4). When a molecule is exposed to a laser field, the field may drive electronic transitions. The simple Born-Oppenheimer ansatz Eq. (2.4) with a single $\Phi_n(\underline{\mathbf{r}};\underline{\mathbf{R}})$

[1] Due to the neglect of any interactions between the electron spins $\underline{\mathbf{s}}$ and nuclear spins $\underline{\sigma}$ the total wave function separates into $\psi_{\mathrm{ges}}(\underline{\mathbf{r}},\underline{\mathbf{R}},\underline{\sigma},\underline{\mathbf{s}}) = \phi(\underline{\mathbf{r}},\underline{\mathbf{R}})f(\underline{\sigma})g(\underline{\mathbf{s}})$. However, the total wave function has to be antisymmetric (or symmetric) under a permutation of identical fermions (bosons). For the hydrogen molecule H_2 the two nuclei (protons) and the two electrons are identical fermions, while for the heavier isotope D_2 the two nuclei are identical bosons. This leads to additional constraints for the electronic and nuclear (rotational) wave functions. For molecules with distinguishable nuclei like HD there is no additional constraint for the nuclear (rotational) wave functions following from symmetry.

is thus not possible. However, as discussed in [56–58] a factorization

$$\psi(\underline{\mathbf{r}}, \underline{\mathbf{R}}, t) = \chi(\underline{\mathbf{R}}, t)\, \Phi(\underline{\mathbf{r}}; \underline{\mathbf{R}}, t) \tag{2.6}$$

with

$$\langle \Phi(\underline{\mathbf{R}}, t) \mid \Phi(\underline{\mathbf{R}}, t) \rangle_{\underline{\mathbf{r}}} = 1 \quad , \tag{2.7}$$

the so-called *exact-factorization*, is formally possible. Here, $\langle ... | ... \rangle_{\underline{\mathbf{r}}}$ abbreviates the integration over the electronic coordinates $\underline{\mathbf{r}}$.

Using the *Born-Huang expansion* (page 406 in [59])

$$\psi(\underline{\mathbf{r}}, \underline{\mathbf{R}}) = \sum_n \chi_n(\underline{\mathbf{R}})\, \Phi_n(\underline{\mathbf{r}}; \underline{\mathbf{R}}) \tag{2.8}$$

the total wave function ψ can be expanded using the electronic eigenstates obtained Φ_n from Eq. (2.3). This expansion is exact if for every $\underline{\mathbf{R}}$ the $\Phi_n(\underline{\mathbf{r}}; \underline{\mathbf{R}})$ form a complete basis for the space spanned by the electronic coordinates $\underline{\mathbf{r}}$. The solutions of Eq. (2.5) can be used to expand the total wave function in Born-Oppenheimer eigenstates,

$$\psi(\underline{\mathbf{r}}, \underline{\mathbf{R}}) = \sum_{n,\nu} c_{n\nu}\, \chi_{n\nu}(\underline{\mathbf{R}})\, \Phi_n(\underline{\mathbf{r}}; \underline{\mathbf{R}}) = \sum_{n,\nu} c_{n\nu}\, \psi^{\mathrm{BO}}_{n\nu}(\underline{\mathbf{r}}, \underline{\mathbf{R}}) \quad , \tag{2.9}$$

which is exact if additionally the nuclear eigenstates $\chi_{n\nu}(\underline{\mathbf{R}})$ form a complete basis for the space spanned by $\underline{\mathbf{R}}$. Inserting the Born-Huang expansion Eq. (2.8) into the molecular Schrödinger equation Eq. (2.2) yields

$$\hat{\mathrm{H}}\, \psi(\underline{\mathbf{r}}, \underline{\mathbf{R}}) = \sum_n \left(\sum_{k=1}^{N_{\mathrm{nuc}}} \frac{\hat{\vec{\mathrm{P}}}_k^{\,2}}{2M_k} + \mathcal{E}_n(\underline{\mathbf{R}}) \right) \chi_n(\underline{\mathbf{R}})\, \Phi_n(\underline{\mathbf{r}}; \underline{\mathbf{R}}) \quad . \tag{2.10}$$

Multiplying from left with $\Phi^*_m(\underline{\mathbf{r}}; \underline{\mathbf{R}})$ and integrating over the electronic coordinates $\underline{\mathbf{r}}$ leads to the $\underline{\mathbf{R}}$-dependent system of equations

$$\langle \Phi_m \mid \hat{\mathrm{H}} \mid \psi \rangle_{\underline{\mathbf{r}}} = \sum_n \sum_{k=1}^{N_{\mathrm{nuc}}} \left\langle \Phi_m \left| \frac{\hat{\vec{\mathrm{P}}}_k^{\,2}}{2\, M_k} \right| \chi_n\, \Phi_n \right\rangle_{\underline{\mathbf{r}}} + \mathcal{E}_m(\underline{\mathbf{R}}) \mid \chi_m \rangle \quad . \tag{2.11}$$

that determine $\chi_m(\underline{\mathbf{R}})$. By applying $\hat{\vec{\mathrm{P}}}_k^{\,2} = -\nabla_k^2$ on $\chi_n(\underline{\mathbf{R}})\, \Phi_n(\underline{\mathbf{r}}; \underline{\mathbf{R}})$ one finds

$$\begin{aligned} \langle \Phi_m \mid \hat{\mathrm{H}} \mid \psi \rangle_{\underline{\mathbf{r}}} = & - \sum_n \sum_{k=1}^{N_{\mathrm{nuc}}} \frac{1}{2M_k} \left(A^{(k)}_{mn} + 2\, \vec{B}^{(k)}_{mn}\, \nabla_k \right) \mid \chi_n \rangle \\ & + \left(\sum_{k=1}^{N_{\mathrm{nuc}}} \frac{\hat{\vec{\mathrm{P}}}_k^{\,2}}{2\, M_k} + \mathcal{E}_m(\underline{\mathbf{R}}) \right) \mid \chi_m \rangle \end{aligned} \tag{2.12}$$

with the *nonadiabatic coupling* terms

$$A_{mn}^{(k)}(\underline{\mathbf{R}}) \;=\; \left\langle \Phi_m(\underline{\mathbf{R}}) \,|\, \nabla_k^2 \,|\, \Phi_n(\underline{\mathbf{R}}) \right\rangle_{\underline{\mathbf{r}}} \tag{2.13}$$

and

$$\vec{B}_{mn}^{(k)}(\underline{\mathbf{R}}) \;=\; \langle \Phi_m(\underline{\mathbf{R}}) \,|\, \nabla_k \,|\, \Phi_n(\underline{\mathbf{R}}) \rangle_{\underline{\mathbf{r}}} \quad . \tag{2.14}$$

If the nonadiabatic couplings are neglected one arrives back at the Born-Oppenheimer equation (2.5).

As shown in the following, the couplings $A_{mn}^{(k)}(\underline{\mathbf{R}})$ can also be derived from $\vec{B}_{mn}^{(k)}(\underline{\mathbf{R}})$.

$$\begin{aligned} \nabla_k \vec{B}_{mn}^{(k)}(\underline{\mathbf{R}}) \;&=\; \nabla_k \,\langle \Phi_m(\underline{\mathbf{R}}) \,|\, \nabla_k \,\Phi_n(\underline{\mathbf{R}}) \rangle_{\underline{\mathbf{r}}} \\ &=\; \langle \nabla_k \,\Phi_m(\underline{\mathbf{R}}) \,|\, \nabla_k \,\Phi_n(\underline{\mathbf{R}}) \rangle_{\underline{\mathbf{r}}} \;+\; \left\langle \Phi_m(\underline{\mathbf{R}}) \,|\, \nabla_k^2 \,\Phi_n(\underline{\mathbf{R}}) \right\rangle_{\underline{\mathbf{r}}} \\ &=\; \langle \nabla_k \,\Phi_m(\underline{\mathbf{R}}) \,|\, \nabla_k \,\Phi_n(\underline{\mathbf{R}}\,) \rangle_{\underline{\mathbf{r}}} \;+\; A_{mn}^{(k)}(\underline{\mathbf{R}}) \quad . \end{aligned} \tag{2.15}$$

Using Eq. (2.15) and the completeness relation of the electronic states for a fixed nuclear geometry $\underline{\mathbf{R}}$ the equation

$$A_{mn}^{(k)}(\underline{\mathbf{R}}) \;=\; \nabla_k \,\vec{B}_{mn}^{(k)}(\underline{\mathbf{R}}) \;-\; \sum_l \,\langle \nabla_k \Phi_m(\underline{\mathbf{R}}) | \Phi_l(\underline{\mathbf{R}}) \rangle_{\underline{\mathbf{r}}} \,\langle \Phi_l(\underline{\mathbf{R}}) | \nabla_k \Phi_n(\underline{\mathbf{R}}) \rangle_{\underline{\mathbf{r}}} \tag{2.16}$$

is obtained. If the electronic eigenstates $\Phi_n(\underline{\mathbf{r}};\underline{\mathbf{R}})$ are chosen to be real the couplings

$$\vec{B}_{mn}^{(k)}(\underline{\mathbf{R}}) \;=\; -\vec{B}_{nm}^{(k)}(\underline{\mathbf{R}}) \tag{2.17}$$

are antisymmetric and

$$\langle \nabla_k \,\Phi_m(\underline{\mathbf{R}}) \,|\, \Phi_l(\underline{\mathbf{R}}) \rangle_{\underline{\mathbf{r}}} \;=\; \vec{B}_{lm}^{(k)}(\underline{\mathbf{R}}) \tag{2.18}$$

yields

$$A_{mn}^{(k)}(\underline{\mathbf{R}}) \;=\; \nabla_k \,\vec{B}_{mn}^{(k)}(\underline{\mathbf{R}}) \;+\; \sum_l \,\vec{B}_{ml}^{(k)}(\underline{\mathbf{R}}) \,\vec{B}_{ln}^{(k)}(\underline{\mathbf{R}}) \quad . \tag{2.19}$$

The requirement for a complete electronic basis set in order to calculate $A_{mn}^{(k)}(\underline{\mathbf{R}})$ can be softened for $m \leq M$ ($M \in \mathbb{N}$) and $n > M$, if $\vec{B}_{mn}^{(k)}(\underline{\mathbf{R}}) \approx 0$ for $m \leq M$ and $n > M$ [60]. Since the couplings $\vec{B}_{mn}^{(k)}(\underline{\mathbf{R}})$ are typically only significantly different from zero for energetically closely spaced Born-Oppenheimer potentials $\mathcal{E}_m(\underline{\mathbf{R}})$ and $\mathcal{E}_n(\underline{\mathbf{R}})$, typically the knowledge of a few $\vec{B}_{mn}^{(k)}(\underline{\mathbf{R}})$ is sufficient to obtain $A_{mn}^{(k)}(\underline{\mathbf{R}})$.

Eq. (2.12) can also be written in vector form (as in [60]) with

$$\psi \;\equiv\; \begin{pmatrix} \chi_1(\underline{\mathbf{R}}) \\ \chi_2(\underline{\mathbf{R}}) \\ \vdots \end{pmatrix} \tag{2.20}$$

such that

$$\hat{\mathrm{H}}\,\psi \;=\; -\sum_{k=1}^{N_{\mathrm{nuc}}} \frac{1}{2M_{\mathrm{k}}} \left(\boldsymbol{\nabla}_k^2 \;+\; \mathbf{A}^{(k)}(\,\underline{\mathbf{R}}\,) \;+\; 2\mathbf{B}^{(k)}(\,\underline{\mathbf{R}}\,)\cdot\boldsymbol{\nabla}_k \right) \psi \;+\; \boldsymbol{\mathcal{E}}(\,\underline{\mathbf{R}}\,)\,\psi \quad . \tag{2.21}$$

Here, $\boldsymbol{\mathcal{E}}(\,\underline{\mathbf{R}}\,)$ is a diagonal matrix containing the Born-Oppenheimer potentials

$$\boldsymbol{\mathcal{E}}(\,\underline{\mathbf{R}}\,) \;=\; \mathrm{diag}(\,\mathcal{E}_1(\,\underline{\mathbf{R}}\,)\,,\,\mathcal{E}_2(\,\underline{\mathbf{R}}\,)\,,\,...\,) \quad , \tag{2.22}$$

$\boldsymbol{\nabla}_k$ is a diagonal matrix containing the nuclear derivatives

$$\boldsymbol{\nabla}_k \;=\; \mathrm{diag}(\,\nabla_k\,,\,\nabla_k\,,\,...\,) \quad , \tag{2.23}$$

and $\mathbf{A}^{(k)}(\,\underline{\mathbf{R}}\,)$ and $\mathbf{B}^{(k)}(\,\underline{\mathbf{R}}\,)$ non-adiabatic coupling matrices with entries according to Eqs. (2.13) and (2.14). Inserting Eq. (2.19) into Eq. (2.21) yields

$$\begin{aligned}
\hat{\mathrm{H}}\psi \;&=\; -\sum_{k=1}^{N_{\mathrm{nuc}}} \frac{1}{2M_{\mathrm{k}}} \Bigg(\boldsymbol{\nabla}_k^2 + [\boldsymbol{\nabla}_k \cdot \mathbf{B}^{(k)}(\,\underline{\mathbf{R}}\,)] + \mathbf{B}^{(k)}(\,\underline{\mathbf{R}}\,)\cdot\mathbf{B}^{(k)}(\,\underline{\mathbf{R}}\,) \\
&\qquad + 2\mathbf{B}^{(k)}(\,\underline{\mathbf{R}}\,)\cdot\boldsymbol{\nabla}_k \Bigg)\,\psi + \boldsymbol{\mathcal{E}}(\,\underline{\mathbf{R}}\,)\psi \\
&=\; -\sum_{k=1}^{N_{\mathrm{nuc}}} \frac{1}{2M_{\mathrm{k}}} \left(\boldsymbol{\nabla}_k + \mathbf{B}^{(k)}(\,\underline{\mathbf{R}}\,) \right)^2 \psi \;+\; \boldsymbol{\mathcal{E}}(\,\underline{\mathbf{R}}\,)\,\psi \\
&\stackrel{!}{=} E\,\psi \quad .
\end{aligned} \tag{2.24}$$

In this compact matrix notation the nuclear momentum operator $\hat{\vec{\mathrm{P}}}_k$ splits according to the product rule

$$\nabla\left(f(\,\underline{\mathbf{R}}\,)\,g(\,\underline{\mathbf{R}}\,)\right) \;=\; \left(\nabla f(\,\underline{\mathbf{R}}\,)\right) g(\,\underline{\mathbf{R}}\,) \;+\; f(\,\underline{\mathbf{R}}\,)\left(\nabla g(\,\underline{\mathbf{R}}\,)\right) \tag{2.25}$$

into a part ($\boldsymbol{\nabla}_k$) that acts only on the nuclear wave functions and a part $\mathbf{B}^{(k)}(\,\underline{\mathbf{R}}\,)$ that acts only on the electronic wave functions[2]. This is even more obvious when expanding the full problem in Born-Oppenheimer eigenstates (Eq. (2.9)). The nuclear

[2] This looks similar to the minimal coupling $\hat{\vec{\mathrm{p}}} \to \hat{\vec{\mathrm{p}}} - q\vec{A}$ (see Section 2.5 where the interaction of a charged particle (charge q) with a laser field (vector potential $\vec{A}$) is described).

kinetic-energy operator leads to the matrix elements[3]

$$\begin{aligned}\left\langle \chi_{n\nu}\,\Phi_n \,|\, \nabla_k^2 \,|\, \chi_{n'\nu'}\,\Phi_{n'} \right\rangle &= \sum_{n''\nu''} \left\langle \chi_{n\nu}\Phi_n \,|\, \nabla_k \,|\, \chi_{n''\nu''}\,\Phi_{n''} \right\rangle \left\langle \chi_{n''\nu''}\,\Phi_{n''} \,|\, \nabla_k \,|\, \chi_{n'\nu'}\,\Phi_{n'} \right\rangle \\ &\equiv \sum_{n''\nu''} \left(i\tilde{\vec{P}}^{(k)}_{n\nu n''\nu''} + \tilde{\vec{B}}^{(k)}_{n\nu n''\nu''} \right)\left(i\tilde{\vec{P}}^{(k)}_{n''\nu'' n'\nu'} + \tilde{\vec{B}}^{(k)}_{n''\nu'' n'\nu'} \right) \\ &= \left(i\tilde{\mathbf{P}}^{(k)} + \tilde{\mathbf{B}}^{(k)} \right)^2_{n\nu n'\nu'} \quad , \end{aligned} \tag{2.26}$$

where the matrices $\tilde{\mathbf{P}}^{(k)}$ and $\tilde{\mathbf{B}}^{(k)}$ contain the elements

$$i\tilde{\vec{P}}^{(k)}_{n\nu n'\nu'} = \left\langle \chi_{n\nu}\,\Phi_n \,|\, (\nabla_k \chi_{n'\nu'})\,\Phi_{n'} \right\rangle \tag{2.27}$$

and

$$\tilde{\vec{B}}^{(k)}_{n\nu n'\nu'} = \left\langle \chi_{n\nu}\,\Phi_n \,|\, \chi_{n'\nu'}\,(\nabla_k \Phi_{n'}) \right\rangle \quad . \tag{2.28}$$

Until now the eigenvalue problem Eq. (2.2) was just reformulated. By choosing appropriate coordinates, exploiting symmetries and introducing approximations the problem will be simplified in the following sections.

2.2 Nuclear Motion in Diatomic Molecules

The treatment of the six-dimensional nuclear motion of molecular hydrogen can be greatly simplified by choosing an appropriate coordinate system. The first simplification arises from introducing center-of-mass

$$\vec{R}_S = \frac{1}{2}\left(\vec{R}_1 + \vec{R}_2 \right) \tag{2.29}$$

and relative coordinates

$$\vec{R} = \vec{R}_2 - \vec{R}_1 \quad . \tag{2.30}$$

After separation of the center-of-mass motion and neglect of the mass polarization term[4] the relative coordinate electronic Hamiltonian reads

$$\hat{\mathrm{H}}(\underline{\mathbf{r}}\,, \vec{R}\,) = -\frac{1}{2\mu}\nabla^2_{\vec{R}} + \hat{\mathrm{H}}_\mathrm{e}(\underline{\mathbf{r}}\,; R\,) \tag{2.31}$$

[3] The completeness relation $\sum_{n\nu} |\chi_{n\nu}\Phi_n\rangle \langle \chi_{n\nu}\Phi_n| = 1$ for the space spanned by the electronic coordinates $\underline{\mathbf{r}}$ and the nuclear coordinates $\underline{\mathbf{R}}$ can be used between $\nabla_k\nabla_k$ here. In Eq. (2.13) this is not so easily possible with completeness relation $\sum_n |\Phi_n\rangle \langle \Phi_n| = 1$ which is valid for every $\underline{\mathbf{R}}$, since ∇_k leads to a variation in $\underline{\mathbf{R}}$.

[4] This usually small correction term follows from the transformation from a fixed coordinate system to a coordinate system where the electron moves relatively to the nuclei. In [61] this term was included to describe the electronic ground state of HeT^+ with very high accuracy.

with reduced mass $\mu = \dfrac{M_A\,M_B}{M_A + M_B}$ and masses M_A (M_B) of the nuclei A (B). The Born-Huang expansion

$$\psi(\underline{\mathbf{r}}\,,\,\vec{R}\,) \;=\; \sum_n \tilde{\chi}_n(\,\vec{R}\,)\,\Phi_n(\underline{\mathbf{r}}\,;\,R\,) \tag{2.32}$$

inserted into Eq. (2.31) yields

$$\hat{\mathrm{H}}\,\psi(\underline{\mathbf{r}}\,,\,\vec{R}\,) \;=\; \sum_n \left(-\frac{1}{2\mu}\nabla^2_{\vec{R}} + \mathcal{E}_n(\,R\,)\right)\tilde{\chi}_n(\,\vec{R}\,)\,\Phi_n(\underline{\mathbf{r}}\,;\,R\,) \quad . \tag{2.33}$$

The spherical symmetry suggests the introduction of spherical coordinates $(\,R\,,\,\theta\,,\,\varphi\,)$ for the description of the relative motion $\vec{R}$ (similarly to the solution of the hydrogen atom in three dimensions). The Laplacian in spherical coordinates is

$$\begin{aligned}\Delta_{\vec{R}} \;=\; \nabla^2_{\vec{R}} \;&=\; \frac{1}{R^2}\,\frac{\partial}{\partial R}\left(R^2\,\frac{\partial}{\partial R}\right) \;+\; \frac{1}{R^2}\left(\frac{1}{\sin\theta}\,\frac{\partial}{\partial\theta}\left(\sin\theta\,\frac{\partial}{\partial\theta}\right) \;+\; \frac{1}{\sin^2\theta}\,\frac{\partial^2}{\partial\varphi^2}\right) \\ &=\; \frac{1}{R^2}\,\frac{\partial}{\partial R}\left(R^2\,\frac{\partial}{\partial R}\right) \;+\; \frac{1}{R^2}\,\Delta_{\theta,\varphi} \quad .\end{aligned} \tag{2.34}$$

Eigenfunctions of $\Delta_{\theta,\varphi}$ are the spherical harmonics $Y_{JM_J}(\,\theta\,,\,\varphi\,)$ fulfilling

$$\Delta_{\theta,\varphi}\,Y_{JM_J}(\theta,\varphi) \;=\; -J\,(\,J\,+\,1\,)\,Y_{JM_J}(\,\theta\,,\,\varphi\,) \quad . \tag{2.35}$$

Using

$$\tilde{\chi}_n(\,\vec{R}\,) \;=\; \sum_{JM_J} \frac{\chi_{nJM_J}(\,R\,)}{R}\,Y_{JM_J}(\theta,\varphi) \tag{2.36}$$

Eq. (2.33) can be written as

$$\begin{aligned}\hat{\mathrm{H}}\,\psi(\underline{\mathbf{r}}\,,\,\vec{R}\,) \;&=\; \sum_{n,J,M_J}\left(-\frac{1}{2\mu R^2}\frac{\partial}{\partial R}\left(R^2\frac{\partial}{\partial R}\right) + \frac{J(J+1)}{2\mu R^2} + \mathcal{E}_n(\,R\,)\right)\frac{\chi_{nJM_J}}{R}\Phi_n\,Y_{JM_J} \\ &=\; E\,\psi(\underline{\mathbf{r}}\,,\,\vec{R}\,)\end{aligned} \tag{2.37}$$

or

$$\begin{aligned}(\hat{\mathrm{H}} - E)\,\psi(\underline{\mathbf{r}}\,,\,\vec{R}\,) \;&=\; \sum_{n,J,M_J}\left[\left(-\frac{1}{2\mu}\frac{\partial^2}{\partial R^2} + \frac{J(J+1)}{2\mu R^2} + \mathcal{E}_n(\,R\,) - E\right)\chi_{nJM_J}\right]\Phi_n\,Y_{JM_J} \\ &\quad - \sum_{n,J,M_J}\frac{1}{2\mu}\left(2\left[\frac{\partial}{\partial R}\chi_{nJM_J}\right]\left[\frac{\partial}{\partial R}\Phi_n\right] + \chi_{nJM_J}\left[\frac{\partial^2}{\partial R^2}\Phi_n\right]\right)Y_{JM_J} \\ &=\; 0 \quad .\end{aligned} \tag{2.38}$$

Analogously to Section 2.1 the Born-Oppenheimer approximation and the treatment of the full problem with non-adiabatic couplings follows from the replacement $\nabla \rightarrow \frac{\partial}{\partial R}$. The wave functions $\chi_{n\nu JM_J}$ describe the vibration of the molecule and the spherical harmonics Y_{JM_J} describe the molecular rotation[5]. The rotation influences the vibration by a centrifugal barrier $J(J+1)/(2\mu R^2)$. The bound Born-Oppenheimer vibrational states $\chi_{n\nu JM_J}(R)$ are normalized according to

$$\iiint R^2 \sin\theta \frac{|\chi_{n\nu JM_J}|^2}{R^2} |Y_{JM_J}(\theta, \varphi)|^2 \, \mathrm{d}R \, \mathrm{d}\theta \, \mathrm{d}\varphi = \int_0^\infty |\chi_{n\nu JM_J}(R)|^2 \, \mathrm{d}R \stackrel{!}{=} 1 \tag{2.39}$$

as the spherical harmonics are normalized to 1. In addition to the mass-polarization term this derivation neglects that the electronic problem is solved in a coordinate system which rotates together with the (fixed) nuclei. Consideration of this effect adds another non-adiabatic coupling term of the form [61]

$$\tilde{A}_{mn}(R) = A_{mn}(R) + \left\langle \Phi_m(R) \right| - \frac{1}{R^2} \left(\hat{\mathrm{L}}_x^2 + \hat{\mathrm{L}}_y^2 \right) \left| \Phi_n(R) \right\rangle_{\underline{\mathbf{r}}} \tag{2.40}$$

with the total angular-momentum operators $\hat{\mathrm{L}}_x^2$ and $\hat{\mathrm{L}}_y^2$ of the electrons. If the projection Λ of the total angular momentum of the electrons on the internuclear axis is different from zero, the centrifugal barrier is modified according to [61]

$$\frac{J(J+1)}{2\mu R^2} \rightarrow \frac{J(J+1) - \Lambda^2}{2\mu R^2} \tag{2.41}$$

with $J(J+1) > \Lambda^2$. In the following the additional couplings in $\tilde{A}_{mn}(R)$, Eq. (2.40), are neglected and only Σ states ($\Lambda = 0$) are considered[6] such that the problem is given by Eq. (2.38).

2.3 Vibrational Motion in Ammonia: the Inversion Motion

The nuclear motion of NH_3 has 12 nuclear degrees of freedom resulting from 4 nuclei $\times$ 3 dimensions. Those can be divided into 3 rotational degrees of freedom, 3 center-of-mass degrees of freedom and 6 vibrational degrees of freedom. An elaborate treatment including the 6 vibrational degrees of freedom as, e.g., in Ref. [62] is a tedious

[5] As noted in Section 2.1 the nuclear spin has to be considered for the symmetry of the total wave function. This leads to a restriction of the possible symmetry of the rotational wave function under exchange of identical Fermions or Bosons.

[6] States with $\Lambda > 0$ will be used within this thesis to describe orientation-dependent ionization of H_2. However, in this case the ionization process is treated within the approximation of spatially fixed nuclei.

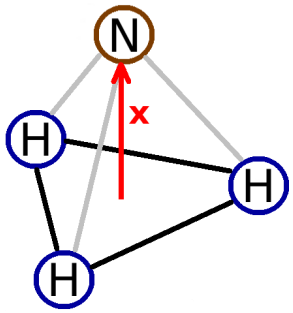

Figure 2.1: Geometry of the NH_3 molecule. The inversion coordinate x (red arrow) describes the distance of the nitrogen atom to the center of the triangle spanned by the three hydrogen atoms (for a negative x the nitrogen atom is located below the triangle).

task even if only the ground state of NH_3 is considered. In many cases, however, considering the inversion (or umbrella) motion is a sufficiently good approximation. This vibration is described by the inversion coordinate x, see Figure 2.1, which describes the distance of the nitrogen atom to the center of the triangle spanned by the three hydrogen atoms. Transitions between the eigenstates of this inversion motion are used for the ammonia maser [63] where the maser frequency is given by the energy difference of the two lowest inversion eigenenergy levels. Luckily, it has also been observed that the inversion motion is the only significantly excited vibration upon strong-field ionization[7] [21] and thus a treatment restricted to this motion is indeed a good approximation. In the simplest approximation the inversion motion Hamiltonian is given by

$$\hat{\mathrm{H}}_{\mathrm{inv}} = \frac{1}{2\mu}\,\hat{\mathrm{p}}^{\,2} + V_{\mathrm{inv}}(x) \tag{2.42}$$

with the reduced mass

$$\mu = \frac{3\,m\,M}{3\,m + M} \tag{2.43}$$

where m is the mass of the hydrogen atom and M is the mass of the nitrogen atom. This reduced mass hints actually to physical similarities of the inversion motion of NH_3 to the vibration of diatomic molecules (discussed the section before). If one would replace the three H atoms of NH_3 by a single atom with mass $3m$ in the center of the triangle, the reduced mass of this "diatomic" case with "internuclear distance" x is given by Eq. (2.43). For the electronic ground state of NH_3, the Born-Oppenheimer potential $V_{\mathrm{inv}}(x)$ of this inversion motion is a double-well potential with two minima at $\pm x_{\mathrm{eq}}$. This leads to the pyramidal shape of the rovibrational ground state of NH_3 as depicted in Figure 2.1. The eigenstates of this inversion motion are calculated and visually shown later in Section 4.1.3 for an improved one-dimensional model. This improved (but still simple) one-dimensional model yields

[7] This holds only for ionization from the highest occupied molecular orbital.

surprisingly good agreement for the inversion energy levels of NH_3 and ND_3 when compared to experiments and higher dimensional theoretical studies.

2.4 Time Scales of Electronic and Nuclear Motions in Small Molecules

Typical time scales of the electronic motion, vibration, and rotation of a molecule can be estimated from the energy differences of the quantum-mechanical eigenstates. A wave packet consisting of two eigenstates $|\,0\,\rangle$ and $|\,1\,\rangle$ with coefficients c_0 and c_1 as well as energies E_0 and E_1 ($\Delta E = E_1 - E_0$),

$$|\,\Psi(t)\,\rangle = c_0\, e^{-iE_0 t}\,|\,0\,\rangle + c_1\, e^{-iE_1 t}\,|\,1\,\rangle = e^{-iE_0 t}\left(c_0\,|\,0\,\rangle + c_1\, e^{-i\Delta E t}\,|\,1\,\rangle\right), \quad (2.44)$$

is periodic within $T = 2\pi/\Delta E$. Energy differences of bound electronic states of H_2 for a fixed nuclear distance are of the order of $\Delta E \approx 0.25$ a.u. This corresponds to a sub-femtosecond time scale $T \approx 0.6$ fs.

In the electronic ground state of neutral molecular hydrogen H_2 the energy difference of the lowest two Born-Oppenheimer vibrational eigenstates leads to a time scale of $T \approx 8$ fs [30]. For the heavier isotope D_2 the oscillation period $T \approx 11$ fs has even been experimentally imaged in real-time [31] using the *Lochfraß* effect (Section 4.6.1). Molecular vibrations thus occur on a few femtosecond time scale.

Rotational energies are given by $E = J(J+1)/(2\,\mu\, R_{\mathrm{fix}}^2)$ within the rigid rotor model. For the equilibrium internuclear distance $R_{\mathrm{fix}} = 1.4$ a.u. of the electronic ground state of H_2 and a wave packet consisting of the states[8] J and $J-2$ one finds a time scale of $T \approx 270/(2J-1)$ fs. The time scale of molecular rotation is thus of the order of 100 fs.

In this thesis short laser pulses on the order of 10 fs are considered. Molecular vibration during the laser field should thus have a larger influence on the dynamics than the rotation of the molecule. In the following, rotational motion is thus considered to be *frozen*.

2.5 Interaction with Intense, Ultrashort Laser Fields

For the moderate to high laser field intensities considered in this work, quantum effects of the electromagnetic radiation play practically no role, i.e. due to the large photon number the photon statistics does not change even for the absorption or emission of hundreds of photons. Thus, the laser field can be treated classically. The electric field $\vec{F}(\vec{r}\,,t\,)$ and magnetic field $\vec{B}(\vec{r}\,,t\,)$ fulfill Maxwell's equations.

[8] A wave packet consisting of directly neighboring states, e.g., J and $J-1$, is not easily producible since the total have function has to be antisymmetric under permutation of the protons (identical Fermions).

Alternatively the fields can be described by the vector potential $\vec{A}(\vec{r},t)$ and scalar potential $\phi(\vec{r},t)$ such that

$$\vec{F}(\vec{r},t) = -\nabla\phi(\vec{r},t) - \frac{\partial}{\partial t}\vec{A}(\vec{r},t) \tag{2.45}$$

$$\vec{B}(\vec{r},t) = \nabla\times\vec{A}(\vec{r},t) \quad . \tag{2.46}$$

The fields $\vec{F}(\vec{r},t)$ and $\vec{B}(\vec{r},t)$ remain invariant under a gauge transformation $T(\vec{r},t)$ which transforms the electromagnetic potentials according to

$$\vec{A}'(\vec{r},t) = \vec{A}(\vec{r},t) - \nabla T(\vec{r},t) \tag{2.47}$$

$$\phi'(\vec{r},t) = \phi(\vec{r},t) + \frac{\partial}{\partial t}T(\vec{r},t) \quad . \tag{2.48}$$

The interaction of a particle with charge q and mass m (electrons, nuclei) in a potential $V(\vec{r})$ in a laser field is described by the Hamiltonian

$$\hat{\mathrm{H}} = \frac{1}{2m}\left(\hat{\vec{\mathrm{p}}} - q\vec{A}(\vec{r},t)\right)^2 + q\phi(\vec{r},t) + V(\vec{r}) \tag{2.49}$$

with "minimal coupling" $\hat{\vec{\mathrm{p}}} \to \hat{\vec{\mathrm{p}}} - q\vec{A}$ [64]. The corresponding Schrödinger equation $i\frac{\partial}{\partial t}\Psi(\vec{r},t) = \hat{\mathrm{H}}\Psi(\vec{r},t)$ remains invariant under the gauge transformation $T(\vec{r},t)$ with

$$\Psi(\vec{r},t)' = \Psi(\vec{r},t)\,e^{-iqT(\vec{r},t)} \quad . \tag{2.50}$$

In addition to $\vec{F}' = \vec{F}$ and $\vec{B}' = \vec{B}$ also the probability density $|\Psi(\vec{r},t)'|^2 = |\Psi(\vec{r},t)|^2$ remains gauge invariant. Operators belonging to observables, $\hat{\mathrm{O}}$, are furthermore form-invariant with respect to the unitary gauge transformation $\hat{\mathrm{T}} = e^{-iqT(\vec{r},t)}$, such that

$$\hat{\mathrm{O}}' = \hat{\mathrm{T}}\,\hat{\mathrm{O}}\,\hat{\mathrm{T}}^\dagger = e^{-iqT(\vec{r},t)}\,\hat{\mathrm{O}}\,e^{iqT(\vec{r},t)} \tag{2.51}$$

and thus

$$\left\langle \Psi'_a \,\middle|\, \hat{\mathrm{O}}' \,\middle|\, \Psi'_b \right\rangle = \left\langle \Psi_a \,\middle|\, \hat{\mathrm{T}}^\dagger\,\hat{\mathrm{T}}\,\hat{\mathrm{O}}\,\hat{\mathrm{T}}^\dagger\,\hat{\mathrm{T}} \,\middle|\, \Psi_b \right\rangle \tag{2.52}$$

holds. This is, e.g., fulfilled for the instantaneous energy operator[65]

$$\hat{\mathcal{H}} \equiv \hat{\mathrm{H}} - q\phi(\vec{r},t) \quad , \tag{2.53}$$

but not for the full Hamiltonian $\hat{\mathrm{H}}$, which however describes the time evolution of the quantum system.

In the following different gauges of the electromagnetic field propagating in free space are discussed. The starting point is the radiation gauge[9] (index "RG"), in

[9] In the case of a free radiation field this is the Coulomb gauge.

which

$$\nabla \cdot \vec{A}_{\mathrm{RG}} = 0 \,, \quad \phi_{\mathrm{RG}} = 0 \tag{2.54}$$

holds. For the Hamiltonian in radiation gauge follows

$$\hat{\mathrm{H}}_{\mathrm{RG}} = \frac{1}{2m} \left(\hat{\vec{\mathrm{p}}}^2 - 2\,q\,\vec{A}_{\mathrm{RG}}(\vec{r},\,t\,) \cdot \hat{\vec{\mathrm{p}}} + q^2 \left| \vec{A}_{\mathrm{RG}}(\vec{r},\,t\,) \right|^2 \right) + V(\vec{r}) \quad . \tag{2.55}$$

The vector potential $\vec{A}_{\mathrm{RG}}$ satisfies the wave equation

$$\nabla^2 \vec{A}_{\mathrm{RG}} = \frac{1}{c^2} \frac{\partial^2}{\partial t^2} \vec{A}_{\mathrm{RG}} \quad , \tag{2.56}$$

due to the Maxwell equation $\nabla \times \vec{B} = \frac{1}{c^2} \frac{\partial}{\partial t} \vec{F}$ (speed of light c). The solutions of Eq. (2.56) can be written as a superposition of plane waves $\exp\left[i(\,\vec{k}\,\vec{r} - \omega\,t) \right]$ with $|\vec{k}\,| = \omega/c = 2\pi/\lambda$. The circular frequency ω and wavelength λ are the experimentally relevant laser-field parameters. The wavelengths considered in this work are of the order $\lambda \geq 100$ nm, while the wave functions of the small molecules considered here extend up to around 1 nm. Thus

$$\left| \vec{k}\,\vec{r} \right| \leq \left| \vec{k}\,\right| \left| \vec{r} \right| \ll 1 \quad , \tag{2.57}$$

such that the dipole approximation

$$e^{i\,\vec{k}\,\vec{r}} \approx 1 \tag{2.58}$$

is well justified. Thus, $\vec{A}_{\mathrm{RG}}(\,\vec{r},\,t\,) \approx \vec{A}_{\mathrm{RG}}(t)$ can be treated as position-independent. This also leads to the neglect of the magnetic field $\vec{B}(\,\vec{r},\,t\,) = \nabla \times \vec{A}_{\mathrm{RG}}(\,\vec{r},\,t\,) \approx 0$, which is well justified for the here considered non-relativistic limit[10].

For the numerical treatment of systems in a laser field within the dipole approximation, usually not the radiation gauge, but rather the velocity gauge (index VG) or length gauge (LG) is adopted. This allows to eliminate the term quadratic in the vector potential (VG) or the vector potential altogether while introducing a non-zero scalar potential (LG). The gauge transformation

$$T_{\mathrm{VG}}(\,\vec{r},\,t\,) = -\frac{q}{2m} \int^{t} \left| \vec{A}_{\mathrm{RG}}(\vec{r},t') \right|^2 \mathrm{d}t' \equiv f(\,\vec{r},\,t\,) \tag{2.59}$$

[10] The magnetic field contributes to the Lorentz force by $q\vec{v} \times \vec{B}$ (classical velocity vector $\vec{v}$). Compared to the contribution of the electric field, $q\vec{F}$, this contribution is (for plane waves) a factor $|\vec{v}\,|/c$ smaller. For a hydrogen atom in the ground state one finds $\langle |\vec{v}\,| \rangle = \alpha c$ with the fine structure constant $\alpha \approx 1/137$.

allows to transform from radiation gauge to velocity gauge with

$$\vec{A}_{\mathrm{VG}} \,=\, \vec{A}_{\mathrm{RG}} \,-\, \nabla\, f(\,\vec{r}\,,\,t\,)\;, \quad \phi_{\mathrm{VG}} \,=\, -\,\frac{q\,\left|\,\vec{A}_{\mathrm{RG}}\,\right|^2}{2m} \quad . \tag{2.60}$$

The corresponding operator in dipole approximation reads[11]

$$\hat{\mathrm{H}}_{\mathrm{VG}} \,=\, \frac{1}{2m}\,\hat{\vec{\mathrm{p}}}^{\,2} \,+\, V(\,\vec{r}\,) \,-\, \frac{q}{m}\,\vec{A}_{\mathrm{RG}}(\,\vec{r}\,,\,t\,)\cdot\hat{\vec{\mathrm{p}}} \tag{2.61}$$

The transformation from radiation gauge to length gauge is achieved with the gauge transformation

$$T_{\mathrm{LG}}(\,\vec{r}\,,\,t\,) \,=\, \vec{A}_{\mathrm{RG}}(\,\vec{r}\,,\,t\,)\cdot\vec{r} \tag{2.62}$$

such that

$$\vec{A}_{\mathrm{LG}} \,=\, \vec{A}_{\mathrm{RG}} \,-\, \nabla(\vec{A}_{\mathrm{RG}}\cdot\vec{r}\,)\;, \quad \phi_{\mathrm{LG}} \,=\, -\vec{F}\cdot\vec{r} \quad . \tag{2.63}$$

In dipole approximation, $\vec{A}_{\mathrm{LG}} = \vec{0}$ follows and the Hamiltonian reads[11]

$$\hat{\mathrm{H}}_{\mathrm{LG}} \,=\, \frac{1}{2m}\,\hat{\vec{\mathrm{p}}}^{\,2} \,+\, V(\vec{r}\,) \,-\, q\,\vec{F}\cdot\vec{r} \quad . \tag{2.64}$$

The interaction of a laser field with a molecule is described by the interaction potential which reads in velocity gauge

$$-\sum_{k=1}^{N_{\mathrm{nuc}}}\frac{Z_k}{M_k}\,\vec{A}_{\mathrm{RG}}(t)\cdot\hat{\vec{\mathrm{P}}}_k \,+\, \sum_{i=1}^{n_{\mathrm{e}}}\vec{A}_{\mathrm{RG}}(t)\cdot\hat{\vec{\mathrm{p}}}_i \,\equiv\, V^{\mathrm{VG}}_{\mathrm{k,int}}(\,\underline{\mathbf{R}}\,,\,t\,) \,+\, V^{\mathrm{VG}}_{\mathrm{e,int}}(\,\underline{\mathbf{r}}\,,\,t\,) \tag{2.65}$$

and in length gauge

$$-\sum_{k=1}^{N_{\mathrm{nuc}}} Z_k\,\vec{F}(t)\cdot\vec{R}_k \,+\, \sum_{i=1}^{n_{\mathrm{e}}}\vec{F}(t)\cdot\vec{r}_i \,\equiv\, V^{\mathrm{LG}}_{\mathrm{k,int}}(\,\underline{\mathbf{R}}\,,\,t\,) \,+\, V^{\mathrm{LG}}_{\mathrm{e,int}}(\,\underline{\mathbf{r}}\,,\,t\,) \quad . \tag{2.66}$$

Results obtained within length- or velocity gauge lead to identical results if no approximations are introduced. For example, the dipole approximation introduces a gauge dependence (outside its validity regime). Furthermore, numerical calculations employ a restricted Hilbert space and the *effort* to obtain converged results is strongly gauge dependent. Usually, one observes a much faster convergence behavior within velocity gauge, which is thus preferably used in numerical calculations. On the other hand, the length gauge leads to a widely used simple picture to describe ionization in the quasistatic regime. The laser field tilts the binding potential of the electron, allowing for the electron to escape the binding potential by tunneling

[11] The more general case not using the dipole approximation is found, e.g., in [65], page 78.

or even by moving over the barrier (if the tilt is strong enough). Typical pictures for ionization processes are discussed in Section 2.6. In velocity gauge, on the other hand, the electron escapes the binding potential by obtaining a "momentum kick". Since the physics of the process is gauge independent, these two pictures are equivalent.

2.6 Ionization Mechanisms

Single ionization (i.e. the removal of a single electron[12]) is one of the most basic processes occurring when an atom or molecule is exposed to an intense, ultrashort laser field. For the ionization process there exist different regimes with corresponding simple physical pictures which will be discussed in the following.

The Keldysh parameter [66]

$$\gamma = \frac{\omega}{F_0/\sqrt{2E_\mathrm{b}}} \tag{2.67}$$

with field strength amplitude F_0 and binding energy E_b (also called ionization potential) compares the time scale of the laser field ($1/\omega$) with the time scale with which a system can react to the laser field $\left(\frac{\sqrt{2E_\mathrm{b}}}{F_0}\right)$. Figure 2.2 shows the separation of different ionization regimes for different (scaled) laser frequencies and field strengths. Furthermore, Figure 2.3 illustrates the ionization processes in the respective ionization regimes discussed in the following for the example of a hydrogen atom.

The laser field changes slowly compared to the time scale of the system for $\gamma \ll 1$. The system can follow the field adiabatically. The time-dependent problem can then be seen as a sequence of time-independent (static) problems. This regime is called *quasistatic regime* (lower row of Figure 2.3). In length gauge, this leads to the simple picture that the laser field tilts the binding potential of the system. Consequently, a previously bound electron can tunnel through the tilted binding potential (*tunneling regime*, Fig. 2.3 bottom left) or, for higher field strengths, leave the system directly over the barrier (*over-the-barrier regime*, Fig. 2.3 bottom center).

For $\gamma \gg 1$, on the other hand, the laser field oscillates quickly compared to the time scale of the system (upper row of Figure 2.3). Thus, the system cannot follow the change of the potential adiabatically. In a simple picture, ionization occurs by absorbing one or multiple photons from the laser field (Fig. 2.3 top center). This regime is thus called *singlephoton regime* ($\omega \geq E_\mathrm{b}$) or *multiphoton regime* ($\omega < E_\mathrm{b}$). Despite this simple picture, this ionization process does not require a quantized radiation field. Any periodic perturbation of the system leads to this behavior. The Fourier transform of a classical field with frequency ω leads to a peak at frequency

[12] Also double- and multiple ionization is possible, occurring with a lower probability. In this thesis, only single ionization is considered.

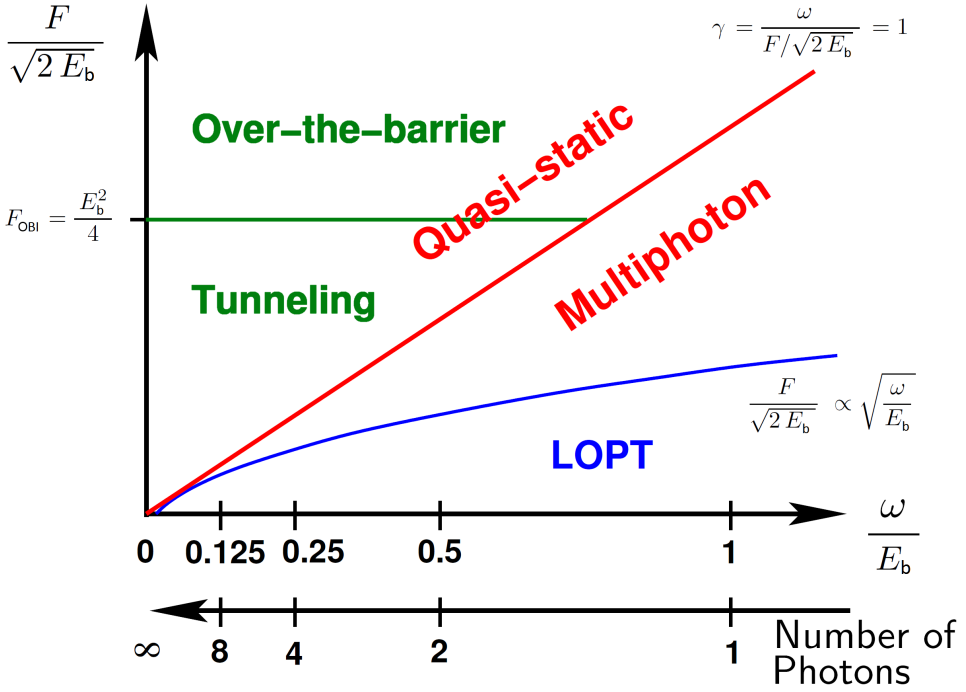

Figure 2.2: Ionization regimes depending on the scaled laser frequency ω/E_b and scaled field strength $F/\sqrt{2E_\mathrm{b}}$. The red line (Keldysh parameter $\gamma = 1$) separates the quasistatic and the multiphoton regimes. The green line further separates the quasistatic regime into the tunneling regime and the over-the-barrier regime. The blue line separates the LOPT regime from the remaining multiphoton regime. This figure is taken from a presentation of Alejandro Saenz (modified).

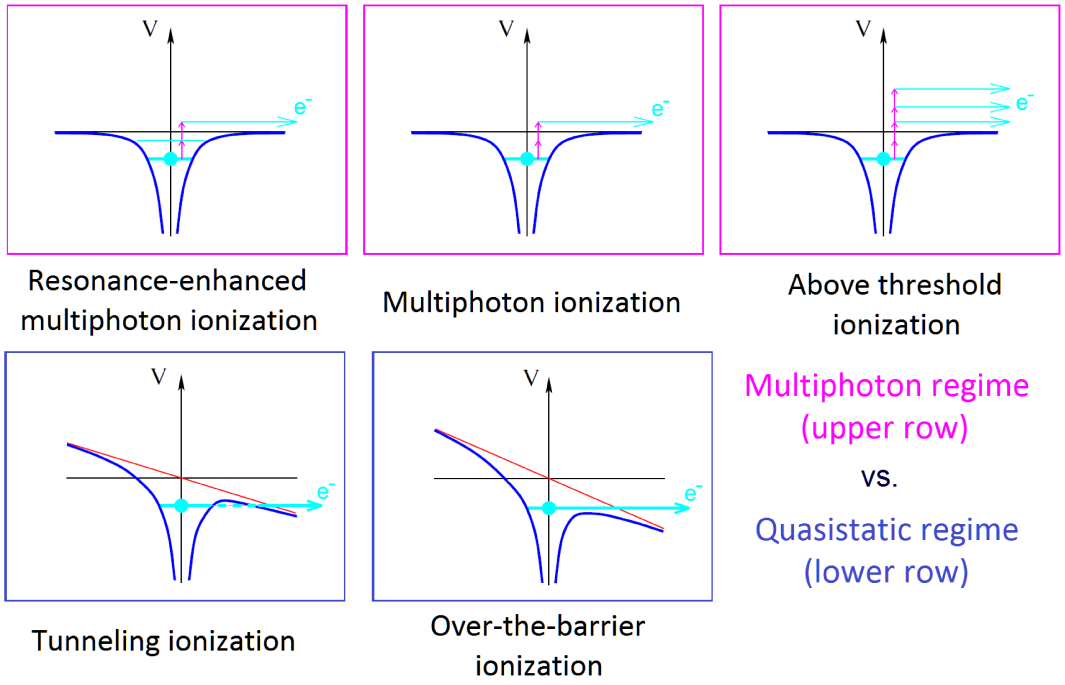

Figure 2.3: Illustration of different ionization processes in intense, ultrashort laser fields for a hydrogen atom (potential according to the dark blue lines). The light blue lines indicate the energy levels of the electron while the light blue arrows indicate the free electron.
Upper row: Multiphoton regime, in which "photons" are absorbed (violet arrows) which may lead to resonance enhanced multiphoton ionization, multiphoton ionization and above threshold ionization.
Lower row: Quasistatic regime, in which the interaction potential of the laser field in lenght gauge (red line) tilts the binding potential (blue line) which enables tunneling ionization and over-the-barrier ionization. The figures are taken from a presentation of Alejandro Saenz (modified).

ω in the frequency/energy domain. The quantized system with its discrete energy levels then reacts to this perturbation. It is thus the quantization of the particle (atom, molecule, ...) and not the quantization of the electromagnetic field which is observed in experiments at the moderate to high intensities discussed here[13]. It is possible that more photons are absorbed than the number required to overcome the ionization threshold. This process is called *above-threshold ionization* (*ATI*, Fig. 2.3 top right). Furthermore, the probability of ionization can be significantly enhanced if one of the bound states of the system is resonantly excited. This process is called *resonance-enhanced multiphoton ionization* (*REMPI*, Fig. 2.3 top left). In the case of small laser intensities (around 10^{12} W/cm^2) single- and multiphoton ionization can be theoretically described within lowest-order perturbation theory ($\rightarrow$ *LOPT* or *perturbative regime*). Starting point is the time-dependent perturbation theory. Typically, a monochromatic field with $\sin(\omega t)$ time dependence is considered. For the duration of the interaction the limit $T \rightarrow \infty$ is taken such that the result becomes time-independent [67]. When comparing results obtained within LOPT to the time-dependent Schrödinger equation one has to consider that ultrashort laser fields (Section 2.7) do not simply consist of a single, sharp frequency ω. They rather have a frequency distribution with bandwidth $\Delta\omega$ where shorter laser fields are broader in frequency space. With increasing laser-field duration $\Delta\omega$ becomes smaller such that the predictions made by LOPT should become more accurate.

2.7 Time Dependence of the Laser Field

In an experiment the exact time dependence of an ultrashort laser field is in most cases only very approximately known. Especially the peak intensity is mostly only known up to around 20% and the carrier-envelope phase can be completely random. For free-electron lasers the situation is even worse, since even the whole laser field shape can be random, though efforts exist to control it [68, 69].

In theory realistic models for the laser field are used. In this thesis mostly linearly polarized laser fields (total laser-field duration T) of type

$$\vec{A}_{\mathrm{RG}}(t) \;=\; \vec{\mathcal{P}}\, A_0\, f_{\mathrm{E}}(\,t\,)\, \sin(\,\omega\, t \,+\, \phi\,) \tag{2.68}$$

are considered. Here $\vec{\mathcal{P}}$ denotes the polarization direction, ω the laser frequency, and ϕ the carrier-envelope phase. The envelope is chosen as

$$f_{\mathrm{E}}(t) = \begin{cases} \cos^2\left(\dfrac{\pi t}{T}\right) & -T/2 \leq t \leq T/2 \\ 0 & \text{else} \end{cases} \quad . \tag{2.69}$$

[13] Observing the quantization of the electromagnetic field is quite challenging and requires dedicated setups, e.g. with a few trapped photons in optical cavities.

The field strength is obtained from the vector potential[14] by $\vec{F}(t) = -\frac{\partial}{\partial t}\vec{A}_{\mathrm{RG}}(t)$. A number of different envelopes is also implemented in the *AMO_TOOLS*, see page 220 in [65]. Figure 2.4 shows the time dependence of a typical laser field (exactly this field will be used several times later in this thesis). Differences between laser fields with Gaussian and $\cos^2$ envelope are only visible near turn-on and turn-off at $t = \pm T/2$ where the $\cos^2$ laser field sharply approaches zero. Following the intuition that most ionization occurs near the peak of the laser field one would thus expect an identical ionization behavior for Gaussian- and corresponding $\cos^2$-envelope laser fields. For very low intensities ($I \lesssim 10^{10}$ W/cm^2), however, the single-photon ionization yield may exceed the N-photon ionization yield by many orders of magnitude. The sharp turn-on(off) of the field with $\cos^2$ envelope leads to pronounced sidebands in the Fourier domain in contrast to the field with Gaussian envelope [65, 70, 71],[15] see Figure 2.5. Thus, instead of N-photon ionization which would be expected for a particular laser frequency $\omega < E_b$, N'-photon ionization with $N' < N$ triggered by a sideband may dominate this ionization behavior. On a *loglog* plot showing the ionization yield vs. intensity, this can be observed as a sudden change of the slope from (approximately) N to N' [71].

In this chapter the basics for the description of molecules and the interaction with laser fields have been introduced. Methods to solve the corresponding time-independent and time-dependent Schrödinger equations are introduced in the next chapter.

[14] For very short fields the shape of $\cos^2$ fields defined by $\vec{A}_{\mathrm{RG}}(t)$ is different from $\cos^2$ fields defined by $\vec{F}(t)$ due to the time derivative of the envelope function $f_{\mathrm{E}}(t)$. An advantage of defining a pulse by $\vec{A}_{\mathrm{RG}}(t)$ is that the zero-net-force condition $\int_{-\infty}^{\infty} \vec{F}(t) = 0$ is fulfilled by construction, $\int_{-\infty}^{\infty} \vec{F}(t) = \vec{A}_{\mathrm{RG}}(-\infty) - \vec{A}_{\mathrm{RG}}(\infty)$.

[15] The Fourier transform of a Gaussian is a Gaussian.

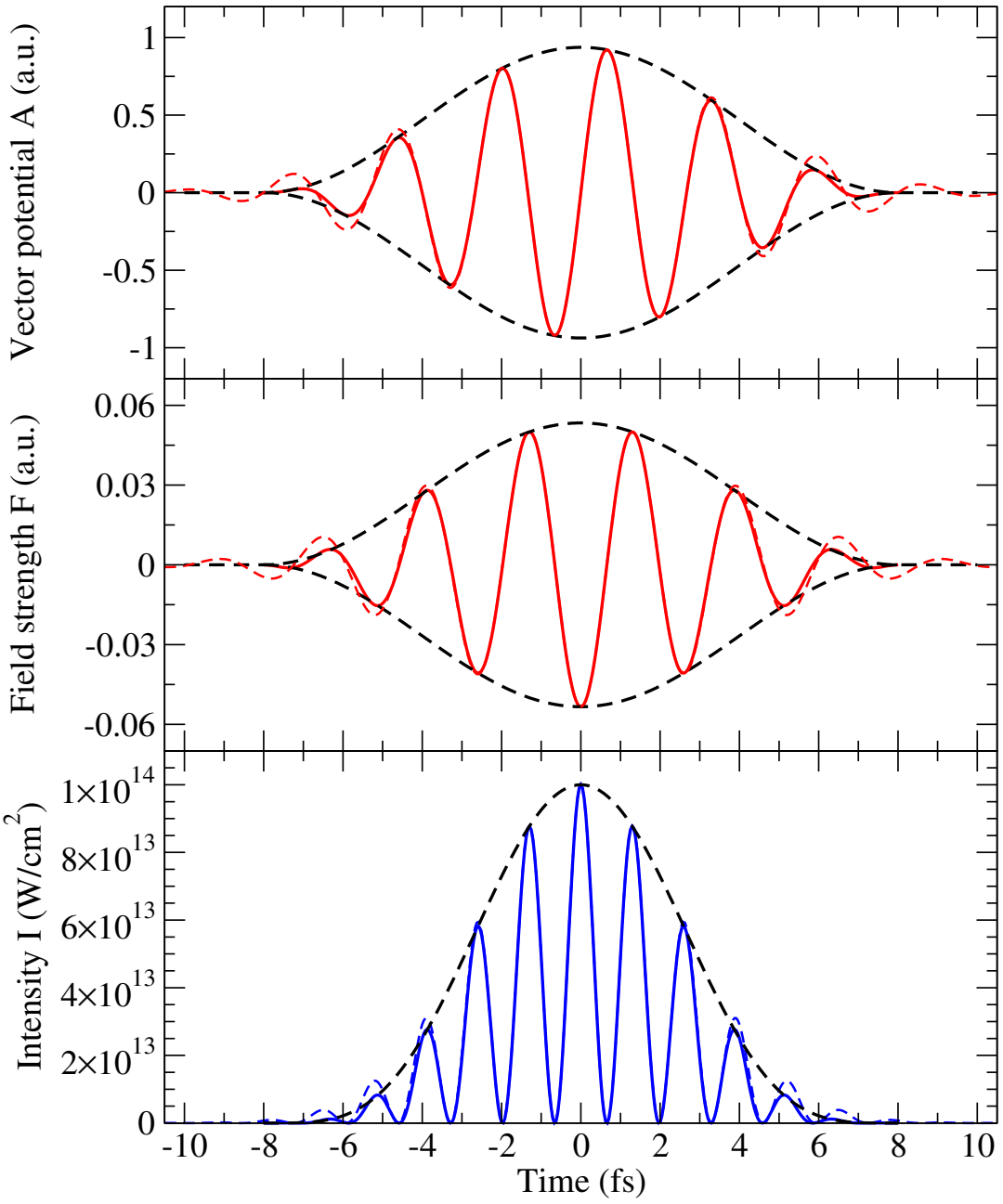

Figure 2.4: Time dependence of a laser field (vector potential, field strength and intensity) as defined in Eq. (2.68) using a $\cos^2$-envelope (full colored lines) or Gaussian envelope (dashed colored lines). The black dashed lines indicate the $\cos^2$ envelope. The field parameters are as follows:
Wavelength $\lambda = 800$ nm ($\omega \approx 1.55$ eV ≈ 0.057 a.u.),
Duration $n_c = \omega T/2\pi = 6$ cycles ($T \approx 16$ fs ≈ 662 a.u.)
Peak intensity $I_0 = 10^{14}$ W/cm^2 ($A_0 \approx 0.937$ a.u., $F_0 \approx 0.0534$ a.u.)
Carrier-envelope phase $\phi = 0$.

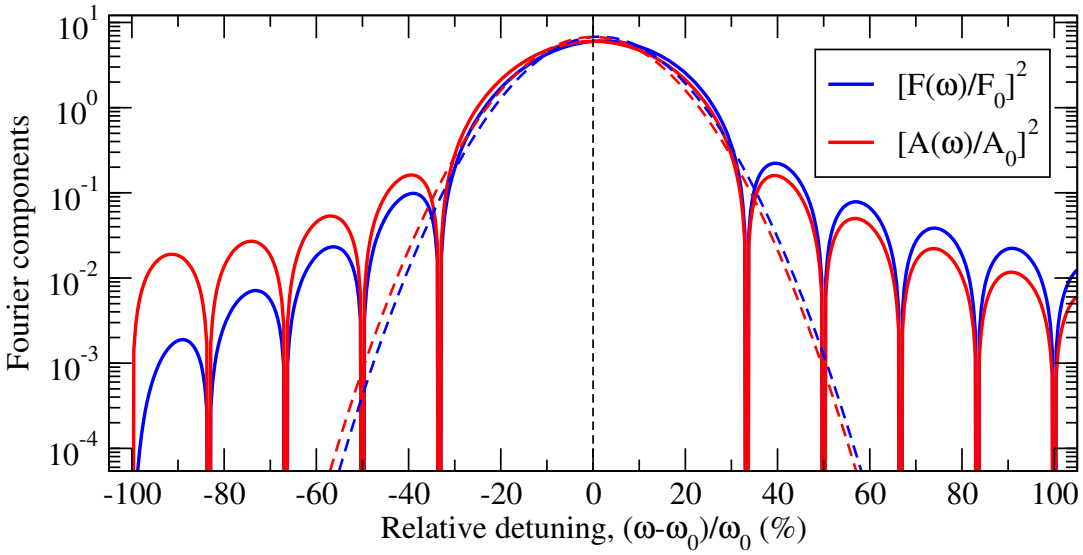

Figure 2.5: Fourier components of a 6-cycle laser field with $\cos^2$ envelope (full colored lines) and Gaussian envelope (dashed colored lines).

3 Computational Methods

In this chapter different numerical approaches to solve the time-independent and time-dependent Schrödinger equation are discussed. Within this thesis, the main approaches to solve the time-independent Schrödinger equation are the matrix algorithm, Section 3.1, and the B-spline method, Section 3.2. While within the former method the Hamiltonian is discretized on a grid, the latter method uses a B-spline representation of the Hamiltonian in order to find eigenenergies and eigenstates by matrix diagonalization. In Section 3.3 the solution of the electronic time-independent Schrödinger equation describing two-electron diatomic molecules (e.g. H_2) using the B-spline method is discussed. For polyatomic molecules (e.g. NH_3) the single-determinant approach using a multicentric B-spline basis is described in Section 3.4. Obtained eigenstates can be used as a basis to solve the time-dependent Schrödinger equation (spectral ansatz) as described in Section 3.5. Alternatively, the time-depdendent Schrödinger equation may be solved directly on a grid using the Split Operator approach and imaginary time propagation, Section 3.6. Finally, the common properties and differences between the grid and the spectral ansatz are discussed in Section 3.7.

3.1 Matrix Algorithm

The technique to investigate simple quantum systems introduced below has been taught in its simplest form by Prof. Ulli Wolff in the computational physics courses at Humboldt university since 2006. It was first published in [1]. The basis is the so-called SLAC derivative that was proposed for lattice fermions in [72].

A one-dimensional position-space lattice is defined. It consists of an odd number of $N = 2M + 1$ points

$$\{ x_1 , x_2 , \dots , x_N \} \;=\; \{ -Ma , -(M-1)a , \dots , -a , 0 , a , \dots , Ma \} \quad . \tag{3.1}$$

that are equidistantly spaced with the lattice spacing a and lie symmetrically around the origin. Wave 'functions' in the Schrödinger representation of quantum mechanics are restricted to this space

$$\Psi(x) \;\equiv\; \begin{pmatrix} \Psi(x_1) \\ \Psi(x_2) \\ \vdots \\ \Psi(x_N) \end{pmatrix} , \tag{3.2}$$

and thus the Hilbert space is approximated by $\mathbb{C}^N$. Intuitively, a bound state that is centered around the origin, can be represented well in this framework, if its size is much smaller than $L = Na$ such that the sites $\pm Ma$ are deeply in the classically forbidden region. Moreover a must be small enough to allow for a good resolution of structures in the wave function. For example, for a simple harmonic oscillator of mass m and frequency ω these conditions amount to $a \ll \sqrt{\hbar/(m\omega)} \ll L$.

Linear operators must become finite matrices now. Functions of the position operator like the potential $V(\hat{\mathrm{x}})$ trivially translate into diagonal matrices such that

$$(\mathbf{V}\Psi)(x) \;\equiv\; \begin{pmatrix} V(x_1)\Psi(x_1) \\ V(x_2)\Psi(x_2) \\ \vdots \\ V(x_N)\Psi(x_N) \end{pmatrix} \quad , \tag{3.3}$$

i.e.

$$(\,\mathbf{V}\,)_{ik} \;=\; \delta_{ik}\, V(x_k) \quad . \tag{3.4}$$

To also implement a canonically conjugate momentum operator $\hat{\mathrm{p}}$ that has to mimic the derivative, boundary conditions have to be imposed. They are chosen to be periodic with period L. Note that this also implies a periodic extension of the diagonal elements of the position operator. This means that odd powers of $\hat{\mathrm{x}}$ create jumps at odd-integer multiples of $L/2$, in particular at $\pm Ma$, which will, however, be seen to cause no problems in our applications here. The first idea that comes to mind now is to represent $\hat{\mathrm{p}}^2$ by a difference operator over three (or more) sites. This would clearly inflict leading discretization errors that are powers of a^2. A better precision is obtained by adopting a Fourier transform, then using a diagonal operator for $\hat{\mathrm{p}}^2$ analogous to the one in discrete position space and then transforming back. This results in a nonlocal matrix representation in position space that couples *all* sites given by

$$(\mathbf{f}(\hat{\mathrm{p}}))_{ik} \;=\; \frac{1}{N}\sum_{j=1}^{N} f(p_j)\,\exp[\,i\,p_j\,(\,x_i\,-\,x_k\,)\,]. \tag{3.5}$$

where the sum over p runs over the values

$$\{\,p_1\,,\,p_2\,,\,\ldots\,,\,p_N\,\} \;=\; \left\{\,-M\,\frac{2\,\pi}{L}\,,\,-(M-1)\frac{2\,\pi}{L}\,,\,\ldots\,,\,M\frac{2\,\pi}{L}\,\right\} \tag{3.6}$$

and periodicity under shifts of p by $\pm 2\pi/a$ holds.

A multiplication of a wave function with the above matrix may be decomposed

into two steps. First

$$\tilde{\Psi}(p) \;=\; a \sum_{k=1}^{N} \exp[\,-i\,p\,x_k\,]\,\Psi(x_k) \;\rightarrow\; \int_{-L/2}^{L/2} dy\, \exp[\,-i\,p\,y\,]\,\Psi(y) \tag{3.7}$$

is computed where the continuum limit $a \rightarrow 0$ at fixed L is indicated (for a continuously defined Ψ). In the second step

$$(f(\,\hat{\mathrm{p}}\,)\,\Psi)(x) \;=\; \frac{1}{L} \sum_{j=1}^{N} f(p_j)\, \exp[\,i\,p_j\,x\,]\,\tilde{\Psi}(p_j) \tag{3.8}$$

is formed. Here x can assume continuous values and inside f obviously p is equivalent to $-id/dx$. The sum over p becomes infinite in the continuum limit.

Returning to finite a and L the formula (setting $l = i - k$)

$$\begin{aligned} (\,\exp[\,i\,\alpha\,\hat{\mathrm{p}}\,]\,)_{ik} \;&=\; \frac{1}{N} \sum_{j=1}^{N} \exp[\,i\,p_j\,(\,\alpha \,+\, x_i \,-\, x_k\,)\,] \\ &=\; \frac{(-1)^l}{N}\, \frac{\sin(\,\pi\,\alpha\,/\,a\,)}{\sin(\,\pi\,(\,\alpha \,+\, la\,)/L\,)} \end{aligned} \tag{3.9}$$

which holds for general α is obtained, allows for the explicit computation of matrix elements of powers of $\hat{\mathrm{p}}$. Comparing powers in α one finds, e.g.,

$$(\,\hat{\mathrm{p}}\,)_{ik} \;=\; \begin{cases} 0 & \text{for} \quad l = 0 \bmod N \\ \dfrac{\pi}{iL}\, \dfrac{(-1)^l}{\sin(\,\pi\,l\,/\,N\,)} & \text{else} \end{cases}, \tag{3.10}$$

$$(\,\hat{\mathrm{p}}^{\,\mathbf{2}}\,)_{ik} \;=\; \begin{cases} \dfrac{\pi^2}{3\,a^2}(1 - a^2/L^2) & \text{for} \quad l = 0 \bmod N \\ \dfrac{2\,\pi^2}{L^2}\, \dfrac{(-1)^l \cos(\,\pi\,l\,/\,N\,)}{\sin^2(\,\pi\,l\,/\,N\,)} & \text{else} \end{cases}. \tag{3.11}$$

Of course, it is evidently also possible to take matrix powers of $(\,\hat{\mathrm{p}}\,)_{ik}$.

To find the eigenvalues of the Schrödinger equation the matrix representation of $\hat{\mathrm{H}}$ is constructed. This matrix is diagonalized to find eigenenergies E_n and eigenfunctions Ψ_n of the system. Clearly, the width L and the number of points N should be sufficiently large to obtain converged results and only a certain number of low-lying energies E_n can be expected to be reliable for any fixed values of N and L.

To diagonalize the matrix, the MATLAB [73] routine *eig* which determines eigenvalues and eigenvectors of a matrix (also for non-Hermitian matrices) is used.

As will be discussed later (Section 4.1.4), the matrix algorithm has a very fast convergence behavior such that around $O(100)$ points are usually sufficient. There-

fore, also higher dimensional problems with for example about $N_x \times N_y = \mathrm{O}\,(\,10^4\,)$ points in two dimensions are within reach on present-day computers. In that case each direction is discretized as before and a rectangle filled with sites

$$\vec{r}_I \;=\; (\,x_{i_1}\,,\,y_{i_2}\,)\,, \quad i_1 = 1,\ldots,N_x\,, \quad i_2 = 1,\ldots,N_y \tag{3.12}$$

is obtained. A unique compound index

$$I \;=\; i_1 \,+\, (i_2 - 1)\,N_x \;=\; 1,\ldots,N_x\,N_y \tag{3.13}$$

is defined. Operators are embedded in the tensor-product state space. The position operators become, e.g.,

$$(\,\hat{\mathrm{x}}\,)_{IK} \;=\; x_{i_1}\,\delta_{i_1k_1}\,\delta_{i_2k_2}\,, \quad (\,\hat{\mathrm{y}}\,)_{IK} \;=\; y_{i_2}\,\delta_{i_1k_1}\,\delta_{i_2k_2}\,. \tag{3.14}$$

Similarly $\hat{\mathrm{p}}_x^2$ leads to a matrix

$$(\,\hat{\mathrm{p}}_{\mathbf{x}}^{\mathbf{2}}\,)_{IK} \;=\; (\,\hat{\mathrm{p}}^{\,\mathbf{2}}\,)_{i_1k_1}\,\delta_{i_2k_2}\,, \quad (\,\hat{\mathrm{p}}_{\mathbf{y}}^{\mathbf{2}}\,)_{IK} \;=\; \delta_{i_1k_1}\,(\,\hat{\mathrm{p}}^{\,\mathbf{2}}\,)_{i_2k_2} \tag{3.15}$$

with the matrices $(\,\hat{\mathrm{p}}^{\,\mathbf{2}}\,)_{ik}$ taken from (3.11) with the obvious substitution of a, L, N by the corresponding quantities referring to the respective direction. Note that in more than one dimension many vanishing matrix elements appear in a typical Hamiltonian. One may thus store it in a sparse-matrix mode as a list of the nonvanishing elements rather than a full matrix. The two-dimensional Henon-Heiles system is treated as an example later in Section 4.1.9.

3.2 B-Spline Method

In this section *B splines* (basis or basic spline) as basis functions to find eigenvalues and eigenfunctions of a Hamiltonian are briefly introduced. B splines are local polynomials which are especially well suited to not only describe bound states, but also continuum states (in contrast to, e.g., Gaussian basis functions). Box discretization (usage of a finite box) leads to a discretized energy spectrum for the continuum states [74]. Due to the locality of the basis states the problem of linear dependencies due to finite machine precision is minimized [75] which allows for systematic convergence studies. Using B splines electronic Schrödinger equations for the description of atoms and small molecules can be solved numerically (see, e.g., the overview articles [74, 75]). Particularly, B splines are used for solving the electronic Schrödinger equation of H_2^+ and H_2 in the fundamental works build on within this thesis [29, 48, 53, 65, 76–78]. In [51, 79–92] B splines are furthermore used for the description of molecular vibration of H_2. Eigenfunctions obtained with the B-spline method can be used as a basis set for the solution of the TDSE describing an atom or molecule exposed to an ultrashort laser field, see Section 3.5.

The essential properties of B splines are now briefly reviewed (a more thorough

discussion is found in, e.g., [93] from page 108, [65] in Chapter 1 and in [74, 75]). In order to define B splines within an interval ("'Box"') $I = [x_{\min}, x_{\max}]$ the following properties must be defined:

1. The B spline order k is chosen. A B spline of order k corresponds to a local polynomial of type $p(y) = a_{k-1}\, y^{k-1} + a_{k-2}\, y^{k-2} + ... + a_0$.

2. The interval I is split into $N-1$ sub-intervals such that a strictly increasing sequence of N break points $\{ x_1 = x_{\min}\, , x_2\, , ...\, , x_N = x_{\max} \}$ with $x_{i+1} > x_i$ is defined.

3. At each break point x_i the degree of differentiability is defined. An increasing knot point sequence $\{ t_1\, , t_2\, , ...\, , t_{N_k} \}$ with $t_{i+1} \geq t_i$ is thus defined such that one or more knot points belong to each break point (μ is the number of knot points at a break point). One knot point ($\mu = 1$) corresponds to the maximum degree of differentiability of the B spline of order k at this break point, each additional knot point reduces the degree of differentiability by 1 (discontinuity for $\mu = k$). The *standard choice* used in, e.g., [65, 74] is $\mu = 1$ for all inner break points and $\mu = k$ for the boundary points, such that $N_k = N + 2\,(k-1)$.

The i-th B spline of order k, $B_i^k(x)$, which is non-zero in the interval (t_i, t_{i+k}), is recursively defined by (page 131 in [93])

$$B_i^1(x) = \begin{cases} 1 & \text{for} \quad t_i \leq x < t_{i+1} \\ 0 & \text{else} \end{cases} \tag{3.16}$$

$$B_i^k(x) = \frac{x - t_i}{t_{i+k-1} - t_i}\, B_i^{k-1}(x) + \frac{t_{i+k} - x}{t_{i+k} - t_{i+1}}\, B_{i+1}^{k-1}(x) \quad . \tag{3.17}$$

Among the most important properties of B splines for the solution of Schrödinger equations is that a complete set of B splines of order k fulfills the completeness relation [74]

$$\sum_i B_i^k(x) = 1 \quad \text{for} \quad x_{\min} \leq x \leq x_{\max} \quad . \tag{3.18}$$

In the case of the standard choice of the boundary conditions this corresponds to a set of $N_B = N + k - 2$ B splines. Figure 3.1 shows the complete set of 11 B splines of order $k = 4$ for the knot point sequence $\{t_i\} = \{0, 0, 0, 0, 1, 2, 3, 4, 5, 6, 7, 8, 8, 8, 8\}$.

In order to solve the time-independent Schrödinger equation

$$\hat{\mathrm{H}}_0\, \psi(x) = E\, \psi(x) \tag{3.19}$$

the wave function ψ is expanded in B splines such that

$$\psi(x) = \sum_{i=1}^{N_B} c_i\, B_i^k(x) \quad . \tag{3.20}$$

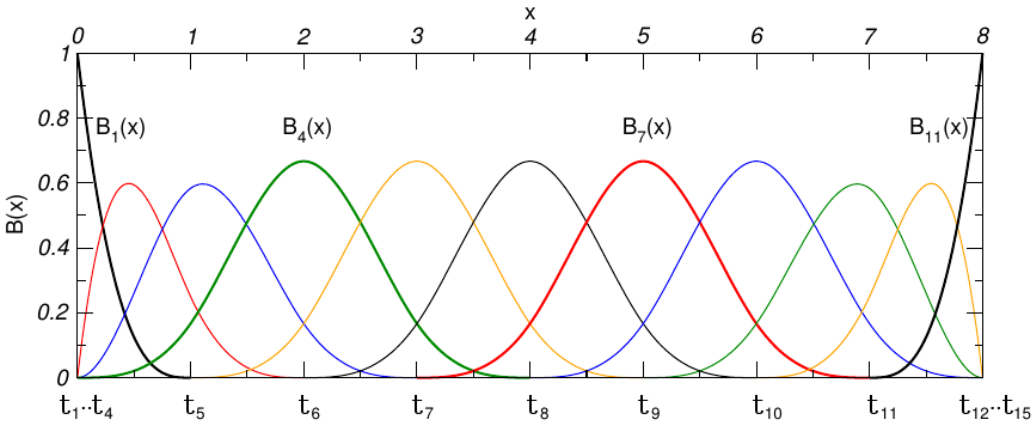

Figure 3.1: Complete set of 11 B splines of order $k = 4$ with knot point sequence $\{t_i\} = \{0, 0, 0, 0, 1, 2, 3, 4, 5, 6, 7, 8, 8, 8, 8\}$. Figure taken from [65] (modified).

By projection on all $B_j^k(x)$ and solution of the system consisting of N_B linear equations one finds eigenfunctions $\psi_n(x)$ with eigenvalues E_n of the system. This corresponds to the solution of the generalized eigenvalue problem

$$\mathbf{H}\, c \;=\; E\, \mathbf{S}\, c \tag{3.21}$$

with column vector $c \;=\; (\, c_1\,,\, c_2\,,\, \ldots\,,\, c_{N_B}\,)^T$ and matrices

$$(\mathbf{H})_{ij} \;=\; \int dx\, B_i^k(x)\, \hat{\mathrm{H}}_0\, B_j^k(x) \quad \text{and} \quad (\mathbf{S})_{ij} \;=\; \int dx\, B_i^k(x)\, B_j^k(x) \tag{3.22}$$

(Hamiltonian matrix and overlap matrix). Due to the locality of B splines (See Figure 3.1) many of these integrals are equal to zero. In order to numerically calculate non-zero integrals the Gauss–Legendre quadrature is especially well suited [94]. This quadrature solves the integral even exactly up to a certain polynomial degree, if the integrand can be written as polynomial.

3.3 Solution of the Electronic Schrödinger Equation of Two-Electron Diatomics, e.g. H_2

This section briefly describes the method to solve the electronic problem of diatomic molecules with two electrons (primarily H_2 and HeH^+) in full dimensionality [65, 76] which has been implemented by Yulian V. Vanne. The two-electron Schrödinger equation

$$\hat{\mathrm{H}}_{\mathrm{e}}^{(2\mathrm{e})}\; \Phi_n^{(2\mathrm{e})}(\,\underline{\mathbf{r}}\,;\,\underline{\mathbf{R}}\,) \;=\; \mathcal{E}_n^{(2\mathrm{e})}(\,\underline{\mathbf{R}}\,)\; \Phi_n^{(2\mathrm{e})}(\,\underline{\mathbf{r}}\,;\,\underline{\mathbf{R}}\,) \tag{3.23}$$

is solved for a fixed nuclear configuration $\underline{\mathbf{R}}$. In the following, the position of the nuclei is chosen to be $(\, x \,=\, 0\,,\, y \,=\, 0\,,\, z \,=\, \pm R/2\,)$ in Cartesian coordinates with the internuclear distance $R \,=\, \left|\, \vec{R}_1 \,-\, \vec{R}_2 \,\right|$. For the electrons prolate spheroidal coordinates $(\, \xi\,,\, \eta\,,\, \phi\,)$ are chosen. The distance of the electron to the z-axis is $r_z \,=\, \sqrt{x^2 \,+\, y^2}$. The distances r_A (r_B) to the nuclei A (B) are

$$r_A \,=\, \sqrt{r_z^2 \,+\, (\, z \,+\, R/2\,)^2} \tag{3.24}$$

and

$$r_B \,=\, \sqrt{r_z^2 \,+\, (\, z \,-\, R/2\,)^2} \quad . \tag{3.25}$$

The coordinates ξ and η are defined as

$$\begin{aligned} \xi \,&=\, \frac{r_A \,+\, r_B}{R} \;\in [\,1\,,\,\infty\,) \\ \eta \,&=\, \frac{r_A \,-\, r_B}{R} \;\in [\,-1\,,\,1\,] \quad . \end{aligned} \tag{3.26}$$

$\phi \;\in [\,0\,,\,2\pi\,)$ corresponds to the angle around the internuclear axis. If one chooses spherical coordinates (r, θ, φ) with

$$\begin{aligned} x \,&=\, r\, \sin\theta\, \cos\varphi \\ y \,&=\, r\, \sin\theta\, \sin\varphi \\ z \,&=\, r\, \cos\theta \end{aligned} \tag{3.27}$$

then ϕ is equivalent to φ. Figure 3.2 illustrates the prolate spheroidal coordinate system. For increasing distances to the origin $(r \,\to\, \infty)$ or decreasing internuclear distances $(R \,\to\, 0)$ prolate spheroidal coordinates become more and more similar to spherical coordinates according to $\xi \,\to\, 2r/R$ and $\eta \,\to\, \cos\theta$. In a discretized representation ξ is restricted to an interval $[\,1\,,\,\xi_{\max}\,]$. Therefore, a radial box size $r_{\max} \,=\, R\xi_{\max}/2$ is introduced similarly to spherical coordinates.

The first step to solve the two-electron problem Eq. (3.23) is the solution of the one-electron problem. A distinct feature of prolate spheroidal coordinates is that the three-dimensional one-electron problem separates into three one-dimensional problems (similarly to the hydrogen atom in spherical coordinates). The Hamiltonian reads in this coordinate system [65]

$$\hat{\mathrm{H}}_{\mathrm{e}}^{(1\mathrm{e})} \,=\, -\frac{1}{2}\,\Delta \,-\, \frac{4\,\xi\,R}{R^2\,(\,\xi^2 \,-\, \eta^2\,)} \tag{3.28}$$

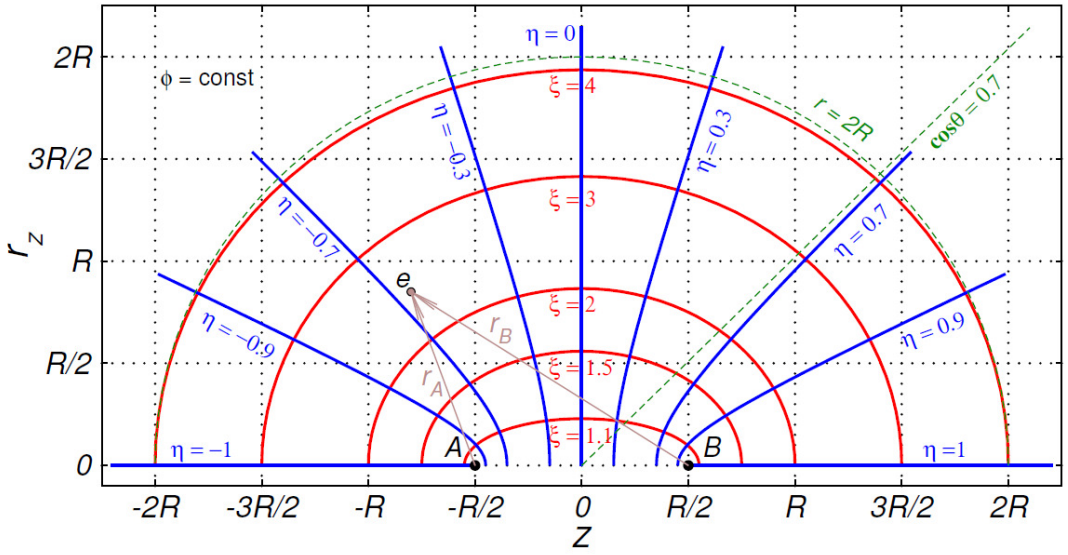

Figure 3.2: Prolate spheroidal coordinate system for ϕ = const. The red (blue) lines show cuts for constant ξ (η). The green dashed lines show cuts in spherical coordinates (r, θ, φ) for constant r or θ. Figure taken from [65].

with Laplacian

$$\Delta = \nabla^2 = \frac{4}{R^2(\xi^2 - \eta^2)}\left(\frac{\partial}{\partial\xi}\left[(\xi^2 - 1)\frac{\partial}{\partial\xi}\right] + \frac{\partial}{\partial\eta}\left[(1 - \eta^2)\frac{\partial}{\partial\eta}\right] + \frac{\partial}{\partial\phi}\left[\frac{(\xi^2 - \eta^2)}{(\xi^2 - 1)(1 - \eta^2)}\frac{\partial}{\partial\phi}\right]\right) . \quad (3.29)$$

Solutions of the eigenvalue equation

$$\hat{H}_e^{(1e)}\,\Phi^{(1e)}(\xi, \eta, \phi; R) = \mathcal{E}_n^{(1e)}(R)\,\Phi_n^{(1e)}(\xi, \eta, \phi; R) \quad (3.30)$$

can be written in the form $\Phi^{(1e)}(\xi, \eta, \phi; R) = \Xi(\xi)\,\Pi(\eta)\,e^{i m \phi}$ where m is a good quantum number (projection of the electron angular momentum on the internuclear axis). The solutions $\Phi^{(1e)}(\xi, \eta, \phi; R)$ with energies $\mathcal{E}^{(1e)}(R)$ are obtained using the B-spline method described in Section 3.2[1]. The big advantage of this method is that it finds both bound and discretized continuum states. The behavior of a typical discretized continuum is discussed in Section 4.1.6.

The one-electron orbitals $\Phi_n^{(1e)}(\xi, \eta, \phi)$ are used as a basis set to solve the two-electron Schrödinger equation (3.23) by the *configuration interaction (CI)* method.

[1] In the homonuclear case additionally the inversion symmetry ($\xi \to \xi$, $\eta \to -\eta$, $\phi \to \phi + \pi$) is exploited.

For this purpose symmetry-adapted and (according to the Pauli principle) anti-symmetrized two-electron wave functions (*configurations*) Υ_i are constructed using the one-electron eigenfunctions $\Phi_n^{(1e)}(\xi, \eta, \phi)$. Inserting this basis into the two-electron Schrödinger equation (3.23) leads to a matrix eigenvalue problem. The diagonalization of the corresponding Hamiltonian matrix yields two-electron orbitals $\Phi_n^{(2e)}(\xi_1, \eta_1, \phi_1, \xi_2, \eta_2, \phi_2; R)$ with energies $\mathcal{E}_n^{(2e)}(R)$. The main challenge that has been resolved in the PhD thesis of Yulian V. Vanne [65] was the efficient implementation of the calculation of the electron-electron interaction integrals using B splines and the prolate spheroidal coordinate system. The two-electron orbitals obtained here are later on also used as basis functions to describe the coupled electronic-vibrational motion of H_2(Section 4.4).

3.4 Single-Determinant Approach to Describe Polyatomic Molecules, e.g. NH_3

In this section the single-determinant multicentric B-spline approach is briefly introduced. The underlying method to describe the electronic molecular structure for a fixed nuclear geometry has been developed by P. Decleva *et. al.* [95]. In a joint effort between the Humboldt University Berlin (A. Saenz *et al.*) and the University of Trieste (P. Decleva *et al.*) this method was further developed to describe strong-field ionization of small polyatomic molecules in ultrashort, intense laser fields. Within the PhD thesis of M. Awasthi [78] a single-active electron approach was developed and demonstrated for the ionization of H_2. A surprisingly good agreement to the configuration interaction approach from the previous section was found [54, 78]. Furthermore, first single-active-electron results for the linear many-electron molecules N_2, O_2, and C_2H_2 were shown in [78]. Within the PhD thesis of S. Petretti [96] the so-called *single-determinant approach* which yields gauge-independent ionization probabilities[2] was developed. This method has been previously successfully applied to describe the ionization of N_2, O_2, CO_2 [11, 97], and H_2O [5, 98]. Within this thesis the single-determinant approach will be applied to study the ionization behavior of the NH_3 molecule.

The starting point is a standard Density Functional Theory (DFT) calculation using the Amsterdam Density Functional (ADF) program [99]. The exchange-correlation potential LB94 is used since it yielded the most accurate ionization probabilities out of all tested potentials [54, 78, 96]. The LB94 potential has the correct asymptotic behavior at large electron distances and is thus especially well

[2] This is in contrast to the previous single-active electron approach where a pronounced gauge dependence for molecules larger than H_2 was observed. Within the single-determinant approach it is allowed to occupy all electronic orbitals during time propagation, even ones that are energetically lower than the initial orbital. It thus allows for a re-ordering of the electronic core during time propagation in contrast to the (frozen-core) single-active-electron approach. The (gauge-independent) total ionization yield is obtained as the summation of ionization yields obtained for all possible initial orbitals.

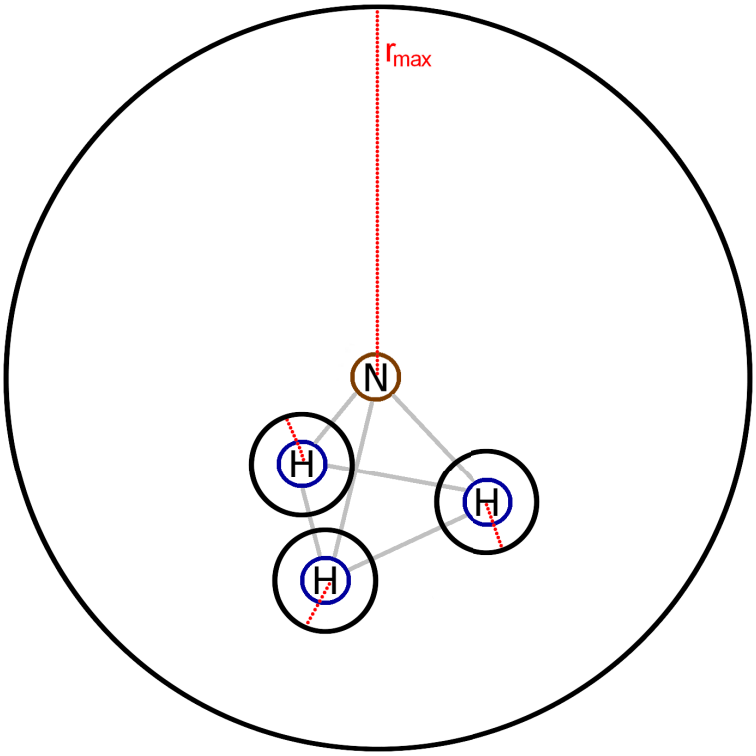

Figure 3.3: Multicentric B-spline approach for the NH_3 molecule. The main B spline basis expansion is performed within a large sphere with box size $r_{\max}$ centered around the nitrogen atom (origin). Three additional, much smaller B spline basis expansions are located within small spheres centered around the hydrogen atoms.

suited to describe the ionization process where an electron leaves the parent ion. The electronic ground-state density $\rho_{\mathrm{ADF}}(\vec{r})$ obtained using ADF is then projected on a multicentric B-spline basis set, see Figure 3.3. A sphere is centered around each nucleus of the molecule with one very large sphere. The radius of this large sphere corresponds to the box size $r_{\max}$ of the basis set. For the NH_3 molecule it is natural to center the large sphere (and thus the origin of the coordinate system) around the nitrogen atom which possesses much more electrons than the hydrogen atoms. The spheres around the off-centered atoms are much smaller and are not allowed to overlap in the current implementation. For each sphere, the radial part is represented using B splines, Section 3.2, while the angular part is represented using spherical harmonics[3]. For the multicentric B-spline basis set, a symmetry-adapted basis set is constructed using group theory. The DFT calculation is then repeated within this basis where the initial state is $\rho_{\mathrm{ADF}}(\vec{r})$ (projected on this basis set).

[3] The spheres are centered at the $\propto 1/r$ divergencies of the Coulomb potentials stemming from the nuclei. Thus, a similar convergence is achieved with much fewer angular momenta and thus a much smaller basis set compared to a single-center basis set expansion.

Thus, after only a few iterations, symmetry-adapted Kohn-Sham orbitals $\phi_{\mathrm{KS}}(\vec{r})$ are obtained. Using the spectral ansatz which is introduced in the next section, the obtained bound and discretized continuum orbitals[4] can be used as a basis set for time propagation.

3.5 The Spectral Ansatz

The orthonormal eigenstates $|\,\psi_n\,\rangle$ found using the B-spline method or matrix algorithm can be used as approximately complete basis

$$\sum_{n=0}^{n_{\max}} |\,\psi_n\,\rangle\,\langle\,\psi_n\,| \;\approx\; 1 \tag{3.31}$$

within a box size L and for energies $E < E_{n_{\max}}$ as an ansatz to solve the TDSE

$$i\,\frac{\partial}{\partial t}\,|\,\Psi(t)\,\rangle \;=\; \hat{\mathrm{H}}\,|\,\Psi(t)\,\rangle \;=\; \Big(\hat{\mathrm{H}}_0 \,+\, \hat{\mathrm{V}}_{\mathrm{int}}(t)\Big)\,|\,\Psi(t)\,\rangle \quad . \tag{3.32}$$

Two common variants of the spectral ansatz are the ansatz with explicit energy phase

$$|\,\Psi(t)\,\rangle \;=\; \sum_{n=0}^{n_{\max}} c_n^{\mathrm{EEP}}(t)\,e^{-i\,E_n\,t}\;|\,\psi_n\,\rangle \tag{3.33}$$

and the ansatz with implicit energy phase

$$|\,\Psi(t)\,\rangle \;=\; \sum_{n=0}^{n_{\max}} c_n^{\mathrm{IEP}}(t)\;|\,\psi_n\,\rangle \quad . \tag{3.34}$$

In the case of no external perturbation $\hat{\mathrm{V}}_{\mathrm{int}}(t) = 0$, the coefficients within the explicit energy phase ansatz remain constant, $\dot{c}_n^{\mathrm{EEP}}(t) = 0$. This ansatz is especially well suited for small perturbations (low laser field strengths, perturbative multiphoton regime) and then requires significantly fewer time steps to converge a numerical calculation than the ansatz with implicit energy phase. For large perturbations (high field strengths, quasistatic regime), on the other hand, the ansatz with implicit energy phase typically requires fewer time steps since the time scales are not simply determined by the system. Rather, situations can occur where the electron is driven by the laser field (quiver motion) rather than the binding potential stemming from the nuclei. The ansatz with implicit energy phase is solely adopted within this thesis. To simplify the notation the index "IEP" is dropped and thus $c_n(t) \equiv c_n^{\mathrm{IEP}}(t)$. Inserting Eq. (3.34) into Eq. (3.32) and multiplying from the left with $\langle\,\psi_m\,|$ yields

[4] The properly discretized continuum orbitals are essential to describe strong-field ionization. Thus, in addition to the correct asymptotic behavior of the LB94 potential, the usage of B splines (instead of, e.g., Gaussians) is a key ingredient of this method since they yield a proper discretized continuum, see also Section 4.1.6.

the system of coupled ordinary differential equations

$$i\,\frac{d}{dt}\,c_m(t) \;=\; E_m\,c_m(t) \;+\; \sum_n \,\langle\,\psi_m\,|\,\hat{\mathrm{V}}_{\mathrm{int}}(\hat{\mathrm{x}},t)\,|\,\psi_n\,\rangle\;c_n(t) \tag{3.35}$$

in order determine the coefficients $c_m(t)$. Eq. (3.35) can be written in matrix notation as

$$i\,\frac{d}{dt}\,c \;=\; (\,\mathbf{E}\;+\;\mathbf{V}_{\mathrm{int}}\,)\,c \tag{3.36}$$

with the coefficient column vector $c(t) = (c_0(t), c_1(t), ..., c_{n_{\max}}(t))^T$ and the diagonal energy matrix $(\mathbf{E}_{mn}) = \delta_{mn}E_n$ and interaction matrix $(\mathbf{V}_{\mathrm{int}})_{mn} = \langle\,\psi_m\,|\,\hat{\mathrm{V}}_{\mathrm{int}}(\hat{\mathrm{x}},t)\,|\,\psi_n\,\rangle$. Often it is possible to separate $\hat{\mathrm{V}}_{\mathrm{int}}(\hat{\mathrm{x}},t) = \hat{\mathrm{d}}(\hat{\mathrm{x}})f(t)$ such that the required integrals for $\mathbf{V}_{\mathrm{int}}$, $\langle\,\psi_m\,|\,\hat{\mathrm{d}}(\hat{\mathrm{x}})\,|\,\psi_n\,\rangle$ (interaction with a laser field in dipole approximation: *dipole matrix*), have to be calculated only once. Given an initial vector $c(t_0)$ (usually only the ground-state is populated initially, $c_0(t_0) = 1$ and $c_{>0} = 0$) Eq. (3.36) can be integrated using a solver for ordinary differential equations. The number of (dipole) matrix elements which have to be stored can be further reduced by exploiting symmetries. For example, in the simplest case of parity symmetry in one dimension, $\langle\,\psi_m\,|\,\hat{\mathrm{x}}\,|\,\psi_n\,\rangle = 0$ if $|\,\psi_m\,\rangle$ and $|\,\psi_n\,\rangle$ have the same parity symmetry (both *gerade* or both *ungerade*). Nevertheless, the number of elements which have to be stored (and applied to the coefficient vector) scales like $n^2_{\max}$. However, especially in multiple spatial dimensions, the exploitation of symmetries and clever choice of states which are included in the time propagation reduces the effort for a numerical calculation tremendously without having to reduce the dimensionality of the problem.

3.6 Split-Operator Method and Imaginary-Time Propagation

The Split-Operator method [100] in combination with imaginary time propagation is to date one of the most widely used method for the description of systems in intense laser fields (in reduced dimensionality, e.g. [19, 56–58, 101–105]). Both methods are introduced in this section.

The *Split-Operator method* aims to solve the TDSE

$$\frac{\partial}{\partial t}\,\Psi \;=\; -i\,\hat{\mathrm{H}}\,\Psi \tag{3.37}$$

in position space. Similarly to the matrix algorithm (Section 3.1) the problem is discretized on a grid

$$\{\,x_1\,,\,x_2\,,\,\ldots\,,\,x_N\,\} \tag{3.38}$$

consisting of N points with constant spacing $\Delta x = L/N = a$ (box size $L = Na$). For a time-independent Hamiltonian $\hat{\mathrm{H}}$ Eq. (3.37) can be solved by the ansatz $\Psi(x,t) =$

$\hat{\mathrm{U}}(t-t_0)\Psi(x,t_0)$ with the time-evolution operator

$$\hat{\mathrm{U}}(t-t_0) \;=\; \exp\Big(-i\;\hat{\mathrm{H}}\cdot(t-t_0)\Big) \;=\; \exp\Big(-i\;\Big(\hat{\mathrm{T}}+\hat{\mathrm{V}}\Big)\cdot(t-t_0)\Big) \quad . \tag{3.39}$$

Here, $\hat{\mathrm{T}}$ is the kinetic-energy operator and $\hat{\mathrm{V}}$ is the potential. As discussed for the matrix algorithm in Section 3.1 $\hat{\mathrm{V}}$ is a diagonal matrix in position space. Thus, also

$$\exp\Big(-i\;\hat{\mathrm{V}}\cdot(t-t_0)\Big) \tag{3.40}$$

is a diagonal matrix with entries

$$\Big(\exp\Big(-i\;\hat{\mathrm{V}}\cdot(t-t_0)\Big)\Big)_{ik} \;=\; \delta_{ik}\exp\left(-i\;V(x_k)(t-t_0)\right) \quad . \tag{3.41}$$

Analogously, the kinetic-energy operator $\hat{\mathrm{T}} = \dfrac{\hat{\mathrm{p}}^2}{2m}$ is a diagonal matrix in momentum space with momenta

$$\{p_1, p_2, \ldots, p_N\} \tag{3.42}$$

spaced by $\Delta p = 2\pi/L$. Thus,

$$\Big(\exp\Big(-i\;\hat{\mathrm{T}}\cdot(t-t_0)\Big)\Big)_{ik} \;=\; \delta_{ik}\exp\left(-i\;\frac{p_k^2}{2m}\,(t-t_0)\right) \tag{3.43}$$

holds for wave functions in momentum space. An initial wave function $\Psi(t_0)$ shall now be propagated in time steps Δt. The symmetric split operator [100]

$$\exp\Big(-i\;\hat{\mathrm{H}}\;\Delta t\Big) \;\approx\; \exp\left(-i\;\frac{\hat{\mathrm{T}}}{2}\;\Delta t\right)\exp\Big(-i\;\hat{\mathrm{V}}\;\Delta t\Big)\exp\left(-i\;\frac{\hat{\mathrm{T}}}{2}\;\Delta t\right) \tag{3.44}$$

leads to an error $\propto \Delta t^3$ (shown, e.g., by a Taylor expansion of both sides of the equation). When describing a system in a laser field the Hamiltonian $\hat{\mathrm{H}} = \hat{\mathrm{T}} + \hat{\mathrm{V}}_0 + \hat{\mathrm{V}}_{\mathrm{int}}(t)$ is time dependent. In this case, the time step Δt must be small compared to the time scale with which $\hat{\mathrm{V}}_{\mathrm{int}}(t)$ changes. For systems in a laser field the time scale of the change of the laser field is comparable to the time scale of the system (electrons), namely attoseconds.

In order to apply Eq. (3.44) numerically the Fourier transformation of the starting wave function, $\mathcal{F}(\Psi)$, is calculated. After applying $\exp\left(-i\;\dfrac{\hat{\mathrm{T}}}{2}\;\Delta t\right)$ the wave function is transformed back into position space using the inverse Fourier transformation $\mathcal{F}^{-1}$. Then $\exp\Big(-i\;\hat{\mathrm{V}}\;\Delta t\Big)$ is applied in position space and the wave function is transformed to momentum space to apply $\exp\left(-i\;\dfrac{\hat{\mathrm{T}}}{2}\;\Delta t\right)$. For multiple appli-

cations of Eq. (3.44) one additionally merges

$$\exp\left(-i\,\frac{\hat{\mathrm{T}}}{2}\,\Delta t\right)\exp\left(-i\,\frac{\hat{\mathrm{T}}}{2}\,\Delta t\right) = \exp\left(-i\,\hat{\mathrm{T}}\,\Delta t\right) \quad . \tag{3.45}$$

After Eq. (3.44) has been applied multiple times a final back transformation $\mathcal{F}^{-1}$ allows to study the result in position space. The Fourier transformation $\mathcal{F}$ is usually implemented as fast-Fourier transformation $\mathcal{F}_{\mathrm{FFT}}$ [106] which costs $\propto NlnN$ [5]. The costs $\propto N$ to multiply the diagonal matrices with the wave functions[6] is negligible for large N compared to the costs of the fast Fourier transformation. In addition to the wave-function vectors (each with length N for N points) only the N-component vectors containing the potential values in position space $V(\{x_k\})$ and the momenta $\{p_k\}$ have to be stored. The linear scaling of storage costs with the number of grid points N can be an advantage for smooth, local problems compared to the quadratic scaling of the spectral ansatz in Section 3.5 with the number of states $O(n_{\mathrm{max}}^2)$, especially for low-dimensional problems.

In order to start the time propagation one requires an initial state $\Psi(x,t_0)$. This is usually the ground state of the system without field. *Imaginary-time propagation* allows to find exactly this ground state. For this purpose one starts with a test state $\left|\,\tilde{\Psi}(t_0)\,\right\rangle$, which can be decomposed in the basis of eigenstates $|\,\psi_n\,\rangle$ of the system as

$$\left|\,\tilde{\Psi}(t_0)\,\right\rangle = \sum_n c_n\,|\,\psi_n\,\rangle \quad . \tag{3.46}$$

The time evolution of this state with the time-independent Hamiltonian $\hat{\mathrm{H}}$ of the system reads

$$\left|\,\tilde{\Psi}(t)\,\right\rangle = \sum_n c_n\,e^{-i\,E_n\,t}\,|\,\psi_n\,\rangle \quad . \tag{3.47}$$

By replacing $t \to -i\,\tau$ (i.e. propagation in imaginary time τ)

$$\left|\tilde{\Psi}(\tau)\right\rangle = \sum_n c_n\,e^{-E_n\,\tau}\,|\,\psi_n\,\rangle \tag{3.48}$$

is obtained. Excited states with energies $E_n > E_0$ thus decay exponentially faster than the ground state, which should be included in the test state with $c_0 \neq 0$. Imaginary time propagation can be combined with the Split-Operator method. The state propagated in imaginary time is then normalized again after one or several time steps. Depending on the choice of the absolute energy in the potential energy $\hat{\mathrm{V}}_0$, the ground state can decay very quickly for a large E_0 or even grow exponentially for a negative E_0. One may thus estimate and add an appropriate constant energy to $\hat{\mathrm{V}}_0$ such that $E_0 \approx 0$. The test state is propagated in imaginary time until the state does not change anymore upon further time propagation and normalization

[5] $N^D lnN$ for D-dimensional problems and N points per direction in space.
[6] N^D for D-dimensional problems and N points per direction in space.

(up to a desired numerical accuracy). A big advantage of this method is that it allows to find the ground state of a system without knowing the eigenstates $|\,\psi_n\,\rangle$ of the discretized system explicitly. While it is possible use the matrix algorithm discussed in Section 3.1 to obtain these states and especially the ground state (this is the exact eigenstate obtained in the limit $\Delta\tau \to 0$ and $\tau \to \infty$ with imaginary time propagation), the numerical costs for such a diagonalization grow quickly with the number of grid points[7]. Thus, imaginary time propagation is especially well suited to find the ground state of a Hamiltonian representation where a time propagation is *simple* while a diagonalization is *difficult* to achieve.

After the ground state $|\,\psi_0\,\rangle$ has been obtained, one can use imaginary time propagation to obtain the first excited state $|\,\psi_1\,\rangle$. For this purpose, the ground state $|\,\psi_0\,\rangle$ is projected out of the wave function after each time step and now all higher excited with energy $E_{\geq 2} > E_1$ decay exponentially faster. Repeating this strategy over and over allows to obtain a set of excited states $|\,\psi_n\,\rangle$. If one is interested in energetically very highly lying eigenstates of the discretized Hamiltonian (for example to project them out in a time propagation because of their bad behavior), it is possible to invert imaginary time propagation, i.e. to replace $t \to i\,\tau$ such that

$$\left|\tilde{\Psi}(\tau)\right\rangle = \sum_n c_n\, e^{E_n\,\tau}\,|\,\psi_n\,\rangle \quad . \tag{3.49}$$

This yields the energetically highest state $|\,\psi_N\,\rangle$ which can afterwards be projected out to obtain $|\,\psi_{N-1}\,\rangle$ and so on.

The split-operator method with its fixed step size Δt is especially well suited for an implementation on a super computer, since the total calculation time can be directly given (as opposed to methods with adaptive step size).

In the next section a different way to propagate a wave function on a grid arising naturally from the time-dependent extension of the matrix algorithm is presented. The connection between a time propagation on a grid with the spectral ansatz in Section 3.5 is discussed.

3.7 Relation between the Grid and the Spectral Ansatz

In order to extend the matrix algorithm to solve the TDSE Eq. (3.37) one can simply use the full matrix representation of $\hat{\mathrm{H}}$ according to Eqs. (3.4) and (3.11) and solve the system of ordinary differential equations using standard methods, preferably

[7] The matrix algorithm can be used for very large grids by implementing the action of the Hamiltonian on a wave function as $\hat{\mathrm{H}}\,\Psi = \left(\mathcal{F}_{\mathrm{FFT}}^{-1}\,\frac{\hat{\mathrm{p}}^2}{2m}\,\mathcal{F}_{\mathrm{FFT}} + \hat{\mathrm{V}}\right)\Psi$ with the Fast-Fourier transformation $\mathcal{F}_{\mathrm{FFT}}$. Then, energetically low eigenstates (or eigenstates within a desired, narrow energy range) can be found by using Lanczos- or Arnoldi methods which partly diagonalize sparse matrices.

with adaptive step size (Runge-Kutta, Adams,...). However, it is can be numerically more efficient to implement the matrix-times-vector step as

$$\hat{\mathrm{H}}\,\Psi = \left(\mathcal{F}_{\mathrm{FFT}}^{-1} \frac{\hat{\mathrm{p}}^2}{2m} \mathcal{F}_{\mathrm{FFT}} + \hat{\mathrm{V}} \right) \Psi \tag{3.50}$$

with the Fast-Fourier transform $\mathcal{F}_{\mathrm{FFT}}$ and $\hat{\mathrm{V}} = \hat{\mathrm{V}}_0 + \hat{\mathrm{V}}_{\mathrm{int}}(t)$. The Fast-Fourier transform scales with $N\,lnN$ much better[8] than a matrix-vector multiplication with a full matrix consisting of N^2 elements[9].

On the other hand the hermitian matrix $\mathbf{H_0}$ describing the time-independent problem can be diagonalized by a unitary transformation $\mathbf{U}$ ($\mathbf{U}\,\mathbf{U}^\dagger = \mathbf{1} = \mathbf{U}^\dagger\,\mathbf{U}$) such that $\mathbf{U}^\dagger\,\mathbf{H_0}\,\mathbf{U} = \mathbf{E}$. Here $\mathbf{E}$ is a diagonal matrix containing the energy eigenvalues E_n while the columns of $\mathbf{U}$ contain the eigenfunctions $|\,\psi_n\,\rangle$ of $\mathbf{H_0}$. This unitary transformation $\mathbf{U}$ can also be applied to the full time-dependent Hamiltonian matrix $\mathbf{H}$ such that

$$\mathbf{U}^\dagger\,\mathbf{H}\,\mathbf{U} = \mathbf{E} + \mathbf{U}^\dagger\,\tilde{\mathbf{V}}_{\mathrm{int}}(t)\,\mathbf{U} \quad . \tag{3.51}$$

Furthermore

$$(\mathbf{U}^\dagger\,\tilde{\mathbf{V}}_{\mathrm{int}}(t)\,\mathbf{U})_{mn} \equiv \langle\,\psi_m\,|\,\hat{\mathrm{V}}_{\mathrm{int}}(\hat{\mathrm{x}},t)\,|\,\psi_n\,\rangle = (\,\mathbf{V}_{\mathrm{int}}\,)_{mn} \tag{3.52}$$

holds. Thus a time propagation on a grid is formally connected to a time propagation with the spectral ansatz from Section 3.5 (implicit energy phase) by the unitary transformation $\mathbf{U}$, if for the spectral ansatz all possible eigenstates of $\mathbf{H_0}$ are used ($n_{\max} = N$). The discretized wave function Ψ and the coefficient vector c are connected by $\mathbf{U}^\dagger\Psi(t) = c(t)$. The knowledge of $\mathbf{U}$ therefore allows for the analysis of the wave function Ψ within the basis of eigenstates $|\,\psi_n\,\rangle$. A main advantage of the spectral method is the possibility to restrict the Hilbert space such that quickly oscillating high-energy eigenstates of the system are neglected. In Section 4.1.6 it is found that the highest energy discretized continuum states (often) behave unphysical. Furthermore, due to their quick oscillation, a significantly smaller time step is required to converge numerical results compared to the case that these states are not propagated. Luckily usually only a small number of the eigenstates obtained by a full diagonalization show this behavior (approximately the highest $5-10\%$). It is thus possible to project these states out when solving the TDSE on a grid using Eq. (3.50). If the states $|\,\psi_m\,\rangle$ are the quickly oscillating states to be neglected the derivative is modified according to

$$\frac{\partial}{\partial t}\,\Psi = -i \left(1 - \sum_m |\,\psi_m\,\rangle\,\langle\,\psi_m\,| \right) \hat{\mathrm{H}}\,\Psi \quad . \tag{3.53}$$

[8] $N^D lnN$ for D-dimensional problems and N points per direction in space.

[9] $\propto N^{D+1}$ non-zero elements for D-dimensional problems and N points per direction in space (see end of Section 3.1).

The projection can be written in matrix form as

$$\sum_m |\psi_m\rangle\langle\psi_m| = \mathbf{M}\mathbf{M}^\dagger \tag{3.54}$$

with the $N \times m_{\max}$ matrix $\mathbf{M}$ containing the $m_{\max}$ eigenfunctions $|\psi_m\rangle$ in their columns. For $m_{\max} \ll n_{\max}$ a much smaller matrix is multiplied with the wave function compared to the conventional spectral ansatz. This method combines advantages of both the grid method (sparseness and quick Fast-Fourier transform) and the spectral method (neglecting highly oscillating states) which leads to a significantly reduced calculation time and increased numerical stability. It is especially well suited for low-dimensional problems where $n_{\max}$ is of the same order of magnitude as N. For higher-dimensional problems (especially multielectron systems), a physically motivated selection of eigenstates (neglect of multiple-ionization continua) leads to an orders of magnitude smaller $n_{\max} \ll N^D$. Thus, the spectral ansatz, Section 3.5, is computationally much less demanding than a grid approach for the solution of the six-dimensional electronic problem of H_2 exposed to a laser field (as in Secs. 4.2 and 4.4). The advantages of all computational methods discussed in this chapter will be combined to solve the problems in the next chapter.

4 Results

In this chapter multiple studies on the nuclear motion of small molecules and its influence on the ionization behavior are presented. While each study is closed in itself, later studies (in most cases) build upon earlier ones and introduce improved computational methods. The matrix algorithm introduced in Section 3.1 is applied to solve various problems in Section 4.1. These applications include the solution of the position-dependent mass Hamiltonian to describe the inversion (or umbrella) motion of ammonia, Section 2.3, and the Morse potential where it is compared to the B-spline method, Section 3.2. The usefulness of the matrix algorithm to describe vibrational motion of diatomic molecules including properly discretized (vibrational) continuum states is shown. In Section 4.2 the method described in Section 3.3 is used to solve the six-dimensional electronic problem of H_2 in intense, ultrashort laser fields for various nuclear geometries (internuclear distances and orientations). The breakdown of the fixed nuclei approximation in the perturbative multiphoton regime reported in [79, 81, 82] is investigated. Futhermore, the transition from the multiphoton to the quasistatic regime (see Section 2.6) is studied for intense 800 nm laser fields. While this study is restricted to fixed nuclear geometries during the ionization process, the development towards a fully correlated treatment of electronic and nuclear motion begins in Section 4.3 for model (1+1)-dimensional H_2^+. Various methods and approximations from Chapters 2 and 3, especially the spectral vs. the grid ansatz (Section 3.7) for the description of electronic motion, are directly compared. The influence of nonadiabatic couplings and a restriction of the electronic basis set is investigated. Additionally, a direct comparison to literature is performed. The method developed and tested in Section 4.3 is extended in Section 4.4 to describe the (6+1)-dimensional correlated electronic-vibrational motion of H_2 in a laser field. Therefore, the spectral ansatz is used for the description of the electronic motion. The study on the breakdown of the fixed nuclei approximation from Section 3.3 is extended on the influence of vibrational dynamics using this method. Furthermore, the method is applied to study the very recently reported breakdown of the fixed nuclei approximation leading to an isotope effect for the ionization of H_2 vs. D_2 [107, 108].

In the second part of this chapter starting with Section 4.5 the ammonia molecule NH_3 and especially the influence of its inversion motion on the ionization behavior is examined. Using the simple description of the inversion motion from Section 4.1.2 a recent experiment on the isotope effect of high-harmonic generation (imaging relative nuclear motion in NH_3^+ vs. ND_3^+ using *PACER*) [21] is explained. The wave packet "race" behind this process is shown. In Section 4.6 the possibility to create and image vibrational (inversion) wave packets in neutral ammonia is investigated.

Therefore, the nuclear geometry dependence leading to *Lochfraß* is exploited and even the possibility to create a real-time movie of a tunneling wave packet in a double-well potential is examined. The calculations in Section 4.6 are performed for several nuclear geometries using the single-determinant approach, Section 3.4, and a parallel (or anti-parallel) orientation of the linearly polarized laser field with respect to the inversion axis. Finally, the method is extended in Section 4.7 to describe the orientation-dependent ionization of NH_3 in linearly and even elliptically polarized laser fields. The orientation-dependent or polarization-direction-dependent ionization yields of NH_3 are presented for various laser field parameters demonstrating their usefulness for orbital imaging.

4.1 Tests and Applications of the Matrix Algorithm

In this section the matrix algorithm from Section 3.1 is applied for solving various time-independent Schrödinger equations. This study has also been published in [1] except for the more detailed study of the bound- and continuum convergence properties of the Morse potential and the direct comparison to B splines in Sections 4.1.5 and 4.1.6.

In a number of cases complex systems can be treated in a simplified manner, if a position-dependent mass is introduced. One prominent example is the concept of an effective electron mass in solid-state physics where position-dependent masses provide a way to obtain corrections to the simplest approach in which a constant effective mass is used (see, e. g., [109] and references therein). As a consequence, Schrödinger equations with a position-dependent mass have been considered in various contexts, for example to study electronic properties of semiconductors [110], He clusters [111], or super-lattice band structures [112].

Also in molecular physics or theoretical chemistry position-dependent masses can occur, if high-dimensional nuclear motion is described using a lower dimensional effective Hamiltonian. A rather well known example is the theoretical description of the inversion motion (umbrella mode) in ammonia molecules (NH_3) in which the nitrogen atom is moving from one side of the plane formed by the three hydrogen atoms to the other. In fact, this involves a collective motion, since the hydrogen-nitrogen bonds change their lengths while the nitrogen atom moves. This is thus an example of strongly coupled vibrational modes, in this case of the symmetric bending and stretching modes. While the main physics of this motion can be captured by an effective one-dimensional double-well potential, an improved approximation is achieved by introducing a position-dependent mass while still maintaining a one-dimensional treatment. The inversion motion of ammonia and its one-dimensional model has been studied extensively in several papers, e. g., in [62, 113–115], and has been exploited for the ammonia maser [63]. Especially Aquino *et al.* [115] obtained very accurate results in comparison to experiment by reducing the two-dimensional problem to a one-dimensional problem with a position-dependent reduced mass. Note that this ansatz is deduced from classical arguments and thus leads to quantum mechanical operator ordering ambiguities, since it is not clear anymore how to order the operators in the kinetic term $p^2/2m$. The accurate and efficient solution of a Schrödinger equation with a position-dependent mass is non-trivial and various efforts were made even recently to find analytical or numerical solutions, e.g., in [109, 116, 117].

In the following it is found that the matrix algorithm, Section 3.1, determines efficiently and accurately the bound states of Schrödinger equations with a position-dependent mass. The algorithm is very flexible and allows to consider different symmetrized or non-symmetrized forms of the kinetic-energy operator. Furthermore, also non-Hermitian Hamiltonians can be treated, including complex ones. Non-

Hermitian PT-symmetric Hamiltonians have recently stirred some interest [118, 119] in connection with the question under which circumstances the spectrum may still remain real. In addition to that, non-Hermitian Hamiltonians (also without PT-symmetry) occur for example in the context of complex optical potentials (see, e.g., [23, 30]).

Hamiltonians with a position-dependent mass or PT symmetry are briefly discussed in Section 4.1.1. Afterwards the performance of the method is discussed for a number of examples. This includes a study of the inversion mode of NH_3 (Sections 4.1.2 and 4.1.4) and ND_3 (Section 4.1.3), bound and continuum states of the Morse potential (Sections 4.1.5 and 4.1.6), a harmonic oscillator with position-dependent mass (Section 4.1.7), and examples of PT-symmetric and non-symmetric non-Hermitian Hamiltonians (Section 4.1.8). In addition to these one-dimensional examples, the application of the algorithm to the two-dimensional Henon-Heiles system is discussed in Section 4.1.9.

4.1.1 Position-Dependent Mass and PT-Symmetric Schrödinger Equations

The replacement $m \to m(\hat{\mathrm{x}})$ shall be performed for one-dimensional quantum systems and, therefore, various ways to order the operators in the kinetic-energy terms are investigated. A whole class of Hermitian Hamiltonians with position-dependent mass is given by the von Roos Hamiltonians [120],

$$\hat{\mathrm{H}} \;=\; \frac{1}{4}\left(\hat{\mathrm{m}}^{\alpha}\hat{\mathrm{p}}\,\hat{\mathrm{m}}^{\beta}\,\hat{\mathrm{p}}\,\hat{\mathrm{m}}^{\gamma} \;+\; \hat{\mathrm{m}}^{\gamma}\,\hat{\mathrm{p}}\,\hat{\mathrm{m}}^{\beta}\,\hat{\mathrm{p}}\,\hat{\mathrm{m}}^{\alpha}\right) \;+\; V(\hat{\mathrm{x}}) \tag{4.1}$$

with

$$\alpha \;+\; \beta \;+\; \gamma \;=\; -1 \tag{4.2}$$

and $\hat{\mathrm{m}} = m(\hat{\mathrm{x}})$ with the usual canonical operators $\hat{\mathrm{p}}$ and $\hat{\mathrm{x}}$. The choice $\alpha = \gamma = 0$, $\beta = -1$ leads to

$$\hat{\mathrm{H}} \;=\; \frac{1}{2}\,\hat{\mathrm{p}}\,\frac{1}{\hat{\mathrm{m}}}\,\hat{\mathrm{p}} \;+\; V(\hat{\mathrm{x}}), \tag{4.3}$$

while with $\alpha = -1$, $\beta = \gamma = 0$ one finds

$$\hat{\mathrm{H}} \;=\; \frac{1}{4}\left(\frac{1}{\hat{\mathrm{m}}}\,\hat{\mathrm{p}}^2 \;+\; \hat{\mathrm{p}}^2\,\frac{1}{\hat{\mathrm{m}}}\right) \;+\; V(\hat{\mathrm{x}}). \tag{4.4}$$

While there is no *priory* reason to favor any of the Hermitian Hamiltonians, for example a specific choice of α, β, and γ, non-Hermitian Hamiltonians are often rejected for general reasons, since they can possess complex eigenvalues. However, in standard quantum mechanics *closed* systems are described by Hermitian Hamiltonians and real eigenvalue spectra. (Note that non-Hermitian Hamiltonians occur, e. g., in the approximate description of open systems with optical potentials.) Regarding the reality of the spectrum, non-Hermitian PT-symmetric Hamiltonians form a special

class as discussed in [118, 119]. Therefore, they are of special interest for possible extensions of standard quantum mechanics. Note, however, that these extensions often also involve a complex potential instead of a position-dependent mass. For the NH_3 molecule the position-dependent reduced mass $\mu(x)$ in [115] was derived within classical mechanics and then translated into quantum mechanics in the form

$$\hat{\mathrm{H}} \;=\; \frac{1}{2\hat{\mathrm{m}}}\,\hat{\mathrm{p}}^2 \;+\; V(\hat{\mathrm{x}}) \tag{4.5}$$

which is non-Hermitian, but convenient for computation. The advantage of Eq. (4.5) is that no first derivative of the wave function occurs. This simplifies the numerical solution with standard approaches. For example, the Numerov-Cooley method [121, 122] can be adopted as was done in [114]. Another possible non-Hermitian choice is

$$\hat{\mathrm{H}} \;=\; \hat{\mathrm{p}}^2\frac{1}{2\,\hat{\mathrm{m}}} \;+\; V(\hat{\mathrm{x}}). \tag{4.6}$$

(Note if both the potential V and the mass m possess inversion symmetry, $V(x) = V(-x)$ and $m(x) = m(-x)$, as is the case for ammonia, then the Hamiltonians in Eqs. (4.5) and (4.6) are P and T symmetric.)

It is important to not only have an efficient and reliable solver for one version of the Hamiltonian, but to be able to compare the results of different versions. Ideally, the results agree sufficiently well and thus the question of the proper form becomes practically inessential for the attempted approximation level. A strong variation of the results with the chosen form of the Hamiltonian, on the other hand, is a clear warning signal. Since non-Hermitian and (for example for $V(x) \neq V(-x)$) in principle even PT non-symmetric Hamiltonians can be obtained for some versions of the Hamiltonians with a position-dependent mass, it is also of interest to have a solver that can handle these cases and that detects possible non-vanishing imaginary components of the eigenvalues. This is, in fact, also an important issue in the general context of PT-symmetric Hamiltonians (or other proposals for extensions of standard quantum mechanics) without position-dependent masses. Since in the majority of cases physically relevant Hamiltonians do not possess analytical solutions, it is important to numerically check whether the eigenvalue spectrum is purely real or not. The algorithm presented below provides a promising solution to this type of problems. Position-dependent masses are easily handled, even for different formulations of the kinetic-energy operator. Furthermore, a number of bound states are obtained simultaneously within a single calculation. Finally, the algorithm can equally well be applied to complex Hamiltonians and thus also to non-Hermitian Hamiltonians with either purely real or partly complex eigenvalues.

4.1.2 The Inversion Motion of NH_3

To calculate the energy levels describing the inversion motion in ammonia with our algorithm, the procedure in [115] is followed and the data points (from table 1 in

[115]) for the double-well potential $V(x)$ describing the inversion mode are fitted by an even polynomial of degree 20. It might be noted that the potential obtained with DFT is in good agreement with the experimental value for the equilibrium geometry in [123] and the obtained barrier height of 2013.5 cm^{-1} agrees well with the one from empirical procedures (2018 $\pm$10 cm^{-1} [62]). In addition, the theoretical study in [62] yields an effective barrier height of 2021 $\pm$ 20 cm^{-1}. The potential is therefore very useful for a one-dimensional study, though the method is nevertheless a little bit questionable, because the theoretical effective barrier in [62] is only obtained, if one takes into account the zero-point vibrational energies of the other vibrational degrees of freedom, which adds a value of 244 $\pm$ 14 cm^{-1} to the barrier height according to [62].
The goal is now to solve the Schrödinger equation,

$$\Psi''(x) \;=\; 2\mu(x)\,[\,V(x) \;-\; E\,]\;\Psi(x) \quad , \tag{4.7}$$

or equivalently,

$$\left(\frac{1}{2\mu(x)}\,\hat{\mathrm{p}}^{\,2} \;+\; V(x)\right)\;\Psi(x) \;=\; E\,\Psi(x) \tag{4.8}$$

with the position-dependent reduced mass

$$\mu(x) \;=\; \frac{3\,m\,M}{3\,m \;+\; M} \;+\; \frac{3\,m\,x^2}{r_0^2 - x^2} \quad , \tag{4.9}$$

where m is the mass of a hydrogen atom, M the one of the nitrogen atom, and $r_0 = 1.00410198$ a. u. is given in [115] as the N-H distance which minimizes the energy of the molecule in planar geometry. The result of the matrix diagonalization is illustrated in Figure 4.1 and the obtained energies are listed in Table 4.1. The states are named using the symmetry label *symmetric* (s) or *antisymmetric* (a) together with an index n where $n = 0$ stands for the energetically lowest state with symmetric or antisymmetric character. Thus 0s designates the symmetric ground state and the other energies are given relative to this level. A comparison of the energy levels found with the matrix algorithm to the energy levels in table 4.1 of [115] shows perfect agreement.

As has been mentioned in Sec. 4.1.7, the obtained eigenenergies should ideally not change drastically, if one puts the position-dependent mass into the Schrödinger equation in another form. Table 4.2 shows the eigenenergies obtained with Eqs. (4.3) to (4.6). A maximum relative deviation of the eigenenergies listed in Table 4.2 of about 0.5% (0.005 cm^{-1}) is found for the 0a state, indicating that the choice where to put the reduced mass has only a very minor influence on the resulting energies within the given accuracy.

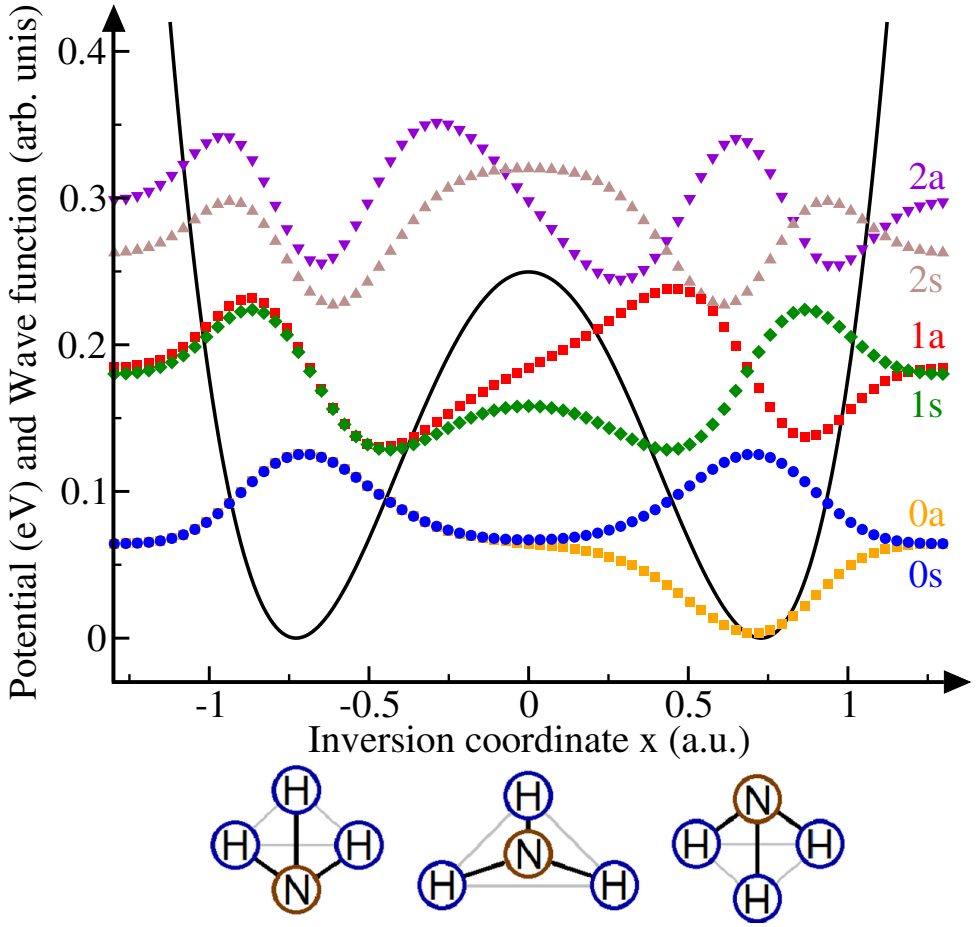

Figure 4.1: Potential curve (solid black line, data from [115]) and vibrational eigenfunctions (colored symbols) of NH_3 labeled by symmetry (s/a) with respect to a reflection at $x = 0$. The eigenfunctions are vertically shifted such that they approach their respective eigenenergies in the limit $|x| \to \infty$. In the calculation, a width of $L = 4$ a.u. and $N = 111$ points were used. Below the x-axis, the corresponding planar ($x = 0$) and pyramidal ($x \neq 0$) geometries are sketched. This figure is also presented in [4].

State	μ=const [115]	Ref. [115]	This work	Experiment
0s	0.00	0.000	0.000	0.000
0a	1.05	0.837	0.837	0.793 [124]
1s	977.23	931.72	931.72	932.43 [125]
1a	1030.12	968.67	968.67	968.12 [125]
2s	1651.69	1596.76	1596.76	1598.47 [126]
2a	2011.44	1885.33	1885.33	1882.18 [126]
3s	2558.75	2389.14	2389.15	2384.17 [126]
3a	3142.66	2902.99	2902.99	2895.61 [126]

Table 4.1: Inversion energy levels of NH_3 (shifted by E_{0s}) in cm^{-1}. The energies of our work were found with $L = 4.0\,\text{a. u.}$, $N = 111$ points and adopting the same 1D potential as in [115]. This table is also presented in [1].

State	Eq. (4.3)	Eq. (4.4)	Eq. (4.5)	Eq. (4.6)
0s	0.000	0.000	0.000	0.000
0a	0.837	0.833	0.837	0.837
1s	931.71	932.01	931.72	931.72
1a	968.64	968.81	968.67	968.67
2s	1596.77	1597.36	1596.76	1596.76
2a	1885.25	1885.45	1885.33	1885.33
3s	2389.03	2389.21	2389.15	2389.15
3a	2902.82	2902.84	2902.99	2902.99

Table 4.2: Inversion energy levels of NH_3 (shifted by E_{0s}) in cm^{-1} for different implementations of the position-dependent reduced mass. In the calculations $L = 4.0\,\text{a. u.}$ and $N = 111$ points were used. This table is also presented in [1].

State	This work μ=const Eq. (4.10)	This work $\mu(x)$ Eq. (4.9)	Experiment [124]
0s	0	0	0
0a	0.05	0.05	0.05
1s	793.8	746.2	745.6
1a	798.3	749.3	749.15
2s	1419.7	1368.4	1359.0
2a	1513.7	1432.0	1429.0
3s	1912.6	1836.4	1830.0
3a	2238.4	2106.4	2106.6

Table 4.3: Inversion energy levels of ND_3 (shifted by E_{0s}) in cm^{-1}. The calculations were done with $L = 4.0$ a.u. and $N = 111$ points. This table is also presented in [1].

4.1.3 Inversion Energy Levels of ND_3

In addition to NH_3, the energy levels of ND_3 which were not calculated in [115] are investigated. This is a further check of the adopted position-dependent mass model. Therefore, the mass of the hydrogen atom is replaced by the mass of deuterium m_D=2.013553212712 amu [127] and the Schrödinger equation (4.5) is solved. The obtained energies are listed in Table 4.3. It turns out that the inversion splitting can be reproduced and the energy levels for higher excited vibrational states have a relative error $\frac{|E_{calc} - E_{exp}|}{E_{exp}} \leq 0.7\%$ in comparison to the experiment whereas the use of the constant reduced mass

$$\mu = \frac{3mM}{3m + M}\left(1 + \frac{3m\sin^2\beta_e}{M}\right) \tag{4.10}$$

from [128] with $\beta_e = 22°13'$ (from [115]) leads to higher energy values and, therefore, larger relative errors (up to 6.6%). Even though the agreement with the experiment is very good, it still has to be noted that according to [62] the barrier height depends on the zero-point vibrational energy of the other vibrational degrees of freedom, and this zero-point vibrational energy depends on the isotope.

4.1.4 Convergence Behavior of NH_3-Inversion Energy Levels

The convergence behavior of the matrix algorithm is discussed on the example of NH_3. Eq. (4.4) is used as Hamiltonian and the number of points N is varied first for fixed $L = 4.5$ a.u. with the result shown in Figure 4.2. In this way the dependence on the resolution given by the lattice spacing was tested. In Figure 4.3 the spacing is held constant at $a = 4.5/151$ a.u. and thus the stability when changing L is tested. The nearly straight lines in the semilogarithmic plot indicate exponential

convergence behavior with respect to both regulators.

The convergence behavior that has been observed is actually physically plausible. As indicated before the only exponentially small sensitivity with respect to (large) L is due to the smallness of the wave functions for bound states deep in the classically forbidden region. The same wave functions in momentum space will also have an exponential fall-off at large momenta so that a dual argument holds in momentum space. This can be understood by considering the sampling theorem [129]. A continuous time signal that contains no frequencies beyond the Nyquist frequency $\omega = \pi/\tau$ can be *exactly* reconstructed from sampling it at discrete times separated by τ (CD player). In analogy, if the support of our bound state wave functions would be *exactly* contained in the interval $[-\pi/a\,,\,\pi/a\,]$ then the *exact* wave function for continuous x could be reconstructed form the Fourier components (discrete and finite in number for finite L). Then there obviously is an exact correspondence between derivatives d/dx and factors $i\,p$. In reality the bound states do not have compact momentum support, but the deviation is only caused by the exponentially small tails for small enough a.

4.1.5 Morse Potential: Bound-State Convergence and Comparison to B Splines

The discrete position (momentum) space introduced in the matrix algorithm is symmetric with respect to $x = 0$ ($p = 0$) as is also the double-well problem discussed in the previous section. Nevertheless, general Hamiltonians can be non-symmetric and may also have a partially continuous spectrum (in the infinite volume). Therefore it is investigated if bound states can still be found accurately and efficiently using the matrix algorithm also in this more general case. A popular example for a non-symmetric potential with bound and continuum states is the Morse potential

$$V(x) \;=\; D_e\,\left(1 \,-\, e^{-\alpha\,(\,x\,-\,x_{\rm e}\,)}\right)^2. \tag{4.11}$$

Often the vibration of a diatomic molecule can be well-described by this potential since it behaves similar to typical Born-Oppenheimer potential energy curves (which support bound vibrational states). The energy spectrum for the bound states of this potential is known analytically [130],

$$E_n \;=\; 2\pi\,\hbar\,\nu_0\,\left(n\,+\,\frac{1}{2}\right) \,-\, \frac{\pi^2\,\hbar^2\,\nu_0^2}{D_e}\,\left(n\,+\,\frac{1}{2}\right)^2, \tag{4.12}$$

with $\nu_0 \;=\; \dfrac{\alpha}{2\pi}\,\sqrt{\dfrac{2D_e}{\mu}}$ where μ is (again) the reduced mass. A Morse potential with model parameters

$$D_e = \mu = 1, \quad \alpha = 0.24, \quad x_{\rm e} = -\frac{3}{7}\,L \tag{4.13}$$

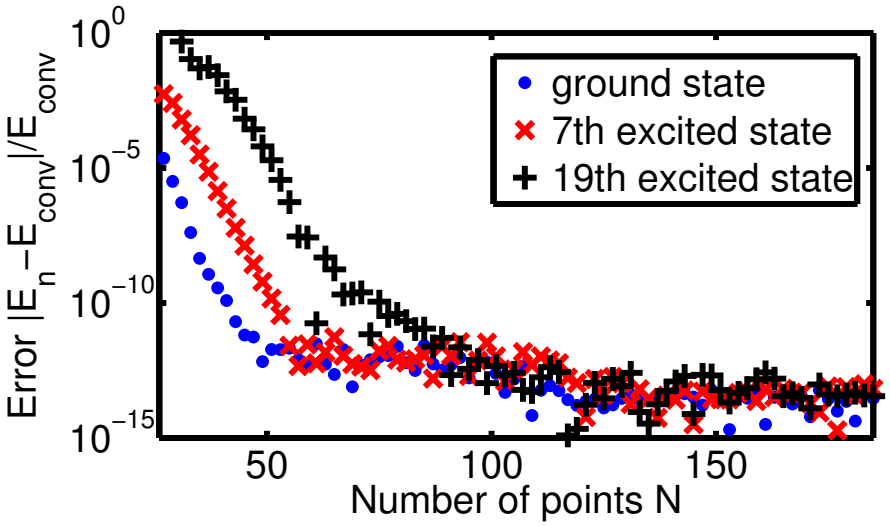

Figure 4.2: Convergence behavior with respect to a variation of the lattice spacing that is proportional to $1/N$ as the width $L = 4.5$ a. u. is held fixed. The ground state and the 7th as well as the 19th excited state are shown. Relative errors of the energies $\frac{|E_n - E_{\text{conv}}|}{E_{\text{conv}}}$ are plotted, where E_{conv} is the 'converged' energy (average over the 10 largest values of N). This figure is also presented in [1].

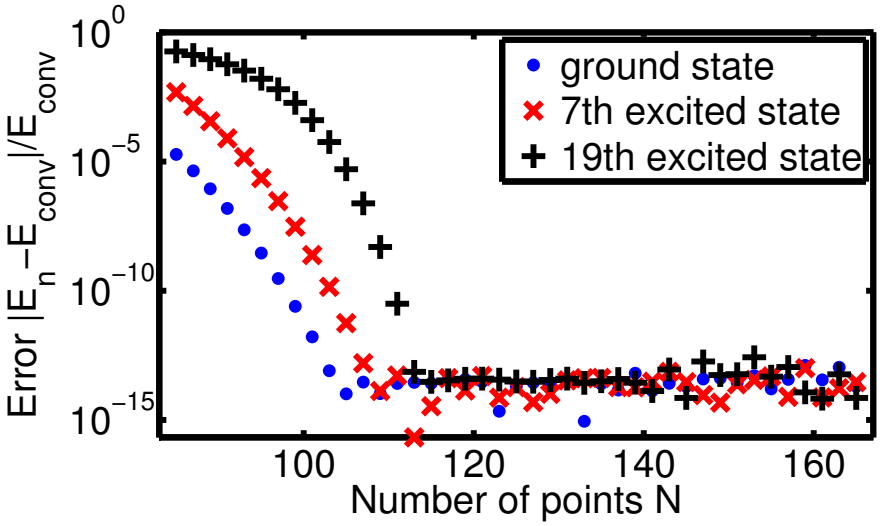

Figure 4.3: As Figure 4.2, but now $a = 4.5/151$ a.u. is fixed and thus L varies proportional to the number of points N. This figure is also presented in [1].

where 6 vibrational bound states exist is investigated. Figure 4.4 shows these bound states obtained with $L = 140$ and $N = 201$ points. The last bound-state has an eigenenergy of $E_5 \approx 0.996$ and is thus energetically just very slightly below the dissociation threshold $D_e = 1$. Thus, the wave function extends quite far into the classically forbidden region.

Figure 4.5 shows the bound state convergence behavior with respect to the lattice spacing a (fixed width $L = 140$) for the matrix algorithm. For comparison also the behavior for B splines (Section 3.2) of order $k = 10$ and a linear knot sequence is shown[1] Both the matrix algorithm and B splines show a very similar convergence behavior. However, the relative error using B splines oscillates less with N_B than with N for the matrix algorithm. As in Section 4.1.4 an exponential convergence behavior is observed and machine precision is reached quickly except for the fifth excited state. This state remains at a relative error of 10^{-11} starting around $N = N_B = 175$. Since this state extends deeply into the classical forbidden region, a box size of $L = 140$ is simply not sufficient to reach machine precision. The variation of the box size in Figure 4.6 (fixed $a = 0.7$) further confirms this observation. Machine precision for the fifth excited state is reached around $N = N_B = 250$ which corresponds to $L = Na = 175$. Again, the box size convergence behavior of the matrix algorithm is similar to Section 4.1.4, but the fifth excited state shows a significantly slower convergence rate with box size than the lower excited states (which already converge at $N = 140, L = 98$). Interestingly, B splines show an initially slower convergence behavior with box size, requiring around $N_B = 175, L = 122.5$ to converge the low lying bound-states with $n < 5$. For the fifth excited state the convergence behavior changes to the behavior of the matrix algorithm at around $N_B = 160$.

Figure 4.7 compares the convergence behavior of B splines of order $k = 6, 8, \ldots, 14$ with the matrix algorithm for the ground state and the fifth excited state. For the convergence with respect to the spacing a, higher B spline orders lead to a faster convergence rate until the exponential behavior of the matrix algorithm is reached. This is expected since higher B spline orders lead to a higher-order (better) approximation of the momentum operator. The initial error at $N_B = 100$ gets slightly worse with increasing B spline order, however. The higher initial (small N_B) error with increasing B spline order k is even more pronounced for the convergence with respect to the width L ($a = 0.7$) shown in the same figure. On the other hand, while all B spline orders k show a similar convergence rate, small orders fail to reach machine precision for large L ($k = 6$ converges to a relative error $> 10^{-13}$ and $k = 8$ to $> 10^{-11}$, $a = 0.7$ is thus too large for $k = 6$ and 8). A B spline order of $k = 10$ thus seems to constitute a compromise between convergence for relatively small box sizes and final accuracy[2].

[1] The B spline result is computed using a simple MATLAB implementation of T. Kiel [131].

[2] In practice, a very large B spline order is furthermore disadvantageous because more B splines overlap with each other ⇒ less integrals for the Hamiltonian and overlap matrices are zero.

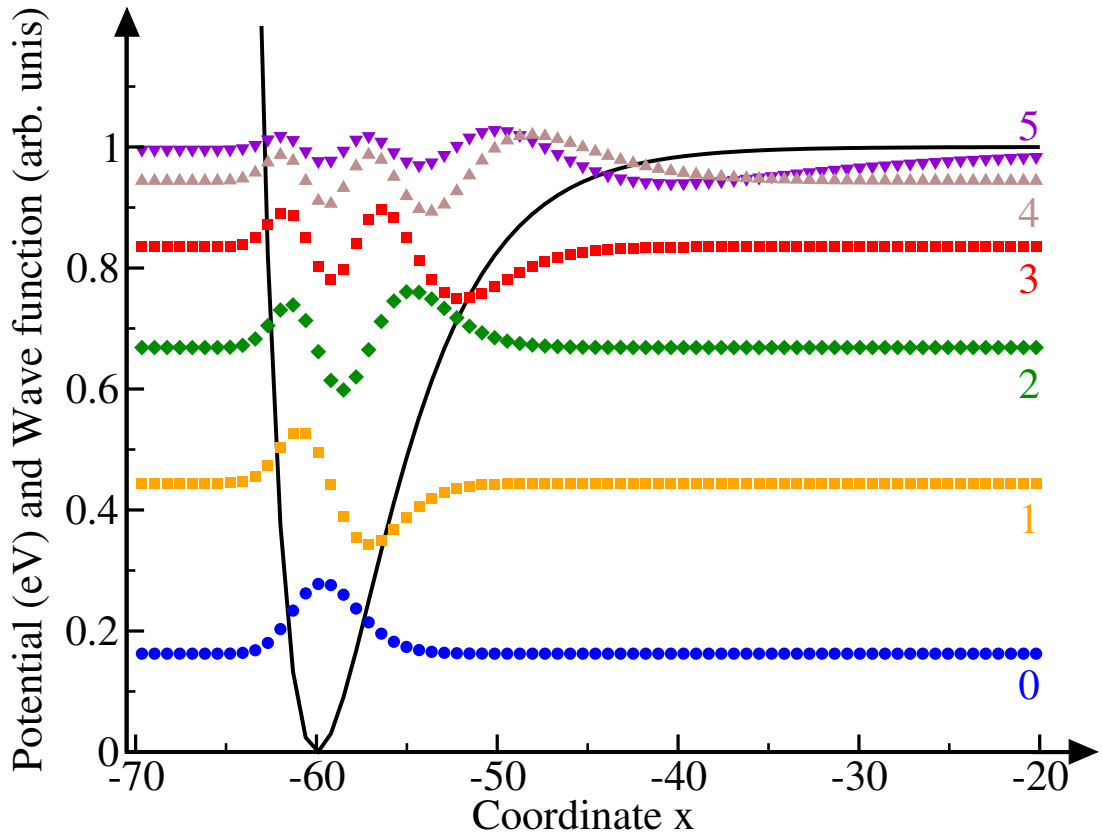

Figure 4.4: Morse potential Eq. (4.11) with parameters according to Eq. (4.13) (solid black line) and corresponding eigenfunctions (colored symbols). The eigenfunctions are vertically shifted such that they approach their respective eigenenergies in the limit $|x| \to \infty$. A width of $L = 140$ and $N = 201$ points were used in the calculation.

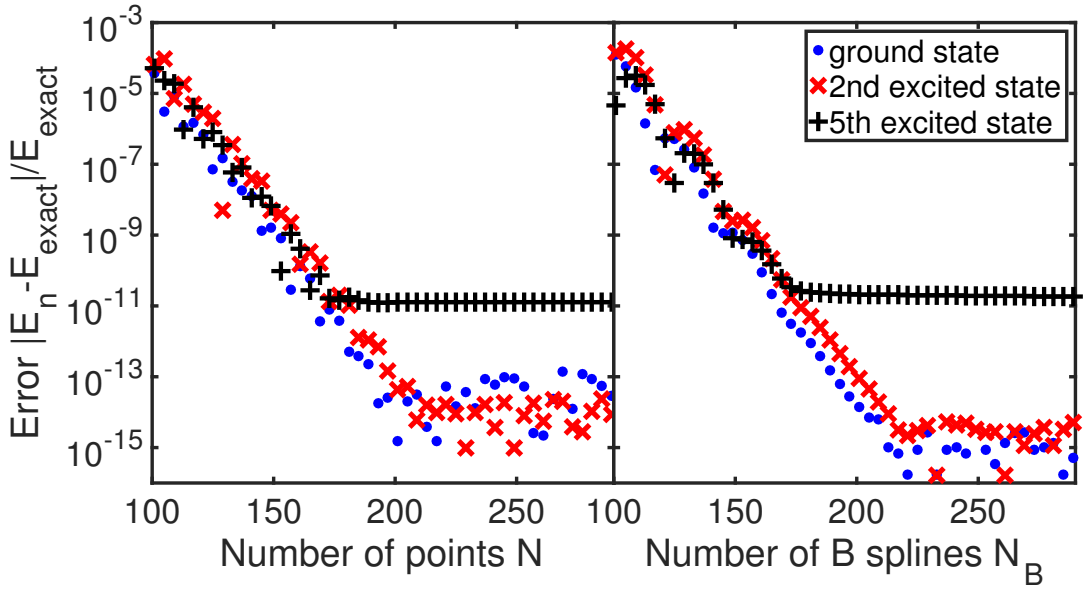

Figure 4.5: Convergence behavior with respect to a variation of the lattice (or knot point) spacing a for the matrix algorithm (left) and B splines of order $k = 10$ (right). The spacing is proportional to $1/N$ as the width is held constant at $L = 140$. The ground state, the 2nd as well as the 5th excited state are shown. Relative errors of the energies $\frac{|E_n - E_{\text{exact}}|}{E_{\text{exact}}}$ are plotted, where E_{exact} is the 'exact' energy, Eq. (4.12), of the Morse potential Eq. (4.11) [parameters Eq. (4.13)].

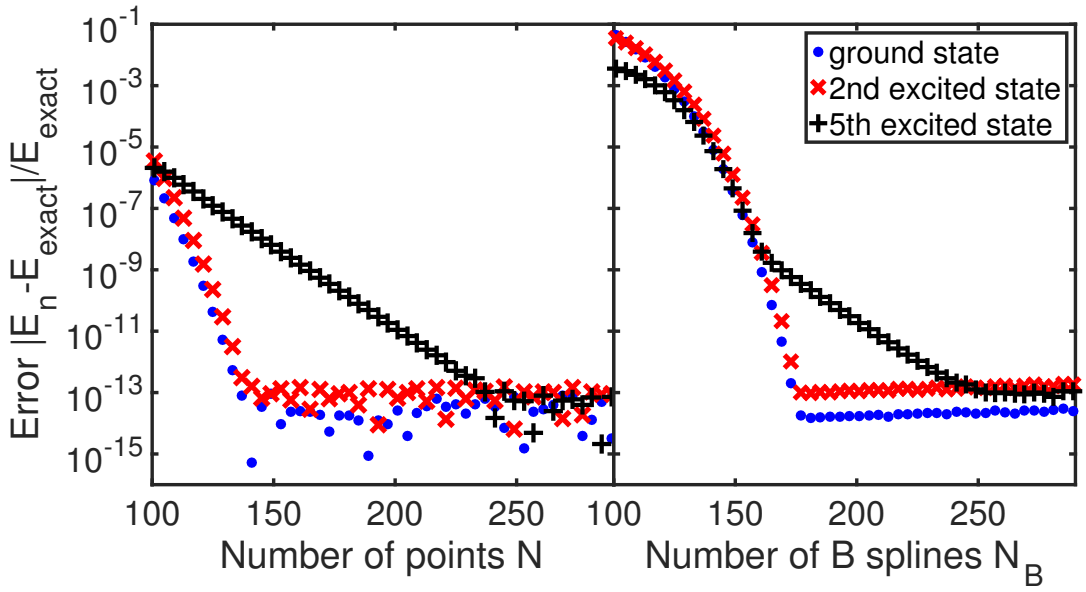

Figure 4.6: As Figure 4.5, but now $a = 140/200 = 0.7$ is fixed and thus L varies proportional to the number of points (or B splines) N (N_B).

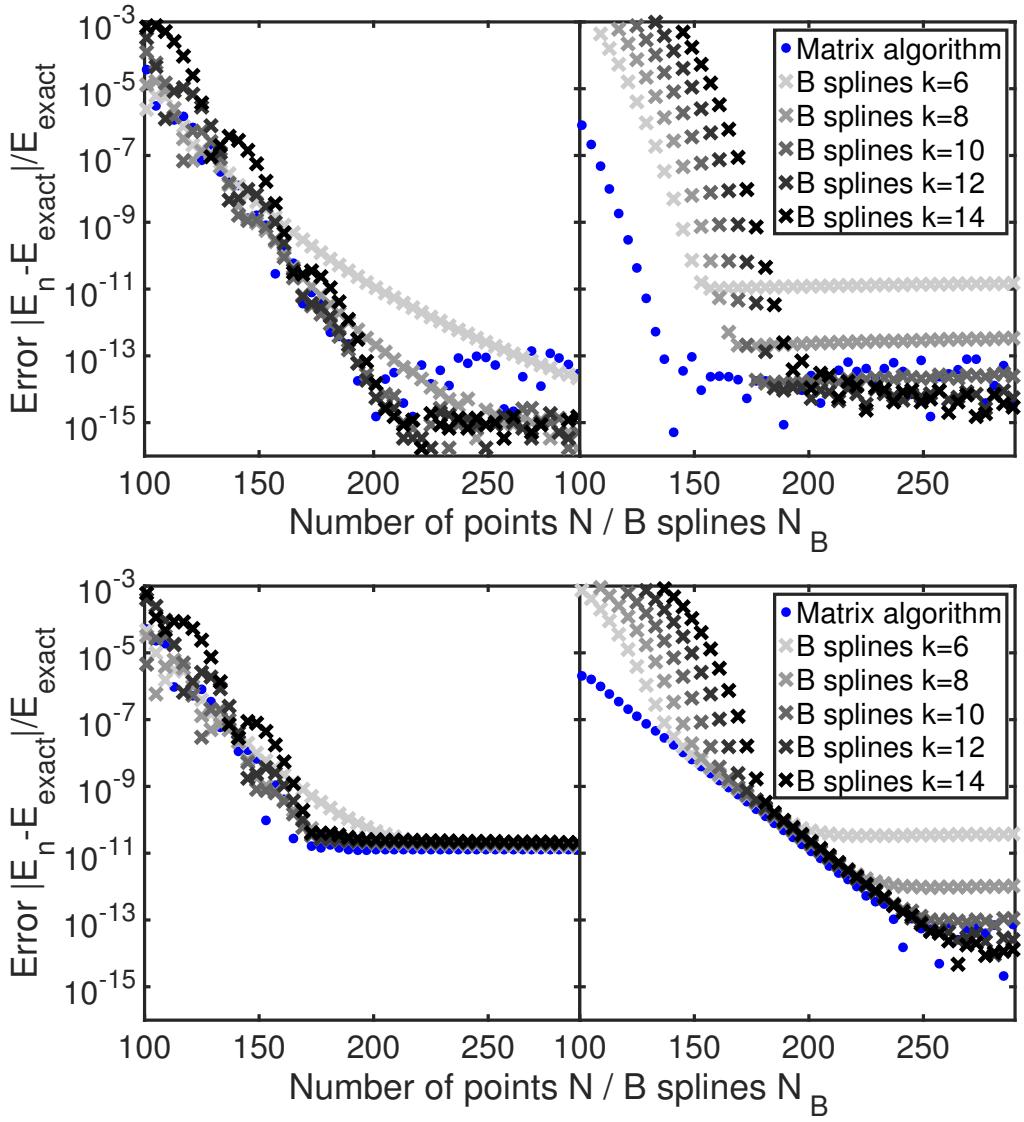

Figure 4.7: Convergence behavior for a variation of the lattice (or knot point) spacing a (left) with width fixed at $L = 140$ as well as variation of the width L (right) with fixed $a = 140/200 = 0.7$. The graph at the top shows the behavior of the ground state while the graph at the bottom shows the fifth excited state. The matrix algorithm (blue points) is compared to B splines of different order k as (grey-shaded crosses) as labeled inside the graph. Relative errors of the energies $\frac{|E_n - E_{\text{exact}}|}{E_{\text{exact}}}$ are plotted, where E_{exact} is the 'exact' energy, Eq. (4.12), of the Morse potential Eq. (4.11) [parameters Eq. (4.13)].

4.1.6 Morse Potential: Properties of the Discretized Continuum, Density of States, and Comparison to B Splines

In addition to the bound states, discretized continuum states are obtained on which the periodic boundary conditions of the box with width L are imprinted. To check whether this discretized continuum can approximately represent the true continuum, the relation

$$\left\langle 0 \left| \hat{\mathrm{x}}^2 \right| 0 \right\rangle \approx \sum_{n=0}^{n_{\max}} \left\langle 0 \left| \hat{\mathrm{x}} \right| n \right\rangle \left\langle n \left| \hat{\mathrm{x}} \right| 0 \right\rangle \tag{4.14}$$

is examined as an example using the discretized states $|\, n \,\rangle$. Using $N = 301$ points, $L = 140$, and $x_{\mathrm{e}} = -60$ the relative error

$$\epsilon(n_{\max}) = \frac{\left| \left\langle 0 \left| \hat{\mathrm{x}}^2 \right| 0 \right\rangle - \sum_{n=0}^{n_{\max}} \left\langle 0 \left| \hat{\mathrm{x}} \right| n \right\rangle \langle n| \hat{\mathrm{x}} \left| 0 \right\rangle \right|}{\left\langle 0 \left| \hat{\mathrm{x}}^2 \right| 0 \right\rangle} \tag{4.15}$$

was calculated. With a restriction of the summation to bound states only $\epsilon(n_{max} = 5) \approx 10^{-6}$ is found. When further increasing $n_{\max}$ the error decreases monotonically until machine precision is reached ($\epsilon(n_{\max}) < 10^{-14}$ for $n_{\max} > 116$). Thus, the completeness relation of the eigenstates is numerically fulfilled, if also the discretized continuum states are considered.

Discretized continuum states may also be used to solve the TDSE describing atoms or molecules exposed to a laser field using the spectral ansatz, see Section 3.5. The initial state is a strongly localized bound state (typically the ground state). If the time-dependent wave function is not significantly reflected at the box boundaries during the time propagation the wave function does not get strongly distorted due to the assumption of a finite box[3]. When the laser field is over the population of discretized continuum states represents, e.g., ionization (electronic continuum) or dissociation (vibrational continuum). However, discretized continuum states $|\, \psi_n \,\rangle$ are orthonormalized

$$\langle\, \psi_n \,|\, \psi_{n'} \,\rangle = \delta_{nn'} \tag{4.16}$$

just like bound states. Non-discretized continuum states $|\, \psi_E \,\rangle$ with (continuous) energy E, in contrary, are energy-normalized such that

$$\langle\, \psi_E \,|\, \psi_{E'} \,\rangle = \delta(E - E') \quad . \tag{4.17}$$

In order to extract observables which involve discretized continuum states from a coefficient vector after the laser field is over (e.g. photoelectron spectra) the discretized continuum states have to be renormalized[4]. This can be achieved, e.g., by

[3] Of course, convergence can be checked by varying the box size L.

[4] For the time propagation itself the discretized continuum states normalized according to Eq. (4.16) are the proper basis. Thus, the discretized diccontinuum states must not be renor-

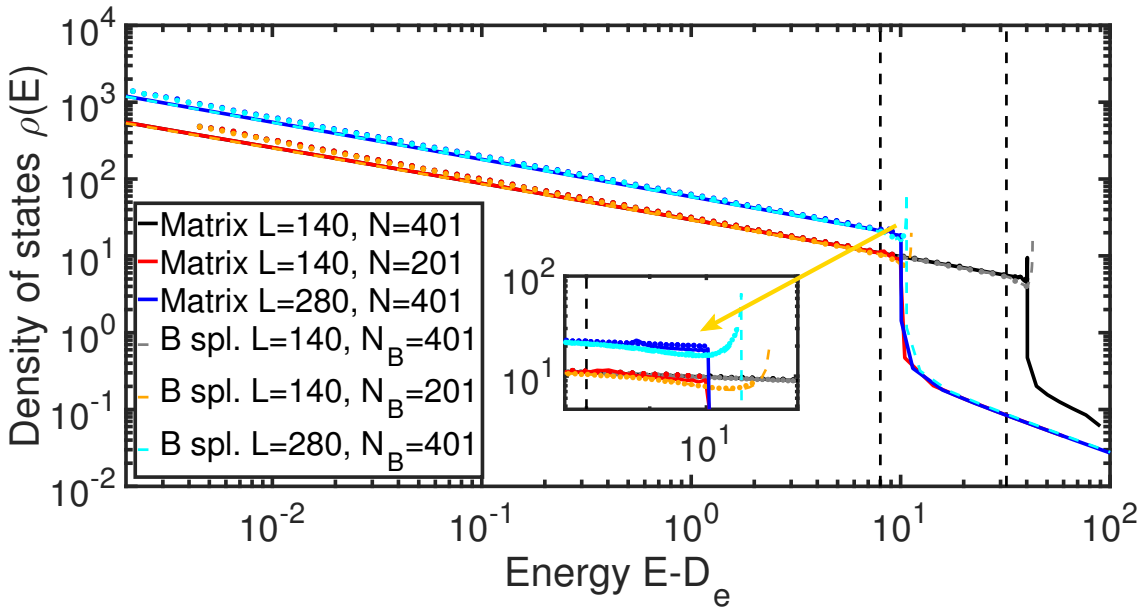

Figure 4.8: Behavior of the density of states $\rho(E)$ for the matrix algorithm (full lines) and B splines (dashed lines) of order $k = 10$ for the Morse potential Eq. (4.11) [parameters Eq. (4.13)]. Points show the corresponding density for $D_e = 0$ (free particle). The dashed vertical line indicate the energy E_{crit} from where the density of states does not smoothly decrease anymore.

matching the asymptotic behavior of the discretized states to analytically known Coulomb functions or, as discussed in the following, using the density of states

$$\rho(E) = \frac{\partial n}{\partial E} \quad . \tag{4.18}$$

Discretized continuum states can then be renormalized using $|\,\Psi_{E_n}\,\rangle \approx \sqrt{\rho(E_n)}\,|\,\psi_n\,\rangle$ (e.g. [65], page 20-21). The energy-resolved photoelectron spectrum $P(E)$ (probability to find an electron at energy E) can thus be obtained from the time-propagated wave function $|\,\Psi(T)\,\rangle$ after the laser field by

$$P(E) \approx \sum_{\mu, E_n^\mu = E} \rho(E_n^\mu) \left|\,\langle\,\Psi(T)\,|\,\Psi_n^\mu\,\rangle\,\right|^2 \tag{4.19}$$

such that the contributions from all continuum channels μ are summed up[5]. From the Taylor expansion

$$\begin{aligned} E(n') = E(n) + \left.\frac{\partial E}{\partial n'}\right|_{n'=n} (n'-n) + \frac{1}{2}\left.\frac{\partial^2 E}{\partial n'^2}\right|_{n'=n} (n'-n)^2 \\ + \frac{1}{6}\left.\frac{\partial^3 E}{\partial n'^3}\right|_{n'=n} (n'-n)^3 + O((n'-n)^4) \end{aligned} \tag{4.20}$$

using $n' = n \pm 1$ and neglecting $O((n'-n)^3)$ one finds

$$\left.\frac{\partial n}{\partial E}\right|_{E_n} = \rho(E_n) \approx \frac{2}{E_{n+1} - E_{n-1}} \quad . \tag{4.21}$$

Figure 4.8 shows the density of states obtained using the matrix algorithm as well as B splines of order $k = 10$ for the Morse potential and different basis set parameters. Both the matrix algorithm and B splines show a qualitatively similar behavior, i.e. the density of states smoothly decreases up to a critical energy E_{crit} where it "breaks out". As a rule of thumb discretized continuum states are physically senseful up to energy E_{crit} and states with higher energy should be neglected in a time propagation using the spectral ansatz[6]. In one dimension the unphysical states are typically the 10-25% highest-energy states (14-22% for the example in Figure 4.8). Despite the very different boundary conditions of the matrix algorithm (periodic) and B splines (particle in a box), a similar behavior of both approaches is expected for the Morse potential since this potential is very high at the lower boundary $x = -L/2$. Due to the periodic boundary conditions of the matrix algorithm it is thus also very high approaching the upper boundary $x \to L/2$.

malized when used for time propagation.

[5] In practice, interpolation to energy E is necessary for each continuum channel

[6] Neglecting these high-energy states (which quickly oscillate in time) also significantly reduces the number of time steps required to reach a target accuracy for propagation routines using an adaptive time step.

Considering a free particle potential (formally a Morse potential with $D_e = 0$, points in Figure 4.8), differences between both methods are exposed[7]. For both methods the Morse potential behavior converges to the free particle behavior with increasing energy up to the critical energy E_{crit}. For B splines the free particle in a box shows the same "break out" behavior as the Morse potential for even larger energies. For the matrix algorithm, however, no such "break out" behavior is observed. The free particle in a periodic potential

$$\frac{1}{2m}\hat{\mathrm{p}}^2 \;=\; \frac{1}{2m}\,\mathcal{F}^{-1}\,p^2\,\mathcal{F} \tag{4.22}$$

is exactly solved within the matrix algorithm. The operation that diagonalizes the Hamiltonian is the discrete Fourier transformation. The resulting eigenenergies are $p_k^2/2m$ where $p_k = k\,2\pi/L,\;\; k = -M, -M{+}1, \ldots, M$. The dependence of the density of states when changing the basis set parameters can directly be understood from this solution. Since $p_{\max} \propto N/L = 1/a \;\Rightarrow\; p_{\max}^2 \propto 1/a^2$ doubling the point spacing a leads to a four times larger maximum energy which can be represented by the basis set. Indeed, the critical energy shown in Figure 4.8 shifts from $E_{\text{crit}} = 8$ to $E_{\text{crit}} = 32$ when doubling the spacing a. When the spacing a is held constant and the width L is doubled, the energy spacing $E_{n+1} - E_{n-1} \propto \left((n+1)^2 - (n-1)^2\right)/L^2 \propto n/L^2$ is four times smaller. For the same energy $E \propto n^2/L^2$, doubling the box size L means also doubling n. Thus, when compared vertically (at the same energies), the density of states is doubled in absolute values when doubling the width L. The behavior of the density of states when changing basis set parameters can also be understood intuitively. A smaller spacing a allows to represent faster oscillations in space and thus higher momenta/energies. For a larger width L, on the other hand, more states can be found that fulfill the boundary conditions of the respective method within an energy interval $[E, E + \Delta E]$.

Considering a time propagation using the spectral ansatz, a wave packet reaching the box boundary will lead to reflections in the case of B splines and periodic wave packet passthroughs in the case of the matrix algorithm. Despite the details discussed before, bound and continuum states of both methods behave very similar and can equally well be used for time propagation. Later (Sections 4.2-4.7) the matrix algorithm will be used to solve the vibrational problem while B splines are used for the solution the electronic problem[8].

[7] The free particle potential $V(x) = V(-x) = 0$ has parity symmetry. The density of states shown in this case is thus the sum of the (independent) densities of states for states with *gerade* (*ungerade*) symmetry.

[8] An exception is Section 4.3 where the matrix algorithm (or grid approach) is used to solve both the electronic and the vibrational problem.

4.1.7 Harmonic Oscillator with Position-Dependent Mass

To compare the present matrix algorithm to the recently published traditional second-order Hartree shooting method [116], the two model Hamiltonians

$$\hat{\mathrm{H}}_1 = \frac{1}{2}\,\hat{\mathrm{p}}\,\frac{1}{1+\hat{\mathrm{x}}^2}\,\hat{\mathrm{p}} + \frac{1}{2}\,\hat{\mathrm{x}}^2 \tag{4.23}$$

and

$$\hat{\mathrm{H}}_2 = \frac{1}{2}\,\hat{\mathrm{p}}\left(\frac{1+\hat{\mathrm{x}}^2}{2+\hat{\mathrm{x}}^2}\right)^2\hat{\mathrm{p}} + \frac{1}{2}\,\hat{\mathrm{x}}^2 \tag{4.24}$$

are implemented. When comparing the eigenenergies obtained by the matrix algorithm with $N = 201$ points and $L = 20$ (which is well within the converged regime), table 1 (for $\hat{\mathrm{H}}_1$) and table 3 (for $\hat{\mathrm{H}}_2$) in [116] is reproduced to all digits. Considering the convergence properties, the same exponential behavior is found as in Section 4.1.4 and Section 4.1.5. One should note that the second-order shooting method in [116] only converges quadratically and, therefore, much larger numbers of evenly spaced points ($N = 640, 960, 1440$ and 2160) were needed to obtain the results.

4.1.8 Non-Hermitian PT-Symmetric and Non-Symmetric Cases

As mentioned in Sec. 4.1.7, the PT-symmetric Hamiltonians examined in Sec. 4.1.7 and 4.1.2 are rather special. Therefore, the more usual form of a PT-symmetric Hamiltonian with a constant mass but a complex potential is discussed. It is demonstrated that the matrix algorithm is also applicable for such types of problems, since complex matrices can also be treated. Therefore, the model Hamiltonian

$$\hat{\mathrm{H}} = \hat{\mathrm{p}}^2 + \hat{\mathrm{x}}^2 + i\,\hat{\mathrm{x}} \tag{4.25}$$

is implemented. According to [118], this PT-symmetric Hamiltonian has the real eigenenergies

$$E_n = 2\,n + \frac{5}{4}. \tag{4.26}$$

In contrast, the non-Hermitian and not PT-symmetric Hamiltonian

$$\hat{\mathrm{H}} = \hat{\mathrm{p}}^2 + \hat{\mathrm{x}}^2 + i\,\hat{\mathrm{x}} - \hat{\mathrm{x}} \tag{4.27}$$

has according to [118] the complex eigenvalues

$$E_n = 2\,n + 1 + \frac{1}{2}\,i \tag{4.28}$$

which can no longer be interpreted as eigenenergies. The relative error of the real part as well as the absolute error of the imaginary part of the eigenvalues obtained

with the matrix algorithm with $N = 101$ points and $L = 25$ is shown in Figure 4.9. The eigenvalues of the Hamiltonian in Eq. (4.25) now contain a small imaginary part (also see Figure 4.9) due to roundoff errors which was not the case for the PT-symmetric Hamiltonians in Eqs. (4.5) and (4.6). The reason is that the matrix representations of Eqs. (4.5) and (4.6) are real, while the matrix representation of Eq. (4.25) is complex. Nevertheless, the very good agreement of our results with Eqs. (4.26) and (4.28) (relative error below 10^{-12} for $n < 45$) shows that our matrix algorithm can also be very helpful to find eigenenergies of PT-symmetric Hamiltonians. In critical cases one could in principle consider increasing the numerical precision (either in steps from single to quadruple precision or, even better, digit-by-digit) to probe further whether the eigenvalue spectrum is purely real or not.

4.1.9 The Two-Dimensional Henon-Heiles System

To demonstrate the performance of the matrix algorithm in two dimensions the Henon-Heiles system [132]

$$\hat{\mathrm{H}} = \frac{1}{2}\left(\hat{\mathrm{p}}_x^2 + \hat{\mathrm{p}}_y^2\right) + \frac{1}{2}\left(\hat{\mathrm{x}}^2 + \hat{\mathrm{y}}^2\right) + \lambda\left(\hat{\mathrm{x}}^2\,\hat{\mathrm{y}} - \frac{\hat{\mathrm{y}}^3}{3}\right) \tag{4.29}$$

is investigated. This model potential is frequently used as a benchmark for numerical methods [133–135], although the potential in Eq. (4.29) is not bounded from below and thus it does not support true bound states but only metastable ones that decay by tunneling through the barriers as is discussed in, e. g., Refs. [135, 136]. $\lambda = 1/\sqrt{80}$ is used to compare the here obtained lowest 36 eigenenergies with the ones obtained from Ref. [135]. When using a $L_x \times L_y = 20 \times 20$ grid with $N_x \times N_y = 61 \times 61$ points, all 36 eigenenergies given in [135] are reproduced within the given accuracy. The obtained ground state wave function is shown together with the potential in Figure 4.10. When increasing the number of grid points to $N_x \times N_y = 81 \times 81$ and $N_x \times N_y = 101 \times 101$ ($L_x \times L_y = 20 \times 20$ held constant) or changing the grid size to $L_x \times L_y = 18 \times 18$ and $L_x \times L_y = 22 \times 22$ ($a_x = a_y = 20/61$ approximately held constant), the obtained energies are stable within an accuracy of at least 12 significant digits[9]. Thus the matrix algorithm is also very suitable for finding bound states of two-dimensional Hamiltonians.

4.1.10 Conclusions

The presented matrix algorithm is easy to implement, flexible, and shows exponential convergence (with respect to the number of grid points N and width L). While other algorithms [116, 137] consist of guessing an initial energy, this algorithm represents

[9] For the larger grid with $L_x \times L_y = 22 \times 22$ one additional state appears within the lowest 37 eigenenergies that is ignored in the comparison since its energy depends on the box size. This state is localized outside the potential well and its appearance is a consequence of the mentioned fact that the Henon-Heiles potential is not bounded from below.

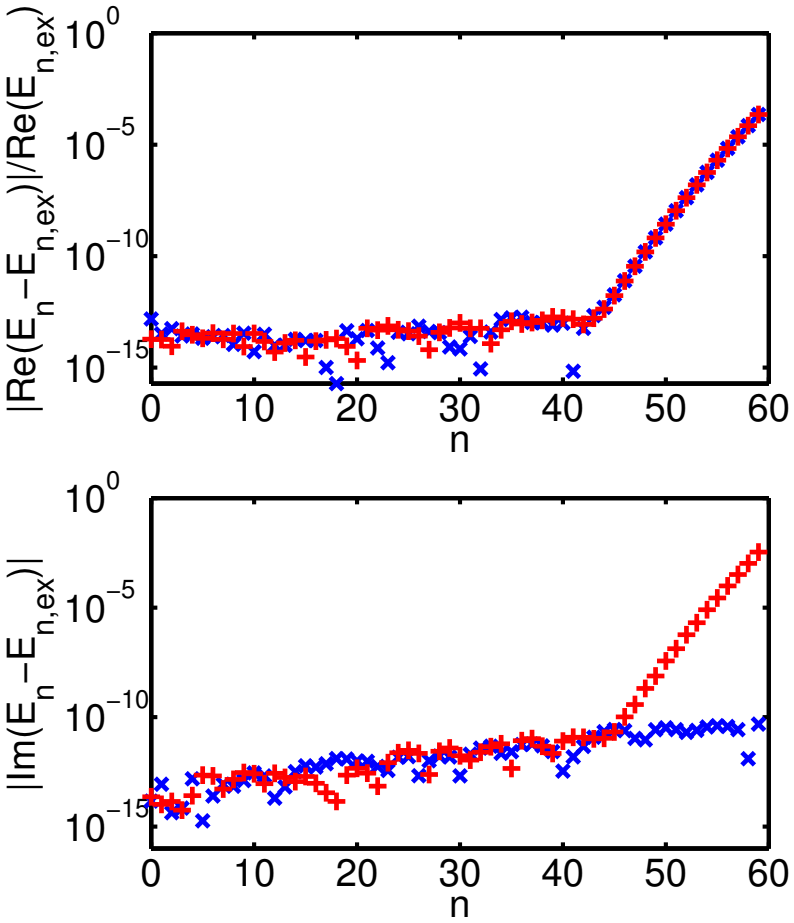

Figure 4.9: **Top**: Relative Error of the real part of the eigenvalues of Eqs. (4.25) [x] and (4.27) [+]. The values were obtained with the matrix algorithm using $N = 101$ points and $L = 25$. The exact values $E_{n,\mathrm{ex}}$ are given by Eqs. (4.26) and (4.28).
Bottom: Absolute Error of the imaginary part of the eigenvalues (same L and N).
This figure is also presented in [1].

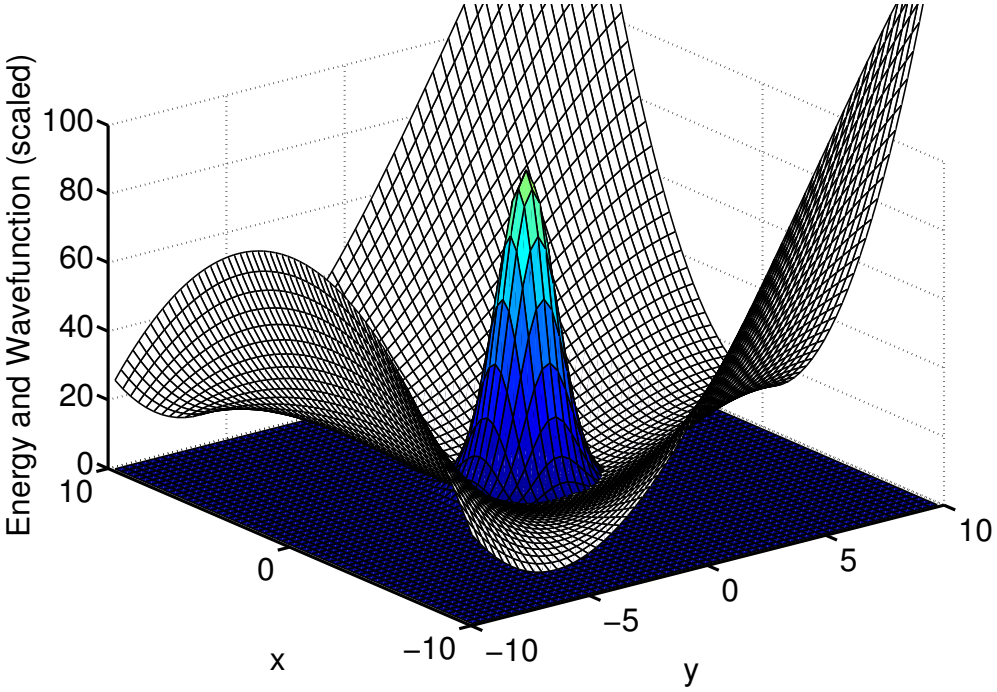

Figure 4.10: Potential energy surface (filled white) and obtained (discrete) ground state wave function (filled blue, scaled arbitrary) of the Henon-Heiles system in Eq. (4.29) with $\lambda = 1/\sqrt{80}$. A $L_x \times L_y = 20 \times 20$ grid with $N_x \times N_y = 61 \times 61$ points was used. This figure is also presented in [1].

a much more direct method, since one finds a set of eigenenergies by just a single matrix diagonalization. To demonstrate the performance of the algorithm it was applied to a one-dimensional model describing the inversion motion of NH_3 and ND_3. Furthermore, different forms for the position-dependent mass Hamiltonian were discussed. A great advantage is the flexibility of the present algorithm to handle their different possible forms. Especially, it is possible to avoid non-Hermitian model Hamiltonians (as used for, e. g., describing inversion of NH_3) that are often only adopted, because the symmetrized Hermitian form of the Hamiltonian leads to a Schrödinger equation that cannot be solved with many of the standard numerical algorithms.

In the case of ammonia it turns out that the eigenenergies do not strongly depend on the choice where one puts the mass into the Hamiltonian. This justifies the underlying classical derivation of the model Hamiltonian with a position-dependent mass. Also the eigenenergies of a Morse potential were determined. The results with the direct comparison to B splines indicate that the algorithm is applicable to find bound and continuum states of general Hamiltonians that may contain asymmetric potentials and include a continuous spectrum. The algorithm was also successfully applied to non-Hermitian Hamiltonians both with or without PT symmetry. This allows to numerically check whether the eigenvalue spectrum of such an Hamiltonian is purely real or not and demonstrates that the algorithm can handle Schrödinger equations with complex eigenvalue spectra. Finally, it was demonstrated with the aid of a two-dimensional problem that the algorithm is straightforwardly applied to higher-dimensional problems, but limited by the increasing numerical efforts due to the exploding number of grid points needed.

For very large problems or to go beyond two dimensions it may be useful to write a routine that applies $\hat{\mathrm{H}}$ to a vector Ψ and renounce at storing any matrix at all. Such a routine would apply FFT twice for each direction in every call with the cost scaling like $N^D \ln N$. If only some low-lying energies are requested, it is also possible to only partly diagonalize the Hamiltonian as will be done in Section 4.3.2. After initial publication of the matrix algorithm, it turned out to be a very useful tool for the further studies and developments presented in this thesis. It was also used in several other studies [6, 138–146].

4.2 Ionization of Molecular Hydrogen — Fixed- and Frozen Nuclei Approximations

In this section the approach to solve the six-dimensional electronic TDSE describing H_2 in ultrashort, intense laser fields using a configuration interaction basis set as described in Section 3.3 combined with the spectral ansatz, Section 3.5, is used to study the influence of nuclear geometry (internuclear distance and alignment) on the ionization behavior. The findings presented in the following have also been published in [3].

In view of the many promising proposals to image and control molecules mentioned in Chapter 1 a deeper understanding of the molecular response to intense, ultrashort laser fields is desirable. Compared to atoms, the nuclear degrees of freedom (vibration and rotation) as well as the multi-centered (non-spherically symmetric) electronic structure of molecules increase the complexity regarding their theoretical treatment. Thus, even molecular hydrogen H_2, despite being the simplest neutral molecule, remains a great challenge for theory when exposed to intense laser fields. This is especially true, if the correlated two-electron Schrödinger equation is solved in all six dimensions. In the case of large laser frequencies, low intensities, and not too extremely short laser field durations, lowest-order perturbation theory (LOPT) may be used. Thus, at first, perturbative one-photon ionization [147] (and references therein) and later on two- to four-photon ionization [148] of H_2 have been studied.

The direct numerical solution of the time-dependent Schrödinger equation (TDSE) describing H_2 in intense laser fields for fixed nuclei and a parallel alignment was first realized on a sophisticated grid [149] and then using a configuration-interaction expansion built from H_2^+ orbitals expressed in prolate spheroidal coordinates [53]. In the perturbative regime, good quantitative agreement between LOPT and TDSE ionization yields has been found [53]. This latter approach has also been applied, e.g., for longer wavelengths and higher intensities as well as for non-parallel alignments of the laser polarization with respect to the molecular axis [28, 29, 48, 77]. It was shown in [48] that a simplified treatment using the molecular strong-field approximation (in velocity gauge) can contradict the behavior obtained from the direct TDSE solution even qualitatively.

In a different approach based on an expansion in Born-Oppenheimer eigenstates and a single-center expansion for the electronic problem, the TDSE has been solved accounting also for vibrational dynamics [79]. This approach neglects nonadiabatic couplings, i.e. $\mathbf{B}(R) = 0$ in the Hamiltonian Eq. (2.24) (Section 2.1) using the Born-Huang expansion. Large differences between the treatment that included the vibrational dynamics and the fixed-nuclei approximation were found [79, 81, 82]. Later applications of this approach concentrated mainly on low laser intensities and studied, e.g., the decay of autoionizing states [89, 90]. Another, more recently introduced approach, again using prolate spheroidal coordinates but Laguerre and Legendre polynomials as basis functions, has been applied to investigate enhanced ionization occurring at large internuclear distances [49]. Most recently, a hybrid

coupled channels approach using infinite range exterior complex scaling has been implemented [52] and even compared to multiphoton ionization yields presented in the following.

In the following section, the method to solve the two-electron TDSE and the basis-set parameters used are briefly discussed. In Section 4.2.2, the method is applied in the perturbative multiphoton regime and compared to the results in Refs. [79, 81, 82]. In particular, the breakdown of the widely used fixed-nuclei approximation is re-investigated in detail with the present approach. Furthermore, the study is extended to non-parallel (random) alignments of the laser polarization with respect to the molecular axis. The internuclear-distance dependent ionization behavior is studied in Section 4.2.3 for the transition from the multiphoton regime to the quasi-static regime. A parallel as well as a perpendicular alignment of the laser polarization with respect to the molecular axis is considered. The ionization yield is compared to the one obtained from the approximate Ammosov-Delone-Krainov (ADK) tunneling rates [26]. Returning to the original Perelomov-Popov-Terent'ev [25] theory, a correction to the ADK tunneling rate is introduced and compared to the TDSE results.

4.2.1 Method (Basis Set Parameters, Symmetry Selection Rules, Levels of Approximation)

The TDSE describing molecular hydrogen exposed to a laser field

$$i\frac{\partial}{\partial t}\Psi(\underline{\mathbf{r}},t) = \left(\hat{\mathrm{H}}_0 + \hat{\mathrm{V}}_{\mathrm{int}}(\underline{\mathbf{r}},t)\right)\Psi(\underline{\mathbf{r}},t) \tag{4.30}$$

is solved using the spectral ansatz[10], Section 3.5, by expanding the time-dependent electronic wave function $\Psi(\underline{\mathbf{r}},t)$ in terms of eigenstates $\Phi_n^{(2e)}(\underline{\mathbf{r}})$ of the field-free electronic Hamiltonian $\hat{\mathrm{H}}_0$. The field-free eigenstates $\Phi_n^{(2e)}(\underline{\mathbf{r}})$ are obtained by configuration interaction using B splines and prolate spheroidal coordinates as described in Section 3.3. The linearly polarized laser field is defined by Eq. (2.68) in Section 2.7. The dipole approximation and the velocity gauge is used and thus the interaction potential with the laser field reads $\hat{\mathrm{V}}_{\mathrm{int}}(\underline{\mathbf{r}},t) = \hat{\mathbf{p}}\cdot\vec{A}(t)$ according to Section 2.5. In order to obtain the ionization yield, the electronic TDSE is solved at a fixed internuclear distance R and alignment angle θ. Here, $\theta = 0$ corresponds to a parallel alignment ($\parallel$) of the polarization vector $\vec{\mathcal{P}}$ with respect to the molecular axis (z axis) and $\theta = \pi/2$ corresponds to a perpendicular alignment ($\perp$). The ionization yield is calculated by

$$Y(R,\theta) = \sum_{n\in\mathrm{continuum}} |\,c_n(R,t=T)\,|^2 = 1 - \sum_{n\in\mathrm{bound}} |\,c_n(R,t=T)\,|^2 \quad . \tag{4.31}$$

[10] The method is also described in detail in previous works [29, 53, 77, 150]

after the laser field ($t = T$) where c_n is the expansion coefficient for $\Phi_n^{(2e)}(\underline{\mathbf{r}})$ in the spectral expansion. The continuum threshold is given by the H_2^+ ground-state energy. The ionization yield (or ionization probability) is normalized such that for $Y = 1$ every molecule is (at least) singly ionized.

The electronic eigenstates $\Phi_n^{(2e)}$ of molecular hydrogen are labeled by their symmetry

$$X\ ^{2S+1}\Lambda_I^{(\mathcal{R})} \tag{4.32}$$

(Herzberg notation [151]). S denotes the total spin of the two-electron system ($2S+1$ is the multiplicity), $\Lambda = \Sigma, \Pi, \Delta, ...$ is the absolute value of the projection of the total electronic angular momentum on the internuclear axis, $I = g, u$ is the inversion symmetry (symmetry with respect to a point reflection at the center of the internuclear axis) and X numbers the states of the same symmetry in energetically ascending order. If the projection of the total electronic angular momentum on the internuclear axis is named M, then $\Sigma \leftrightarrow |M| = 0$, $\Pi \leftrightarrow |M| = 1$, $\Delta \leftrightarrow |M| = 2$, and so on. For Σ states the molecule additionally has the reflection symmetry $(\mathcal{R}) = +, -$ with respect to an arbitrary plane through the internuclear axis. The electronic ground state of H_2 is $1\ ^1\Sigma_g^+$ and in most cases the initial state of the time propagation. The symmetries of states that have to be considered for a time propagation are now discussed. Due to the neglect of relativistic effects the total spin $S = 0$ remains conserved.

First the case that the polarization vector $\vec{\mathcal{P}}$ points along the internuclear axis (z axis) is considered[11]. The transition matrix element to other electronic states

$$V_{\mathrm{int},mn}(R, t) = \left\langle \Phi_m(R) \middle| V_{\mathrm{int}}(\underline{\mathbf{r}}, t) \middle| \Phi_n(R) \right\rangle_{\underline{\mathbf{r}}} \quad , \tag{4.33}$$

can be written as

$$V_{\mathrm{int},mn}^{\mathrm{VG}}(R, t) = -i A_0 f_{\mathrm{E}}(t) \sin(\omega t + \phi) \left\langle \Phi_m(R) \middle| \sum_{i=1}^{n_e} \frac{d}{dz_i} \middle| \Phi_n(R) \right\rangle_{\underline{\mathbf{r}}} \tag{4.34}$$

$$V_{\mathrm{int},mn}^{\mathrm{LG}}(R, t) = -A_0 \left(\frac{\partial}{\partial t} f_{\mathrm{E}}(t) \sin(\omega t + \phi) \right) \left\langle \Phi_m(R) \middle| \sum_{i=1}^{n_e} z_i \middle| \Phi_n(R) \right\rangle_{\underline{\mathbf{r}}} \tag{4.35}$$

with Cartesian coordinates z_i as in Section 3.3. The interaction potential separates according to

$$V_{\mathrm{int},mn}(R, t) = f(t) D_{mn}(R) \tag{4.36}$$

[11] Such a static alignment of the polarization vector $\vec{\mathcal{P}}$ would mean for the nowadays common realization using short laser fields that a coherent rotational wave packet has to be created. In this wave packet many rotational quantum numbers J are occupied. However, the sharper this alignment is realized at a certain time t the faster this wave packet will evolve in time.

into a time dependence $f(t)$ and a dipole matrix $D_{mn}(R)$. The integral

$$\left\langle \Phi_m(R) \,|\, \hat{\mathrm{D}} \,|\, \Phi_n(R) \right\rangle_{\underline{\mathbf{r}}} \tag{4.37}$$

is non-zero only if $\Phi^*_m(\,\underline{\mathbf{r}}\,;\,R\,)\,\hat{\mathrm{D}}(\,\underline{\mathbf{r}}\,)\,\Phi_n(\,\underline{\mathbf{r}}\,;\,R\,)$ contains a contribution that is symmetric with respect to all symmetry operations of symmetry group $D_{\infty h}$ (group of homonuclear diatomic molecules). The symmetry operations are π-rotations around the internuclear axis, a point reflection at the center of the internuclear axis, and mirroring at a plane containing the internuclear axis. Since the dipole operator is symmetric with respect to a rotation around the internuclear axis, the total electron angular momentum Λ must be identical for Φ_m and Φ_n. Analogously the reflection symmetry ($\mathcal{R}$) has to be the same for Φ_m and Φ_n. On the other hand, the dipole operator is antisymmetric with respect to a point reflection at the center of the internuclear axis. Thus, the inversion symmetry I of Φ_m and Φ_n has to be different. Starting from the 1 $^1\Sigma_g^+$ ground state, a linearly polarized thus drives electronic transitions between states with $^1\Sigma_g^+ \leftrightarrow {}^1\Sigma_u^+$ symmetry for a parallel alignment[12]. Thus, only states with $^1\Sigma_g^+$ and $^1\Sigma_u^+$ symmetry have to be considered within the approximations made here[13]. For a perpendicular alignment of the laser polarization vector $\vec{\mathcal{P}}$ with respect to the internuclear axis,

$$\hat{\mathrm{D}}^{\mathrm{VG}} = \sum_{i=1}^{n_\mathrm{e}} \frac{d}{dx_i} \qquad \text{and} \qquad \hat{\mathrm{D}}^{\mathrm{LG}} = \sum_{i=1}^{n_\mathrm{e}} x_i \quad , \tag{4.38}$$

allowed (non-zero) transitions $^1\Sigma_g^+ \leftrightarrow {}^1\Pi_u \leftrightarrow {}^1\Delta_g \leftrightarrow \ldots$ and $^1\Sigma_u^+ \leftrightarrow {}^1\Pi_g \leftrightarrow {}^1\Delta_u \leftrightarrow \ldots$ follow analogously from symmetry considerations. Starting from the 1 $^1\Sigma_g^+$ ground state, only states with $^1\Sigma_g^+, {}^1\Pi_u, {}^1\Delta_g, \ldots$ symmetry have to be considered in this case. Finally, for a skew alignment of the laser polarization with respect to the internuclear axis for which $\hat{\mathrm{D}}$ contains both an z and x (or y) component, transitions

$$\begin{array}{ccccccc} {}^1\Sigma_g^+ & \leftrightarrow & {}^1\Pi_u & \leftrightarrow & {}^1\Delta_g & \leftrightarrow & \ldots \\ \updownarrow & & \updownarrow & & \updownarrow & & \updownarrow \\ {}^1\Sigma_u^+ & \leftrightarrow & {}^1\Pi_g & \leftrightarrow & {}^1\Delta_u & \leftrightarrow & \ldots \end{array} \tag{4.39}$$

to all symmetries are allowed. Thus, a skew alignment is the computationally most expensive case.

The basis-set parameters adopted for the present calculations are discussed in detail in [29]. Briefly, a box size of about 350 a.u. with 350 B splines of order $k = 10$ were used along the ξ coordinate (knot distribution: geometric progression with

[12] The dipole selection rule for the absorption of a photon leads analogously to $\Delta J = \pm 1$ for rotational transitions. This is neglected if the rotation is frozen to a fixed J. Physically sensible results obtained with a frozen rotation should thus be practically independent from the choice of the fixed rotational quantum number J.

[13] The neglected coupling Eq. (2.40) would lead to the population of states with additional symmetries.

$g = 1.05$ for the first 40 intervals and linear progression afterwards). 30 B splines of order 8 with a linear knot sequence were used along the η coordinate and highly oscillatory H_2^+ orbitals with more than 19 nodes along η were omitted in the CI calculation. The CI expansion consists of a very long configuration series where one electron occupies the H_2^+ ground-state $1\sigma_g$ while the other is occupying one of the remaining (bound or discretized continuum) H_2^+ eigenstates. This configuration series is mainly responsible to describe ionization. Together with additional CI configurations which represent doubly excited situations (responsible for the description of correlation and doubly excited states), this corresponds to about 6000 configurations per symmetry. Obtaining sufficiently converged TDSE solutions is computationally much more challenging for the 800 nm laser fields discussed in Sec. 4.2.3 compared to the perturbative regime in Sec. 4.2.2.

For the results shown in Sec. 4.2.2, states with energies up to 1 a.u. above the ionization threshold were included in the time propagation (0.5 a.u. are already sufficient). For non-parallel alignments, states with maximum absolute values of the component of the total angular momentum along the internuclear axis were included up to $\Lambda_{\max} = 7$ (convergence was found already with $\Lambda_{\max} = 4$). Furthermore, convergence with respect to the box size has been checked by doubling the box size. Most importantly, the CI expansion as described in [29] leads to an imperfect description of the ground-state of H_2, especially its energy. When comparing the multiphoton spectra obtained with the present method to methods that involve a practically correct ground-state energy (or possibly to future experimental ones), it is reasonable to correct for the error in the ground-state energy. As it was done in the perturbative study of H_2 in Ref. [148], a correction is obtained by shifting (or redefining) the laser frequency ω in the final graphs. Thus, a shifted frequency $\omega = \omega_{\text{num}} + \Delta\omega$ with $\Delta\omega = 0.0092$ a.u.[14] is used for our results shown in Sec. 4.2.2 (ω_{num} is the frequency used in the numerical calculation). It was found that this frequency shift $\Delta\omega$ is reduced when using a more complete CI expansion, but other than this shift no significant change in the ionization behavior was observed.

In the case of 800 nm (Sec. 4.2.3), states with energies up to 10 a.u. above the ionization threshold were included as in [29]. Furthermore, at this wavelength the treatment of the perpendicular alignment is much more challenging than the parallel one. Figure 4.11 shows the typical convergence of the total ionization yield with respect to $\Lambda_{\max}$ for two different intensities and internuclear distances. For the purpose of this work, the values of $\Lambda_{\max} = 7 - 11$ were used to obtain sufficiently converged ionization yields, while higher values would be needed to obtain fully converged photoelectron spectra. A similar convergence behavior was observed with respect to the box size.

Within the *fixed-nuclei approximation* (FNA), the ionization yield $Y_{\text{FNA}}(\theta) = Y(R_{\text{eq}}, \theta)$ is approximated by the electronic response at the equilibrium internuclear

[14] The shift $\Delta\omega = 0.0092$ a.u. corrects the energy difference between the $1^1\Sigma_g^+$ and $1^1\Sigma_u^+$ state and thus especially the resonance position of the $1^1\Sigma_g^+ \rightarrow 1^1\Sigma_u^+$ transition at the equilibrium internuclear distance.

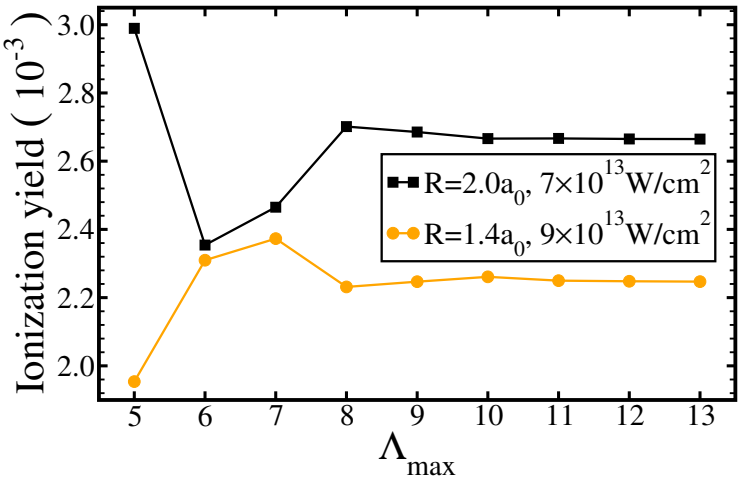

Figure 4.11: Convergence of the total ionization yield for a perpendicular-aligned H_2 molecule with respect to the maximal absolute value of the component of the total angular momentum along the internuclear axis, $\Lambda_{\max}$, in a 20-cycle $\cos^2$-shaped 800 nm laser field. This figure is also presented in [3].

distance $R_{\text{eq}} = 1.4$ a.u. A treatment fully including vibrational dynamics (FULL) as in [79, 81, 82] is beyond the scope of this section and will be performed later in Section 4.4. For now the nuclear vibration is taken into account by "freezing" the initial nuclear wave function $\chi(R)$ (vibrational ground state of the electronic Born-Oppenheimer ground-state potential) during the time propagation. Within this *frozen-nuclei approximation* (FROZ)[15], the R-integrated ionization yield

$$Y_{\text{FROZ}}(\theta) = \int \mathrm{d}R\, Y(R,\theta)\, |\chi(R)|^2 \tag{4.40}$$

is obtained from $Y(R,\theta)$ for a range of internuclear distances where the nuclear wave function $\chi(R)$ of the initial state is nonvanishing, namely $R = 1.0 - 2.5$ a.u. In Sec. 4.2.2 (4.2.3), 61 (31) points separated by $\Delta R = 0.025$ a.u. (0.05 a.u.) were used. Furthermore, different alignments of the laser polarization with respect to the molecular axis are considered, especially also non-parallel ones ($\theta \neq 0$). In the case of a randomly aligned molecular ensemble, the alignment-averaged ionization yield

$$Y_{\text{avg,X}} = \int_0^{\pi/2} \mathrm{d}\theta \sin(\theta) Y_{\text{X}}(\theta) \text{ with X = FNA or FROZ} \tag{4.41}$$

is calculated from the fixed- or the frozen-nuclei ionization yields $Y_{\text{X}}(\theta)$ obtained

[15] There exists no unified terminology for this level of approximation. It was termed frozen-nuclei limit in [152] and "frozen-nuclei approximation" throughout this thesis.

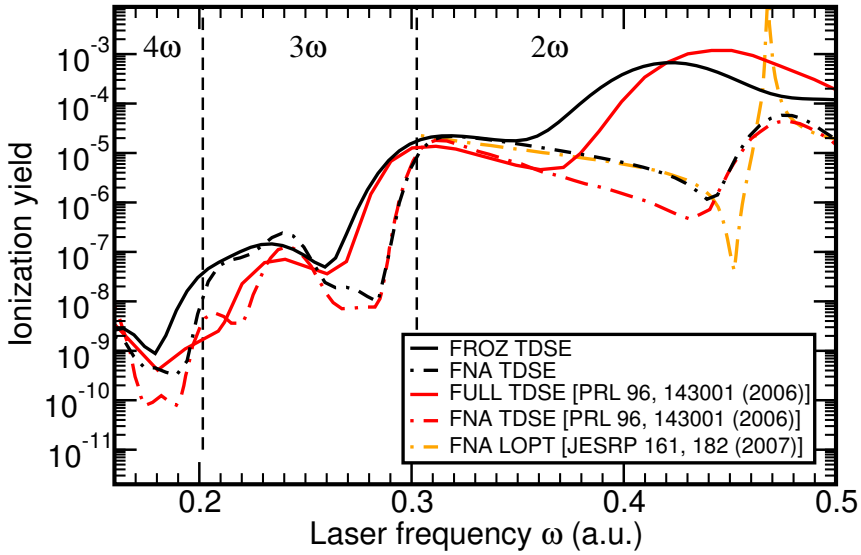

Figure 4.12: Ionization yields as a function of the laser frequency ω for parallel-aligned H_2 exposed to $T = 10$ fs, $I = 10^{12}$ Wcm^{-2} cos^2-shaped laser fields. The dashed vertical lines indicate the borders between the two-, the three-, and the four-photon ionization regimes (2ω, 3ω, 4ω). The ionization yields obtained within the fixed-nuclei (FNA TDSE) and the frozen-nuclei (FROZ TDSE) approximation are compared to the perturbative fixed-nuclei (FNA LOPT) and the TDSE results fully including vibrational motion (FULL TDSE) extracted from Refs. [79, 81, 82]. This figure is also presented in [3].

for various alignment angles θ. In the case of perturbative one-photon ionization, Eq. (4.41) can be simplified to $Y_{\text{avg}}^{(1\omega)} = \frac{1}{3}Y_{\parallel} + \frac{2}{3}Y_{\perp}$. For the here discussed few- to many-photon ionization processes, however, the whole integration in Eq. (4.41) has to be performed. Thus, 10 angles separated by $\Delta\theta = \pi/18$ were used in Sec. 4.2.2. Clearly, non-parallel alignments are geometrically preferred over parallel ones due to the $\sin(\theta)$-factor. However, enhanced ionization of the formed H_2^+ ion at larger internuclear distances which occurs for a parallel alignment may obscure this fact in experiments.

4.2.2 Perturbative Multiphoton Regime

The ionization behavior for laser fields in the perturbative multiphoton regime with a peak intensity of $I = 10^{12}$ W/cm^2, total duration $T = 10$ fs, carrier-envelope phase $\phi = \pi/2$ and laser frequencies varying between $\omega = 0.16 - 0.5$ a.u. is studied. This allows to directly compare the results obtained with the present method to those previously reported in [79, 81, 82].

Figure 4.12 shows the obtained ionization yields in direct comparison to the TDSE

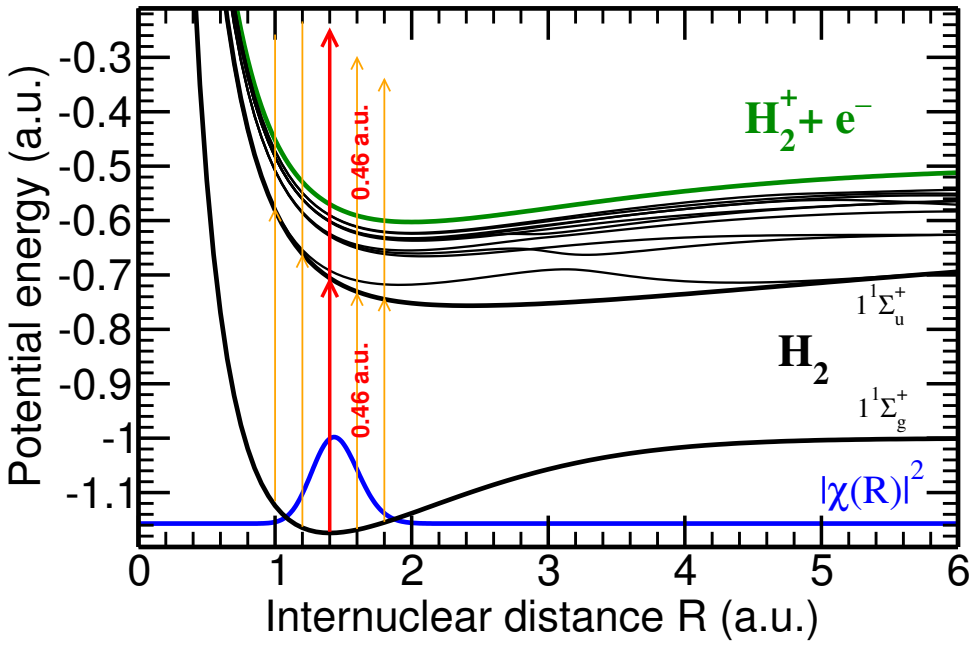

Figure 4.13: Potential-energy surfaces of H_2 (black lines), H_2^+ ionization threshold (orange/light grey line) and vibrational ground-state density $|\chi(R)|^2$ (blue/dark grey line). Furthermore, the resonant enhanced multiphoton ionization (REMPI) process $1^1\Sigma_g^+ \rightarrow 1^1\Sigma_u^+ \rightarrow H_2^+(1\sigma_g) + e^-$ for different fixed internuclear separations is indicated by red (grey) vertical arrows. This figure is also presented in [3].

and LOPT results reported in [79, 81, 82] (parallel alignment, i.e. $\theta = 0$). A good qualitative and partly also quantitative agreement is found between the results obtained here and the FNA TDSE results reported in Refs. [79, 81, 82]. Furthermore, the agreement between our FNA TDSE ionization yields and the FNA LOPT yields for two-photon ionization obtained in [82] is very good. Differences between the TDSE and LOPT ionization yields are found only around $\omega \approx 0.46$ a.u. where the simple LOPT approach used in [82] diverges due to the resonant enhanced multiphoton ionization (REMPI) process $1^1\Sigma_g^+ \rightarrow 1^1\Sigma_u^+ \rightarrow H_2^+(1\sigma_g) + e^-$ (see Figure 4.12). In fact, a similarly good quantitative agreement between LOPT and TDSE ionization yields obtained with the present approach was found already earlier for one-, two-, three- and four-photon ionization of H_2 (laser field parameters $T =$ 15 fs, $I = 2 \times 10^{12}$ Wcm^{-2}), see Fig. 3 in Ref. [53]. A recent independent study using the hybrid coupled channels approach [52] confirms the FNA TDSE ionization yields obtained here and the quantitative deviations to Refs. [79, 81, 82].

Although vibrational dynamics on a timescale of the order of 10 fs is expected to affect the ionization behavior and thus a perfect quantitative agreement between FROZ and FULL TDSE is not expected, Figure 4.12 shows that the ionization yield obtained within FROZ TDSE behaves qualitatively surprisingly similar to the FULL TDSE results of Refs. [79, 81, 82]. When comparing the FROZ and FULL TDSE ionization yields with their respective FNA results, both treatments show the same breakdown of the FNA, in particular an up to 3 orders of magnitude change of the ionization yield around $\omega \approx 0.44$ a.u. Thus, already the rather simple FROZ treatment allows for an explanation of this preeminent breakdown of the FNA. Clearly, the ionization yield $Y(R)$ must strongly depend on the internuclear distance R in order to obtain an ionization yield significantly different compared to the FNA, see Eq. (4.40). At first glance, a strong dependence of the ionization yield on the internuclear distance R may not be expected since the transition dipoles do not dramatically depend on R in the vicinity of the equilibrium distance $R_{\text{eq}} = 1.4$ a.u. (see, e.g., [81]). However, for REMPI, the energy differences between the electronic states determine where the resonance frequency or energy is located and thus play a crucial role. For molecules, these resonance frequencies depend significantly on the nuclear configuration. As an example, for the already mentioned REMPI process $1^1\Sigma_g^+ \rightarrow 1^1\Sigma_u^+ \rightarrow H_2^+(1\sigma_g) + e^-$, Figure 4.13 illustrates that at larger internuclear distances $R > 1.4$ a.u. significantly lower laser frequencies $\omega < 0.46$ a.u. are required to fulfill the resonance condition.

The dependence of the ionization yield $Y(R)$ on the internuclear distance R and the corresponding contribution $Y(R)\,|\chi(R)|^2$ of internuclear distances to the R-integrated ionization yield (Eq. (4.40)) is shown in Figure 4.14. In general, the ionization yield $Y(R)$ changes many orders of magnitude with varying R. It might be surprising that for $\omega = 0.2, 0.29$, and ≥ 0.38 a.u. the equilibrium distance $R_{\text{eq}} = 1.4$ a.u. practically does not contribute at all to the total ionization yield. Of course, large differences between the FNA and FROZ or FULL treatment are observed for these frequencies in Figure 4.12. In particular, for the breakdown of the FNA in the two-photon regime between 0.38 a.u. $\leq \omega \leq$ 0.47 a.u., one can see how the

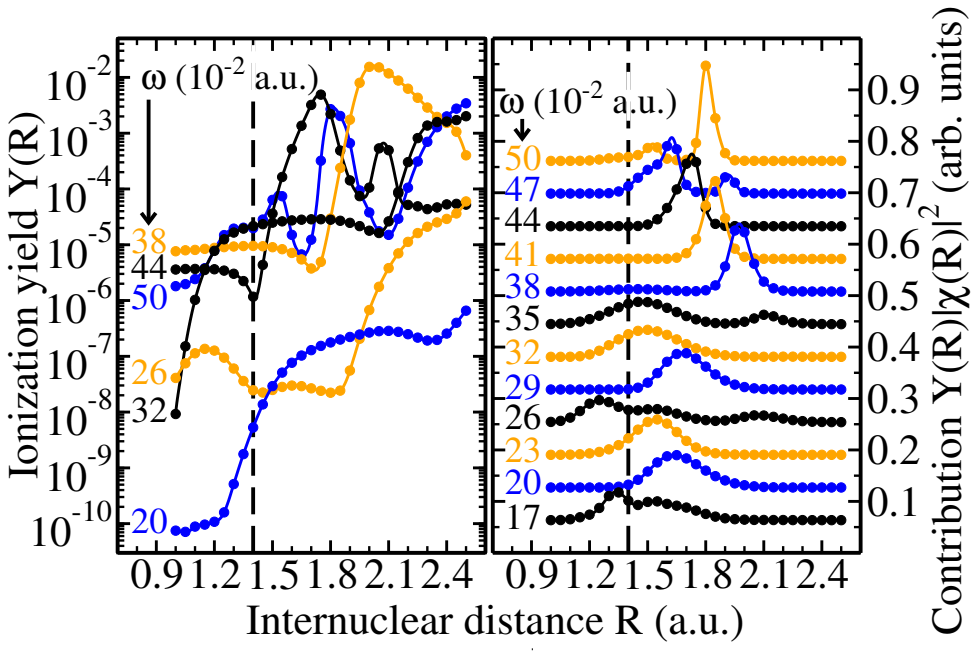

Figure 4.14: Ionization of parallel-aligned H_2 for $T = 10$ fs, $I = 10^{12}$ Wcm^{-2} $\cos^2$-shaped laser fields and different laser frequencies ω. The left panel shows the fixed-nuclei ionization yields $Y(R)$ as a function of the internuclear distance R, whereas the right panel displays the contribution $Y(R)\,|\chi(R)|^2$ to the frozen-nuclei ionization yield in Eq. (4.40) (for better visibility scaled and vertically shifted). This figure is also presented in [3].

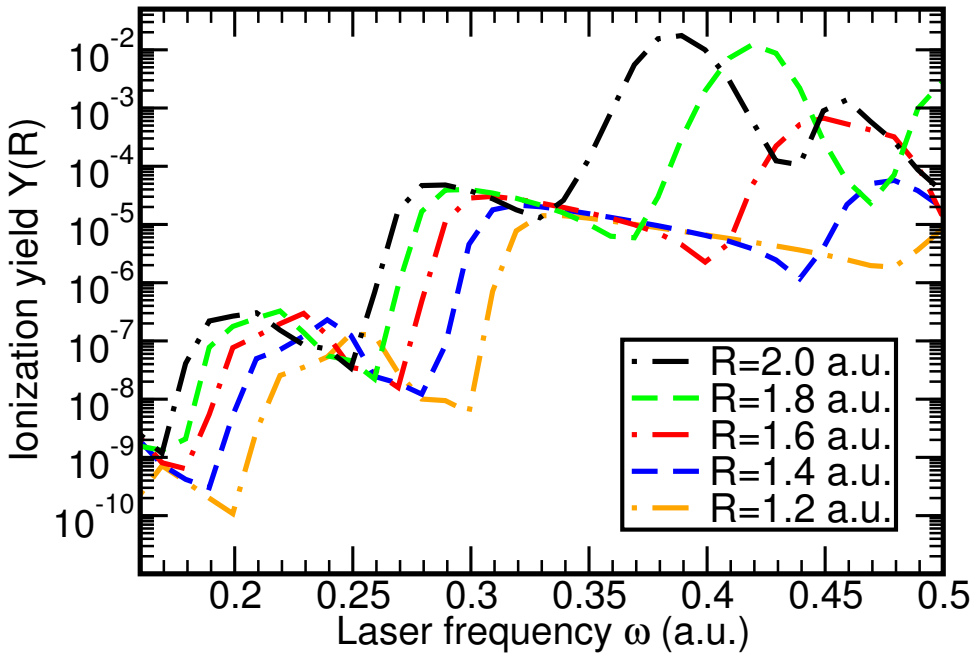

Figure 4.15: Fixed-nuclei ionization yields $Y(R)$ for parallel-aligned H_2 as a function of the laser frequency ω for different internuclear distances R. Laser parameters as in Figure 4.14. This figure is also presented in [3].

R-integrated ionization yield is dominated by increasingly larger internuclear distances with lower and lower laser frequency. This is compatible with the expectation stemming from the simple picture in Figure 4.13.

Figure 4.15 displays how the frequency-dependence of the fixed-nuclei ionization yield $Y(R)$ changes with internuclear distance. For increasing internuclear distance, the threshold between N and $N+1$ photon ionization shifts to lower laser frequencies. Thus, while at the equilibrium distance $R_{\mathrm{eq}} = 1.4$ a.u. four-photon (three-photon) ionization occurs at the laser frequency $\omega = 0.2$ a.u. (0.29 a.u.), three-photon (two-photon) ionization occurs at larger internuclear distances. This leads to a significantly enhanced ionization yield at larger internuclear distances and thus pronounced differences between the fixed- and the frozen-nuclei ionization approximations (see also Figures 4.12 and 4.14). This enhancement of ionization is thus conceptually similar to the enhancement for a $\cos^2$ envelope compared to a Gaussian envelope discussed in Section 2.7. Here it is not the bandwidth of the laser field but the (binding) energy "bandwidth" (or spread) introduced by the vibrational degree of freedom which allows for ionization by a smaller number of photons.

Figure 4.15 shows how the previously mentioned two-photon REMPI $1^1\Sigma_g^+ \rightarrow 1^1\Sigma_u^+ \rightarrow \mathrm{H}_2^+(1\sigma_g) + e^-$ requires lower and lower laser frequencies (and also strongly increases in magnitude) with increasing internuclear distance. The frequency shift of the ionization thresholds and resonance frequencies with internuclear distance can also be seen in the perturbative ionization cross sections in Figures 1-3 of Ref. [148]. Similar to the comparison of LOPT and TDSE in Ref. [53], only the two-photon resonances are, however, clearly visible as peaks in the ionization yield when solving the TDSE for short (order of $T = 10$ fs) fields. Noteworthy, also the resonance due to the second autoionizing state with $^1\Sigma_g$ symmetry belonging to the Q(1) series, Q(1) $^1\Sigma_g(2)$, is visible at $R = 2$ a.u. and around $\omega = 0.47$ a.u. in Figure 4.14 as reported in Ref. [148]. Despite the fact that the nuclear probability density $|\chi(R \approx 2.0 \text{ a.u.})|^2$ is very small, this resonance still contributes noticeably to the total ionization yield, see the second hump for $\omega = 0.47$ a.u. in Figure 4.14, right panel.

So far, only a parallel alignment of the laser polarization with respect to the molecular axis has been considered. However, an experiment with unaligned molecules (i.e. random alignment) can experimentally easier be realized. Compared to a parallel alignment, a non-parallel alignment is computationally much more expensive. This is due to the broken cylindrical symmetry. In this case, not only electronic eigenstates with $^1\Sigma_g^+$ and $^1\Sigma_u^+$ symmetry, but considerably more symmetries have to be taken into account. However, since a single FNA TDSE calculation for parallel alignment in the perturbative regime is nowadays extremely fast (order of one second), it is comparatively simple to extend the previous study and to include the full alignment dependence together with the R dependence.

Figure 4.16a shows the FNA and the FROZ TDSE ionization yields for a parallel, a perpendicular, and a random alignment. The FNA TDSE behavior is similar to the behavior of the perturbative cross sections reported in Ref. [148]. For both, FNA and FROZ TDSE, the ionization yield for a parallel alignment is almost always higher than for a perpendicular alignment, whereas the alignment-averaged result

lies in between. The alignment dependence of the ionization yield is rather small in the three- and four-photon ionization regime. In contrast, the result for a perpendicular alignment differs strongly from the parallel one in the two-photon case, especially in the frozen-nuclei treatment. The contributions $Y_{\mathrm{FROZ}}(\theta)\sin(\theta)$ of different alignment angles θ to the alignment-averaged ionization yield, see Eq. (4.41), are shown in Figure 4.16b. In contrast to the R dependence (Figure 4.14) the alignment dependence is very smooth and a large portion of possible alignment angles contributes to the total ionization. In the three- and four-photon regime where the θ dependence of $Y_{\mathrm{FROZ}}(\theta)$ is rather small, the geometrically preferred alignment angles $\theta \lesssim \frac{\pi}{2}$ contribute most due to the $\sin(\theta)$ factor. In the two-photon regime, this geometrical preference competes with a strong dependence of the ionization yield $Y_{\mathrm{FROZ}}(\theta)$ on θ that shows the opposite trend, i.e. ionization is strongly enhanced for a parallel alignment. In conclusion, intermediate alignment angles around $\theta \approx \frac{\pi}{8}$ contribute most. Despite this huge alignment dependence for two-photon ionization, the previously discussed breakdown of the FNA is clearly seen in Figure 4.16a also for randomly aligned molecules.

4.2.3 Intense 800 nm Laser Fields

The ionization behavior of hydrogen molecules exposed to intense laser fields with the ubiquitous Ti:sapphire wavelength of 800 nm is investigated. The response to frequency-doubled 400 nm laser fields has been studied earlier [29]. First, 800 nm $\cos^2$ laser fields with $n_{\mathrm{c}} = 20$ cycles (FWHM of about 20 fs), carrier-envelope phase $\phi = 0$ and peak intensities I varying between 2×10^{13} to $1.3 \times 10^{14}\,\mathrm{W/cm^2}$ are considered. For this range of laser intensities, the Keldysh parameter [66]

$$\gamma = \omega \frac{\sqrt{2I_p}}{F} \tag{4.42}$$

(with the electron binding energy $I_p(R = 1.4\text{ a.u.})$ and peak laser electric field strength F) varies for molecular hydrogen between $\gamma = 0.67$ and 2.6. This corresponds to the transition between the quasi-static ($\gamma \ll 1$) and the multiphoton ($\gamma \gg 1$) regime. The dependence of the ionization yield $Y(R)$ on the internuclear distance R and the corresponding contribution $Y(R)\,|\chi(R)|^2$ of internuclear distances to the R-integrated ionization yield (Eq. (4.40)) is shown in Figure 4.17. One can see a significant increase of the ionization yield $Y(R)$ with internuclear distance R, for example about 4 orders of magnitude for the intensity of $2 \times 10^{13}\,\mathrm{W/cm^2}$. The R dependence of $Y(R)$ is very smooth compared to laser parameters in the perturbative regime, Figure 4.14, and notably smoother than in the case of 400 nm [29]. This behavior was already observed earlier for shorter 6-cycle 800 nm laser fields in Ref. [28] and is expected from the quasi-static picture in which the ionization rate depends smoothly (exponentially) on the R-dependent binding energy $I_p(R)$ [23, 153]. However, on top of this smooth behavior resonance structures can still be observed.

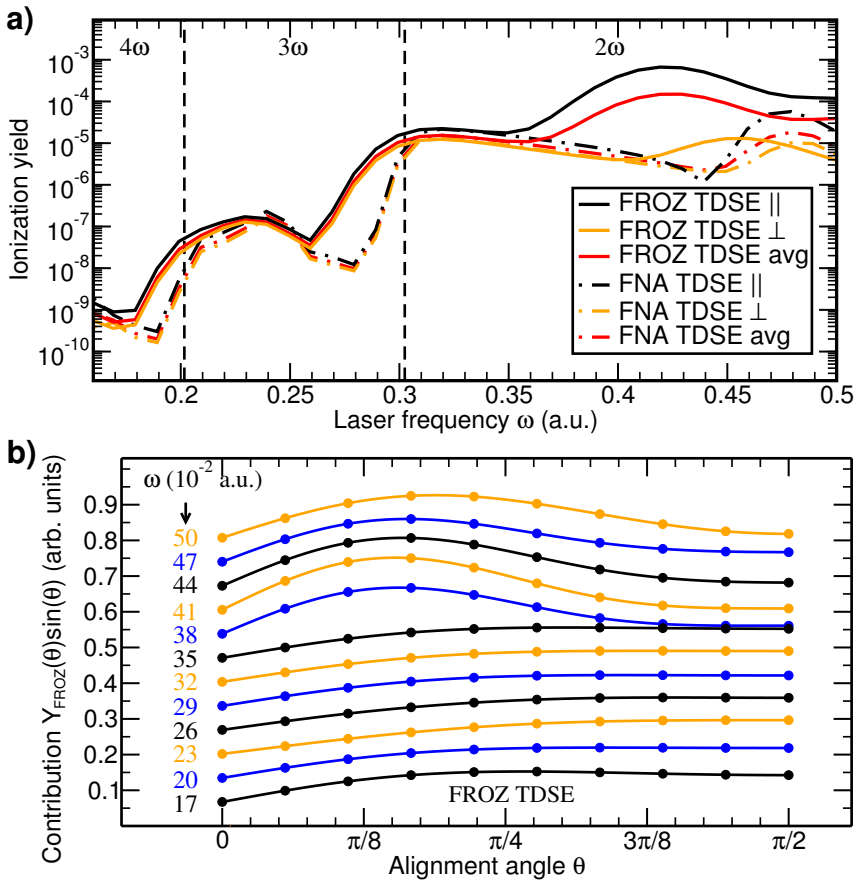

Figure 4.16: a) Fixed- (FNA) and frozen-nuclei (FROZ) ionization yields as a function of the laser frequency ω for $T = 10$ fs, $I = 10^{12}$ Wcm^{-2} $\cos^2$-shaped laser fields and a parallel ($\|$), perpendicular ($\perp$) and random (avg) alignment of the H_2 molecule. b) Contribution $Y_{\mathrm{FROZ}}(\theta)\sin(\theta)$ to the alignment-averaged frozen-nuclei ionization yield in Eq. (4.41) (for better visibility scaled and vertically shifted). This figure is also presented in [3].

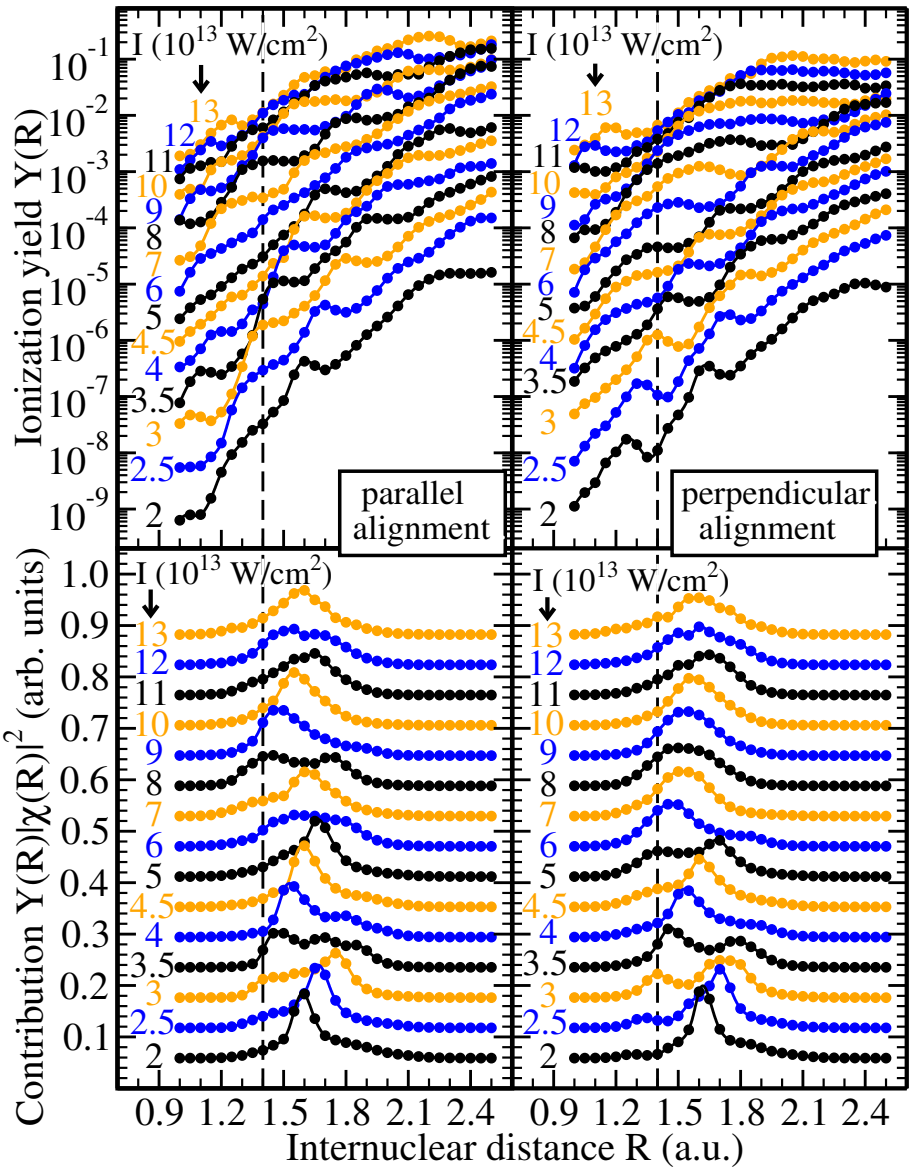

Figure 4.17: Ionization of H_2 molecules exposed to 20-cycle $\cos^2$-shaped 800 nm laser fields and different laser peak intensities I. The upper panel shows the fixed-nuclei ionization yields $Y(R)$, whereas the lower panel displays the contribution $Y(R)\,|\chi(R)|^2$ to the frozen-nuclei ionization yield in Eq. (4.40) (scaled and vertically shifted). The left (right) panel shows the result for a parallel (perpendicular) alignment of the molecule with respect to the field axis. This figure is also presented in [3].

When comparing the result for a parallel and a perpendicular alignment of the molecule, i. e. the left and the right panels of Figure 4.17, differences occur in the resonance behavior, especially resonance positions are shifted. Overall, one observes that the ionization behavior is quite similar for both alignments, i. e. the alignment dependence of the ionization yield is not a large (orders of magnitude) effect. The lower panel of Figure 4.17 shows that the main contribution $Y(R)\,|\chi(R)|^2$ to the R-integrated ionization yields is shifted to larger internuclear distances $R > 1.4$ a.u. due to the strong increase of $Y(R)$ with increasing R. Nevertheless, this effect is smaller than the previously discussed breakdown of the FNA for two-photon ionization in Figure 4.14.

The ionization yields can be compared to those obtained using the Ammosov-Delone-Krainov (ADK) tunneling rates Γ_{ADK} [26, 27]. The ion yield

$$Y_{\mathrm{ADK}}(R) = 1 - \exp\left\{-\int \Gamma_{\mathrm{ADK}}[F_{\mathrm{e}}(t), I_p(R)]dt\right\} \tag{4.43}$$

is obtained by integrating the tunneling rate where $F_{\mathrm{e}}(t)$ is the envelope function of the electric field and the integration is performed over the whole laser field duration. For consistency, the vertical binding energy $I_p(R)$ obtained from the field-free CI calculation is used. Instead of using the envelope $F_{\mathrm{e}}(t)$ and the cycle-averaged ADK rate Γ_{ADK}, one may also perform the integral in Eq. (4.43) using the time-dependent electric field $F(t)$ and the static (instantaneous) rate $\sqrt{\pi\kappa^3/(3F(t))}\Gamma_{\mathrm{ADK}}[F(t), I_p(R)]$. For the R-dependent ionization yields $Y_{\mathrm{ADK}}(R)$ shown in the following, the relative difference when using cycle-averaged or static rates remains below 1.3% and is thus negligible. Noteworthy, in the here studied transition regime with $\gamma = 0.67 - 2.6$ the validity condition for ADK, $\gamma \ll 1$, is not (strictly) fulfilled. The popular ADK rates differ from the Perelomov-Popov-Terent'ev (PPT) [25] rates by the restriction to the quasi-static regime $\gamma \ll 1$, the introduction of effective quantum numbers n^* and l^* for non-hydrogenic atoms (or molecules), an application of the Stirling approximation for the evaluation of factorials, and a rearrangement of the final expression. It is usually assumed that the pre-exponential factor in the ionization rate is less important than the exponential one. Returning to the original PPT theory [25], a simple correction to cycle-averaged ADK rates Γ_{ADK} is obtained by replacing the exponential

$$\exp\left[-\frac{2\kappa^3}{3F_{\mathrm{e}}}\right] \to \exp\left[-\frac{2\kappa^3}{3F_{\mathrm{e}}}\, g(\gamma)\right] \tag{4.44}$$

while leaving the prefactor unchanged. The function g is defined as [25]

$$g(\gamma) = \frac{3}{2\gamma}\left\{\left(1 + \frac{1}{2\gamma^2}\right)\mathrm{arcsinh}\gamma - \frac{\sqrt{1+\gamma^2}}{2\gamma}\right\} \tag{4.45}$$

with $\gamma = \kappa\omega/F_{\mathrm{e}}$ and $\kappa = \sqrt{2I_p(R)}$. Thus, starting from Eq. (7) in Ref. [27], one arrives at what will be called "frequency-corrected ADK" (FC-ADK, first used by

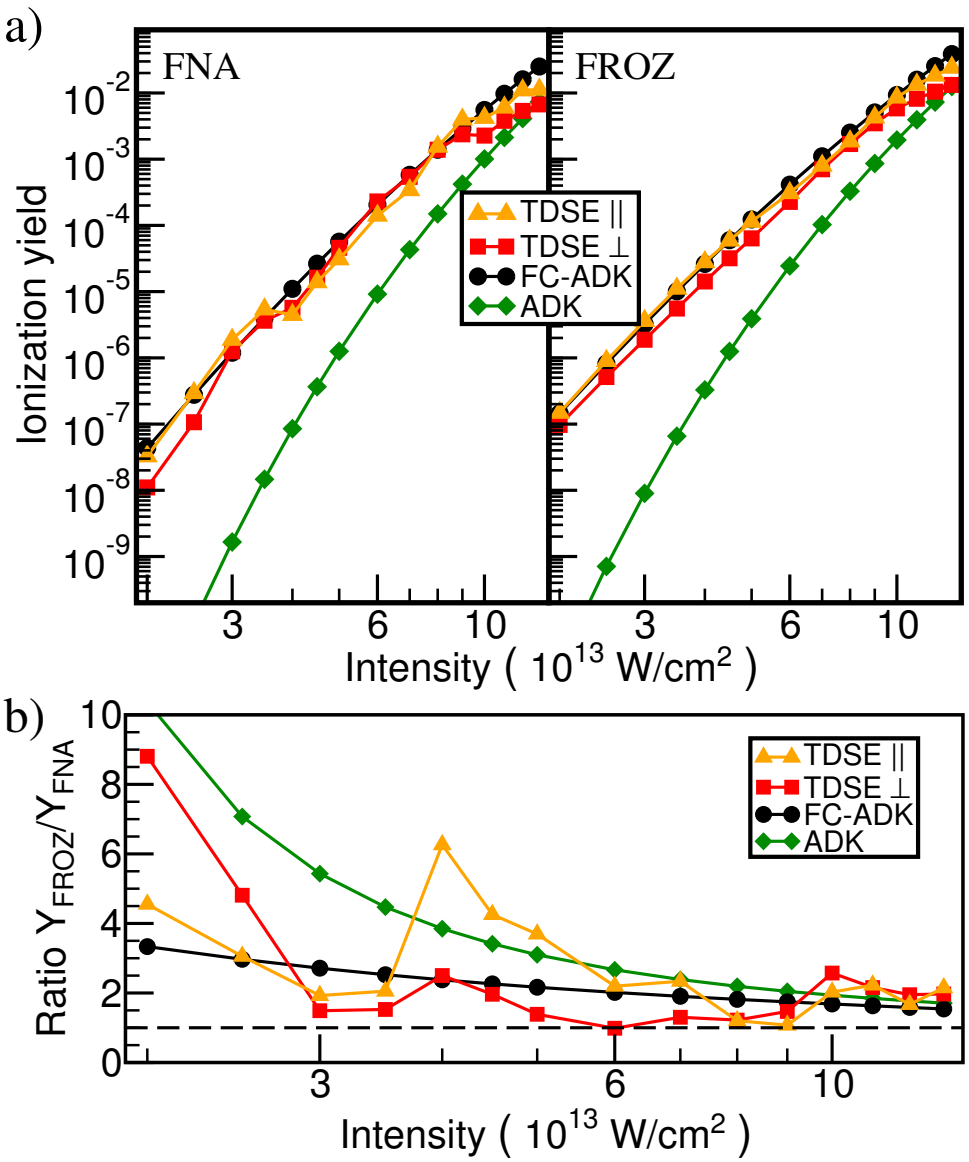

Figure 4.18: Fixed- (FNA, left panel) and frozen-nuclei (FROZ, right panel) ionization yields of H_2 as a function of the peak intensity of a 20-cycle $\cos^2$-shaped 800 nm laser field for a parallel and a perpendicular alignment of the molecule are compared with those predicted by the ADK model with (FC-ADK) and without (ADK) frequency correction. b) Ratio $Y_{\mathrm{FROZ}}/Y_{\mathrm{FNA}}$ of the ionization yields shown in a). The dashed horizontal line indicates $Y_{\mathrm{FROZ}}/Y_{\mathrm{FNA}} = 1$. This figure is also presented in [3].

Yulian V. Vanne)

$$\Gamma_{FC-ADK} = N_e \sqrt{\frac{3F_e}{\pi\kappa^3}(2/\kappa - 1)} \frac{F_e}{8\pi} \left(\frac{4e\kappa^3}{(2/\kappa - 1)F_e} \right)^{2/\kappa} \times \exp\left[-\frac{2\kappa^3}{3F_e}\, g(\gamma) \right]$$

in the following where $e = 2.718...$ and $N_e = 2$ is the number of active electrons. Noteworthy, $g(\gamma)$ is a frequency-dependent modification to the standard ADK formula and the only ω-dependent term in Eq. (4.46). In the limit $\gamma \ll 1$ Eq. (4.46) reduces to the standard atomic ADK rate multiplied with the number of active electrons N_e.

Applying both ADK and FC-ADK at the equilibrium internuclear distance leads to their predictions within the FNA, whereas the R integration similar to Eq. (4.40) results in the predictions within FROZ. Figure 4.18a shows the FNA and FROZ TDSE ionization yields for parallel and for perpendicular alignment compared to the ADK and FC-ADK results. For both, fixed and frozen nuclei, one observes a rather small alignment dependence, i.e. the TDSE results for parallel and perpendicular alignment always agree within a factor of 3 (FNA) or 2 (FROZ) with a (mostly) slightly higher ionization yield for parallel alignment. Assuming that the alignment dependence relates to the symmetry of the initial state, this result is expected since the electronic ground state of H_2 is almost spherically symmetric. For the same reason, a simple one-electron one-center model potential [29, 77, 154] provides a good approximation for the ionization behavior of H_2. Most interestingly, while the ionization yields obtained with standard ADK differ from the TDSE results by several orders of magnitude, FC-ADK and TDSE ionization yields agree astonishingly well over the whole intensity range. The ratio $Y_{\mathrm{FROZ}}/Y_{\mathrm{FNA}}$ of the ionization yields in Figure 4.18a are shown in Figure 4.18b. The ionization yield is significantly enhanced within FROZ TDSE compared to the FNA, similar to the breakdown of the FNA for two-photon ionization in Figure 4.12. Depending on the laser intensity (and alignment), this enhancement reaches almost one order of magnitude. ADK and FC-ADK predict a smooth increase of the ratio with decreasing intensity. While the overall behavior of the TDSE ratios agree well with FC-ADK, the TDSE ratios become more and more structured with decreasing intensity since resonance structures become more and more pronounced (see also Figure 4.17). For example, at intensity $I = 4 \times 10^{13}\,\mathrm{W/cm^2}$, one finds $Y_{\mathrm{FROZ}}/Y_{\mathrm{FNA}} = 6.3$ (2.5) in the case of a parallel (perpendicular) alignment. At this laser intensity, a channel closing is expected such that 13 photons are required to overcome the ionization threshold at $R \leq 1.35$ a.u. while 12 photons are sufficient at $R > 1.35$ a.u. This leads to a strong increase of the ionization yield at internuclear distances which are slightly larger than the equilibrium distance (see Figure 4.17) and thus to a strongly increased ionization yield after the integration over internuclear distances.

Figure 4.19 shows the R-dependent ionization yields for parallel-aligned H_2 exposed to 800 nm $\cos^2$-laser fields with $n_c = 40$ cycles (FWHM of about 40 fs), carrier-envelope phase $\phi = 0$ and peak intensities I between 10^{13} to $10^{14}\,\mathrm{W/cm^2}$. One observes that the R dependence becomes significantly smoother with increas-

ing intensity, i.e. multiphoton resonances are, as expected, less and less pronounced when approaching the quasi-static regime. Comparing the TDSE ionization yields to standard ADK, one finds that ADK qualitatively predicts the correct R dependence of the ionization yield while it may differ quantitatively by several orders of magnitude. The quantitative agreement improves with increasing intensity, i.e. decreasing Keldysh parameter γ. In contrast to standard ADK, however, FC-ADK and TDSE ionization yields agree quantitatively surprisingly well for the whole intensity range. Of course, similar to standard ADK, FC-ADK is not well suitable for extremely intense laser fields where, in the quasi-static length-gauge picture, over-the-barrier ionization is possible and tunneling formulas tend to overestimate the total ionization yield [153, 155]. It was found already in Ref. [28] that it is possible to predict the R dependence of the TDSE ionization yield with ADK even for $\gamma \gtrsim 1$, if the obtained yield $Y_{\mathrm{ADK}}(R)$ is multiplied with a constant prefactor. Considerably shorter 800 nm $\cos^2$-laser fields with $n_{\mathrm{c}} = 6$ cycles (FWHM of about 6 fs), carrier-envelope phase $\phi = 0$ and peak intensities I between 3.5×10^{13} to $1.06 \times 10^{14}\,\mathrm{W/cm^2}$ were investigated in Ref. [28]. The prefactors needed to match ADK to TDSE ionization yields range up to 75 for $3.5 \times 10^{13}\,\mathrm{W/cm^2}$ [16]. The TDSE ionization yields for these laser fields are recalculated in order to compare them with ADK and especially the here introduced FC-ADK with a higher R resolution. For fully converged results, the basis set as described in Sec. 4.2.1 is extended by a second (long) configuration series where one electron occupies the H_2^+ exited state $1\sigma_u$ while the other is occupying one of the remaining (bound or discretized continuum) H_2^+ eigenstates. The resulting TDSE ionization yields are in good agreement with Ref. [28]. The R-dependent ionization yields for parallel-aligned H_2 exposed to these $n_{\mathrm{c}} = 6$ cycle fields are shown in Figure 4.20. Compared to $n_{\mathrm{c}} = 40$ cycle laser fields (Figure 4.19), resonances are much less pronounced since a shorter laser field is broader in the frequency domain. When compared to the TDSE, FC-ADK again predicts the correct R dependence almost quantitatively. Large scaling factors as required to match the behavior of ADK ionization yields to the TDSE results are thus not required for FC-ADK.

Despite the intrinsic short-coming of FC-ADK to describe resonances, the excellent agreement between TDSE and FC-ADK in the transition from the quasi-static to the multiphoton regime confirms the usefulness of the FC-ADK rates from Eq. (4.46), as shown for a range of laser intensities and laser field durations in Figures 4.18-4.20.

4.2.4 Conclusions

The ionization behavior of molecular hydrogen exposed to high frequency, low intensity as well as intense low-frequency (800 nm) laser fields has been studied the-

[16] Unfortunately, as it turns out the ADK rate in [28] had an additional prefactor $\sqrt{\pi\kappa^3/(3F)}$, i. e. $\sqrt{\pi\kappa^3/(3F)}\Gamma_{\mathrm{ADK}}$ was used instead of Γ_{ADK}. Thus, the more correct scaling factors for obtaining agreement between ADK and TDSE results in [28] are 75, 14, 5, and 2.5 for the laser peak intensities 3.5, 5.4, 7.8, and 10.6×10^{13} $\mathrm{W/cm^{-2}}$, respectively.

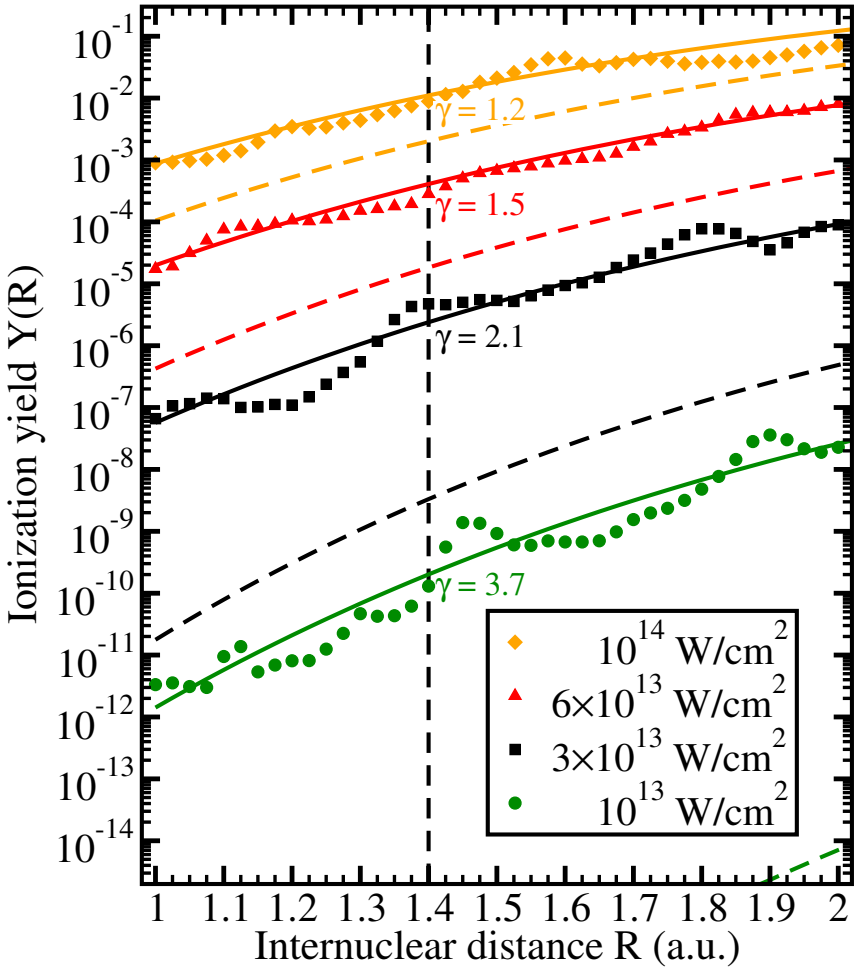

Figure 4.19: Ionization yields for a parallel-aligned H_2 molecule in 40-cycle $\cos^2$-shaped 800 nm laser fields with different peak intensities are compared with those predicted using ADK (dash lines) and frequency-corrected ADK (solid lines) ionization rates. The corresponding Keldysh parameters γ are given inside the graph. The dashed vertical line indicates the equilibrium internuclear distance $R_{\text{eq}} = 1.4$ a.u. This figure is also presented in [3].

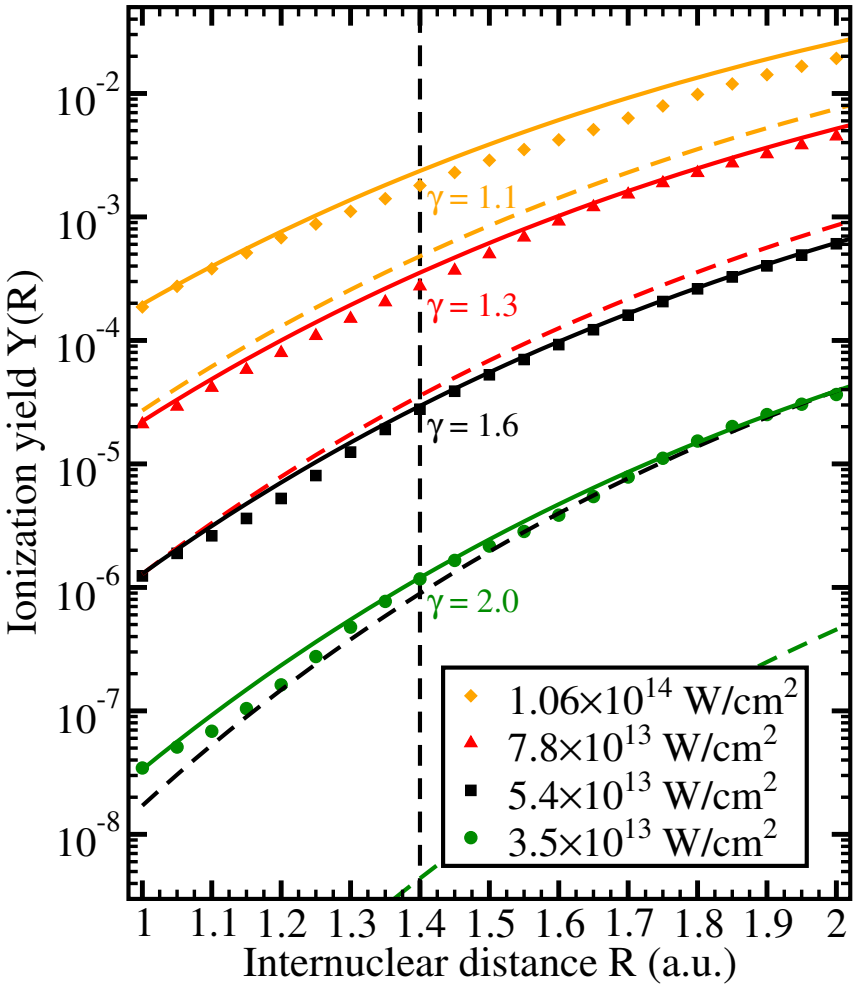

Figure 4.20: As Figure 4.19, but for 6-cycle laser fields and other laser peak intensities. This figure is also presented in [3].

oretically by solving the full-dimensional time-dependent two-electron Schrödinger equation. In the perturbative multiphoton ionization regime a good agreement between our TDSE results and TDSE as well as LOPT results reported in literature was found. Furthermore, a surprisingly strong dependence of the fixed-nuclei ionization yields $Y(R)$ on the internuclear distance R was found. This effect, caused by REMPI, offers a new explanation for the previously reported breakdown of the fixed-nuclei approximation for two-photon ionization [79, 81, 82]. The explanation, based on the frozen-nuclei approximation, still neglects vibrational dynamics during the laser field and considers only the initial spread of the nuclear wave function $\chi(R)$ in the initial state. Thus, this effect is expected to be important also for heavier molecules even though the actual laser-induced vibrational dynamics may be negligible. Noteworthy, the frozen-nuclei approximation is computationally much simpler than the fully coherent treatment of electronic and nuclear motion and it provides a very simple picture for the interpretation of results (vertical transitions between electronic Born-Oppenheimer potentials). The alignment-dependence of the ionization yield turns out to be rather small for three- and four-photon ionization. In contrast, it is very pronounced in the two-photon regime. Nevertheless, even for randomly aligned molecules, the breakdown of the fixed-nuclei approximation for two-photon ionization is clearly visible.

For intense 800 nm laser fields in the transition between the multiphoton and the quasi-static regime, a comparably small alignment dependence is found. On the other hand, a pronounced increase of the fixed-nuclei ionization yield $Y(R)$ with increasing internuclear distance R is observed. This increase is well understood by the exponential dependence of the quasi-static ionization rate on the binding energy $I_p(R)$. The smooth R dependence is superimposed by multiphoton resonances which become less and less pronounced when approaching the quasi-static regime. It is found that while ADK qualitatively describes the increase of $Y(R)$ with R, it completely fails quantitatively for $\gamma \gtrsim 1$ (which is outside the validity region of ADK, $\gamma \ll 1$). Thus, motivated by the original PPT theory, FC-ADK was introduced as a simple modification of the standard ADK formula. The quantitative agreement between the FC-ADK and the TDSE results for H_2 is astonishing and manifests the usefulness of the modified ADK formula.

Clearly, the true effect of vibrational dynamics during the laser field on the breakdown of the FNA would be of interest. The first step towards a fully correlated treatment of electronic and vibrational motion is taken in the following section where (1+1)-dimensional model H_2^+ is investigated.

4.3 Fully Correlated Electronic and Vibrational Motions: the (1+1)-Dimensional H_2^+ Model

In this chapter the fully correlated electronic and nuclear motion for a (1+1)-dimensional model describing H_2^+ in a laser field is investigated. For this model, the corresponding time-dependent Schrödinger equation can be solved directly on a grid. This allows for a direct test and comparison of the methods and approximations discussed in Chapters 2 and 3. The H_2^+ model Hamiltonian from Refs. [56–58, 105]

$$\begin{aligned}\hat{\mathrm{H}} = &-\frac{1}{M}\frac{\partial^2}{\partial R^2} + \frac{1}{\sqrt{0.03 + R^2}} - \frac{1}{2\,\mu_e}\frac{\partial^2}{\partial x^2} \\ &- \frac{1}{\sqrt{1 + (x - R/2)^2}} - \frac{1}{\sqrt{1 + (x + R/2)^2}} + V_{\mathrm{int}}(x\,,t) \\ = &\ \hat{\mathrm{H}}_0 + V_{\mathrm{int}}(x\,,t)\end{aligned} \tag{4.46}$$

with electronic coordinate x, internuclear distance R, proton mass M, and reduced mass of the electron $\mu_e = \dfrac{2\,M}{2\,M+1} \approx 1$ is used. The interaction potential $V_{\mathrm{int}}(x\,,t)$ describing the interaction with a linearly polarized field pointing along the x direction reads $V_{\mathrm{int}}^{\mathrm{LG}}(x\,,t) = q_e\,x\,F(t)$ in length gauge and $V_{\mathrm{int}}^{\mathrm{VG}}(x\,,t) = q_e\,\hat{\mathrm{p}}_x\,A(t)$ in velocity gauge with the electric field amplitude $F(t)$, the vector potential amplitude $A(t)$, and the reduced electron charge $q_e = \dfrac{2\,M\,+\,2}{2\,M\,+\,1} \approx 1$.

The wave function $\Psi(x,R,t)$ can be discretized on a two-dimensional grid spanning

$$\{\,x_1\,,\,x_2\,,\,\ldots\,,\,x_{N_x}\,\} \;=\; \{\,-M_x a_x\,,\,-(M-1)a_x\,,\,\ldots\,,\,0\,,\,\ldots\,,\,M_x a_x\,\} \tag{4.47}$$

and

$$\{\,R_1\,,\,R_2\,,\,\ldots\,,\,R_{N_R}\,\} \;=\; \{\,0\,,a_R\,,\,\ldots\,,\,(N_R-1)a_R\,\} \tag{4.48}$$

with $N_x = 2M_x + 1$ $[N_R = 2M_R + 1]$ points covering a box size of $L_x = N_x\,a_x$ $[L_R = N_R\,a_R]$ with spacing a_x $[a_R]$ for x $[R]$, respectively. The wave function is written in vector form as

$$\Psi(x,R,t) \equiv \begin{pmatrix} \Psi(x_1,R_1,t) \\ \Psi(x_2,R_1,t) \\ \vdots \\ \Psi(x_{N_x},R_1,t) \\ \Psi(x_1,R_2,t) \\ \vdots \\ \Psi(x_{N_x},R_{N_R},t) \end{pmatrix} . \tag{4.49}$$

In the following the discretized TDSE

$$i\,\frac{\partial}{\partial t}\,\Psi(x,R,t) \;=\; \hat{\mathrm{H}}\,\Psi(x,R,t) \tag{4.50}$$

is solved in different ways combining the methods discussed in Chapter 3. The goal is to deepen the understanding of the practicability and convergence behavior of these methods and to examine the influence of approximations on the dynamics observed in strong laser fields. The Born-Oppenheimer electronic eigenstates of the model potential are calculated in Section 4.3.1. Different ways for calculating the ground state of the full Hamiltonian are discussed in Section 4.3.2. In Section 4.3.3 the TDSE is solved on a two-dimensional grid. This approach is compared to the solution of the TDSE using electronic eigenstates within the adiabatic approximation, Section 4.3.4, as well as the full solution including nonadiabatic couplings, Section 4.3.5.

4.3.1 Born-Oppenheimer Eigenstates

The Born-Oppenheimer potentials of the H_2^+ model are obtained by solving the electronic time-independent Schrödinger equation

$$\begin{aligned}\hat{\mathrm{H}}_\mathrm{e}\;\Phi_n(x;R) = \Bigg(&-\frac{1}{2\,\mu_e}\,\frac{\partial^2}{\partial x^2} + \frac{1}{\sqrt{0.03\,+\,R^2}} - \frac{1}{\sqrt{1\,+\,(x\,-\,R/2)^2}} \\ &- \frac{1}{\sqrt{1\,+\,(x\,+\,R/2)^2}}\Bigg)\,\Phi_n(x;R) \;=\; \mathcal{E}_n(R)\;\Phi_n(x;R)\end{aligned} \tag{4.51}$$

for a set of internuclear distances R (as discussed in Section 2.1). Born-Oppenheimer vibrational eigenstates $\chi_{n\nu}$ are then obtained by solving the Born-Oppenheimer equation

$$\left(-\frac{1}{M}\,\frac{\partial^2}{\partial R^2} \;+\; \mathcal{E}_n(R)\right)\chi_{n\nu}(R) \;=\; E_{n\nu}\,\chi_{n\nu}(R) \quad . \tag{4.52}$$

The diagonalizations are done directly on the grid using the matrix algorithm described in Section 3.1. Figure 4.21 shows the obtained Born-Oppenheimer potentials of the H_2^+ model potential using the matrix algorithm to solve Eq. (4.51) with $L_x = 100$ a.u. and $N_x = 201$ points. For comparison, the potential energy surfaces of the real H_2^+ molecule obtained with B_DAM_ECS_1E described in Section 3.3 are shown. 200 B splines of order 10 (linear knot sequence) and a box size of $r_\mathrm{max} = 100$ a.u. are used in ξ direction and 24 B splines of order 8 are used in η direction. The potential energy surfaces of three-dimensional H_2^+ and of the model potential show qualitatively a comparable behavior, but disagree quantitatively significantly. Distinct features of the three-dimensional H_2^+ calculation like the sharp avoided crossing seen for the first and second exited state with σ_g symmetry at $R = 4.05$ a.u. are not reproduced by the one-dimensional model potential. It would be easily possible to

match the potential energy surfaces of the electronic ground state by introducing, e.g., an R-dependent softening parameter $a(R)$ such that

$$\frac{1}{\sqrt{1 + (x \pm R/2)^2}} \longrightarrow \frac{1}{\sqrt{a(R) + (x \pm R/2)^2}} \quad . \tag{4.53}$$

However, this would not lead to matching excited state energies and, of course, the wave functions would still be completely different compared to the three-dimensional case. Thus, solely the model Hamiltonian, Eq. (4.46), is used in the following to allow for direct comparison with Refs. [56, 57]. The ionization behavior of H_2^+ can be discussed on a qualitative level using this model potential. Keep in mind, however, that processes like rescattering are strongly enhanced in a one-dimensional model compared to a three-dimensional calculation.

Figure 4.21 additionally shows the probability densities of the vibrational Born-Oppenheimer ground states obtained by solving Eq. (4.52) using the matrix algorithm with $L_R = 10$ a.u. and $N_R = 201$ points[17]. In the following, we will find the ground state of the full H_2^+ model Hamiltonian and compare it to the approximate Born-Oppenheimer ground state.

4.3.2 Ground State of the Full Hamiltonian

The ground state of the two-dimensional Hamiltonian $\hat{H}_0$, Eq. (4.46), is calculated using the matrix algorithm as described in the end of Section 3.1. The non-vanishing Hamiltonian matrix elements are stored in sparse matrix mode. The energetically lowest eigenfunction, i.e. the ground state $\Psi_0^{(\mathrm{diag})}(x, R)$ of $\hat{H}_0$, is found using the MATLAB[73] method EIGS (Arnoldi iteration)[18].

Alternatively, imaginary time propagation as described in Section 3.6 can be used to obtain the ground-state wave function $\Psi_0^{(\mathrm{i}\tau)}(x, R)$ of $\hat{H}_0$. It seems natural to implement the kinetic energy operator as

$$\mathcal{F}_{\mathrm{FFT}}^{-1} \left(\frac{\hat{p}_x^2}{2\mu_e} + \frac{\hat{p}_R^2}{M} \right) \mathcal{F}_{\mathrm{FFT}} \quad . \tag{4.54}$$

However, within MATLAB and for $N_x \leq 700$ and $N_R \leq 700$ it was found that it is notably faster to reshape the wave function to a matrix, multiply the $\frac{\hat{\mathbf{p}}_\mathbf{x}^\mathbf{2}}{2\mu_e}$ and $\frac{\hat{\mathbf{p}}_\mathbf{R}^\mathbf{2}}{M}$ matrices on the properly reshaped wave function matrix and convert the matrices back. The matrices $\hat{\mathbf{p}}_\mathbf{x}^\mathbf{2}$ and $\hat{\mathbf{p}}_\mathbf{R}^\mathbf{2}$ are the full matrices from the matrix algorithm Eq. (3.11) of dimension $N_x \times N_x$ and $N_R \times N_R$, respectively. The multiplication

[17] All results shown in Figure 4.21 are unchanged when the box size or point (B spline) density is increased.

[18] This approach is feasible as long as the number of non-vanishing matrix elements is small enough to fit into the RAM.

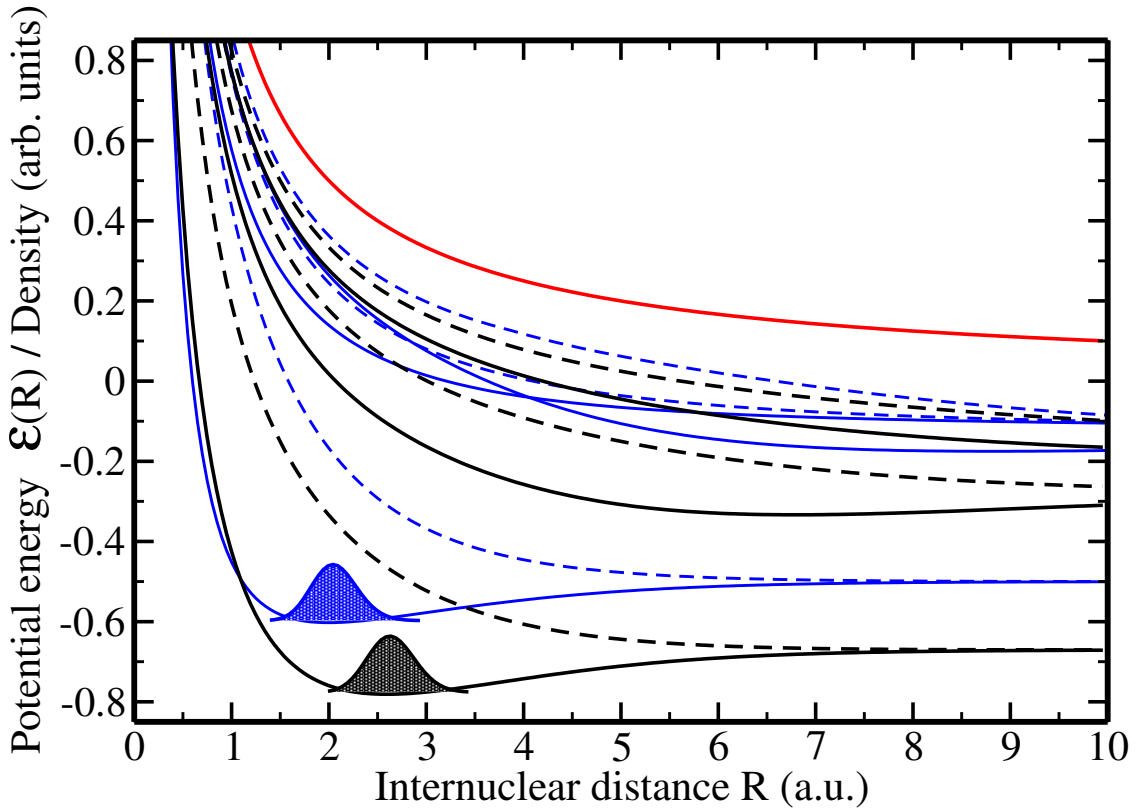

Figure 4.21: Born-Oppenheimer potentials and vibrational ground-state density of H_2^+. The full (dashed) black lines show the three lowest-lying eigenstates of the one-dimensional H_2^+ model potential with even (odd) symmetry with respect to a reflection $x \leftrightarrow -x$. The full (dashed) blue lines show the three lowest-lying eigenstates of the three-dimensional H_2^+ potential with σ_g (σ_u) symmetry. The full red line displays the H^++H^++e^- ionization continuum $\mathcal{E}(R) = 1/R$ (indistinguishable from the softened potential $\mathcal{E}(R) = 1/\sqrt{R^2 + 0.03}$ on the scale of this graph). Furthermore, the black (blue) shaded area displays the vibrational ground-state density of the model (real) H_2^+ electronic ground-state Born-Oppenheimer potential.

of the $\hat{\mathrm{p}}^2$ operators with the reshaped wave function matrix then looks like

$$\hat{\mathrm{p}}_{\mathbf{x}}^{\mathbf{2}}\,\Psi(x,R,t) \;\equiv\; \hat{\mathrm{p}}_{\mathbf{x}}^{\mathbf{2}} \begin{pmatrix} \Psi(x_1,R_1,t) & \Psi(x_1,R_2,t) & \dots & \Psi(x_1,R_{N_R},t) \\ \Psi(x_2,R_1,t) & \Psi(x_1,R_2,t) & \dots & \Psi(x_1,R_{N_R},t) \\ \vdots & \vdots & \ddots & \vdots \\ \Psi(x_{N_x},R_1,t) & \Psi(x_{N_x},R_2,t) & \dots & \Psi(x_{N_x},R_{N_R},t) \end{pmatrix}, \tag{4.55}$$

$$\hat{\mathrm{p}}_{\mathbf{R}}^{\mathbf{2}}\,\Psi(x,R,t) \;\equiv\; \hat{\mathrm{p}}_{\mathbf{R}}^{\mathbf{2}} \begin{pmatrix} \Psi(x_1,R_1,t) & \Psi(x_2,R_1,t) & \dots & \Psi(x_{N_x},R_1,t) \\ \Psi(x_1,R_2,t) & \Psi(x_2,R_2,t) & \dots & \Psi(x_{N_x},R_2,t) \\ \vdots & \vdots & \ddots & \vdots \\ \Psi(x_1,R_{N_R},t) & \Psi(x_2,R_{N_R},t) & \dots & \Psi(x_{N_x},R_{N_R},t) \end{pmatrix}. \tag{4.56}$$

Starting from an initial state $\Psi^{(i)}(x,R,0)$, imaginary time propagation is performed using the MATLAB routine ODE45[19].
Four different initial states (or initial guesses) are compared:

1. A uniform wave function $\Psi^{(i)}(x,R,0) \;=\; 1/\sqrt{N_x\,N_R}$.

2. The Born-Oppenheimer ground state $\Psi^{(i)}(x,R,0) \;=\; \chi_{00}(R)\,\Phi_0(x;R)$ obtained according to Section 4.3.1. Since the signs of the $\Phi_0(x;R)$ are random for each R since they are numerically obtained by matrix diagonalization, they are fixed such that $\sum\limits_i \Phi_0(x_i;R_j) > 0 \;\; \forall\, j$.

3. As 2., but with alternating signs $\sum\limits_i \Phi_0(x_i;R_j) > 0$ for all odd j and < 0 for all even j. While this yields the same probability density $\left|\Psi^{(i)}(x,R,0)\right|^2$ as case 2 it can be translated to a very quickly oscillating nuclear wave function ($\chi_{00}(R)$ but with changing sign between each neighboring R).

4. The ground state $\Psi^{(i)}(x,R,0) \;=\; \Psi_0^{(\mathrm{diag})}(x,R)$ obtained by matrix diagonalization as described in the beginning of this section.

The propagation using ODE45 is done in steps of $\Delta t = 5$ a.u., then the wave function is renormalized and compared to the wave function before the propagation step[20]. The corresponding difference

$$\left\|\, \Psi(\,t\,+\,\Delta t\,) - \Psi(\,t\,)\,\right\| \;=\; \sqrt{\sum_{i,k} \Big(\Psi(x_i,R_k,t+\Delta t) - \Psi(x_i,R_k,t)\Big)^2} \tag{4.57}$$

is a measure for the convergence reached for the imaginary time propagation.

[19] Runge-Kutta solver of order 4 and 5 with adaptive step size.
[20] Of course, the step size for the imaginary time propagation itself is adaptive within ODE45.

Figure 4.22 shows the development of the difference $\| \Psi(t + \Delta t) - \Psi(t) \|$ with increasing number of function calls[21] for the four initial states discussed before. As in the previous section $L_x = 100$ a.u., $N_x = 201$, $L_R = 10$ a.u., and $N_R = 201$ are used. The relative tolerance for the ODE45 routine is set to 10^{-10}. Furthermore, convergence for both an additional absolute tolerance of 10^{-16} and no additional absolute tolerance are shown. Regarding the behavior of different initial states, the uniform wave function (1.) and the state with quickly oscillating signs (3.) converge very similarly, requiring around 200,000 function calls to reach a difference in the order of 10^{-16}. The Born-Oppenheimer ground state (2.) converges with the same rate, but requires only around 150,000 function calls for the same tolerance and starts with a much smaller difference due to its similarity with the full ground state. Both no absolute tolerance and absolute tolerance 10^{-16} behave very similarly in the aforementioned cases. Adding the absolute tolerance simply increases the number of function calls required to reach convergence. If no absolute tolerance is set, even the true ground state obtained by matrix diagonalization requires around 5,000 function calls to reach the same level of convergence, but showing a much faster convergence rate than the other cases. These extra propagation steps are not needed when the absolute tolerance is set to 10^{-16}. In the following, the obtained ground states $\Psi_0(x, R)$ and especially the influence of the absolute tolerance on them are examined.

Figure 4.23 compares ground state $\Psi_0^{(\mathrm{diag})}(x, R)$ obtained by diagonalization with the ground state $\Psi_0^{(\mathrm{i}\tau)}(x, R)$ after additional imaginary time propagation with and without setting the absolute tolerance for ODE45 to 10^{-16}. Cuts along the electronic coordinate x are shown for different values of R. At the equilibrium internuclear distance $R = 2.587$ a.u. one can see only one maximum in the wave functions despite the two nuclear centers. This is the typical behavior of the ground state of H_2^+ and also H_2; the nuclei are still so close to each other that one basically finds a one-center behavior at the equilibrium geometry, as also observed for H_2 in Section 4.2. For this internuclear distance as well as $R = 4.952$ a.u. all obtained ground states $\Psi_0(x, R)$ agree perfectly. For $R = 4.952$ the two-center character is clearly seen. However, the wave function is already very small (order of $10^{-8} \Rightarrow 10^{-16}$ for the probability density). Clearly, one is already deep in the classically forbidden region of the nuclear problem. At even larger internuclear distances between $R = 5.920$ a.u. and $R = 9.950$ a.u., i.e. even deeper in the classically forbidden region for the nuclei, $\Psi_0^{(\mathrm{i}\tau)}(x, R)$ without absolute tolerance shows a quickly oscillating behavior which is not seen for $\Psi_0^{(\mathrm{diag})}(x, R)$. Furthermore, the absolute values of $\Psi_0^{(\mathrm{diag})}(x, R)$ are much smaller, for $R = 9.950$ a.u. even by 8 orders of magnitude. Agreement on the machine precision level between $\Psi_0^{(\mathrm{diag})}(x, R)$ and $\Psi_0^{(\mathrm{i}\tau)}(x, R)$ is reached after setting the absolute tolerance to 10^{-16}, indicating the importance of the absolute tolerance for time propagations on a grid at positions where the wave function is small.

[21] A function call is a call of the function implementing $\dfrac{\partial}{\partial t}\Psi = -i\,\hat{\mathrm{H}}\,\Psi$ for one specific time.

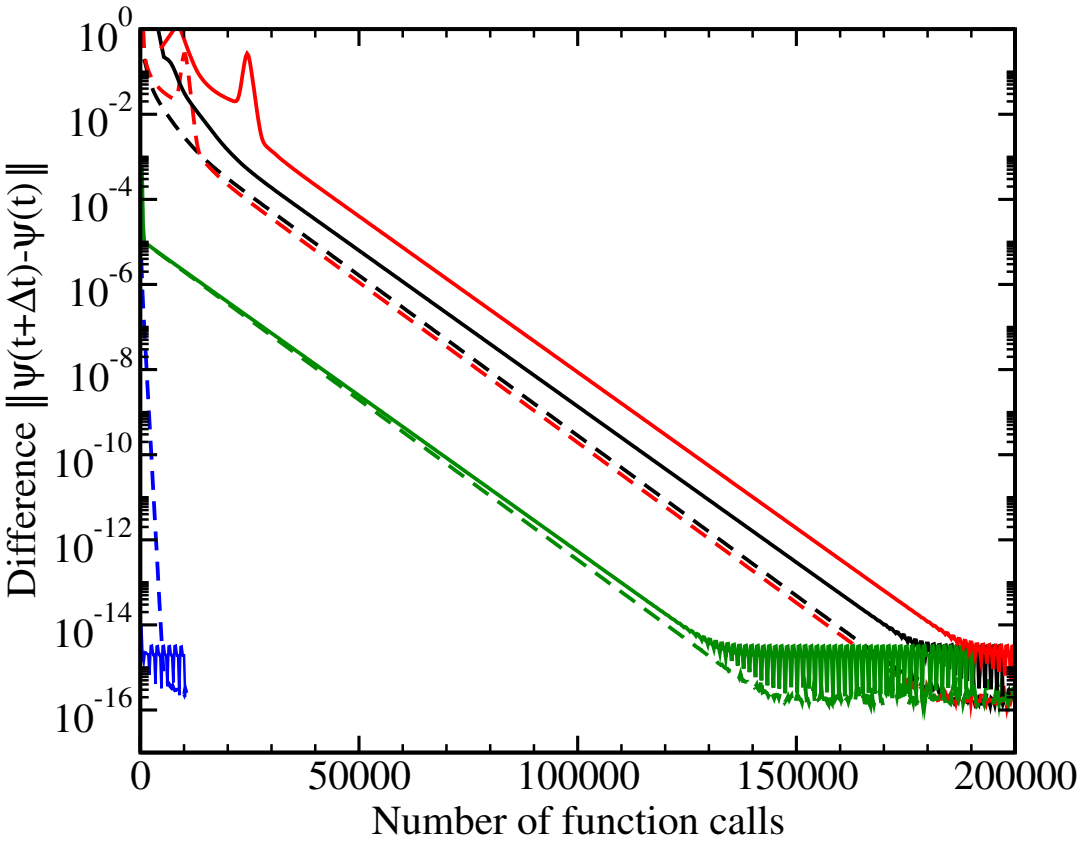

Figure 4.22: Convergence behavior of the ground state $\Psi_0^{(i\tau)}(x,R)$ obtained using imaginary time propagation (difference according to Eq. (4.57) depending on the total number of function calls). The absolute tolerance of the ODE45 routine is set to 10^{-16} (full lines) or none (dashed lines) in combination with a relative tolerance of 10^{-10}. The initial states $\Psi^{(i)}(x,R,0)$ are the uniform state (1., black), the Born-Oppenheimer ground state (2., green), the state with Born-Oppenheimer ground state density but quickly oscillating signs (3., red) and the full ground state obtained by matrix diagonalization (4., blue).

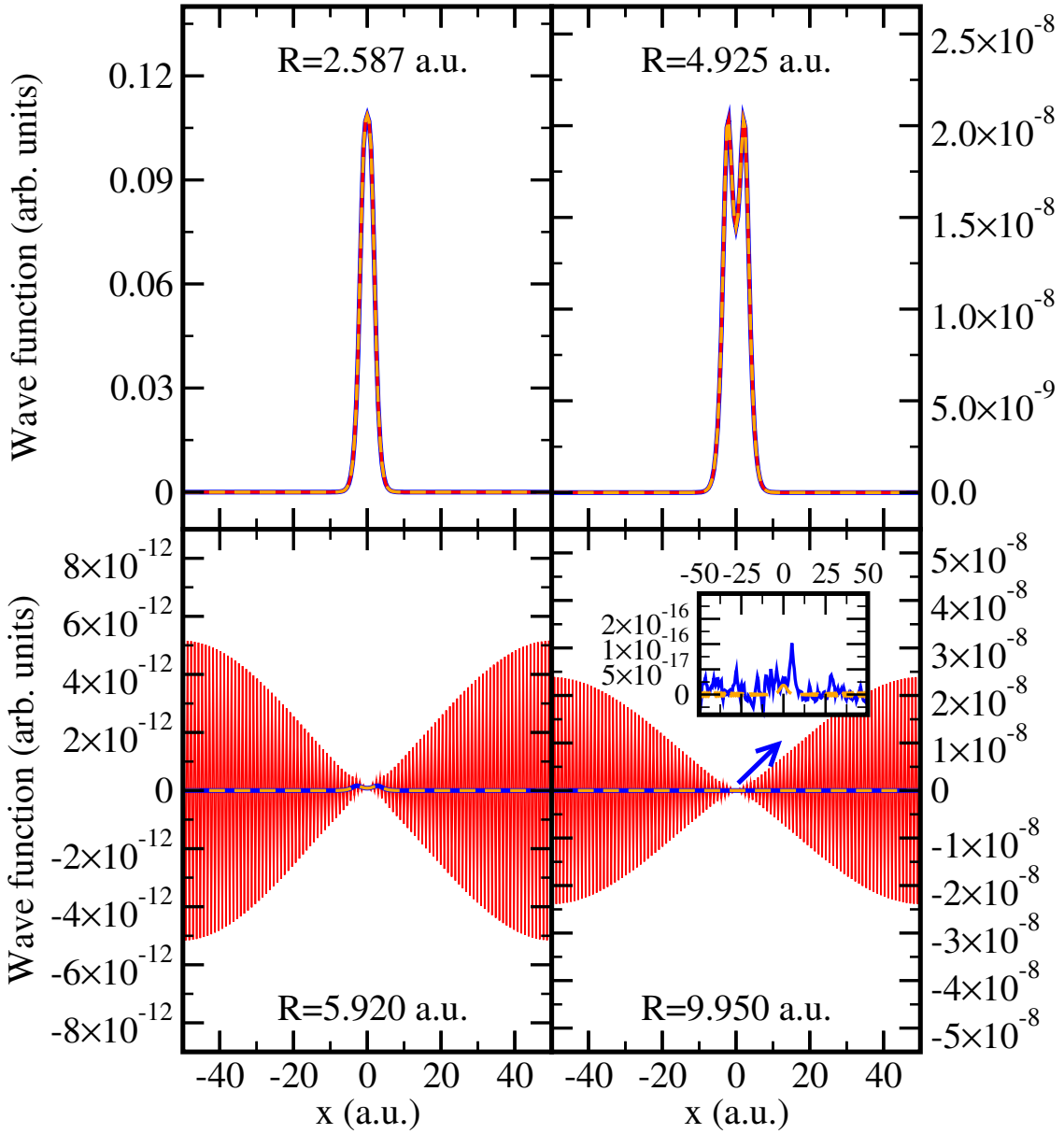

Figure 4.23: Cuts showing the ground-state wave function $\Psi_0^{(\mathrm{diag})}(x,R)$ obtained from matrix diagonalization (solid blue line) and $\Psi_0^{(\mathrm{i}\tau)}(x,R)$ obtained by imaginary time propagation without setting an absolute tolerance (solid red line) and with absolute tolerance set to 10^{-16} (dashed orange line) at four fixed internuclear distances R (values given inside the graph). At $R = 9.95$ a.u. the inset enlarges $\Psi_0^{(\mathrm{diag})}(x,R)$ and $\Psi_0^{(\mathrm{i}\tau)}(x,R)$. Sharp edges stem from the spacing (or resolution) $\Delta x \approx 0.5$ a.u. of the basis set.

4.3.3 Direct Solution of the TDSE on a Two-Dimensional Grid

In this section the TDSE

$$i\,\frac{\partial}{\partial t}\,\Psi(x,R,t) \;=\; \Big(\,\hat{\mathrm{H}}_0 \;+\; V_{\mathrm{int}}(\,x\,,\,t\,)\,\Big)\,\Psi(x,R,t) \tag{4.58}$$

is solved directly in the two-dimensional grid representation with the ODE45 Matlab routine using the relative tolerance 10^{-10} and the absolute tolerance of 10^{-14}. Starting point is the ground state $\Psi_0^{(\mathrm{diag})}(x,R) = \Psi(x,R,0)$ of $\hat{\mathrm{H}}_0$ obtained by matrix diagonalization as described in Section 4.3.2. The action of $\hat{\mathrm{H}}_0$ on $\Psi(x,R,t)$ is implemented identically to the case of imaginary time propagation as also studied in the aforementioned section. The interaction potential $V_{\mathrm{int}}(\,x\,,\,t\,)$ then simply leads to an additional vector-vector (*small* matrix-matrix) multiplication in the case of length (velocity) gauge. In order to directly compare nuclear probability densities with Ref. [56] the same field-strength magnitude

$$F(t) = \begin{cases} F_0\,(t/t_{\mathrm{ramp}})\,\sin(\omega t) & \text{for } 0 \le t \le t_{\mathrm{ramp}} \\ F_0\,\sin(\omega t) & \text{for } t_{\mathrm{ramp}} < t \\ 0 & t < 0 \end{cases} \tag{4.59}$$

with corresponding vector potential

$$A(t) = \begin{cases} F_0\,\big(\omega\,(t/t_{\mathrm{ramp}})\,\cos(\omega t) \;-\; \sin(\omega t)\big)/\omega^2 & \text{for } 0 \le t \le t_{\mathrm{ramp}} \\ (F_0/\omega)\,\cos(\omega t) & \text{for } t_{\mathrm{ramp}} < t \\ 0 & t < 0 \end{cases} \tag{4.60}$$

is used. The linear ramp-up has a duration of $t_{\mathrm{ramp}} = 20\pi/\omega \approx 7.6$ fs and the frequency $\omega \approx 0.1998$ a.u. corresponds to a wavelength of $\lambda = 228$ nm. Furthermore, the studied peak field strengths are $F_0^{(1)} \approx 0.0267$ a.u. and $F_0^{(2)} \approx 0.0534$ a.u. which correspond to the peak intensities $I^{(1)} = 2.5 \times 10^{13}$ W/cm^2 and $I^{(2)} = 10^{14}$ W/cm^2.

The nuclear probability density $|\,\chi(R,t)\,|^2$ is extracted directly from the full time-dependent wave function $\Psi(x,R,t)$ as

$$|\,\chi(R_k,t)\,|^2 \;=\; \sum_{i=1}^{N_x} \big|\,\Psi(x_i,R_k,t)\,\big|^2 \quad . \tag{4.61}$$

Figures (4.24) and (4.25) show the obtained nuclear probability densities for the peak intensities $I^{(1)} = 2.5 \times 10^{13}$ W/cm^2 and $I^{(2)} = 10^{14}$ W/cm^2, respectively. The graphs were obtained using the box parameters $N_x = 301$, $L_x = 150$ a.u., $N_R = 301$, and $L_R = 15$ a.u. The agreement to the points extracted from Ref. [56] is excellent[22],

[22] Note that there is a typo in the label of Fig. 1 in Ref. [56]. This graph does not show the probability density $|\,\chi(R,t)\,|^2$, but instead the absolute value of the exact nuclear wave function $|\,\chi(R,t)\,|$.

except for small visible differences for $I = 10^{14}$ W/cm^2 at $t = 18.62$ fs ($R > 8$ a.u.) and $t = 15.3$ fs ($R \approx 6$ a.u.). Increasing the box parameters to $N_x = 1001$, $L_x = 400$ a.u., $N_R = 601$, $L_R = 20$ a.u. leaves the nuclear probability density unchanged on the scale of this graph. Convergence of the present calculation thus does not explain the small difference to Ref. [56].

Differences between length and velocity gauge are not visible on the scale of Fig. (4.24) and (4.25). Thus, the averaged absolute difference

$$\Delta_{\text{avg}}(\chi^{(A)}, \chi^{(B)}, t) = \frac{1}{N_R} \sum_k \left| \left| \chi^{(A)}(R_k, t) \right|^2 - \left| \chi^{(B)}(R_k, t) \right|^2 \right| \tag{4.62}$$

as well as the maximum absolute difference

$$\Delta_{\text{max}}(\chi^{(A)}, \chi^{(B)}, t) = \max_R \left(\left| \left| \chi^{(A)}(R, t) \right|^2 - \left| \chi^{(B)}(R, t) \right|^2 \right| \right) \tag{4.63}$$

of the nuclear probability densities are examined. The absolute differences between length and velocity gauge are shown in Figure 4.62 for the probability densities discussed before. The averaged absolute differences increase with propagation time and always remains below 4×10^{-5}. Furthermore, this difference is slightly higher for $I = 10^{14}$ W/cm^2 compared to $I = 2.5 \times 10^{13}$ W/cm^2. The maximum absolute difference is about one order of magnitude higher than the averaged one which indicates that a small range of internuclear distances R contributes strongly to the averaged difference between the two gauges. With maximum absolute differences remaining below 3×10^{-4} for all R, times and intensities shown the gauge dependence is indeed very small.

4.3.4 Solution of the TDSE using Electronic Born-Oppenheimer Eigenstates: Adiabatic (Born-Oppenheimer) Approximation

Following Section 2.1 the TDSE can alternatively be solved using the Born-Huang expansion

$$\Psi(x, R, t) \; = \; \sum_n \chi_n(R, t)\, \Phi_n(x; R) \tag{4.64}$$

with electronic eigenstates $\Phi_n(x; R)$ and time-dependent vibrational wave functions $\chi_n(\, R\, ,\, t\,)$. Using the vector form

$$\Psi \; \equiv \; \begin{pmatrix} \chi_1(R, t) \\ \chi_2(R, t) \\ \vdots \end{pmatrix} \tag{4.65}$$

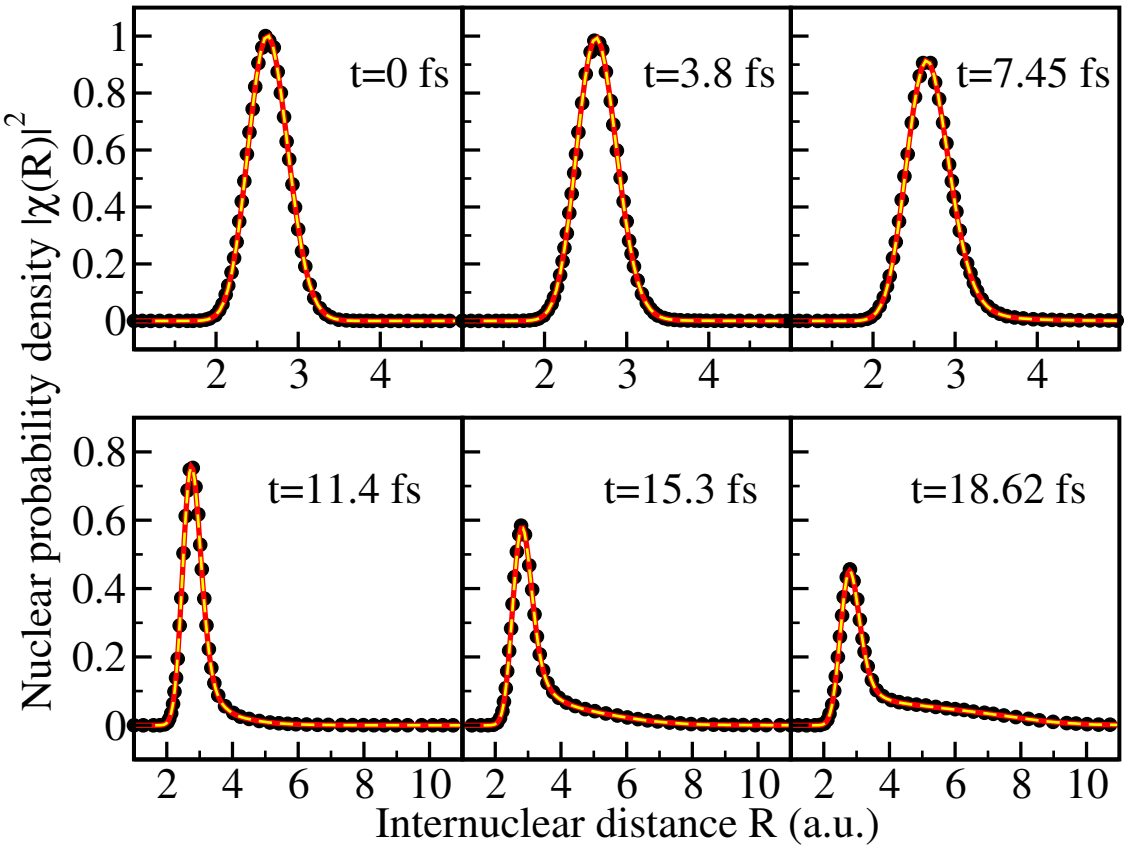

Figure 4.24: Time evolution of the nuclear probability density for peak intensity $I = 2.5 \times 10^{13}$ W/cm^2. The full red line is obtained using velocity gauge while the dashed yellow line shows the result obtained in length gauge with the same box parameters. The black points are the results extracted from Ref. [56].

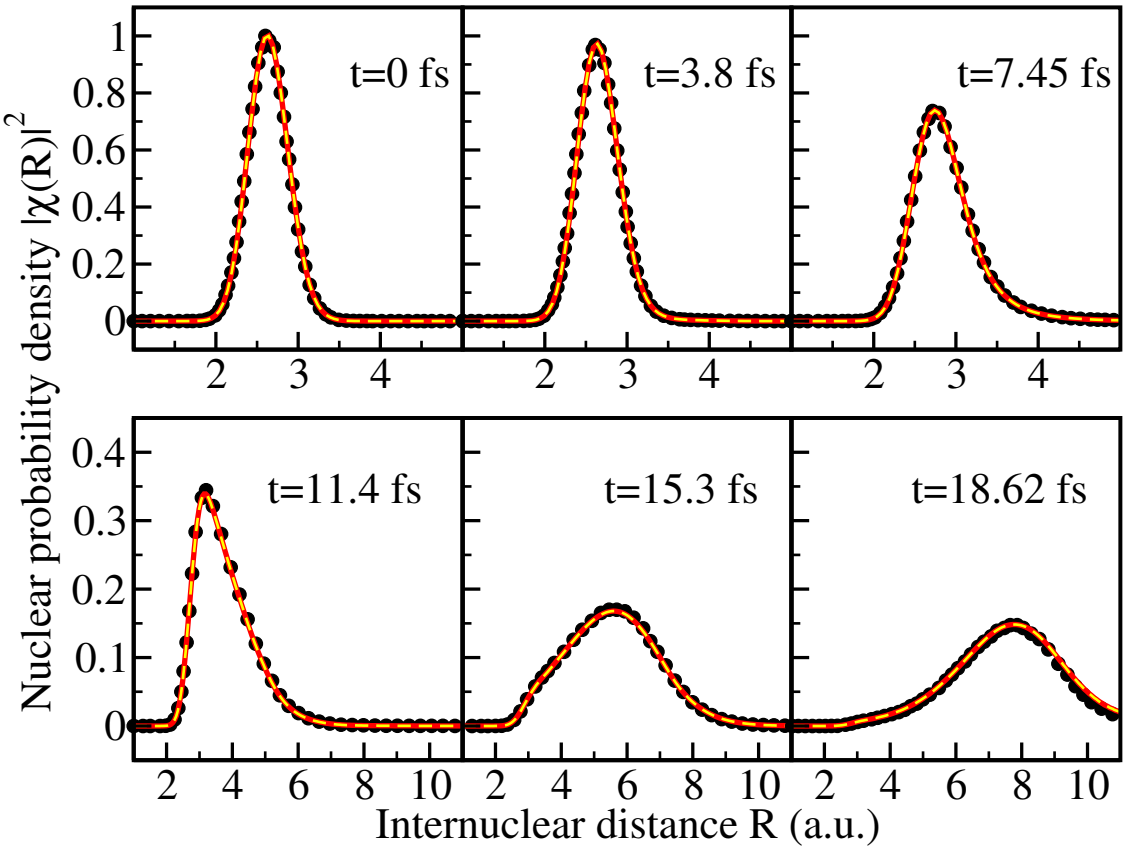

Figure 4.25: As Figure 4.24, but for peak intensity $I = 10^{14}$ W/cm^2.

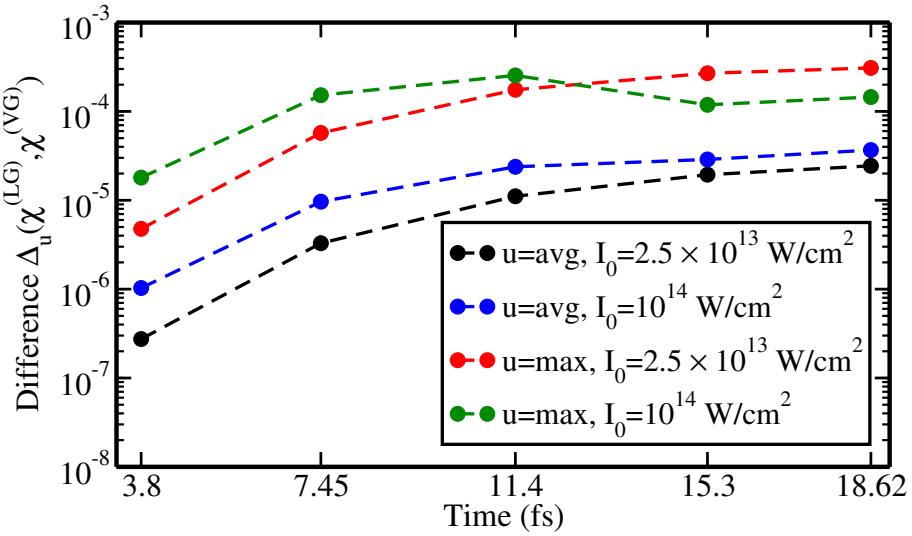

Figure 4.26: Absolute differences Δ_{avg} (Eq. (4.62)) and Δ_{max} (Eq. (4.63)) between length gauge (LG) and velocity gauge (VG).

the TDSE can (similarly to Eq. (2.24)) be written as

$$i\,\frac{\partial}{\partial t}\,\Psi \;=\; -\,\frac{1}{M}\,\left(\,\frac{\boldsymbol{\partial}}{\boldsymbol{\partial R}}+\mathbf{B}(\,R\,)\right)^{2}\,\Psi \;+\;(\;\boldsymbol{\mathcal{E}}(\,R\,)\;+\;\mathbf{V}_{\mathrm{int}}(\,R\,,\,t\,)\;)\;\Psi \tag{4.66}$$

with the diagonal matrices

$$\boldsymbol{\mathcal{E}}(\,R\,) \;=\; \mathrm{diag}(\,\mathcal{E}_1(\,R\,)\,,\,\mathcal{E}_2(\,R\,)\,,\,...\,) \quad , \tag{4.67}$$

$$\frac{\boldsymbol{\partial}}{\boldsymbol{\partial R}} \;=\; \mathrm{diag}\left(\,\frac{\partial}{\partial R}\,,\,\frac{\partial}{\partial R}\,,\,...\,\right) \quad , \tag{4.68}$$

the nonadiabatic coupling matrix $\mathbf{B}(\,R\,)$ with entries

$$B_{mn}(\,R\,) \;=\; \left\langle\,\Phi_m(\,R\,)\,\middle|\,\frac{\partial}{\partial R}\,\middle|\,\Phi_n(\,R\,)\,\right\rangle_x \quad , \tag{4.69}$$

and the laser field interaction matrix $\mathbf{V}_{\mathrm{int}}(\,R\,,\,t\,)$ with entries

$$V_{\mathrm{int},mn}(\,R\,,\,t\,) \;=\; \langle\,\Phi_m(\,R\,)\,|\,V_{\mathrm{int}}(\,x\,,\,t\,)\,|\,\Phi_n(\,R\,)\,\rangle_x \quad . \tag{4.70}$$

Within the dipole approximation $\mathbf{V}_{\mathrm{int}}(\,R\,,\,t\,)$ separates into a time-dependent prefactor and a time-independent dipole matrix

$$\mathbf{V}^{\mathrm{LG}}_{\mathrm{int}}(\,R\,,\,t\,) \;=\; q_e\,F(t)\,\mathbf{D}^{\mathrm{LG}}(\,R\,) \quad ,\mathrm{or} \tag{4.71}$$

$$\mathbf{V}^{\mathrm{VG}}_{\mathrm{int}}(\,R\,,\,t\,) \;=\; -\,i\,q_e\,A(t)\,\mathbf{D}^{\mathrm{VG}}(\,R\,) \quad , \tag{4.72}$$

with dipole matrix elements

$$D^{\mathrm{LG}}_{mn}(\,R\,) \;=\; \langle\,\Phi_m(\,R\,)\,|\,x\,|\,\Phi_n(\,R\,)\,\rangle_x \quad ,\mathrm{and} \tag{4.73}$$

$$D^{\mathrm{VG}}_{mn}(\,R\,) \;=\; \left\langle\,\Phi_m(\,R\,)\,\middle|\,\frac{\partial}{\partial x}\,\middle|\,\Phi_n(\,R\,)\,\right\rangle_x \quad , \tag{4.74}$$

respectively.

Within the adiabatic (Born-Oppenheimer) approximation used for the subsequent calculations the nonadiabatic couplings vanish, $\mathbf{B}=\mathbf{0}$. In the following, the box parameters $N_x = 301$, $L_x = 150$ a.u., $N_R = 301$, and $L_R = 15$ a.u. are used. Using these parameters converged results were obtained in the previous section. The set of coupled vibrational wave functions $\chi_n(\,R\,,\,t\,)$ is time propagated directly on the grid[23]. The nuclear momentum operator is applied similar to Eq. (4.56) replacing $\Psi(x_n, R_k, t) \rightarrow \chi_n(R_k, t)$. The electronic Born-Oppenheimer eigenstates $\Phi_n(x;R)$ are calculated according to Section 4.3.1. However, since the signs of the eigenstates $\Phi_n(x;R)$ obtained from matrix diagonalization are random for each R, the signs have to be adjusted such that the basis is continuous in R. The states are sorted

[23] Relative tolerance set to 10^{-13} and absolute tolerance set to 10^{-16}.

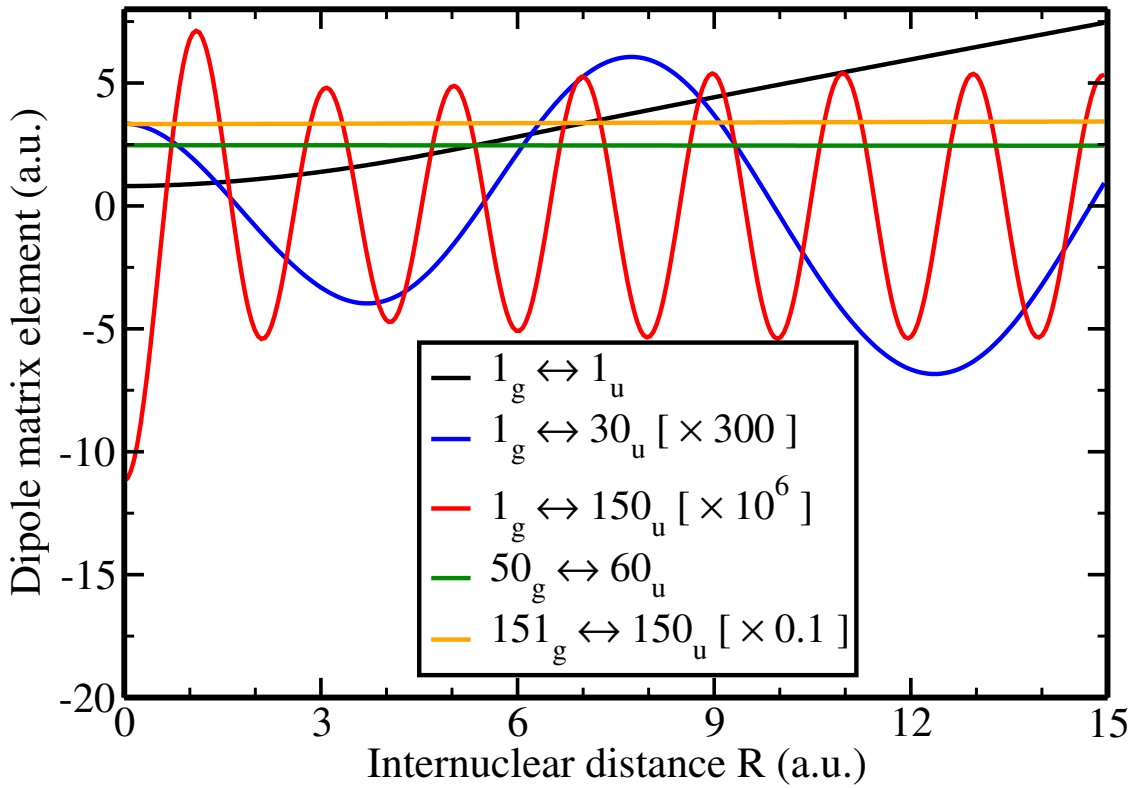

Figure 4.27: Dipole matrix elements $D^{\mathrm{LG}}_{mn}(R)$ for selected transitions. Some elements have been scaled by a factor to be able to show all elements on a linear scale on the same graph, scaling factors are given inside the legend [in square brackets].

by increasing energy for each symmetry (*gerade* and *ungerade*) independently. A reference position R_k to fix the signs is chosen, in this case the first point R_1. If for a neighboring position $k+1$ one finds

$$||\Phi_n(x;R_k) + \Phi_n(x;R_k+1)|| \; < \; ||\Phi_n(x;R_k) - \Phi_n(x;R_k+1)|| \tag{4.75}$$

the sign of $\Phi_n(x;R_{k+1})$ is flipped, i.e. $\Phi_n(x;R_{k+1}) \to -\Phi_n(x;R_{k+1})$, and otherwise left unchanged. After the signs of all states n have been adapted, if necessary, one moves on to the next neighbor such that iteratively all signs from $k=1$ to $k=N_R$ are fixed. Afterwards, elements of the dipole transition matrices $\mathbf{D}(R)$ are smooth functions of R, see Figure 4.27.

Time propagation is performed using the laser field described in Section 4.3.3 with peak intensity $I = 2.5 \times 10^{13}$ W/cm^2. Within the adiabatic (Born-Oppenheimer) approximation the initial state is the Born-Oppenheimer ground state

$$\Psi(x,R,t=0) \; = \; \chi_{00}(R)\,\Phi_0(x;R) \quad . \tag{4.76}$$

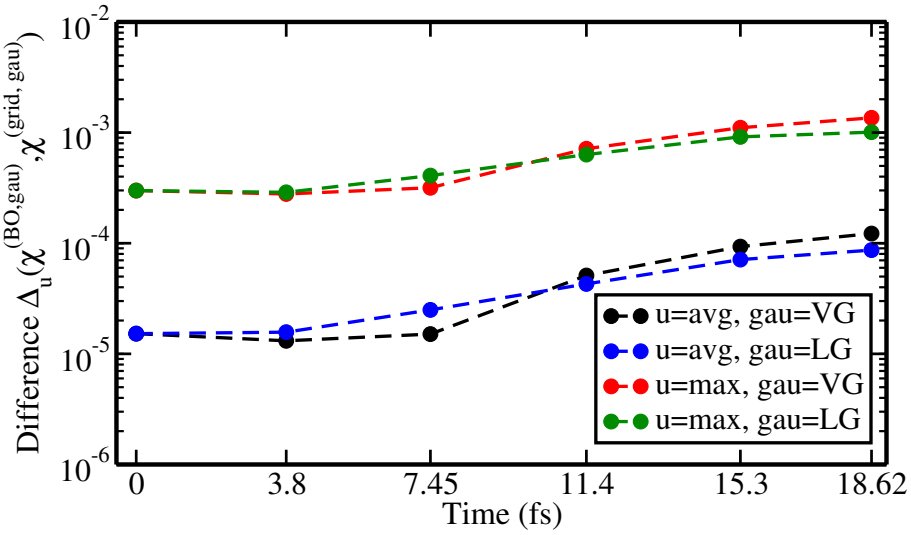

Figure 4.28: Absolute differences Δ_{avg} (Eq. (4.62)) and Δ_{max} (Eq. (4.63)) between nuclear probability densities obtained using the Born-Oppenheimer approximation (BO) vs. direct grid propagation (grid) for both length gauge (LG) and velocity gauge (VG). The peak intensity is $I = 2.5 \times 10^{13}$ W/cm^2.

This state is obtained by matrix diagonalization as described in Section 4.3.1. The time propagation including all electronic states (obtained by diagonalization) yields a nuclear probability density which is indistinguishable from the ones in Figure 4.24 on the scale of this graph. Figure 4.28 shows the maximum and average relative difference between the solution within the adiabatic (Born-Oppenheimer) approximation and the direct time propagation on the grid. Length gauge and velocity gauge behave similarly in this comparison. The overall behavior of the absolute differences is qualitatively similar to the behavior of the gauge dependence in Figure 4.26. Quantitatively the differences between the propagation types are almost an order of magnitude higher than for the gauge dependence. They remain below $\Delta_{\text{avg}} < 2 \times 10^{-4}$ and $\Delta_{\text{max}} < 2 \times 10^{-3}$. Thus, the observed dynamics are indeed generated by the laser field interaction $\mathbf{V}_{\text{int}}$ and the neglect of $\mathbf{B}$ seems to be a very good approximation for the investigated laser parameters.

A main advantage of using eigenstates to solve the TDSE is the possibility to restrict the number of eigenstates included in the time propagation to a smaller number $n_{\text{max}} < N_x$, see Section 3.5. In the following the convergence behavior with respect to n_{max} is checked. This is done on the example of the "ionization yield"

$$Y = \sum_{n \in \text{continuum}} ||\chi_n(R,t)||^2 = 1 - \sum_{n \in \text{bound}} ||\chi_n(R,t)||^2 \quad . \tag{4.77}$$

Note that for the laser field used here the resulting value Y cannot be interpreted

as a physical ionization yield since it is an unrealistic laser field not fulfilling the zero net force condition. Furthermore, the ionization yield is defined only after the laser field is over. In general eigenstate populations (and thus also the ionization yield Eq. (4.77)) are gauge dependent quantities during the laser field (page 149 in Ref. [65]).

The "ionization yield" for a basis where only P (in %) of the lowest electronic eigenstates of each symmetry are included in the time propagation is defined as $Y^{(P)}$. The relative error of the ionization yield within this basis is defined as

$$\epsilon(P) = \frac{\left| Y^{(P)} - Y^{(100\%)} \right|}{Y^{(100\%)}} \quad . \tag{4.78}$$

Figure 4.29 shows the error obtained in velocity gauge. The error does not strongly change with propagation time and is already far below $\epsilon = 10^{-2}$ when only $P = 40\%$ of the states are included. This accuracy is more than sufficient for typical plots of the ionization yield on a logarithmic plot. Including more states further reduces the error, for $P = 80\%$ it is below $\epsilon = 10^{-6}$. In contrast, the basis set restriction in length gauge, Figure 4.30, shows a much less systematic convergence behavior. The error strongly depends on the propagation time and a higher P can yield a larger error, especially for longer propagation times. Furthermore, for $P > 40\%$ the error decreases only very slowly with increasing P and stays above $\epsilon = 10^{-5}$ for $t \geq 11.4$ fs even for $P = 90\%$. This indicates that time propagation with a restricted number of eigenstates is significantly less stable when using length gauge[24], although for $P \geq 40\%$ the errors are also smaller than $\epsilon = 10^{-2}$. Length gauge ionization yields may thus be still "accurate enough".

4.3.5 Solution of the TDSE using Electronic Born-Oppenheimer Eigenstates: Full Solution

In order to solve the full TDSE, Eq. (4.66), the nonadiabatic coupling matrix elements $B_{mn}(R)$, Eq. (4.69), have to be calculated. From the R-grid perspective it seems natural to implement $\partial/\partial R = i\,\hat{\mathrm{p}}_R$ as Fourier derivative using the matrix representation of $\hat{\mathrm{p}}$, Eq. (3.10). Figure 4.31 shows selected coupling matrix elements $B_{mn}(R)$ obtained using the aforementioned Fourier derivative (derivative using Fourier transformation, FT). A very oscillatory and seemingly unphysical behavior is found which peaks at the discretization borders at $R = 0$ and $R = 15$ a.u. Clearly, even the diagonal transition matrix element

$$B_{00}(R) = \left\langle \Phi_0(R) \left| \frac{\partial}{\partial R} \right| \Phi_0(R) \right\rangle_x = \frac{1}{2}\frac{\partial}{\partial R}\left(\langle \Phi_0(R) \,|\, \Phi_0(R) \rangle_x \right) = 0 \tag{4.79}$$

[24] Similarly, a less stable behavior of length gauge compared to velocity gauge is observed for the restriction of angular momenta included three-dimensional time propagations, even for the Dirac equation [55].

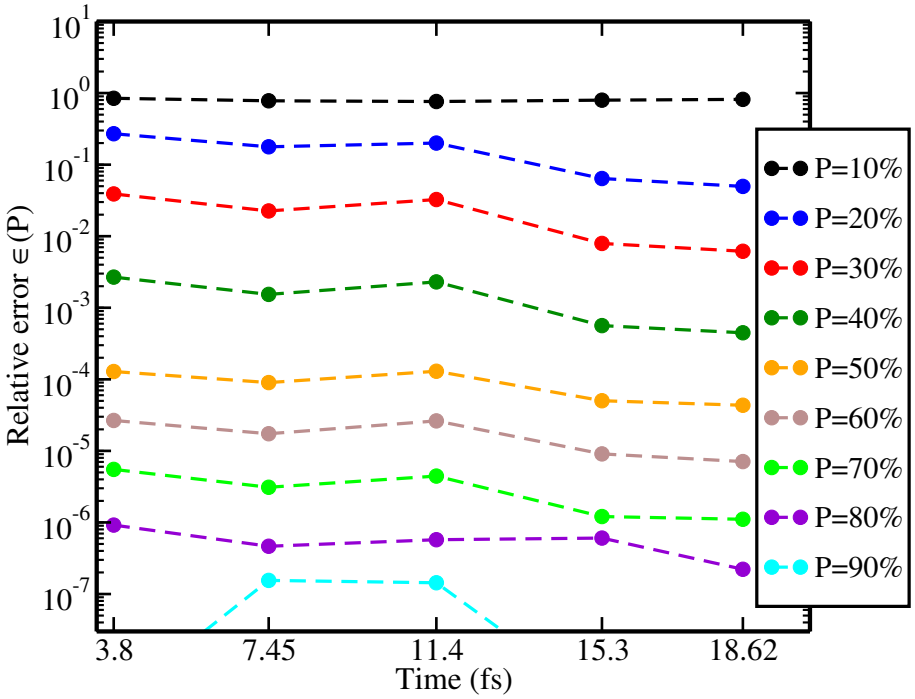

Figure 4.29: Relative error $\epsilon(P)$ of the ionization yield Y^P (Eq. (4.78)) calculated for a restricted basis in velocity gauge and for peak intensity $I = 2.5 \times 10^{13}$ W/cm^2.

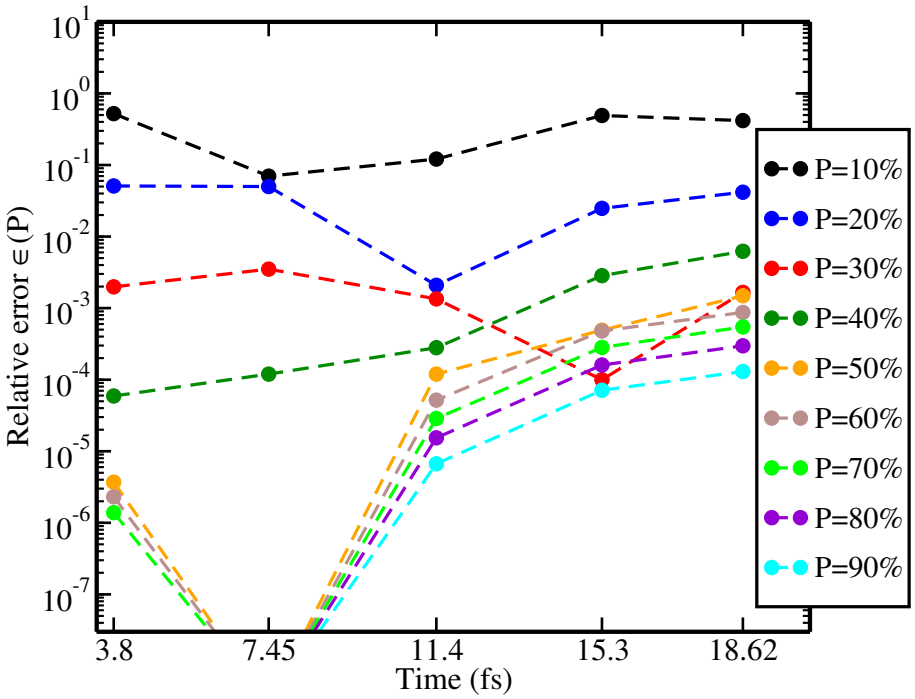

Figure 4.30: As Figure 4.29, but for length gauge.

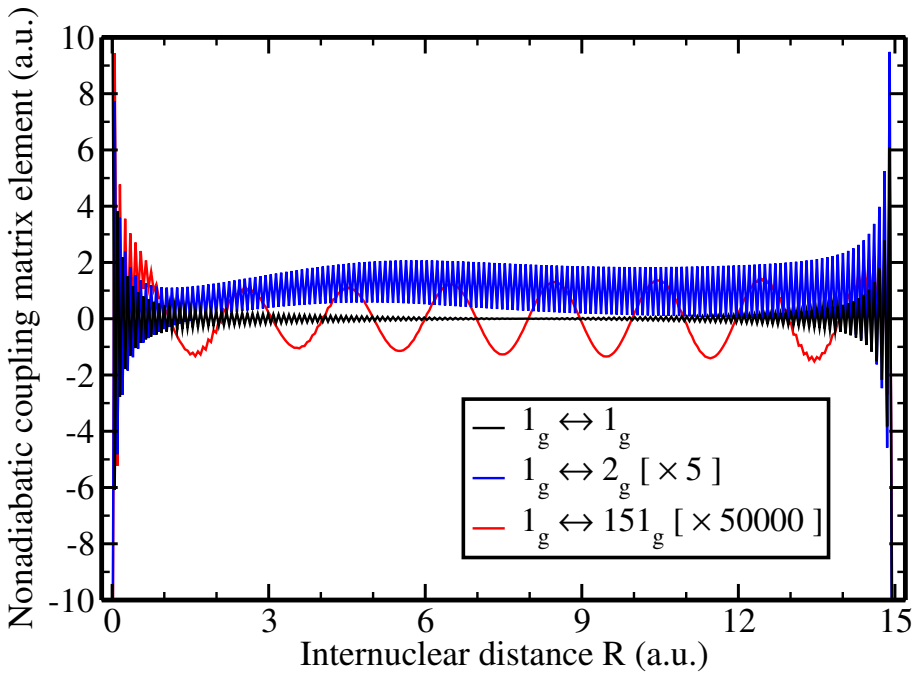

Figure 4.31: Nonadiabatic coupling matrix elements $B_{mn}(R)$ for selected transitions obtained using the Fourier derivative. Some elements have been scaled by a factor to be able to show all elements on a linear scale on the same graph, scaling factors are given inside the legend [in square brackets].

which should be zero because of the normalization $\langle \Phi_0(R) | \Phi_0(R) \rangle_x = 0$ is far from zero when the Fourier derivative is used. This behavior can be understood with Figure 4.32 which shows the electronic ground-state wave function $\Phi_0(x = 0; R)$ and its Fourier derivative $\frac{\partial}{\partial R}\Phi_0(x = 0; R)$. $\Phi_0(x = 0; R)$ is a smoothly decreasing function which has a maximum at $R = 0$ and is zero at $R = 15$ a.u. This is expected since the electron ground-state density is located around $x = 0$ (potential minimum) for $R = 0$. With increasing R the region where the electron is bound moves outwards ($x = \pm R/2$) and thus the density at the origin ($x = 0$) decreases. The Fourier derivative $\frac{\partial}{\partial R}\Phi_0(x = 0; R)$ shows a strongly oscillatory behavior similar to the nonadiabatic coupling matrix element $B_{00}(R)$. Considering the underlying periodic boundary conditions of the Fourier approach the wave function jumps from its maximum value to zero between its borders at $R = 0$ and $R = 15$ a.u. A Fourier expansion works well for smooth functions but introduces large oscillations when sharp edges occur (Gibbs' phenomenon). The sharp edge due to the periodic boundary conditions thus explains the strongly oscillatory, unphysical behavior of the Fourier derivative.

In order to avoid the Gibbs' phenomenon the coupling matrix elements $B_{mn}(R)$ are alternatively calculated using finite differences (FD). For each grid point R_k additional, very close grid points are generated and used to approximate the first

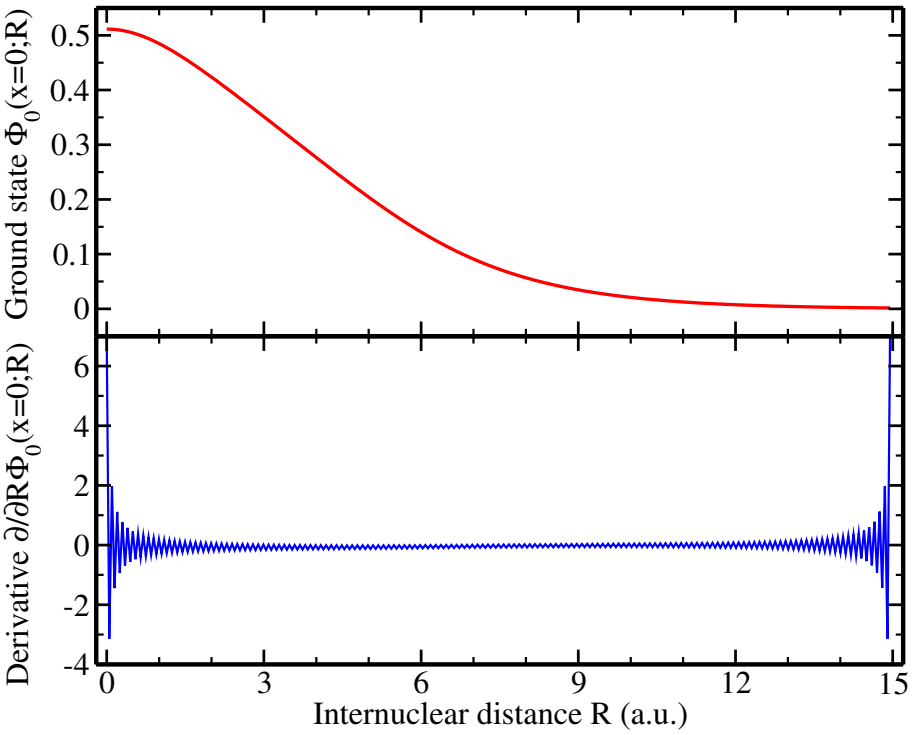

Figure 4.32: Electronic ground state wave function $\Phi_0(x;R)$ (top) and its Fourier derivative $\frac{\partial}{\partial R}\Phi_0(x;R)$ (bottom) at electronic coordinate $x = 0$ (origin).

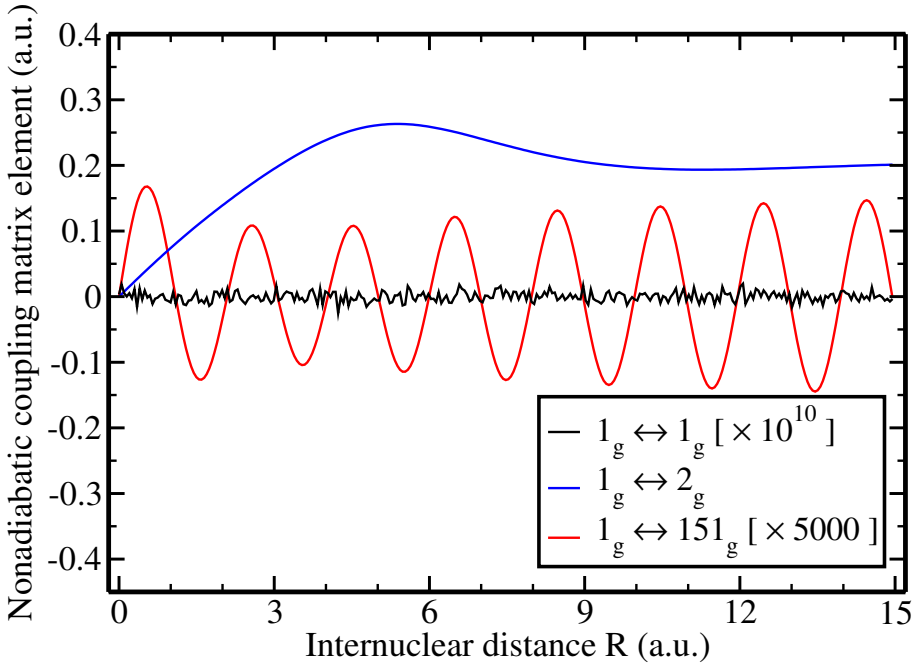

Figure 4.33: As Figure 4.31, but obtained using finite differences.

derivative $\partial/\partial R$. A variation of the finite-difference order and the spacing $\tilde{a}$ of the additional grid points showed that

$$f'(x) \approx \frac{1}{\tilde{a}}\left(\frac{1}{280}f(x-4\tilde{a}) - \frac{4}{105}f(x-3\tilde{a}) + \frac{1}{5}f(x-2\tilde{a}) - \frac{4}{5}f(x-\tilde{a}) + \frac{4}{5}f(x+\tilde{a}) - \frac{1}{5}f(x+2\tilde{a}) + \frac{4}{105}f(x+3\tilde{a}) - \frac{1}{280}f(x+4\tilde{a})\right) \quad (4.80)$$

with $\tilde{a} = 10^{-4}$ a.u. yields very stable matrix elements $B_{mn}(R)$ and is thus used in the following. The nonadiabatic coupling matrix elements obtained using finite differences are shown in Figure 4.33. They are now very smooth functions of R (similar to the dipole matrix elements) and the diagonal coupling $B_{00} \ll 10^{-11}$ a.u. is very close to the expected zero.

The ground state of the Hamiltonian (i.e. the initial state for the time propagation) is no longer given by the Born-Oppenheimer ground state, Eq. (4.76), when nonadiabatic couplings are considered. Thus, the ground state of the full Hamiltonian is found by imaginary time propagation as described in Section 4.3.2. The initial guess is the Born-Oppenheimer ground state. Imaginary time propagation is performed until a difference, Eq. (4.57), of 10^{-15} is reached. The TDSE including nonadiabatic couplings, Eq. (4.66), is then solved for parameters identical to the previous section. Figure 4.34 shows the absolute differences for different ways of solving Eq. (4.66) compared to the direct solution on the two-dimensional grid (Section 4.3.3). The full solution using finite differences to calculate nonadiabatic couplings agrees extremely

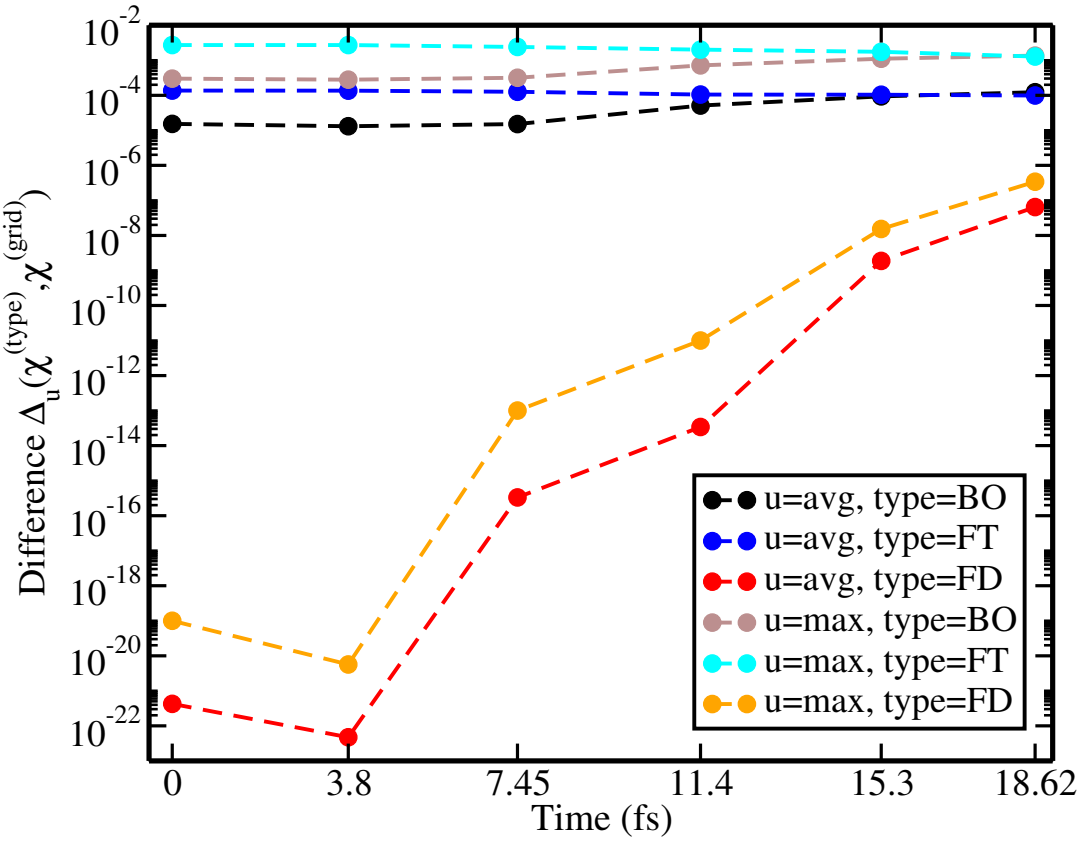

Figure 4.34: Absolute differences Δ_{avg} (Eq. (4.62)) and Δ_{max} (Eq. (4.63)) between nuclear probability densities obtained using direct grid propagation (grid) vs. different types of spectral propagation (type), namely the Born-Oppenheimer approximation (BO), full solution using Fourier derivatives (FT) and full solution using finite differences (FD). The peak intensity is $I = 2.5 \times 10^{13}$ W/cm^2 and velocity gauge is used.

well with the direct grid solution for short times ($\Delta < 10^{-19}$ until $t = 3.8$ fs). The difference then slowly increases with time, but remains $\Delta < 10^{-6}$ for $t = 18.62$ fs. When the nonadiabatic couplings are calculated using the (unphysical) Fourier derivative the differences are initially about one order of magnitude higher than for the Born-Oppenheimer approximation but remain constant with time. For $t = 18.62$ fs the difference Δ using the Fourier derivative for $\mathbf{B}$ thus becomes (surprisingly) even slightly smaller than for the Born-Oppenheimer approximation. Figure 4.35 shows the different nuclear probability densities at $t = 18.62$. Indeed, the result using the Fourier derivatives oscillates around the finite difference (=direct grid) result while the result within the Born-Oppenheimer approximation is vertically shifted. Thus, even though the Fourier derivative $\mathbf{B}$ matrix elements behave extremely unphysical, they indeed describe the correct nonadiabatic dynamics (but introduce an oscillatory behavior limiting the accuracy).

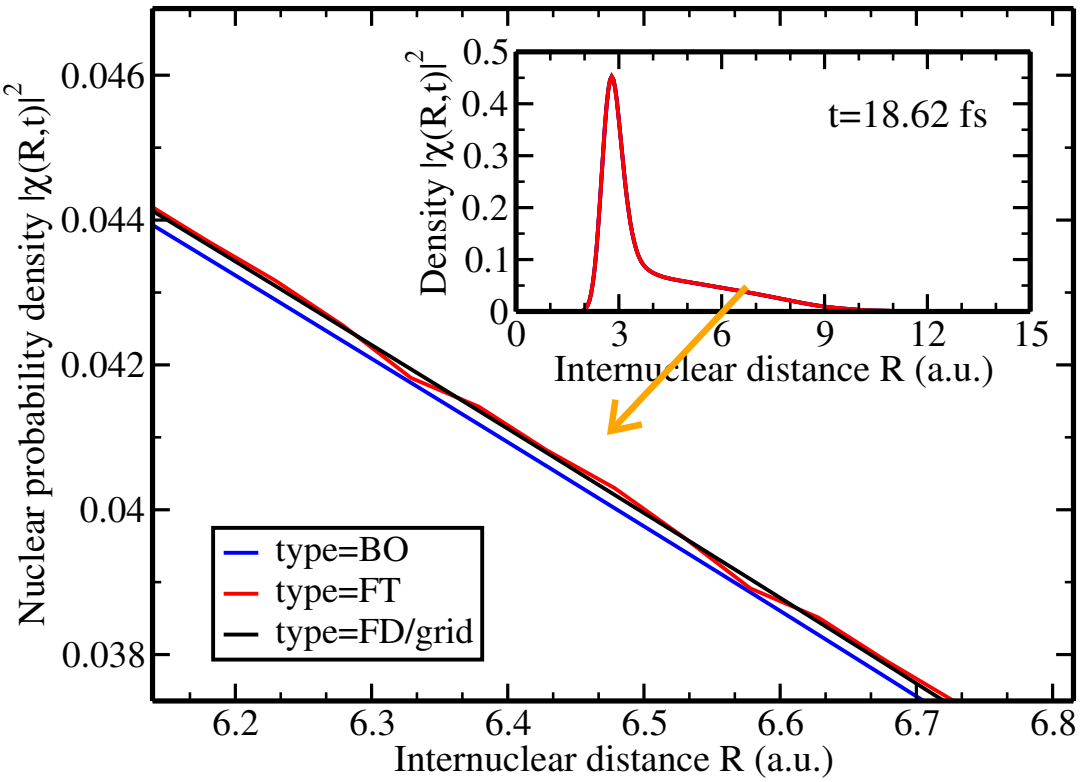

Figure 4.35: Nuclear probability density $|\chi(R,t)|^2$ at $t = 18.62$ fs for $I = 2.5 \times 10^{13}$ W/cm^2, velocity gauge and different TDSE solution types. Shown is the Born-Oppenheimer approximation (BO) and the full TDSE solution using the Fourier derivative (FT) or finite differences (FD, identical to the direct grid solution on this scale) for the calculation of $\mathbf{B}$.

4.3.6 Conclusions

Different techniques to find the ground state of a "complicated" Hamiltonian (imaginary time propagation vs. matrix diagonalization) and solving the TDSE (direct propagation on a grid vs. expansion in electronic eigenstates) have been compared. For the imaginary time propagation setting not only a relative, but also a proper absolute tolerance turned out to be very important to obtain an accurate ground state. The direct time propagation on the grid (using an adaptive step size and the matrix-algorithm matrices) nicely reproduced the *exact nuclear wave function density* of Ref. [56]. When comparing the direct grid propagation to the adiabatic (Born-Oppenheimer) approximation very good agreement was found. When restricting the number of electronic states in the time propagation velocity-gauge ionization yields turned out to behave much more stable than the one in length gauge. After nonadiabatic couplings calculated by finite differences have been included in the time propagation perfect agreement was found compared to the direct grid propagation. If the Fourier derivative is used to calculate nonadiabatic coupling matrix elements, however, unwanted oscillations are introduced. This leads to a significantly less stable behavior but seemingly still the correct nonadiabatic dynamics, especially when compared to the Born-Oppenheimer approximation. Due to its disadvantages, however, the Fourier derivative should be avoided for the calculation of nonadiabatic coupling matrices. The findings made in this section are essential for the following where a method to study the correlated (6+1)-dimensional electronic-vibrational motion of H_2 is developed.

4.4 Fully Correlated Electronic and Vibrational Motions: Molecular Hydrogen

In Section 4.2 the ionization behavior of H_2 has been studied in detail by solving the TDSE at (multiple) fixed internuclear distances R using the spectral ansatz with six-dimensional electronic eigenstates. Specifically, the breakdown of the fixed-nuclei approximation (FNA TDSE) in the perturbative multiphoton regime reported in [79, 81, 82] has been studied in Section 4.2.2 up to the level of the frozen-nuclei approximation (FROZ TDSE). A satisfactorily good qualitative agreement to the correlated treatment of electronic and nuclear motion (FULL TDSE) reported in [79, 81, 82] was found already for the FROZ TDSE approximation and thus a simple R integration of the ionization yield. A strong R dependence of the ionization yield is caused by resonances which depend critically on electronic transition energies. These transition energies change with the internuclear distance R such that the main contribution to the ionization yield typically stems from resonances located at internuclear distances other than the equilibrium distance. The influence of the vibrational dynamics occurring during the laser field on the ionization behavior of H_2 remains, however, still unclear. These vibrational dynamics are expected to be very fast with a timescale in the order of 10 fs or even 1 fs (if many vibrational states are coherently populated by, e.g., ionization), see also Section 2.4.

Another breakdown of the FNA was observed in a very recent experiment [107]. Here, a pronounced difference in the ionization yields of the isotopes H_2 vs. D_2 was found. The effect agrees quantitatively to a previous prediction within the weak-field asymptotic theory (WFAT) [108]. The WFAT predicts the ionization yield ratio $\Gamma_{H_2}/\Gamma_{D_2}$ for static fields while the experiment was conducted for circularly polarized 800 nm laser field with duration 28 fs (FWHM). These rather long circularly polarized laser fields were chosen in the experiment in order to mimic the situation of a static field as close as possible. It was claimed recently that the "Born-Oppenheimer approximation" fails for small field strengths [156] in contrast to the WFAT. Meant is specifically the breakdown of using R-integrated ionization yields, i.e. the FROZ TDSE approximation. Clearly, a direct comparison to the FULL TDSE is desirable.

A novel method to study the ionization behavior of diatomic molecules within FULL TDSE is developed in the following. The basic idea of the newly developed approach is introduced in the next section in comparison to an existing implementation. In Section 4.4.2 the procedure to obtain six-dimensional electronic eigenstates depending smoothly on the internuclear distance R is described. The calculation of dipole and nonadiabatic coupling matrices using these states is described in Sections 4.4.3 and Section 4.4.4. The dipole matrix elements are used in Section 4.4.5 to solve the TDSE within the adiabatic (Born-Oppenheimer) approximations in direct comparison with Refs. [79, 81, 82]. This study is extended including nonadiabatic couplings in Section 4.4.6. Finally, the developed method is applied in Section 4.4.7 to study the recently measured isotope effect in the ionization of H_2 vs. D_2 [107, 108, 156].

4.4.1 Basic Idea of the Method

The six-dimensional electronic Born-Oppenheimer eigenstates $\Phi_n^{(2e)}$ from Section 3.3 can also be used as a basis to describe the seven-dimensional correlated electronic vibrational dynamics of H_2 exposed to laser fields. For this purpose the methods developed and tested in Section 4.3, especially Sections 4.3.4 and 4.3.5 are used. Therefore, the one-dimensional electronic model H_2^+ eigenstates are replaced by the six-dimensional electronic eigenstates $\Phi_n^{(2e)}$. The spectral ansatz is used for the electronic problem while the vibrational problem is directly discretized on a grid. The TDSE used here to describe H_2 differs from Section 4.3 by an additional centrifugal barrier, see Eq. (2.38) in Section 2.2. It reads in vector form

$$i\,\frac{\partial}{\partial t}\,\Psi \;=\; -\,\frac{1}{2\,\mu}\,\left(\,\frac{\boldsymbol{\partial}}{\boldsymbol{\partial R}}+\mathbf{B}(\,R\,)\right)^2\Psi \;+\;\left(\,\boldsymbol{\mathcal{E}}(\,R\,)\,+\,\frac{J(J+1)}{2\,\mu\,R^2}\;+\;\mathbf{V}_{\mathrm{int}}(\,R\,,\,t\,)\right)\Psi \tag{4.81}$$

with rotational quantum number J and reduced mass $\mu = M_A M_B/(M_A + M_B)$ ($= M/2$ with proton mass M for H_2). The velocity gauge (in dipole approximation) is used for $\mathbf{V}_{\mathrm{int}}(\,R\,,\,t\,)$ due to its faster convergence behavior and higher stability, see Section 4.3.4. Considering the scaling of the spectral vs. the grid ansatz, Section 3.7, the spectral ansatz is of big advantage for the six-dimensional electronic problem. If the configuration-interaction series is strongly restricted (especially if configurations describing double ionization are neglected as done in the following) the number of states n_{max} used for time propagation is much smaller than the number of B splines describing the whole six-dimensional space. Furthermore, neglecting highly energetic electronic continuum states reduces a possible stiffness of the TDSE (set of coupled first-order ordinary differential equations). For the one-dimensional vibrational motion, however, the linear scaling of the problem with respect to the number of grid points N_R is preferable compared to the quadratic n_{max}^2 scaling of the spectral ansatz. In general the number of vibrational states would not be much smaller than N_R. Furthermore, due to the larger nuclear mass, the vibrational energies are much smaller than the electronic ones and thus the energetically highest vibrational states do not introduce a significant stiffness to the TDSE. Due to the much better linear scaling of the grid ansatz for the vibrational motion each individual time propagation presented in the following could be performed on a single core of a standard computer.

A method using the spectral ansatz (with eigenstates obtained in a B spline basis) for both electrons and nuclei has been previously implemented and used in, e.g., [51, 79–92] requiring a supercomputer. Clearly, using a grid with linear N_R scaling instead of quadratic n_{max}^2 scaling is a key advantage of the method developed here. Furthermore, the prolate spheroidal coordinate system used for the description of H_2, Section 3.3, is much more efficient than the expansion in spherical coordinates used in [51, 79–92]. Particularly at large internuclear distances R a large number of angular momenta is required to properly describe the non-spherical behavior of the H_2 molecule (with electrons elongated along the internuclear axis). The prolate

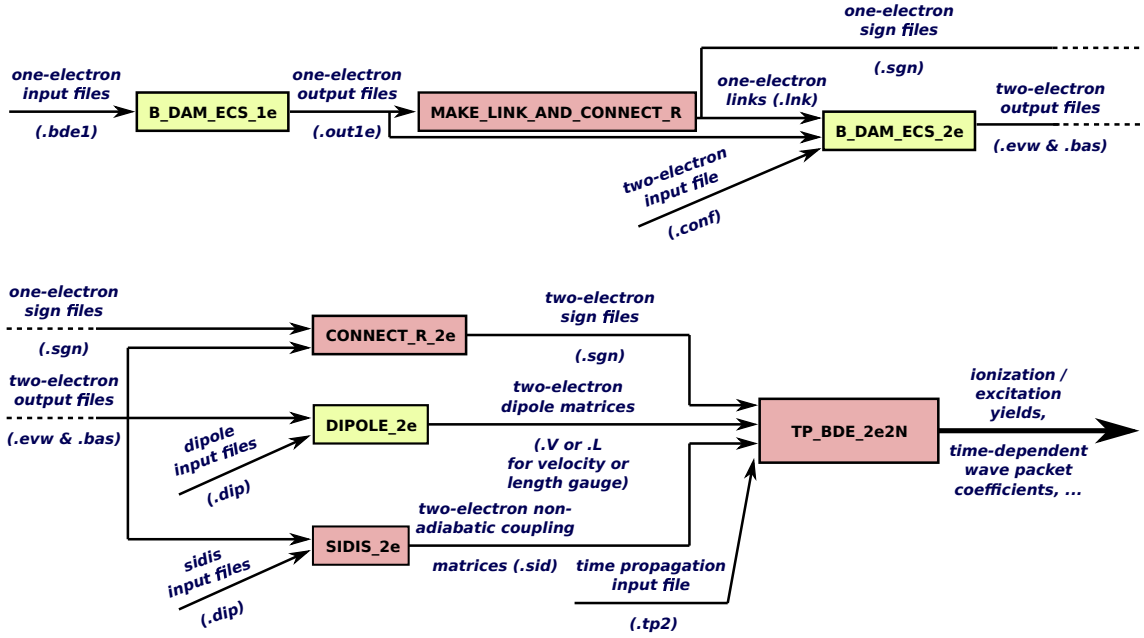

Figure 4.36: Flow diagram for the developed method. Program inputs and outputs and file extensions are given at the arrows. Newly developed programs are shown in red boxes while previously existing, unmodified programs (from [65]) are shown in yellow boxes.

spheroidal coordinate system additionally allows for a simple treatment of the $1/r$ Coulomb divergencies at the positions of the nuclei such that a much smaller basis set expansion compared to spherical coordinates is required [65]. Lastly, while for the eigenstate expansion in [51, 79–92] an energy grid for the electronic continuum is chosen, the electronic states used here are obtained within a single, consistent basis set for the whole range of internuclear distances R.

4.4.2 Following Electronic States Along the Internuclear Distance R

For the one-dimensional model potential the numerically obtained electronic states $\Phi_n(x\,;R)$ are "followed" along the internuclear distance R by comparing the two possible signs between neighboring R and choosing the one leading to a smaller difference, see Eq. (4.75) in Section 4.3.4. For each symmetry the states are sorted by energy and the non-crossing rule [157] ensures that indeed the correct states between neighboring R are compared to each other. In the one-dimensional case the non-crossing rule is well fulfilled since R is indeed the only parameter changing in the basis set. For three-dimensional H_2^+, on the other hand, the prolate spheroidal coordinates ξ and η, Eq. (3.26) in Section 3.3, explicitly depend on R. Thus, when fixing the box size $r_{\max} = R\xi_{\max}/2$ the coordinate system deforms with R and a

strict fulfillment of the non-crossing rule is not to be expected. Furthermore, the three-dimensional H_2^+ states $\Phi^{(1e)}(\xi, \eta, \phi; R)$ energetically approach each other much closer than the one-dimensional model states $\Phi_n(x; R)$, see Figure 4.21 in Section 4.3. A very small grid spacing ΔR is thus required for three-dimensional H_2^+ to resolve these very sharp avoided crossings (where the electronic eigenstates change their behavior). The solution of the time-independent Schrödinger equation separates according to $\Phi^{(1e)}(\xi, \eta, \phi; R) = \Xi(\xi)\,\Pi(\eta)\,e^{i m \phi}$ (see Section 3.3). The angular momentum projection on the internuclear axis m is a good quantum number by which states can be characterized. $\Xi(\xi)$ and $\Pi(\eta)$ are obtained using B splines. Numerical matrix diagonalization yields random signs for both $\Xi(\xi)$ and $\Pi(\eta)$. The newly implemented program MAKE_LINK_AND_CONNECT_R follows the electronic eigenstates $\Phi^{(1e)}(\xi, \eta, \phi; R)$ along R by comparing their B-spline coefficient vectors $c_n^{(\xi)}(R)$ and $c_n^{(\eta)}(R)$ as follows:

1. As a starting point (reference) the equilibrium internuclear distance $R = R_{\text{eq}}$ is chosen. States are then followed from R_{eq} to R_{N_R} and afterwards from R_{eq} to R_1 in steps ΔR.

2. For each state n at R_k (reference for which the signs of the electronic states have already been found) the corresponding state m at $R_{k\pm1}$ which minimizes the coefficient-vector differences between $c_n^{(\{\xi,\eta\})}(R_k)$ and $c_m^{(\{\xi,\eta\})}(R_{k\pm1})$ as well as the two signs for $c_n^{(\xi)}(R_{k\pm1})$ and $c_n^{(\eta)}(R_{k\pm1})$ leading to this minimum are found. Ideally each state n would now have a unique partner m. However, it occasionally occurs that for several states n_i at R_k the same partner state m at $R_{k\pm1}$ would minimize the difference.

3. To resolve this conflict (several n_i with same partner m) the state $n_{\min}$ which leads (in absolute numbers) to the minimal coefficient-vector difference to state m is found. The assignment $n_{\min} \to m$ is locked in. For the remaining states $m_j \neq m$ which don't have a partner yet other partner states $n_i \neq n_{\min}$ states which minimize the difference are found. Step 3 is repeated until no more conflicts appear and thus for each n a unique partner state m (with signs for $c_n^{(\xi)}(R_{k\pm1})$ and $c_n^{(\eta)}(R_{k\pm1})$ adapted correspondingly) is found.

The program MAKE_LINK_AND_CONNECT_R outputs a .SGN file for each internuclear distance R containing the order of the one-electron states and their B-spline coefficient-vector signs obtained from the previous procedure (see Figure 4.36 for the schematic program flow). Furthermore, a .LNK file is created for each internuclear distance R which only contains the order of the one-electron states. Similarly to the .LNK created by MAKE_LINK the one-electron basis is used together with an input file defining the configurations for configuration interaction to solve find two-electron eigenstates $\Phi_n^{(2e)}$ of H_2 using B_DAM_ECS_2E[25] (see Figure 4.36).

[25] When using the standard MAKE_LINK program the one-electron states are simply sorted by energy for each symmetry. If one uses the same configuration series specification for dif-

After all two-electron states $\Phi_n^{(2e)}$ have been calculated using B_DAM_ECS_2E the newly implemented program CONNECT_R_2E (see Figure 4.36) follows the two-electron states along R similarly to the one-electron case. The signs from the one-electron .SGN files are used and the configuration-interaction coefficient vectors $c_n^{(CI)}$ are compared with neighboring R (instead of $c_n^{(\xi)}$ and $c_n^{(\eta)}$ in the one-dimensional case). A final .SGN file is created which contains the order of the two-electron states at each R as well as their corresponding signs. In parallel to CONNECT_R_2E dipole matrix elements (or non-adiabatic coupling matrix elements) can be already calculated using the DIPOLE_2E (SIDIS_2E) programs[26], see Figure 4.36. For the time-propagation the output matrices created by these programs are read in together with the informations in the .SGN files. Thus, none of the programs implemented by Y. V. Vanne to calculate electronic states $\Phi_n^{(2e)}$ at fixed R (B_DAM_ECS_1E, B_DAM_ECS_2E, DIPOLE_2E) has been modified.

A variation of the grid spacing ΔR showed that (at least) $\Delta R = 0.001$ a.u. is required for the procedure to follow electronic states along R to become stable. Since this translates to 10000 electronic basis sets to cover an R-range of 10 a.u. the basis sets have to be necessarily much more restricted than the ones used for the fixed- and frozen-nuclei approximations described in Section 4.2.1. Two basis sets $\mathcal{A}$ and $\mathcal{B}$ have been calculated where basis $\mathcal{B}$ is a larger, more expensive basis set which is used to check the results obtained within basis $\mathcal{A}$ for convergence[27]. For basis $\mathcal{A}$ (calculated for $R = 0.01-9.999$ a.u.), a box size of $r_{\max} = 120$ a.u. with 130 B splines of order $k = 10$ were used along the ξ coordinate (knot distribution: geometric progression with $g = 1.06$ for the first 35 intervals and linear progression afterwards). 24 B splines of order 8 with a linear knot sequence were used along the η coordinate and highly oscillatory H_2^+ orbitals with more than 15 nodes along η were omitted in the CI calculation. The CI expansion consists of a very long configuration series where one electron occupies the H_2^+ ground-state $1\sigma_g$ while the other is occupying one of the remaining (bound or discretized continuum) H_2^+ eigenstates. This configuration series is mainly responsible to describe ionization. Additional CI configurations represent doubly excited situations (responsible for the description of correlation and doubly excited two-electron states) and include (one-electron) angular momentum

ferent R the corresponding one-electron basis behaves differently for each R. It is thus essential that the .LNK files created by MAKE_LINK_AND_CONNECT_R are used for B_DAM_ECS_2E, since this assures that the one-electron states behave as smooth as possible as a function of R.

[26] For basis $\mathcal{A}$ described in the following typically around 2 $(0-8)$ out of 1548 one-electron states are switched in order each step $\Delta R = 0.001$ a.u. by MAKE_LINK_AND_CONNECT_R. Afterwards, typically around 80 out of 1972 two-electron states are switched in order each step $\Delta R = 0.001$ a.u. by CONNECT_R_2E. This large number of re-orderings despite the small step size illustrates the importance of following the electronic states by their coefficients (rather than energy) for the success of this method.

[27] The total hard disk space used by basis $\mathcal{A}$ and $\mathcal{B}$ together is 7.4 TB. At the time of writing, the present approach is thus indeed quite costly with respect to disk space. However, since for the time propagation typically a much larger step size is used, the disk space usage can be greatly reduced by deleting all basis files of unused internuclear distances R.

projections up to $m = 4$. The obtained ground-state energy is almost identical to the one obtained with the basis set described in Section 4.2.1. Basis set $\mathcal{B}$ (calculated for $R = 0.001 - 15$ a.u.) differs from basis set $\mathcal{A}$ by the discretization along the ξ direction. Basis $\mathcal{B}$ uses a box size of $r_{\max} = 200$ a.u. and 200 B splines of order $k = 10$ were used along the ξ coordinate (knot distribution: geometric progression with $g = 1.06$ for the first 30 intervals and linear progression afterwards).

In the following sections the behavior of transition dipole- and non-adiabatic coupling matrix element obtained by this approach are discussed.

4.4.3 Behavior of the Transition Dipole Matrix Elements

The program TP_BDE_2E2N which will be presented step by step in the following sections reads in the dipole files created by the regular DIPOLE_2E program together with the .SGN files, see Figure 4.36. A RUN_MODE is specified as launch parameter which defines a specific task. RUN_MODE = 0 is used for this section. After reading all dipole and .SGN files it allows to select and store dipole matrix elements $D_{mn}(R)$, exactly as they would be used for time propagation, on the hard disk. Figure 4.37 shows the transition-dipole elements in length gauge between the $1^1\Sigma_g^+$ ground state and the six energetically lowest lying bound states with $^1\Sigma_u^+$ symmetry. Comparing basis $\mathcal{A}$ with a basis yielding practically exact results for the lowest-lying bound states[28] yields good qualitative agreement, but visible quantitative differences. These differences are due to the restriction of the configuration series similarly to the deviation of the eigenenergies ([65], page 155-158). The agreement between dipole matrix elements obtained with the basis $\mathcal{A}$ and the exact results is on a similar level (or even slightly better) than in Fig. 2 of Ref. [81]. Interestingly, the zoomed in sector shows that the transitions $1^1\Sigma_g^+ \leftrightarrow 3^1\Sigma_u^+$ and $1^1\Sigma_g^+ \leftrightarrow 4^1\Sigma_u^+$ ($1^1\Sigma_g^+ \leftrightarrow 5^1\Sigma_u^+$ and $1^1\Sigma_g^+ \leftrightarrow 6^1\Sigma_u^+$) switch their behavior at around $R = 0.83 - 0.84$ a.u. (for basis $\mathcal{A}$) within a very small R range. This is the typical behavior at an avoided crossing. Indeed, the very small spacing $\Delta R = 0.001$ a.u. is required to resolve this crossing. Using a more accurate basis this transition is qualitatively identical but occurs around $R = 0.56 - 0.57$ a.u. It has been studied with a different method in Ref. [158].

Figure 4.38 shows dipole matrix elements $D_{mn}^{\mathrm{LG}}(R)$ involving electronic continuum states ($25^1\Sigma_u^+$ is the first discretized electronic continuum state of this symmetry). While the dipole matrix elements behave smoothly for significant R intervals, they also show some very sharp spikes. They are thus also influenced by very sharp avoided crossings (as already seen for the energetically lowest bound states). Absolute values of the dipole elements quickly decrease with increasing energy (or state number) separation between the states. Furthermore, overall larger absolute values are observed at larger internuclear distances R. At larger R the electronic states are further extended along the internuclear axis (z direction). Thus, a larger $|z|$

[28] Box size $r_{\max} = 120$ a.u., geometric progression with $g = 1.15$ and only 26 B splines along ξ. The configuration series is (almost) complete up to one-electron angular momenta $l = 5$ and thus very accurate H_2 bound states are found.

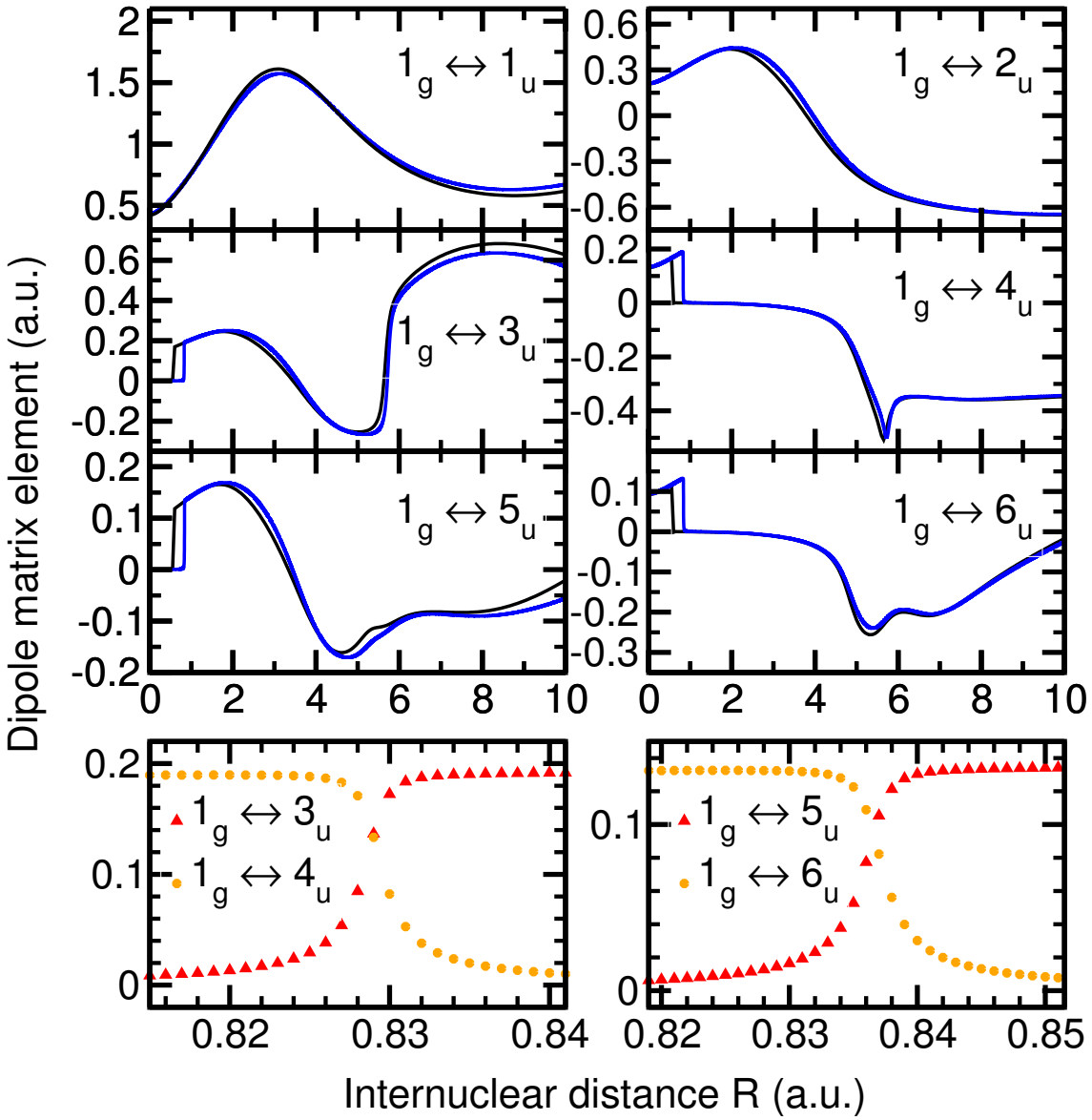

Figure 4.37: Dipole matrix elements $D_{1n}^{\mathrm{LG}}(R)$ between the $1^1\Sigma_g^+$ (abbreviated as 1_g) ground state of H_2 and the 6 energetically lowest states n_u with $^1\Sigma_u^+$ symmetry. The full blue lines in the upper part show the dipole moments obtained using basis $\mathcal{A}$ while the full black lines show a practically exact reference calculation (complete configuration interaction series). The lower part shows a zoomed in sector of dipole matrix elements obtained with basis $\mathcal{A}$.

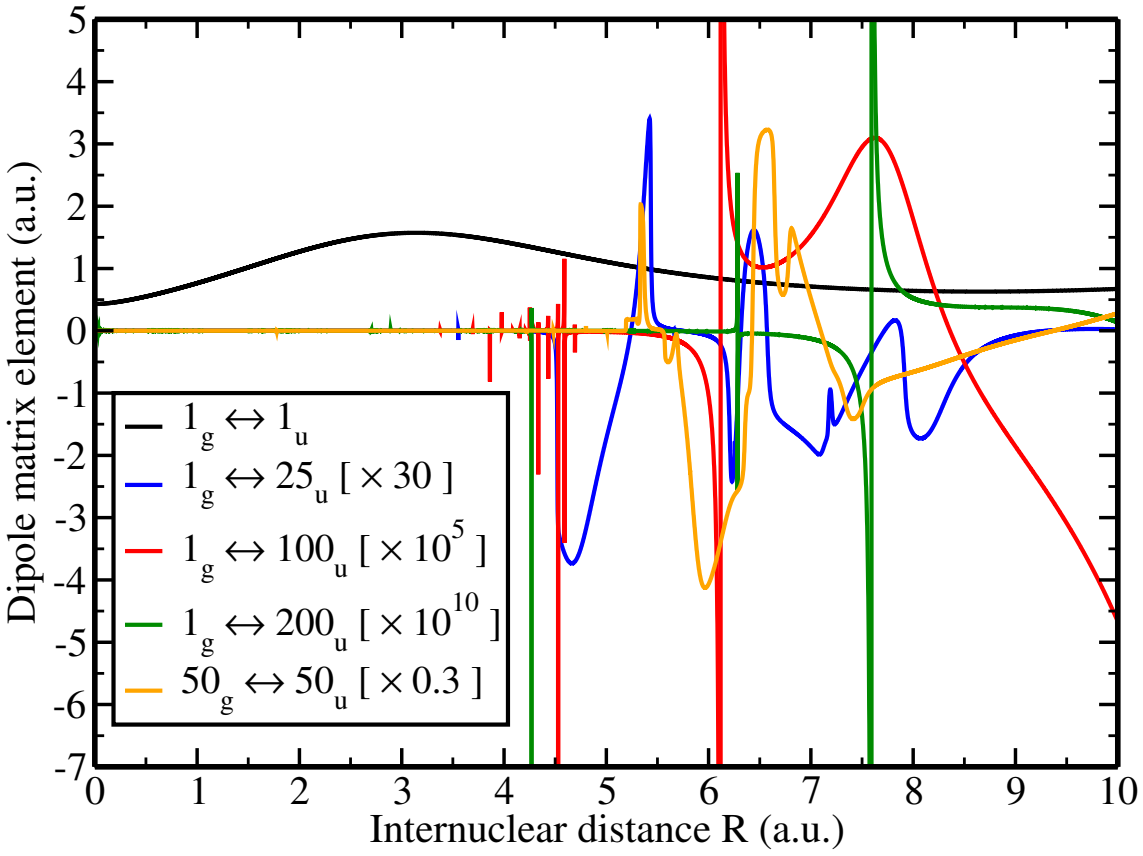

Figure 4.38: Dipole matrix elements $D^{\mathrm{LG}}_{mn}(R)$ between the states $m^1\Sigma^+_g$ (abbreviated as m_g) and $n^1\Sigma^+_u$ (abbreviated as n_u), selected transitions. Some elements have been scaled by a factor to be able to show all elements on a linear scale on the same graph, scaling factors are given inside the legend [in square brackets].

contributes to the transition dipole moments compared to smaller internuclear distances. Time propagations including vibrational motion will realistically require a larger grid spacing $\Delta R \gg 0.001$ a.u. such that the narrow features of $\mathbf{D}(R)$ seen here will not be resolved.

4.4.4 Sidis-Relation and Non-Adiabatic Coupling Matrices

In order to investigate non-adiabatic effects for diatomic molecules one requires the coupling matrix

$$B_{mn}(R) = \left\langle \Phi_m(R) \left| \frac{d}{dR} \right| \Phi_n(R) \right\rangle_{\underline{\mathbf{r}}} \quad . \tag{4.82}$$

For the diagonal elements

$$B_{nn}(R) = 0 \tag{4.83}$$

follows for real $\Phi_n(\underline{\mathbf{r}}; R)$ from the R derivative of the normalization of the electronic eigenstates $\langle \Phi_n(R) \,|\, \Phi_n(R) \rangle_{\underline{\mathbf{r}}} = 1$. It is possible to calculate $B_{mn}(R)$ using finite differences [159], for which (in the case of H_2 six dimensional) overlap integrals with a small variation of the internuclear distance R have to be calculated. This can be avoided for diatomic molecules using the Sidis relation

$$\begin{aligned} B_{mn}(R) = \frac{1}{R}\Bigg\{ & \frac{1}{2}(\mathcal{E}_m - \mathcal{E}_n) \left\langle \Phi_m(R) \middle| \sum_{i=1}^{n_e} \vec{r}_i{}^2 \middle| \Phi_n(R) \right\rangle_{\underline{\mathbf{r}}} \\ & + (\mathcal{E}_m - \mathcal{E}_n)^{-1} \left\langle \Phi_m(R) \middle| \hat{\mathrm{T}}_e \middle| \Phi_n(R) \right\rangle_{\underline{\mathbf{r}}} \Bigg\}, \end{aligned} \tag{4.84}$$

which has been derived analytically in [160] in prolate spheroidal coordinates[29]. Thus, the problem can be reduced to integrals with electronic one-particle operators which can be easily calculated (similar to the dipole matrix). Since $\sum \vec{r}_i{}^2$ and $\hat{\mathrm{T}}_e$ are symmetric with respect to all symmetry operations, the non-adiabatic couplings lead to electronic transitions only between states with the same symmetry, particularly $X\ {}^1\Sigma_g^+ \leftrightarrow X'\ {}^1\Sigma_g^+$ and $X\ {}^1\Sigma_u^+ \leftrightarrow X'\ {}^1\Sigma_u^+$. Expressed in prolate spheroidal coordinates one finds

$$\vec{r}^{\,2} = \frac{R^2}{4}\left(\xi^2 + \eta^2 - 1\right) \tag{4.85}$$

and

$$\begin{aligned} \frac{\hat{\mathrm{p}}^2}{2} = -\frac{1}{2}\Delta = -\frac{2}{R^2(\xi^2-\eta^2)} \Bigg(& \frac{\partial}{\partial\xi}\left[(\xi^2-1)\frac{\partial}{\partial\xi}\right] + \frac{\partial}{\partial\eta}\left[(1-\eta^2)\frac{\partial}{\partial\eta}\right] \\ & + \frac{\partial}{\partial\phi}\left[\frac{(\xi^2-\eta^2)}{(\xi^2-1)(1-\eta^2)}\frac{\partial}{\partial\phi}\right]\Bigg) \quad . \end{aligned} \tag{4.86}$$

The program SIDIS_2E (see Figure 4.36) implements the calculation of the non-adiabatic coupling matrix elements $B_{mn}(R)$ using Eqs. (4.84) to (4.86) in analogy to DIPOLE_2E. The obtained nonadiabatic coupling matrices (.SID files) are read in together with the .SGN files into TP_BDE_2E2N and are also stored for visualization using RUN_MODE = 0.

Figure 4.39 shows the nonadiabatic coupling matrices for a selection of transitions. For the transitions between ${}^1\Sigma_g^+$ states basis $\mathcal{A}$ agrees qualitatively very well to the very accurate basis (as in Section 4.4.3) while showing quantitative differences. Furthermore, the agreement to the couplings obtained in [161] is excellent keeping

[29] An alternative derivation of the Sidis relation which may allow for a generalization to more-than-diatomic molecules can be found in [159].

in mind that in this reference the couplings for $R < 1$ a.u. had to be obtained by interpolation. Thus, the switching of the behavior for the couplings $2^1\Sigma_g^+ \leftrightarrow 3^1\Sigma_g^+$ and $2^1\Sigma_g^+ \leftrightarrow 4^1\Sigma_g^+$ at $R = 0.93$ a.u. and the large peak in $3^1\Sigma_g^+ \leftrightarrow 4^1\Sigma_g^+$ were overlooked in [161]. The huge peak for the $3^1\Sigma_g^+ \leftrightarrow 4^1\Sigma_g^+$ couplings visible in the zoomed in section (together with the switching behavior with respect to $2^1\Sigma_g^+$) resembles a very narrow avoided crossing. Similar avoided crossings are seen for $5^1\Sigma_g^+ \leftrightarrow 6^1\Sigma_g^+$, $3^1\Sigma_u^+ \leftrightarrow 4^1\Sigma_u^+$ and $5^1\Sigma_u^+ \leftrightarrow 6^1\Sigma_u^+$ where especially the last two crossings were already observed in the behavior of the dipole matrix elements (Section 4.4.3). The coupling between $1^1\Sigma_u^+ \leftrightarrow 40^1\Sigma_u^+$ shows that bound-continuum couplings behave qualitatively very similar to the dipole matrix elements. Again, it will not be possible to resolve all narrow features of $\mathbf{B}(R)$ in a time propagation including vibrational motion where a larger spacing $\Delta R \gg 0.001$ a.u. is required.

4.4.5 Correlated Electronic-Vibrational Motion in the Multiphoton Regime: Adiabatic (Born-Oppenheimer) Approximation

In this section the breakdown of the FNA in the perturbative regime, Section 4.2.2, is further studied. In order to investigate the influence of vibrational dynamics during the laser field, the correlated treatment of electronic and vibrational motion (FULL TDSE) similarly to [79, 81, 82] is performed. As in Section 4.3.4 the TDSE, Eq. (4.81), is solved neglecting nonadiabatic couplings $\mathbf{B}(R) = 0$ (which were also neglected in [79, 81, 82]) and using $J = 1$ (as in [79, 81, 82]). The initial state is the Born-Oppenheimer ground state $\Psi(t = 0) = \chi_{1_g 0}(R)\, \Phi_{1_g}^{\mathrm{H_2}}(\xi_1, \eta_1, \phi_1, \xi_2, \eta_2, \phi_2; R)$. The solution on the FULL TDSE level is implemented in TP_BDE_2E2N as RUN_MODE = 2 (J is given as a run parameter). The ionization yield

$$Y_{\mathrm{FULL}} = \sum_{n \in \mathrm{continuum}} ||\chi_n(R, t = T)||^2 = 1 - \sum_{n \in \mathrm{bound}} ||\chi_n(R, t = T)||^2 \quad . \quad (4.87)$$

is obtained from the norm of the vibrational wave functions $\chi_n(R, t)$ after the laser field is over[30] ($t = T$). Due to the much higher computational demands compared to the FNA TDSE and FROZ TDSE approximations the FULL TDSE calculations are restricted to a parallel orientation of the polarization vector with respect to the internuclear axis. Unless noted otherwise, basis $\mathcal{A}$ and an energy cutoff $E_{\mathrm{cut}} = 1$ a.u. above the continuum threshold are used for time propagation (with an absolute and relative tolerance of 10^{-10}). This results in $N_g = 467$ electronic eigenstates with $^1\Sigma_g^+$ symmetry and $N_u = 461$ electronic eigenstates with $^1\Sigma_u^+$ symmetry (for each internuclear distance). The vibrational wave functions $\chi_n(R, t)$ are discretized

[30] This definition includes both dissociative and non-dissociative ionization. By projecting $\chi_n(R, T)$ on the vibrational Born-Oppenheimer eigenstates $\chi_{n\nu}(R)$ one can furthermore distinguish between the dissociative (vibrational continuum) and non-dissociative (vibrational bound state) contributions.

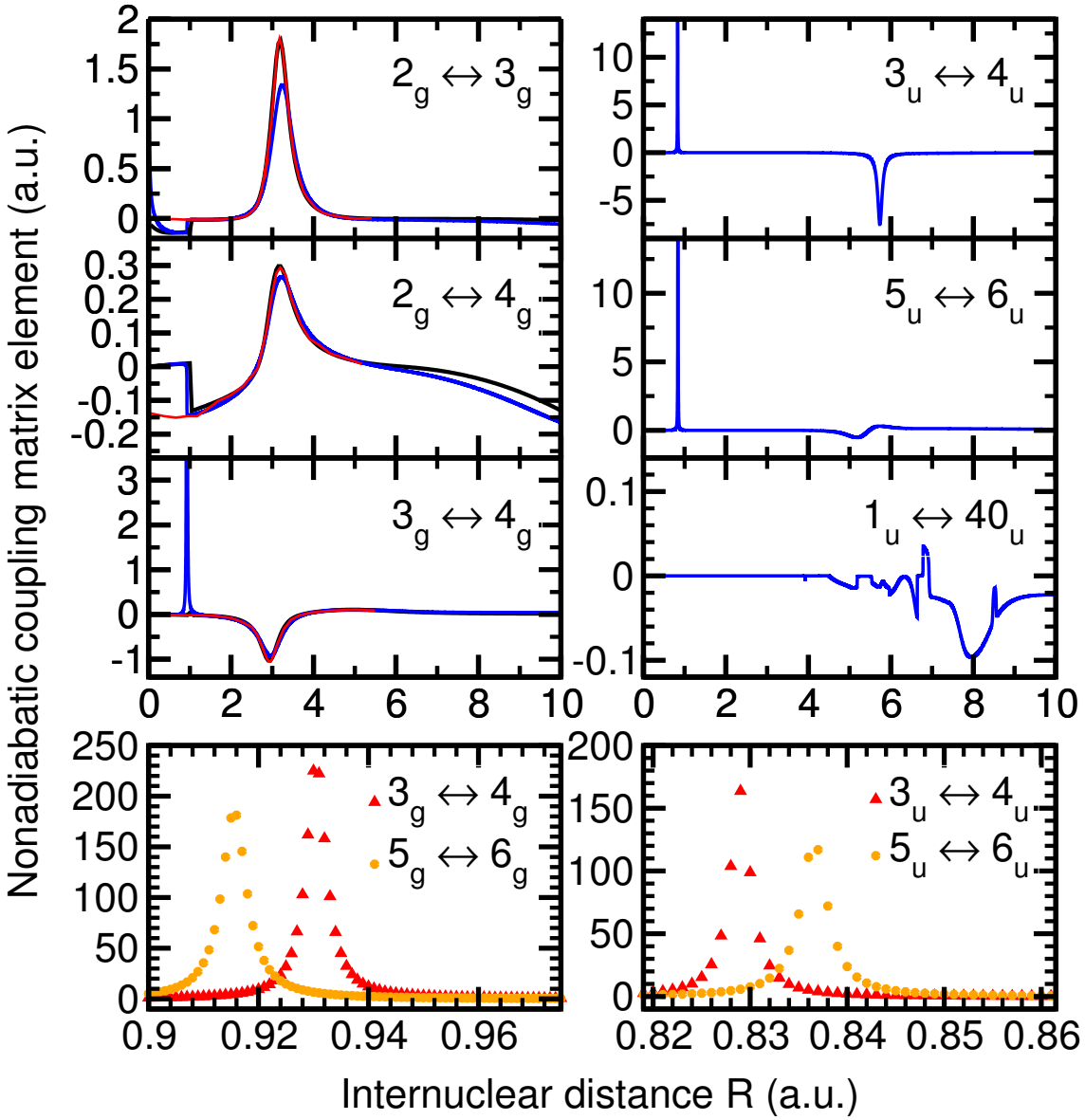

Figure 4.39: Nonadiabatic coupling matrix elements $B_{mn}(R)$ between states with ${}^1\Sigma_g^+$ symmetry (abbr. as n_g) or ${}^1\Sigma_u^+$ symmetry (abbr. as n_u). The full blue lines in the upper part show the dipole moments obtained using basis $\mathcal{A}$ while the full black lines show a practically exact reference calculation (complete configuration interaction series). The full red lines have been extracted from Ref. [161]. The lower part shows a zoomed in sector of nonadiabatic coupling matrix elements obtained with basis $\mathcal{A}$.

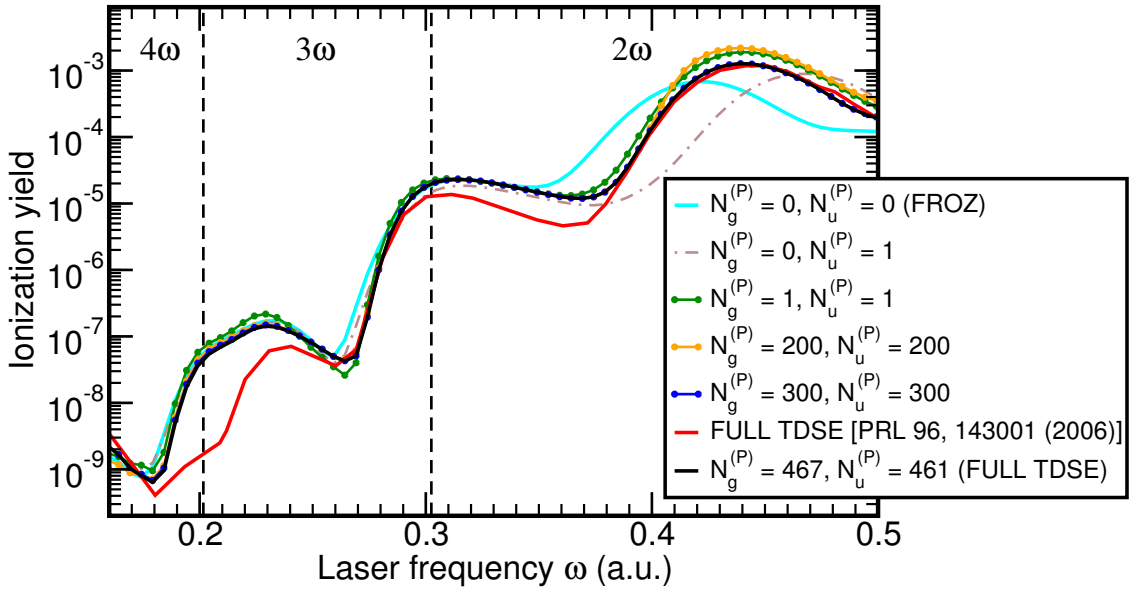

Figure 4.40: Ionization yields as a function of the laser frequency ω for parallel-aligned H_2 exposed to $T = 10$ fs, $I = 10^{12}$ W/cm^2 $\cos^2$-shaped laser fields. The dashed vertical lines indicate the borders between the two-, the three-, and the four-photon ionization regimes (2ω, 3ω, 4ω). Ionization yields are obtained with different numbers $N_g^{(P)}$ and $N_u^{(P)}$ of electronic states for which nuclear vibration ($\partial/\partial R$) is enabled. Furthermore, the FULL TDSE ionization yield from Ref. [79] is shown.

on a grid covering $R = 0.05 - 9.95$ a.u. with spacing $\Delta R = 0.05$ a.u., resulting in $N_R = 199$ grid points for each electronic state.

The FROZ TDSE approximation corresponds to setting $\frac{\partial}{\partial \boldsymbol{R}} = \mathbf{0}$ in the TDSE, Eq. (4.81). Vibrational motion can be subsequently turned on per electronic state by including the nuclear derivative $\partial/\partial R$ for the propagation of $\chi_n(R,t)$. Figure 4.40 shows the transition from FROZ TDSE to FULL TDSE. $N_g^{(P)}$ ($N_u^{(P)}$) denotes the number of the energetically lowest states with $^1\Sigma_g^+$ ($^1\Sigma_u^+$) symmetry for which the nuclear vibration ($\partial/\partial R$) is turned on, respectively[31]. For three- and four-photon ionization FROZ TDSE and FULL TDSE agree very well. Quantitative differences up to almost an order of magnitude are found mainly in the two-photon regime in the $1^1\Sigma_g^+ \rightarrow 1^1\Sigma_u^+ \rightarrow H_2^+(1\sigma_g)+e^-$ REMPI region around $\omega = 0.34-0.5$ a.u. Including the vibrational motion only in the two states involved in the REMPI process,$N_g^{(P)} = N_u^{(P)} = 1$, leads to an ionization yield which agrees almost quantitatively to the FULL TDSE ($N_g^{(P)} = 467$ and $N_u^{(P)} = 461$) solution. Including the nuclear vibration

[31] Even though vibrational motion for states higher than $N_g^{(P)}$ ($N_u^{(P)}$) is disabled, vibrational wave functions $\chi_n(R,t)$ with higher n (all up to $N_g = 467$ and $N_u = 461$) are changing in time because electronic transitions to these states occur due to the laser field.

only in the intermediate state $1^1\Sigma_u^+$ ($N_g^{(P)} = 0$ and $N_u^{(P)} = 1$), however, leads to a very different result. Thus, the correlated electronic-vibrational motion in both the $1^1\Sigma_g^+$ and $1^1\Sigma_u^+$ states leads to the main effect. Increasing the number of states with included nuclear vibration from $N_g^{(P)} = N_u^{(P)} = 1$ to $N_g^{(P)} = N_u^{(P)} = 200$ changes the ionization yield in the REMPI region only very slightly. The ionization yield in the REMPI region visibly decreases when increasing from $N_g^{(P)} = N_u^{(P)} = 200$ to $N_g^{(P)} = N_u^{(P)} = 300$ and afterwards stays unchanged until $N_g^{(P)} = 467$ and $N_u^{(P)} = 461$ (FULL TDSE). The region between $N_g^{(P)} = N_u^{(P)} = 200$ and $N_g^{(P)} = N_u^{(P)} = 300$ corresponds to discretized electronic continuum states with an energy $E \approx 0.4$ a.u. above the continuum threshold. Those states are energetically resonantly populated by ionization $1^1\Sigma_u^+ \rightarrow H_2^+(1\sigma_g) + e^-$ in the REMPI region. Nuclear vibration during the laser field changes the frequency required for a resonant (vertical) transition between electronic states. Thus, due to its extreme energy dependence, REMPI leads not only to a breakdown of the FNA TDSE due to the spread of the initial vibrational wave function (FROZ TDSE), but also because of nuclear vibration within electronic states excited by REMPI where even the effect of those in the electronic continuum is visible. In the two-photon REMPI region the ionization yields obtained within this work are on top of the result reported in [79, 81, 82]. For lower laser frequencies ω, however, quantitative differences up to an order of magnitude between the present ionization yields and the reported ones remain. As discussed in Section 4.2.2, however, there are notable differences already on the FNA TDSE level and thus quantitative agreement within FULL TDSE is not expected.

In order to check the convergence behavior the FULL TDSE calculations have additionally been performed with basis $\mathcal{B}$ with $E_{\text{cut}} = 1$ a.u. and $R = 0.025 - 14.975$ a.u. with spacing $\Delta R = 0.025$ a.u. as well as basis $\mathcal{A}$ as before but with $E_{\text{cut}} = 2$ a.u. Figure 4.41 shows the FULL TDSE ionization yields obtained with basis $\mathcal{A}$ ($E_{\text{cut}} = 1$ a.u. and 2 a.u.) and basis $\mathcal{B}$ as well as FROZ TDSE (basis $\mathcal{A}$, $E_{\text{cut}} = 1$ a.u.) and the FULL TDSE results reported in [81] for peak intensites 10^{12} W/cm^2, 10^{13} W/cm^2, and 2×10^{14} W/cm^2. Quantitative agreement for the FULL TDSE calculations performed with the improved basis sets compared to the smallest basis shown is excellent, especially for 10^{12} W/cm^2. For 10^{13} W/cm^2 and 2×10^{14} W/cm^2 tiny deviations are visible only on a closer look. Qualitatively the ionization yields for peak intensity 10^{13} W/cm^2 behave very similar to the ones at 10^{12} W/cm^2. For peak intensity 2×10^{14} W/cm^2 the ionization yield is close to saturation ($Y = 10^0 = 1$), but the qualitative behavior is still comparable to the lower intensities. The increased intensity mainly leads to an increase of the overall ionization yield by orders of magnitude. Quantitative differences from the present FULL TDSE results to the ones reported in [81] up to an order of magnitude are also similar for all intensities shown.

The convergence behavior of the excitation yield (calculated similarly to Eq. (4.87), but with summation over all excited states) is shown in Figure 4.42. It is similar to the convergence of the ionization yield discussed before. The agreement of the FULL TDSE excitation yield for peak intensity 10^{12} W/cm^2 to the one from [81] is even

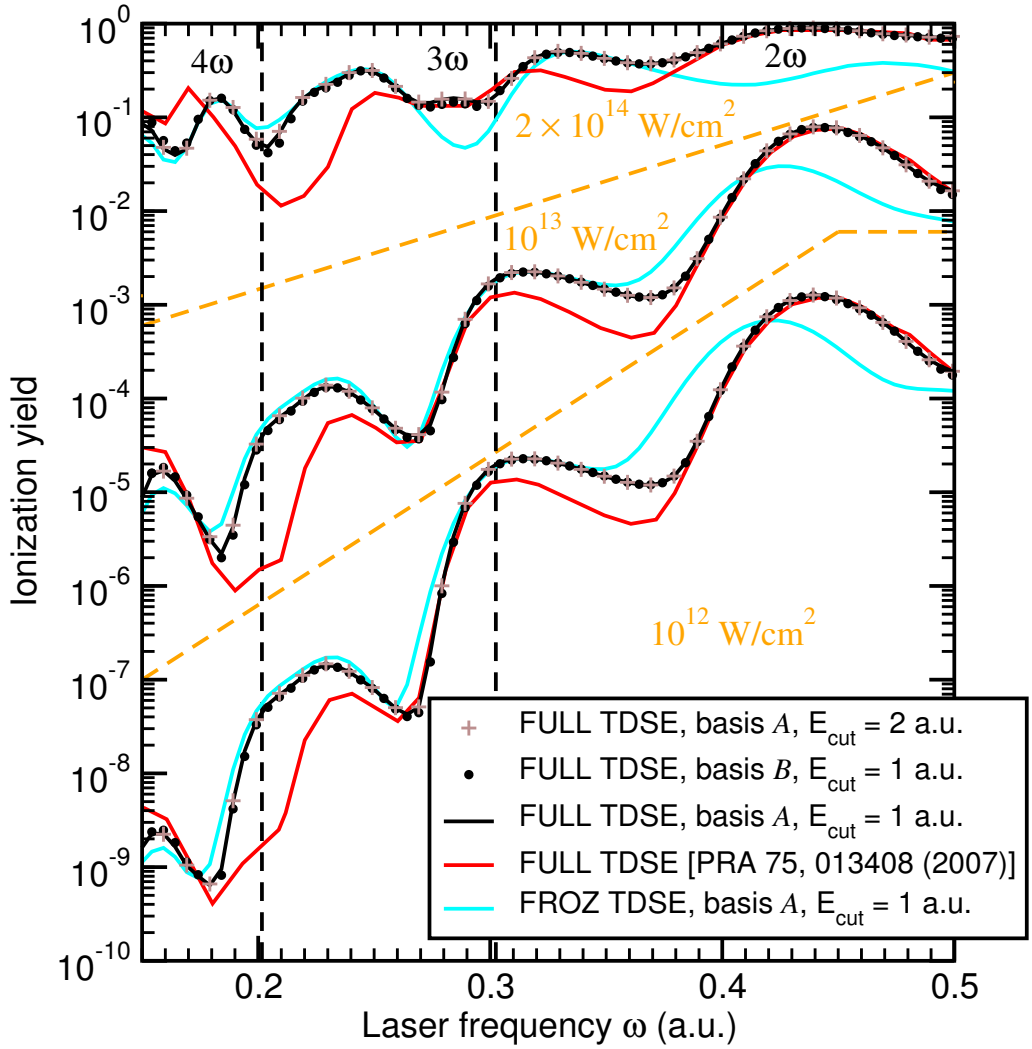

Figure 4.41: Ionization yields as a function of the laser frequency ω for parallel-aligned H_2 exposed to $T = 10$ fs $\cos^2$-shaped laser fields. The dashed orange lines separate the three shown peak intensities $I = 10^{12}$ W/cm^2, $I = 10^{13}$ W/cm^2, and $I = 2 \times 10^{14}$ W/cm^2. The dashed vertical lines indicate the borders between the two-, the three-, and the four-photon ionization regimes (2ω, 3ω, 4ω). FULL TDSE ionization yields computed with different basis sets as well as the FROZ TDSE ionization yields are shown. Furthermore, the FULL TDSE ionization yield from Ref. [81] is shown.

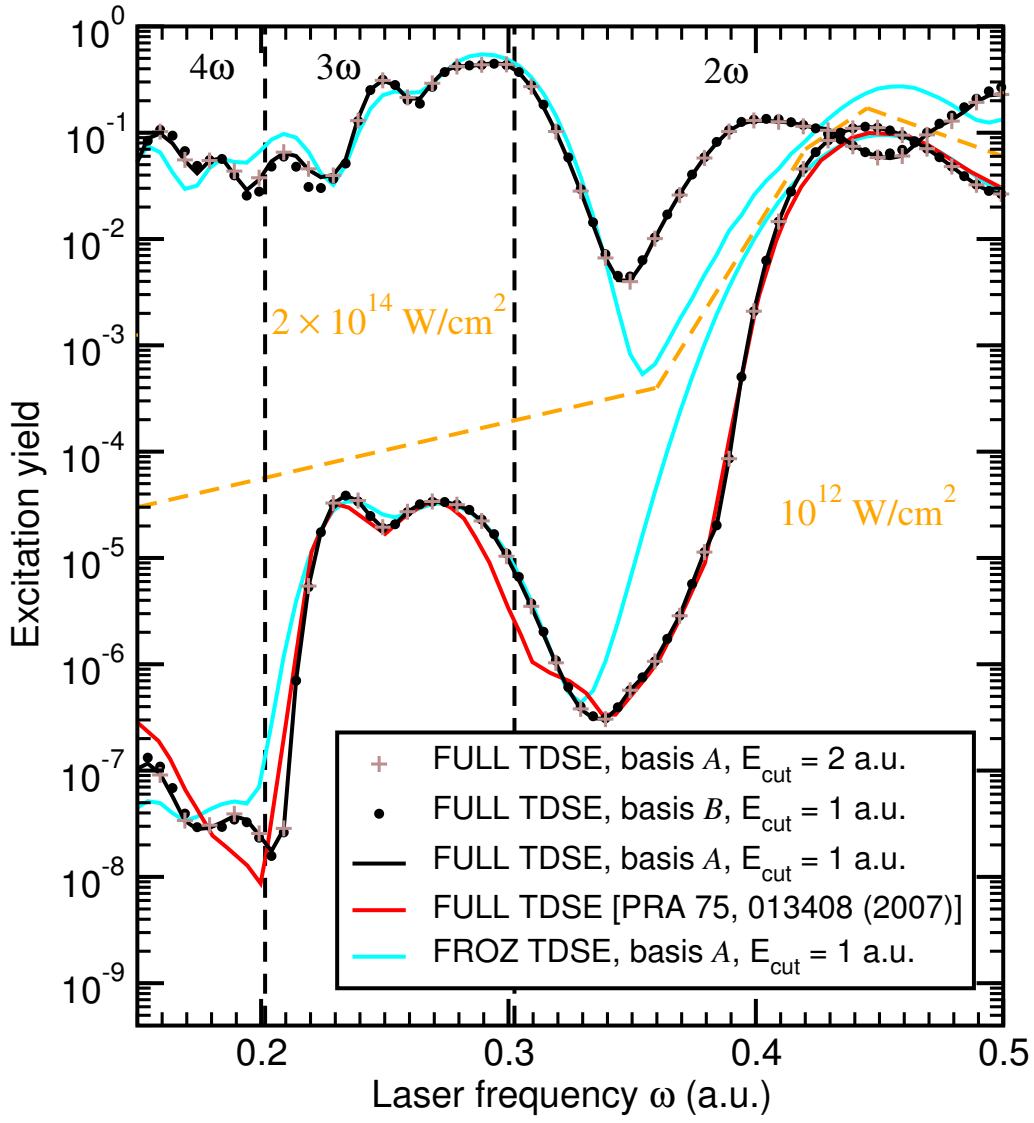

Figure 4.42: As Figure 4.41, but showing excitation yields and peak intensities $I = 10^{12}$ W/cm^2 and $I = 2 \times 10^{14}$ W/cm^2 only.

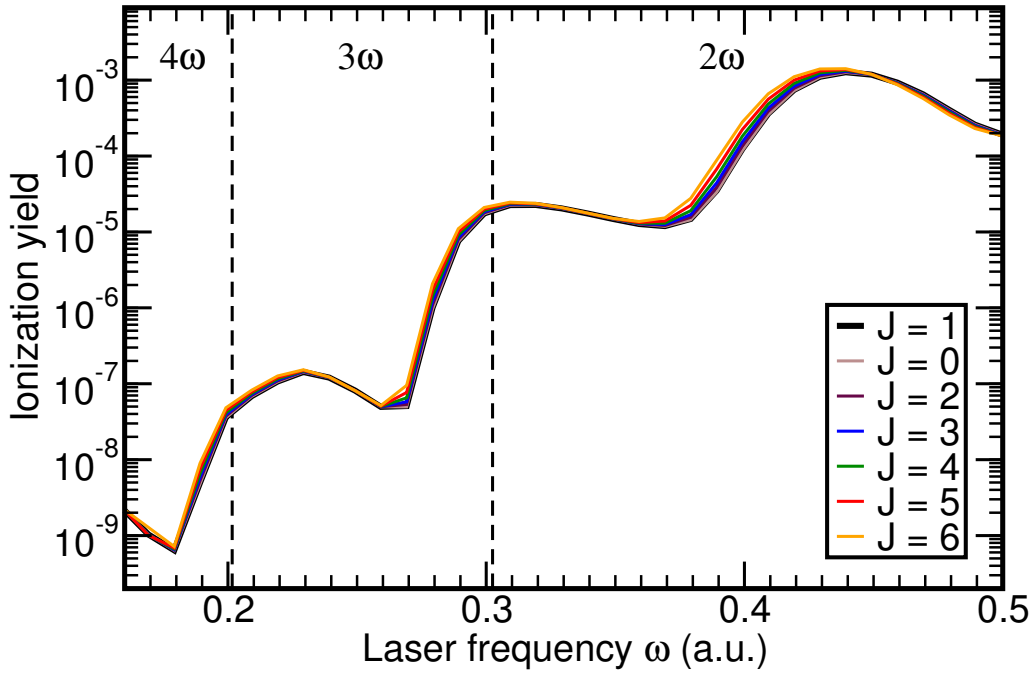

Figure 4.43: FULL TDSE ionization yields obtained for different rotational quantum numbers J leading to different centrifugal barriers $J(J+1)/(M\,R^2)$. Laser parameters are identical to Figure 4.40. The dashed vertical lines indicate the borders between the two-, the three-, and the four-photon ionization regimes (2ω, 3ω, 4ω).

better than for the ionization yield, i.e. differences remain well below half and order of magnitude. Interestingly, the excitation yield for peak intensity 10^{12} W/cm^2 at $\omega \approx 0.45$ a.u. (REMPI) even exceeds the excitation yield at 2×10^{14} W/cm^2 at the same frequency. Significant differences between FROZ TDSE and FULL TDSE excitation yields are again located at the REMPI frequency region $\omega = 0.34 - 0.5$ a.u. For lower frequencies both peak intensity 10^{12} W/cm^2 and 2×10^{14} W/cm^2 behave qualitatively quite similar. For these frequencies the excitation yield at intensity 2×10^{14} W/cm^2 is close to saturation.

For all results shown so far the rotational quantum number in the TDSE, Eq. (4.81), has been set to $J = 1$. Figure 4.43 shows the variation of the (fixed) rotational quantum number from $J = 0$ to $J = 6$. While there is practically no difference between $J = 0$ and $J = 1$, the ionization yields change more and more with increasing J. Of course, the rotational barrier $J(J+1)/(M\,R^2)$ grows quadratically with J. The barrier tends to displace the vibrational wave functions towards larger R. The largest dependency on J is observed in the REMPI frequency region $\omega = 0.34 - 0.5$ a.u.

4.4.6 Correlated Electronic-Vibrational Motion in the Multiphoton Regime: Full Solution

In this section the TDSE, Eq. (4.81), is solved including nonadiabatic couplings $\mathbf{B}(R)$ calculated using the Sidis relation (Section 4.4.4). This method is called the FULL+NA TDSE in the following. In order to calculate the initial state imaginary time propagation (starting from the Born-Oppenheimer ground state) is performed as described in Section 4.3.2. This imaginary time propagation is implemented in TP_BDE_2E2N as RUN_MODE = 4. All time propagations in this section are performed using basis $\mathcal{A}$ ($E_{\text{cut}} = 1$ a.u.) and an absolute and relative tolerance of 10^{-12}. Imaginary time propagation is performed in steps $\Delta t = 5$ a.u. until a difference

$$\left\| \Psi(t + \Delta t) - \Psi(t) \right\| = \sqrt{\sum_{n,k} \Big(\chi_n(R_k, t + \Delta t) - \chi_n(R_k, t) \Big)^2} \tag{4.88}$$

of 3×10^{-12} (i.e. slightly higher as the tolerance) is reached. After the ground state of the system is found using imaginary time propagation, real time propagation with laser field (which is implemented as RUN_MODE = 3) is performed.

Similarly to subsequently turning on nuclear vibration in the lowest electronic states by increasing $N_g^{(P)}$ ($N_u^{(P)}$) as described in the beginning of Section 4.4.5, also the nonadiabatic couplings can be subsequently turned on. $N_g^{(B)}$ ($N_u^{(B)}$) denotes the number of energetically lowest states with ${}^1\Sigma_g^+$ (${}^1\Sigma_u^+$) symmetry for which the nonadiabatic coupling elements $B_{mn}(R)$ are included (i.e. not set to zero), respectively[32]. Figure 4.44 shows the obtained ionization yields for $I = 10^{12}$ W/cm^2 pulses with $N_g^{(B)}$ and $N_u^{(B)}$ increasing from $N_g^{(B)} = N_u^{(B)} = 0$ (FULL TDSE) up to $N_g^{(B)} = N_u^{(B)} = 50$. Good agreement for all obtained ionization yields is found. Similarly to the observations in one dimension, Section 4.3.5, nonadiabatic couplings have practically no influence on the ionization behavior, especially when compared to other effects (like the centrifugal barrier dependency). Other observables may behave differently. It has to be kept in mind that Eq. (4.87) is only an approximate definition of the ionization yield when nonadiabatic couplings are included in the TDSE solution. For $N_g^{(B)} = N_u^{(B)} = 40$ and 50 the full ground state obtained by imaginary time propagation already includes a significant portion of electronic Born-Oppenheimer continuum states. Thus, Eq. (4.87) would imply ionization even if no laser field is applied. The field-free continuum state population Y_0 has to be substracted from the obtained ionization yield for $N_g^{(B)} = N_u^{(B)} = 40$ and 50 in order to find perfect agreement with the adiabatic approximation. For $N_g^{(B)} = N_u^{(B)} > 50$ stiffness problems are observed for the TDSE solution, i.e. time propagation with adaptive step size needs an enormous amount of function calls to reach the desired

[32] For FULL+NA TDSE nuclear vibration caused by $\partial/\partial R$ is included up to the maximum of $N_g^{(P)} = N_g = 467$) and $N_u^{(P)} = N_u = 461$.

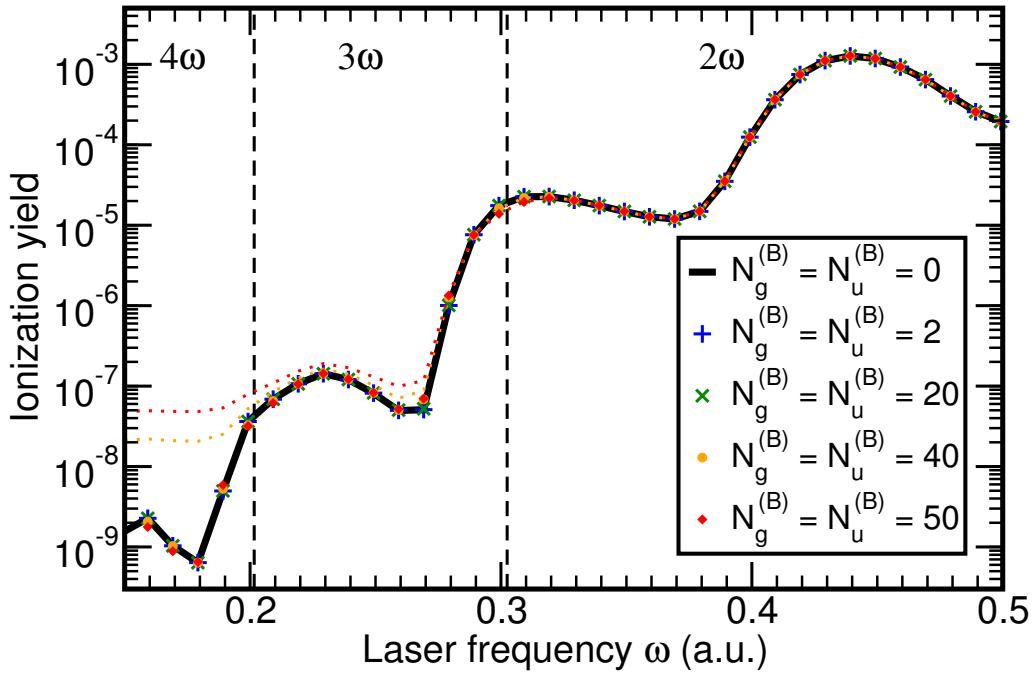

Figure 4.44: FULL+NA TDSE ionization yields obtained for different numbers $N_g^{(B)}$ and $N_u^{(B)}$ of electronic states for which nonadiabatic couplings are included. Laser parameters are identical to Figure 4.40. The dashed vertical lines indicate the borders between the two-, the three-, and the four-photon ionization regimes (2ω, 3ω, 4ω). For $N_g^{(B)} = N_u^{(B)} = 40$ and 50 colored dotted lines show the ionization yield obtained directly from Eq. (4.87) while the colored points show the ionization yield minus the continuum state population without field.

accuracy. A much smaller step size (around $\Delta R = 0.001$ a.u.) would be required to resolve the sharp features of the nonadiabatic couplings discussed before, see Section 4.4.4. Luckily, it is unlikely that nonadiabatic couplings for $N_g^{(B)} = N_u^{(B)} > 50$ strongly influence the ionization yield since those states are energetically already significantly deep in the continuum (the continuum threshold for basis $\mathcal{A}$ is located at $n_g^{\text{thres}} = 31$, $n_u^{\text{thres}} = 25$).

Figure 4.45 shows the FULL+NA TDSE ionization yield ($N_g^{(B)} = N_u^{(B)} = 50$) compared to the FULL TDSE ionization yield for the already previously investigated peak intensities 10^{12} W/cm^2, 10^{13} W/cm^2, and 2×10^{14} W/cm^2. Perfect agreement between FULL+NA TDSE and FULL TDSE is found for all intensities, i.e. higher intensities do not seem to increase nonadiabatic effects.

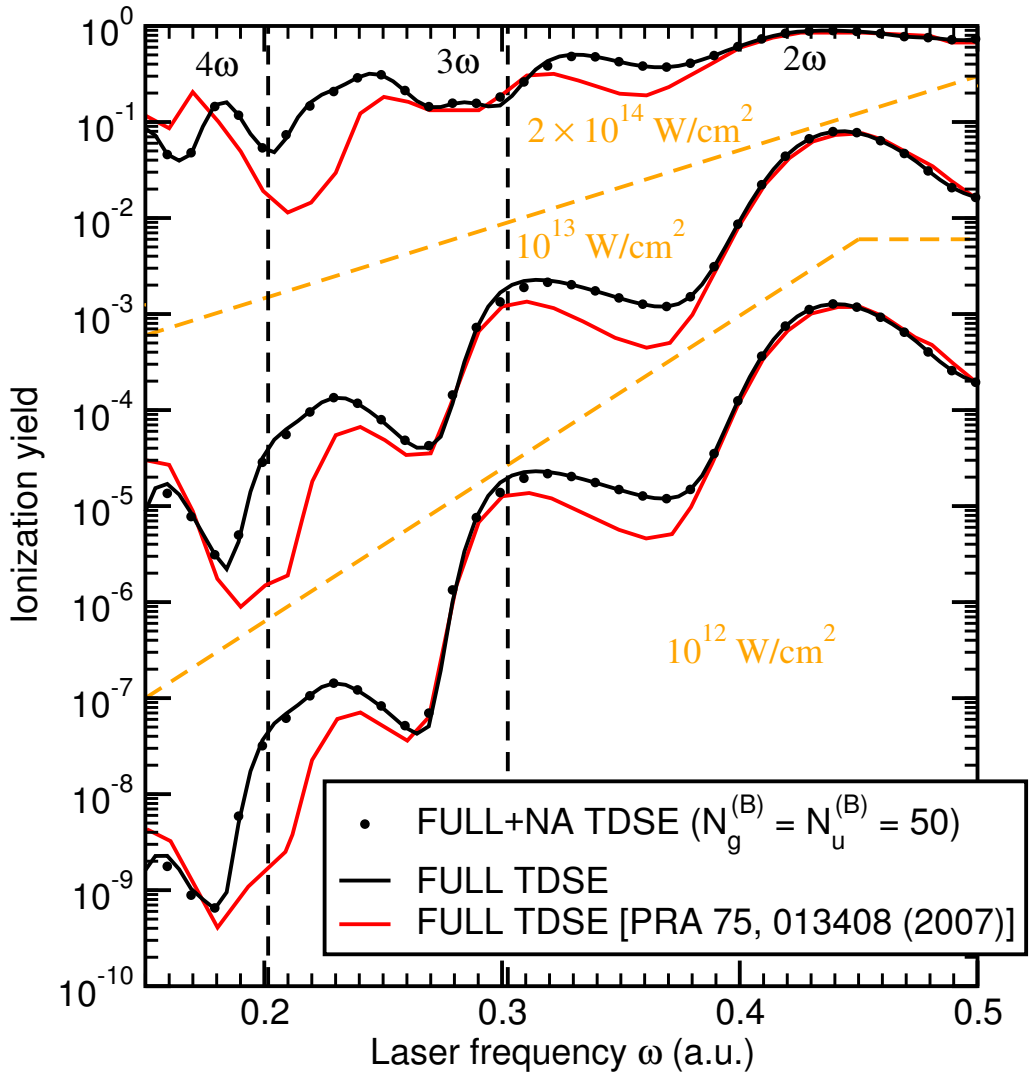

Figure 4.45: FULL TDSE vs. FULL+NA TDSE ($N_g^{(B)} = N_u^{(B)} = 50$) ionization yields as a function of the laser frequency ω for parallel-aligned H_2 exposed to $T = 10$ fs $\cos^2$-shaped laser fields. The dashed orange lines separate the three shown peak intensities $I = 10^{12}$ W/cm^2, $I = 10^{13}$ W/cm^2, and $I = 2 \times 10^{14}$ W/cm^2. The dashed vertical lines indicate the borders between the two-, the three-, and the four-photon ionization regimes (2ω, 3ω, 4ω). FULL TDSE shown for comparison are extracted from Ref. [81].

4.4.7 Isotope Dependence of the Ionization Yield: H_2 vs. D_2

The pronounced isotope effect (and thus breakdown of the FNA) in the ionization yields Y_{H_2}/Y_{D_2} [107, 108, 156] is investigated for short, linearly polarized laser fields for a parallel alignment. The newly developed approach as well as approximations previously discussed in this theses are used. While these laser fields do not necessarily yield quantitatively similar results compared to static fields, a qualitatively comparable isotope effect is expected. Furthermore, it is clearly also interesting to understand the isotope effect occurring for intense, ultrashort laser fields.

Figure 4.46 shows FULL TDSE ionization yields for H_2 exposed to 6 cycle, 800 nm laser fields with peak field strength $F_0 = 0.02 - 0.06$ a.u. (peak intensity $I = 1.4 \times 10^{13} - 1.26 \times 10^{14}$ W/cm^2). Results for different basis set parameters are shown in order to examine the convergence behavior. The variation of basis set parameters indicates that $E_{\text{cut}} = 2$ a.u., Basis $\mathcal{B}$ and an R grid with $\Delta R = 0.025$ a.u. with $R_{\text{max}} = 10$ a.u. are required for ionization yields which are stable enough for reliable ionization-yield ratios. These basis-set parameters are used in the following.

Figure 4.47 shows the ionization yield (or rate) ratios for various levels of approximations and in comparison with [107, 108]. $R-$integrated static ionization rates and time- and R-integrated ADK rates (obtained as described in Section 4.2.3) are very close to each other and seemingly match best to the experiment. It seems thus that the effect for static fields observed in [107, 108] is well explained by the different initial spreads of the vibrational wave function $\chi_0(R)$ of H_2 and D_2 and the strong (exponential) R dependence of the ionization rate on the internuclear distance as observed in Section 4.2.3. The small horizontal offset between static rates and time-integrated ADK rates is easily understood considering the time-dependence. For a laser field with peak field strength F_0 also intensities $\tilde{F} \lesssim F_0$ contribute to the total ionization yield. The effective field strength F of a laser field with peak value F_0 is thus slightly lower than F_0. The WFAT result for parallel orientation of the laser polarization with respect to the molecular axis ($\|$) is also in good agreement to the experiment. Note that for the perfect agreement between experiment and WFAT shown in Fig. 4a of Ref. [107] not the WFAT $\|$ result from [108] is shown, but the approximated formula $\Gamma_{H_2}/\Gamma_{D_2} \approx \exp\left([1 - 1/\sqrt{2}]0.0017/F^2\right)$ also reported in [108]. It was recently attempted to establish the connection between the WFAT results and the R-integrated static ionization rates [156]. While the R-integrated static rate ratio in [156] agrees perfectly to the result shown here, the WFAT result is (for no obvious reason) very different from the previously reported ones and even further away from the experiment[33]. For 6 cycle 800 nm laser pulses both FROZ TDSE and FC-ADK (obtained as described in Section 4.2.3) show a very similar ratio which is significantly lower as compared to the experiment and static rates / ADK rates. As discussed in Section 4.2.3 FC-ADK leads to less R-dependent (and much larger) ionization yields compared to ADK for 800 nm laser fields at small field strengths ($\gamma > 1$, multiphoton effects). For larger field strengths ($\gamma \lesssim 1$) FC-ADK approaches ADK as expected. Surprisingly, within the FULL TDSE treatment which not only

[33] It is, however, quite close to the FROZ TDSE result.

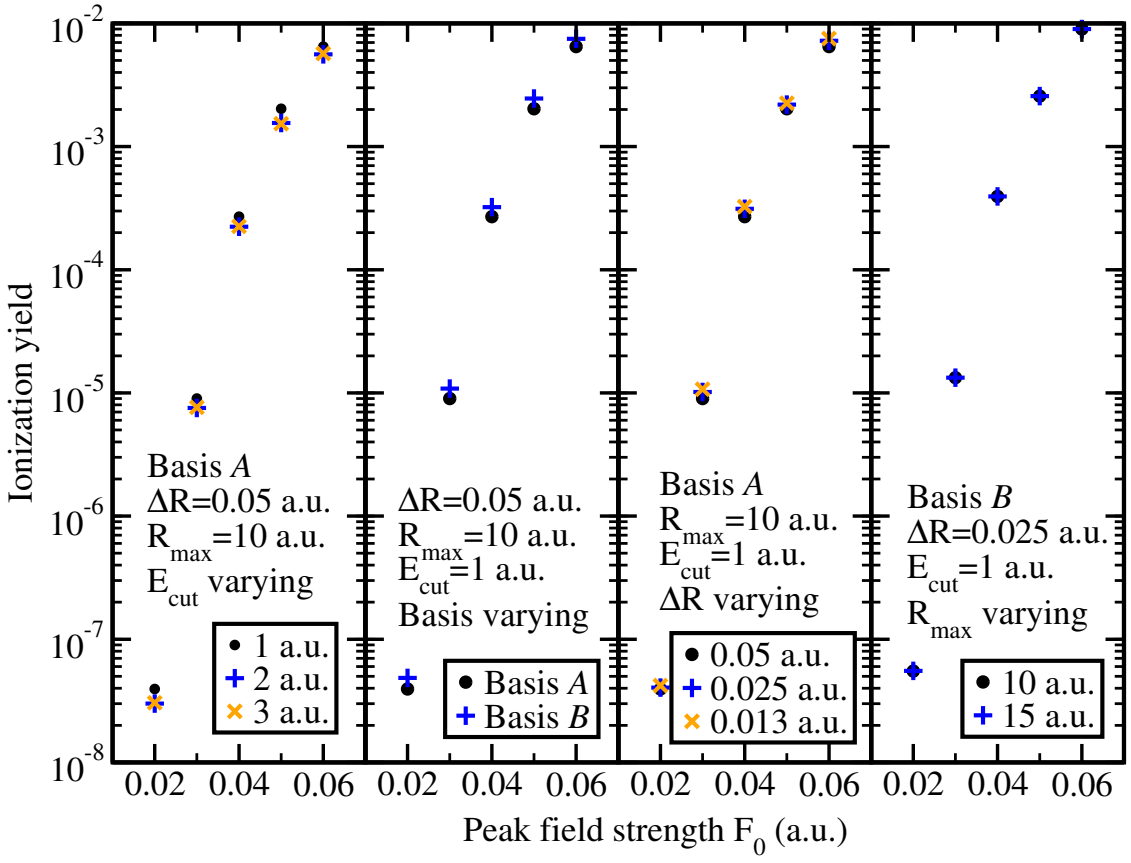

Figure 4.46: Variation of basis set parameters for FULL TDSE ionization yields of H_2 exposed to 6 cycle, 800 nm laser fields with different peak field strengths F_0. Within each subplot one basis set parameter is varying while the remaining ones are kept fixed.

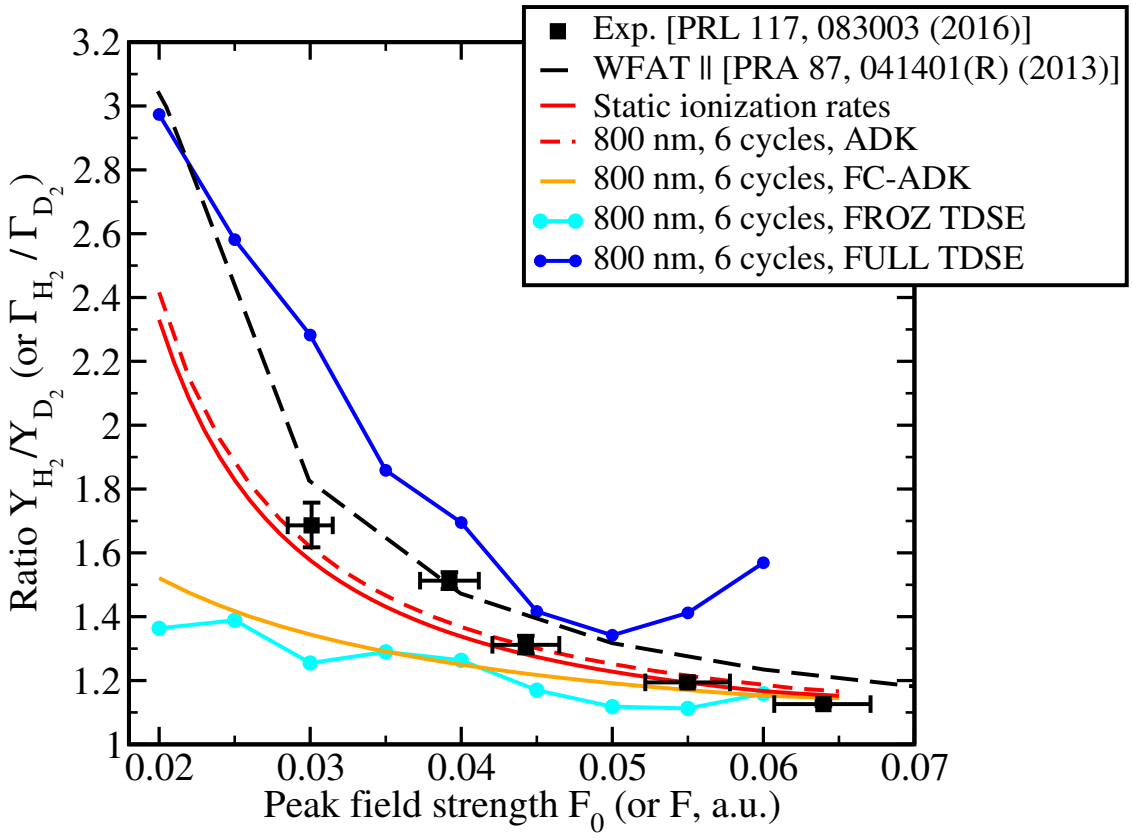

Figure 4.47: Ionization yield ratios Y_{H_2}/Y_{D_2} (rate ratios $\Gamma_{H_2}/\Gamma_{D_2}$ for static fields) as a function of the peak field strength F_0 (F for static fields) obtained with different approaches. The experimental ratio (circularly polarized fields) is extracted from Ref. [107] and the WFAT ratio (static fields) for a parallel orientation of the laser polarization with respect to the internuclear axis are extracted from Ref. [108].

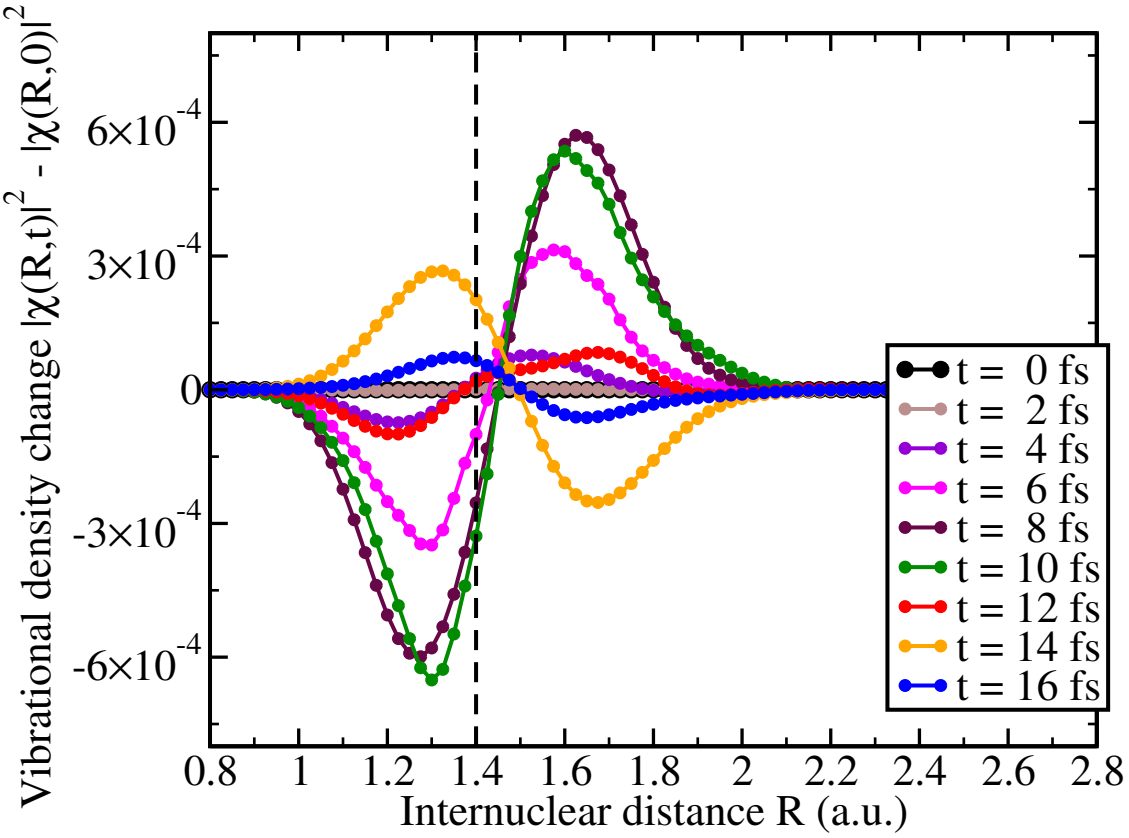

Figure 4.48: Snapshots of the vibrational probability density change $|\chi(R,t)|^2 - |\chi(R,t=0)|^2$ of H_2 exposed to a 6 cycle 800 nm laser field (field starts at $t = 0$ and ends at $t = 16$ fs) for peak field strength $F_0 = 0.02$ a.u.

includes the initial spread of the vibrational wave function but also the vibrational dynamics during the laser field, the ratio is significantly enhanced (instead of lowered) compared to the experiment. Thus, indeed a breakdown of the FROZ TDSE approximation as claimed in [156] is observed. The vibrational dynamics during the laser field causing this strongly increased isotope dependence are investigated in the following.

The vibrational probability density change $|\chi(R,t)|^2 - |\chi(R,t=0)|^2$ during the laser field is shown in Figure 4.48. Qualitatively, until the peak of the field around $t = 8$ fs, the probability density $|\chi(R,t)|^2$ is increased at internuclear distances larger than the equilibrium distance, $R \geq 1.4$ a.u. and decreased for smaller internuclear distances $R < 1.4$ a.u. compared to the initial one $|\chi(R,t=0)|^2$, i.e. the probability density moves towards larger R during the field. The largest difference is observed around the center of the field around $t = 8$ fs and then decreases again until the field is ends at $t = 16$ fs. From $t = 14$ fs to $t = 16$ fs the nuclear wave packet seemingly already returns backwards towards smaller internuclear distances R.

The H_2 ionization yield at $F_0 = 0.02$ a.u. as a function of the number of low-lying

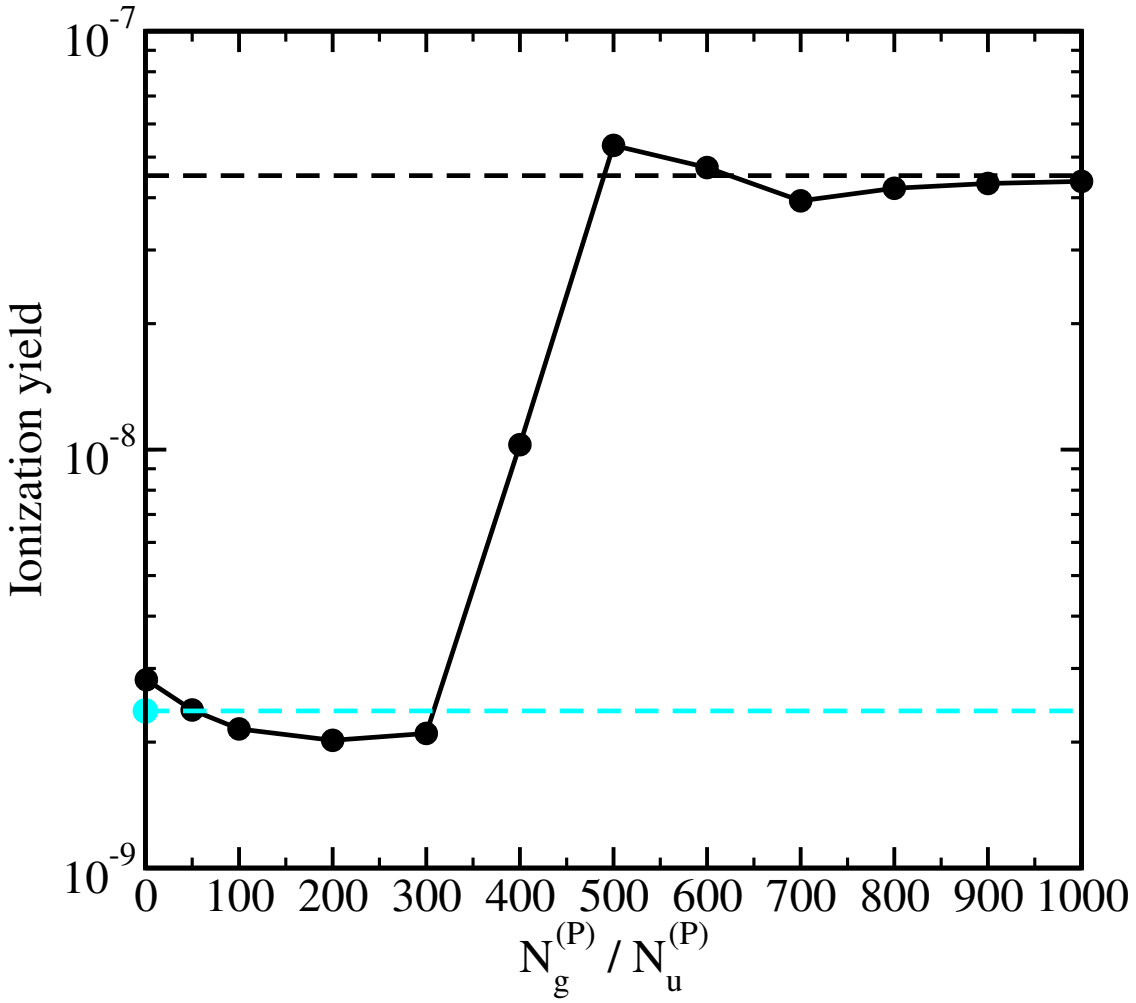

Figure 4.49: Ionization yield of H_2 exposed to a 6 cycle 800 nm laser field for peak field strength $F_0 = 0.02$ a.u. The full black with line with points shows ionization yields obtained with different numbers $N_g^{(P)} = N_u^{(P)}$ (first point $N_g^{(P)} = N_u^{(P)} = 1$) of electronic states for which nuclear vibration ($\partial/\partial R$) is enabled. The dashed black line shows the FULL TDSE result (nuclear vibration enabled for all electronic states) while the dashed cyan line (and cyan point) shows the FROZ TDSE result ($N_g^{(P)} = N_u^{(P)} = 0$).

states $N_g^{(P)}$ and $N_u^{(P)}$ with ${}^1\Sigma_g^+$ and ${}^1\Sigma_u^+$ symmetry for which vibrational motion $(\partial/\partial R)$ is enabled during time propagation is shown in Figure 4.49. The ionization yield converges towards the FULL TDSE result starting from $N_g^{(P)} = N_u^{(P)} = 500$, i.e. the vibrational dynamics of states deep in the electronic continuum is responsible for the influence of vibrational dynamics on H_2 ionization yields and thus the different isotope effects comparing FULL TDSE to FROZ TDSE. The vibrational wave packets launched in the electronic continuum drift away from their initial position. Thus, recombination to neutral H_2 is prevented and the ionization yield Y_{H_2} is notably enhanced. The reduced mass for the vibration of D_2 is significantly larger than the one of H_2, $\mu_{D_2} = 2\mu_{H_2}$. Thus, the D_2^+ vibrational wave packets drift away significantly slower and recombination towards neutral D_2 is much more probable. The corresponding ratio Y_{H_2}/Y_{D_2} is strongly enhanced for FULL TDSE compared to FROZ TDSE as observed in Figure 4.47.

4.4.8 Conclusions

The programs MAKE_LINK_AND_CONNECT_R, CONNECT_R_2E and SIDIS_2E have been implemented in order to obtain electronic states, dipole transition moments and nonadiabatic couplings as a continuous function of the internuclear distance R. It turned out that a very small grid spacing $\Delta R = 0.001$ a.u. is required to reliably follow electronic states along R and resolve the surprisingly sharp features (avoided crossings) of the electronic states which are visible in the resulting transition dipoles and nonadiabatic couplings. The program TP_BDE_2E2N using these dipoles and nonadiabatic couplings has been implemented to solve the TDSE describing the fully correlated electronic-vibrational motion of H_2 exposed to laser fields. This method has been applied to study the influence of vibrational dynamics on the breakdown of the FNA (studied earlier in Section 4.2.2 up to the FROZ TDSE level). For the studied two- to four-photon ionization regime and intensities between $10^{12} - 2 \times 10^{14}$ W/cm^2 ionization yields in qualitative (and partly quantitative) agreement to [79, 81, 82] were found. Indeed, vibrational dynamics on all electronic states involved in the $1^1\Sigma_g^+ \rightarrow 1^1\Sigma_u^+ \rightarrow H_2^+(1\sigma_g) + e^-$ REMPI (including the final continuum states) was found to significantly influence the FULL TDSE ionization yield compared to FROZ TDSE. The (fixed) centrifugal barrier $J(J+1)/(MR^2)$ (and thus rotation) also has a visible effect on the ionization yield. No visible effect was found for the FULL+NA TDSE approach including nonadiabatic couplings when compared to FULL TDSE. A recently measured isotope effect [107] in the ionization of H_2 vs. D_2 has also been investigated. Already R-integrated static ionization rates agree nicely to the experiment. However, intense, ultrashort 800 nm laser fields behave quantitatively slightly different. While within the FROZ TDSE approximation the ionization yield ratio Y_{H_2}/Y_{D_2} is lower than the one obtained for static fields, the FULL TDSE treatment including vibrational dynamics predicts a ratio larger than the static field ratio. Fast vibrational dynamics in highly energetic continuum states of H_2 efficiently enhances the ionization yield of the H_2 isotope. This effect is less pronounced for the slower vibrational dynamics in the D_2

isotope.

This section concluded the examination of the H_2 molecule. The ionization behavior of a polyatomic molecule, namely the ammonia molecule NH_3, is investigated in the remaining part of this thesis.

4.5 Attosecond Nuclear Motion in the Ammonia Cation

In this section a recent experiment [21] on time-resolved imaging of relative nuclear motion in the ammonia cation isotopes ND_3^+/NH_3^+ using the *PACER* technique (see Chapter 1) is theoretically investigated. Therefore, the inversion (or "umbrella") motion of NH_3 and ND_3 is studied within a simple one-dimensional model, see Sections 2.3 and 4.1. The results presented in the following were published in [2].

As previously mentioned Chapter 1, the *PACER* technique is based on high-harmonic generation [19, 20] of different isotopes. In order to isolate the effect of nuclear motion on the high-harmonic spectra from the electronic ones, the ratio of the spectra obtained with different isotopes is formed, since heavier isotopes possess slower nuclear motion but leave the electronic response (within the Born-Oppenheimer approximation) unchanged. Time information is encoded in the high-harmonic order where a higher order corresponds to a longer excursion time of the liberated electron before recollision. Therefore, *PACER* allows for producing a movie of the relative nuclear motions in the formed molecular cations with sub-fs time resolution. This is in contrast to *Lochfraß* where nuclear dynamics in neutral molecules is observed. However, both *Lochfraß* and *PACER* require a change of nuclear geometry upon ionization. If such a change is absent, ionization would result in a transition from a single initial rovibronic state of the neutral molecule to a single rovibronic state of the molecular ion. In this case neither a nuclear wave packet in the created ion nor in the remaining neutral molecule is formed and thus no nuclear dynamics is initiated that could be observed subsequently. On the other hand, with increasing difference between the Born-Oppenheimer potential curves or hyper-surfaces a broader wave packet involving a larger range of rovibrational states is excited and thus more pronounced and faster nuclear dynamics is launched. This explained the initially surprising experimental finding [20] that the isotope effect in CD_4/CH_4 was more pronounced than in H_2/D_2 despite the fact that much heavier and thus expectedly slower nuclei are involved [162]. The importance of a change in nuclear geometry was also highlighted in a recent *PACER* experiment on D_2O/H_2O [5]. Since ionization from the electronic ground state of water that populates the electronic ground state of the cation is accompanied with only a small change of the geometry while a substantial change accompanies the transition to the first electronically excited state of the water cation, the *PACER* signal is dominated by this second process, despite the fact that the population of excited ionic states is substantially suppressed in intense laser fields due to their increased binding potential. As a consequence the ionization from lower-lying orbitals could for the first time be experimentally detected without the need for a pre-alignment of the molecule.

The largest drawback of the *PACER* method is that the time in which the nuclear dynamics can be monitored is limited by the wavelength of the driving laser field. The first experiments that used a wavelength of 800 nm were thus limited to

approximately the first 1.6 fs [20] of the dynamics induced in the molecular cation. The present work is motivated by the very recent experimental study of Kraus and Wörner investigating ND_3/NH_3 [21] with wavelengths up to 1800 nm. The 1800 nm laser field extends the time window in which nuclear dynamics can be traced to 3.6 fs [21]. With the availability of even longer wavelengths in experiments (for example, 3.5 μm [163]) the need for an accurate theoretical description of the induced nuclear dynamics for longer time intervals becomes increasingly important. Especially at long times the nuclear wave packets reveal the more interesting non-harmonic nature of the Born-Oppenheimer potential energy surfaces. Therefore, one should be able to detect a signal which qualitatively differs from the short-time behavior that was predicted for a large set of molecules in [162] within the harmonic / normal-mode approximation. Note that neutral ammonia is an example for a molecule with a strongly coupled, non-harmonic vibration (and was not considered in [162]).

Assuming the validity of the three-step model [12, 164], see also Chapter 1, it was demonstrated in [19] that the ratio of the high-harmonic spectra for two different isotopes is approximately given by the ratios of the nuclear autocorrelation functions of the two isotopes. The autocorrelation function describes the overlap between the initial nuclear wave function before ionization into which coherent recombination occurs and the time-dependent wave packet of the ion that was created upon strong-field ionization and that evolves between the time of ionization and high-harmonic emission. For a simple system like H_2/D_2 the autocorrelation functions can be calculated theoretically. This was done in [19, 20] using field-free potential curves of the neutral and the ion and thus ignoring the pronounced geometry dependence of the strong-field ionization rates and yields as observed in observed in Section 4.2 and earlier [23, 24, 28, 29]. This effect was later included and found to be important in the analysis of the *PACER* experiment in [165]. For larger molecules the theoretical calculation of the autocorrelation function is more complicated or may even be prohibitively difficult. In such a case, it may alternatively be obtained from experimental photoelectron spectra [5, 21]. However, in one-photon ionization the transition amplitude depends often only very weakly on the nuclear geometry and thus corresponds in such a case to Franck-Condon factors. This is in contrast to strong-field ionization where pronounced deviations from the Franck-Condon approximation can occur. A way to correct the autocorrelation functions for non-Franck-Condon effects was proposed in [21]. The extraction of the autocorrelation functions from experimental photoelectron spectra has the advantage that — in contrast to theoretical calculations — very accurate autocorrelation functions can be obtained in full dimensionality for any molecule. In fact, aside from the strong-field correction, they are exact within the experimental accuracy of the photoelectron spectra. A disadvantage is that the autocorrelation functions and therefore the nuclear motion that is measured in a *PACER* experiment cannot be easily inverted to reveal the wave-packet dynamics that is the original goal of such experiments.

In the following section, the theoretical approach using a one-dimensional model for the inversion ("umbrella") motion of ammonia is discussed and applied in Sec-

tion 4.5.2. The model qualitatively leads to the same autocorrelation functions as the ones obtained from experimental photoelectron spectra. Furthermore, two physically different ways of correcting the ionic wave packet for non-Franck-Condon effects in strong fields are briefly discussed. Three different experimentally relevant initial states are discussed, especially drawing attention to the fact that the vibrational initial state in neutral ammonia is most likely a thermal mixture. Most importantly, it is shown that the maximum in the ratio of the autocorrelation functions of ND_3 relative to NH_3 around 5 fs predicted in [21] can be understood when visualizing the time evolution of the wave packets launched in the NH_3^+ and ND_3^+ cations.

4.5.1 Theoretical Approach

The inversion motion of the neutral NH_3 and ND_3 molecules (Section 2.3) is treated using the matrix algorithm as described in Sections 4.1.2 and 4.1.3. Thus, vibrational energies are in surprisingly good agreement with experimental ones are found for NH_3 and ND_3. For the results presented in this paper, $N = 301$ points and a grid size of $L = 3.6$ a.u. are used. All results obtained remained unchanged when a larger or finer grid was used. In fact, due to the exponentially fast convergence behavior of the matrix algorithm with respect to the grid spacing L/N, the observables presented in this paper are already converged using only $N = 61$ points and $L = 3.6$ a.u. Thus the large number of $N = 301$ points is only used to make the discretized wave functions look smooth without the need for an interpolation.

To describe the nuclear motion in the NH_3^+ and ND_3^+ molecular cations with the Hamiltonian

$$\hat{\mathrm{H}}_{\mathrm{ion}} \;=\; \frac{\hat{\mathrm{p}}^2}{2\mu} \;+\; V_{\mathrm{ion}}(x) \tag{4.89}$$

the potential

$$V_{\mathrm{ion}}(x) \;=\; V_0 \;+\; K_1\,x^2 \;+\; K_2\,x^4 \tag{4.90}$$

has been taken from [166] ($K_1 = 0.51978$ mdyne Å^{-1} and $K_2 = 1.64812$ mdyne Å^{-3} where 1 mdyne ≈ 0.22937 Å^{-1} and 1 Å ≈ 1.8897 a.u.). In contrast to the description of neutral ammonia, the constant reduced mass

$$\mu \;=\; \frac{3m + M}{3\,m\,M} \tag{4.91}$$

is used for the cation with the nitrogen mass M and the hydrogen / deuterium mass m (same values as in Sections 4.1.2 and 4.1.3). Note that the position-dependent mass adopted for neutral ammonia stems from the vibrational coupling with the stretching mode of the hydrogen atoms and is thus less relevant for the description of the cation in which the vibration is nearly harmonic. Some low-lying eigenfunctions of NH_3 and NH_3^+ obtained with this method are shown in Figure 4.50.

In an experiment, the ratio of the high-harmonic spectra of ND_3 relative to NH_3

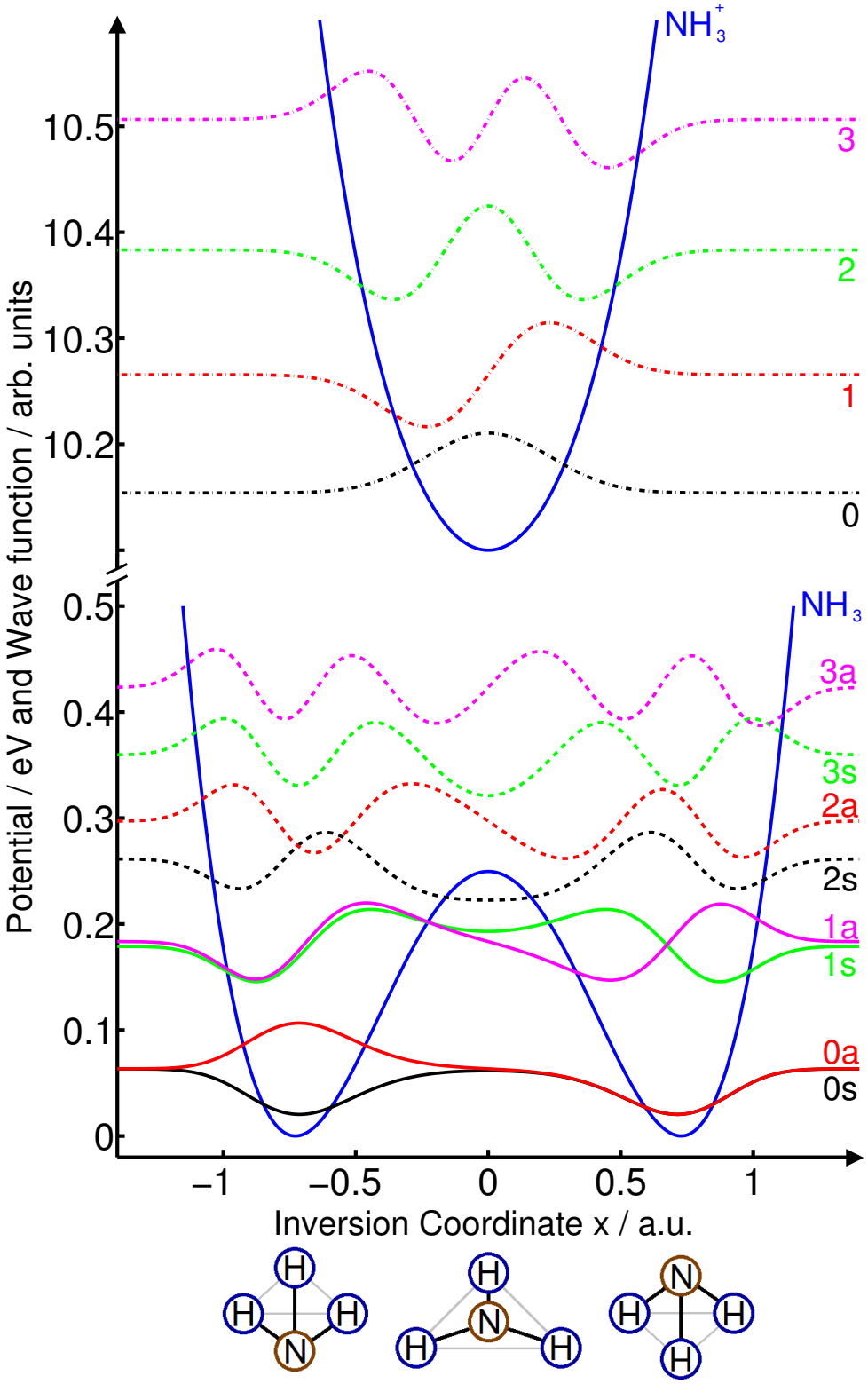

Figure 4.50: Potential curves of NH_3 (data from [115]), NH_3^+ (data from [166]), and energetically lowest wave functions. The wave functions have been shifted by constants such that their values at $|x| \to \infty$ display the eigenenergies. This figure is also presented in [2].

can be approximately mapped on the autocorrelation function ratio [5, 19–21]

$$\frac{|\,C_{\mathrm{ND_3}}(t)\,|^2}{|\,C_{\mathrm{NH_3}}(t)\,|^2} \quad . \tag{4.92}$$

The underlying idea is that at the time of ionization ($t = 0$) the nuclear wave function of the initial state of the neutral molecule is transferred to the potential surface of the ion. While the emitted electron is driven by the laser field, the nuclear wave packet evolves on the ionic potential surface. In a linearly polarized laser field the electron is driven back to its parent ion where it can recombine and emit the energy acquired from the laser field during its excursion as high-harmonic radiation. In order to yield a macroscopically measurable signal, the emission from many molecules has to occur coherently. This requires the recombination into exactly the initial state, both electronically and rovibrationally. A measure of the fulfillment of this condition for the nuclear part is the autocorrelation function

$$C(t) \;=\; \left\langle \chi_{\mathrm{neutral}}(t=0) \,\middle|\, \Phi_{\mathrm{ion}}(t) \right\rangle \tag{4.93}$$

which is the overlap between the nuclear wave function of the initial state $\chi_{\mathrm{neutral}}(t = 0)$ of the neutral molecules and the time-dependent wave packet $\Phi_{\mathrm{ion}}(t)$ of the ion. In the present work the latter is obtained by simply multiplying the propagator

$$\hat{\mathrm{U}}(t) \;=\; \exp\left(-\,i\,\hat{\mathrm{H}}_{\mathrm{ion}} t\right) \tag{4.94}$$

with the initial ionic wave function $|\Phi_{\mathrm{ion}}(t = 0)\rangle$ (using EXPM in MATLAB [73]). Even though our model is one-dimensional, it is beyond the harmonic (normal mode) approximation that was made in [162] to calculate the autocorrelation function ratio for a set of molecules (not including NH_3). Thus, more than only the short-time dynamics can be described.

The two lowest-lying inversion eigenstates of NH_3 and ND_3 (defined as $|\,0s\,\rangle$ and $|\,0a\,\rangle$ in Fig. 4.50) are energetically almost degenerate and have thus both to be taken into account when considering the initial state in the neutral molecule. Three different initial states of the neutral molecule are considered:

1. A coherent superposition

$$|\chi_{\mathrm{neutral}}(t=0)\rangle \;=\; \frac{1}{\sqrt{2}}\left(\,|\,0s\,\rangle \;+\; e^{i\varphi}\,|\,0a\,\rangle\,\right) \quad . \tag{4.95}$$

   For $\varphi = 0$ or $\varphi = \pi$, this wave packet is localized in only one of the two potential minima of the neutral molecule.

2. A thermal mixture with initial density operator

$$\hat{\rho}_{\mathrm{neutral}}(t=0) \;=\; \frac{1}{2}\left(\,|\,0s\,\rangle\,\langle 0s|\;+\;|\,0a\,\rangle\,\langle 0a|\,\right) \quad . \tag{4.96}$$

Due to the very small energy splitting between the $|\,0s\,\rangle$ and the $|\,0a\,\rangle$ states and the comparatively large energy separation from higher states, the Boltzmann statistics predicts that only those two states will be substantially populated for the very large temperature interval $4\ \mathrm{K} < T < 300\,\mathrm{K}$.

3. A single state

$$|\chi_{\mathrm{neutral}}(t=0)\rangle \;=\; |\,0s\,\rangle \quad \text{or} \quad |\chi_{\mathrm{neutral}}(t=0)\rangle \;=\; |\,0a\,\rangle \quad . \tag{4.97}$$

While the experimental efforts to cool the system down to $T < 1$ K such that dominantly the $|\,0s\,\rangle$ state is occupied might be quite large, a beam of only $|\,0a\,\rangle$ states could be easily created using a quadrupole lens like it was done for the ammonia maser [63].

Using the inversion symmetry of the problem it will be shown in chapter 4.5.2 that the autocorrelation functions (and thus high-harmonic spectra) in the case of the coherent superposition is independent of φ and that the autocorrelation functions obtained in this case are equal to the case of the thermal mixture.

The ionic wave packet expressed in the basis of the stationary ionic eigenstates $\left|\tilde{\Phi}_{n,\mathrm{ion}}\right\rangle$ is

$$|\,\Phi_{\mathrm{ion}}(t)\,\rangle \;=\; \sum_n c_n \left|\,\tilde{\Phi}_{n,\mathrm{ion}}\,\right\rangle \exp\left(-i\,\frac{\mathrm{E}_n}{\hbar}\,t\right) \tag{4.98}$$

and thus the autocorrelation function is (as in [21])

$$\begin{aligned} C(t) \;&=\; \left\langle\, \chi_{\mathrm{neutral}}(t=0) \,\middle|\, \Phi_{\mathrm{ion}}(t) \,\right\rangle \\ &=\; \sum_n c_n \left\langle\, \chi_{\mathrm{neutral}}(t=0) \,\middle|\, \tilde{\Phi}_{n,\mathrm{ion}} \,\right\rangle \exp\left(-i\,\frac{\mathrm{E}_n}{\hbar}\,t\right) \quad . \end{aligned} \tag{4.99}$$

For a simple Franck-Condon (FC) transition the wave-packet coefficients are

$$c_n^{\mathrm{FC}} = \left\langle\, \tilde{\Phi}_{n,\mathrm{ion}} \,\middle|\, \chi_{\mathrm{neutral}}(t=0) \,\right\rangle \tag{4.100}$$

and the autocorrelation function can easily be reconstructed from the vibrational energies and the Franck-Condon factors. This was done for D_2O/H_2O in [5] to reconstruct the autocorrelation function in full dimensionality from the energies and Franck-Condon factors measured in [167]. In strong laser fields (SF), however, the transition may not be simply a Franck-Condon transition, since the electronic transition matrix element can depend strongly on the nuclear geometry R yielding [23, 24]

$$c_n^{\mathrm{SF}} \propto \left\langle\, \tilde{\Phi}_{n,\mathrm{ion}}(R) \,\middle|\, \Gamma^{\frac{1}{2}}(R) \,\middle|\, \chi_{\mathrm{neutral}}(R, t=0) \,\right\rangle \tag{4.101}$$

with the geometry-dependent ionization rate $\Gamma(R)$ (neglecting the phase of a possibly complex Γ). Allowing for a direct comparison with Ref. [21] the same atomic ionization model [66]

$$\Gamma(I_p) \propto \exp\left(-\frac{2}{3}\frac{(2I_p)^{3/2}}{F}\right) \tag{4.102}$$

with the ionization potential I_p and the field-strength F is used. Within our one-dimensional model c_n^{SF} can directly be calculated using $I_p(x) = V_{\mathrm{ion}}(x) - V_{\mathrm{neutral}}(x)$. This weighting is, however, not possible without a theoretical calculation and therefore was not done in [21]. In another, though more approximate, approach the coefficients are calculated as [168, 169]

$$c_n^{\mathrm{SF,appr.}} \propto \left\langle \tilde{\Phi}_{n,\mathrm{ion}} \middle| \chi_{\mathrm{neutral}}(t=0) \right\rangle \Gamma(\, I_p(n)\,) \tag{4.103}$$

where $I_p(n) = I_p(0) + (E_n - E_0)$. For this version of the strong-field weighting only the vibrational energies E_i are needed. Therefore, this correction can easily be applied without the need for a theoretical calculation and was thus adopted in [21]. Both versions of strong-field weighting are compared below.

4.5.2 Results and Discussion

Figure 4.51 shows the populations of the NH_3^+ vibrational eigenstates for a Franck-Condon transition and after strong-field weighting according to either Eqs. (4.101) or (4.103) for the coherent superposition (Eq. (4.95)) and for the thermal mixture (Eq. (4.96)). The field strength F is set to the peak field strength corresponding to a laser field with peak intensity $5 \times 10^{13}\ \frac{\mathrm{W}}{\mathrm{cm}^2}$. The case of a coherent superposition as in Eq. (4.95) is now discussed in more detail. Since the inversion symmetry $V(x) = V(-x)$ of the system is not broken at any time, the ionic wave packet separates into

$$|\Phi_{\mathrm{ion}}(t)\rangle \;=\; \frac{1}{\sqrt{2}}\left(\, |\Phi_{\mathrm{ion,s}}(t)\rangle \;+\; e^{i\varphi}\; |\Phi_{\mathrm{ion,a}}(t)\rangle \,\right) \tag{4.104}$$

where $|\Phi_{\mathrm{ion,s}}(t)\rangle$ ($|\Phi_{\mathrm{ion,a}}(t)\rangle$) is the wave packet obtained if the initial state in the neutral molecule is only $|\,0s\,\rangle$ ($|0a\rangle$). This can be seen considering that the $|\,0s\,\rangle$ ($|0a\rangle$) state in the neutral molecule results in a ionic wave packet that consists solely of symmetric (antisymmetric) components. The autocorrelation function for the coherent superposition in Eq. (4.95) can now be rewritten as

$$C(t) \;=\; \big\langle \chi_{\mathrm{neutral}}(t=0) \big| \Phi_{\mathrm{ion}}(t) \big\rangle \;=\; \frac{1}{2}\left(\, \big\langle 0s \big| \Phi_{\mathrm{ion,s}}(t) \big\rangle \;+ \big\langle 0a \big| \Phi_{\mathrm{ion,a}}(t) \big\rangle \,\right) \tag{4.105}$$

and is thus completely independent of the phase φ between the $|\,0s\,\rangle$ and the $|\,0a\,\rangle$ state.

For the thermal mixture in Eq. (4.96) no phase relation between $|\,0s\,\rangle$ and $|\,0a\,\rangle$

exists from the start. Clearly, for such a statistical mixture there is an independent HHG emission from those molecules in the $|\,0s\,\rangle$ and those in the $|\,0a\,\rangle$ state. However, while the molecules are in an incoherent state, the amplitudes describing the emitted light have to be added coherently for all molecules in order to obtain a macroscopic signal ("phase matching"). Since the dipole moment is directly proportional to the complex autocorrelation function (see Eq. (10) in [19]), it follows that the complex autocorrelation functions of the molecules starting in either $|\,0s\,\rangle$ or $|\,0a\,\rangle$ have to be added coherently. As a consequence, the result (Eq. (4.105)) is identical for the thermal mixture in Eq. (4.96) and for the coherent superposition in Eq. (4.95).

Figure 4.52 displays the calculated autocorrelation functions of NH_3 and ND_3 as well as their ratio for a Franck-Condon transition. Additionally, the ratio after strong-field weighting is shown. It should be noted that after strong-field weighting and normalization of the ionic wave function one arrives at $|\Phi_{\mathrm{ion}}(t=0)\rangle \neq |\chi_{\mathrm{neutral}}(t=0)\rangle$ and thus $|C(t=0)| \neq 1$. The autocorrelation functions in the strong-field weighted case were scaled to $|C(t=0)| = 1$ as this is the only option in an experiment-only study like [21] because χ_{neutral} and Φ_{ion} are not known. This introduces an error to the ratio since $|C_{\mathrm{NH_3}}(t=0)| \neq |C_{\mathrm{ND_3}}(t=0)|$. In the present case of NH_3 and ND_3, however, it is found that the error

$$\left| \frac{|C_{\mathrm{ND_3}}(t=0)|^2}{|C_{\mathrm{NH_3}}(t=0)|^2} - 1 \right| \tag{4.106}$$

is smaller than 2%. In addition to this error stemming from the "relative" strong-field weighting, also the absolute ionization yield is slightly isotope dependent. Assuming a sufficiently small ionization yield Y (no saturation), the relative difference of the ionization yields can be approximated by [23]

$$\frac{Y_{\mathrm{ND_3}}}{Y_{\mathrm{NH_3}}} \approx \frac{\int |\chi_{\mathrm{neutral,ND_3}}(x,t=0)|^2\, \Gamma(x)\, dx}{\int |\chi_{\mathrm{neutral,NH_3}}(x',t=0)|^2\, \Gamma(x')\, dx'} \approx 0.98 \tag{4.107}$$

which is again a small effect in the few-percent range.

It is remarkable that the strong-field weighting according to Eq. (4.103) yields quantitatively almost exactly the same wave-packet populations and autocorrelation ratio as Eq. (4.101) even though both weighting procedures appear physically completely different. Tests with varying field strengths have shown that the agreement in the population of the ionic wave packet when using Eq. (4.103) instead of Eq. (4.101) improves with increasing field strength. It is the content of a further study to investigate the reason for the good agreement between both strong-field weighting methods found for NH_3 and whether larger deviations occur for other molecules. Indeed, the good agreement between both approaches is a bit surprising considering the different physical pictures behind them. For the correction using geometry-dependent ionization yields, Eq. (4.101), a coherent vertical transition to the ionic state is assumed. In the other case, Eq. (4.103), the correction is performed

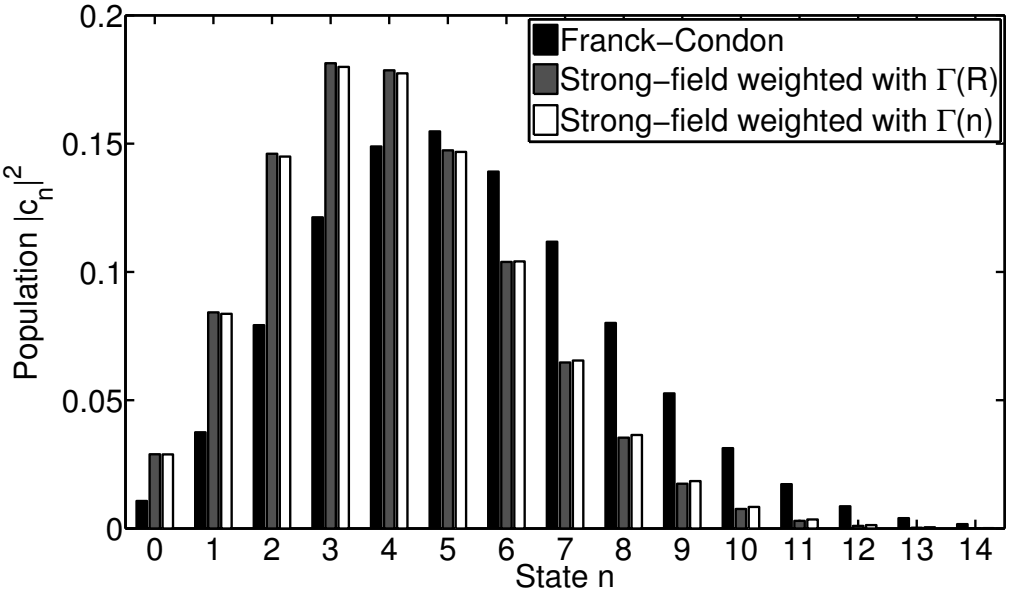

Figure 4.51: Population of NH_3^+ vibrational states for a Franck-Condon transition (Eq. (4.100)) and the strong-field weighted case for a peak intensity of $5 \times 10^{13} \frac{\mathrm{W}}{\mathrm{cm}^2}$ with $\Gamma = \Gamma(R)$ (Eq. (4.101)) and $\Gamma = \Gamma(n)$ (Eq. (4.103)). This figure is also presented in [2].

independently (incoherently) using the energy of each individual vibrational state. The short- and the long-time behavior of the autocorrelation functions presented in Figure 4.52 is now discussed in more detail.

For short times ($t < 9$ fs) the autocorrelation functions agree well for all considered initial states (in the experiment [21] the first 3.5 fs were accessible). As in Fig. 2 of Ref. [21], the autocorrelation function ratios show a clear maximum around 5 fs. When comparing the autocorrelation functions and ratios to Fig. 2(d) and (f) of Ref. [21], one finds a very good qualitative but not a full quantitative agreement. As in [21] the strong-field weighting decreases the contrast of the signal but does not change it qualitatively. Due to the restricted dimensionality of the employed model, it is expected that the real autocorrelation functions tend faster towards zero than the calculated ones due to the influence of the other vibrational degrees of freedom (non-perfect overlap of the ground-state wave functions of the neutral and the ion with respect to these degrees of freedom). Considering that this should strongly affect the autocorrelation-function ratio at positions where small numbers with rather large errors are divided by each other, the agreement of Figure 4.52 and Fig. 2 of Ref. [21] is surprisingly good.

For longer times ($t > 9$ fs) the autocorrelation ratios start to be qualitatively pronouncedly different when comparing the coherent superposition or thermal mixture to a single state. The intensity recurrences of the autocorrelation functions for the

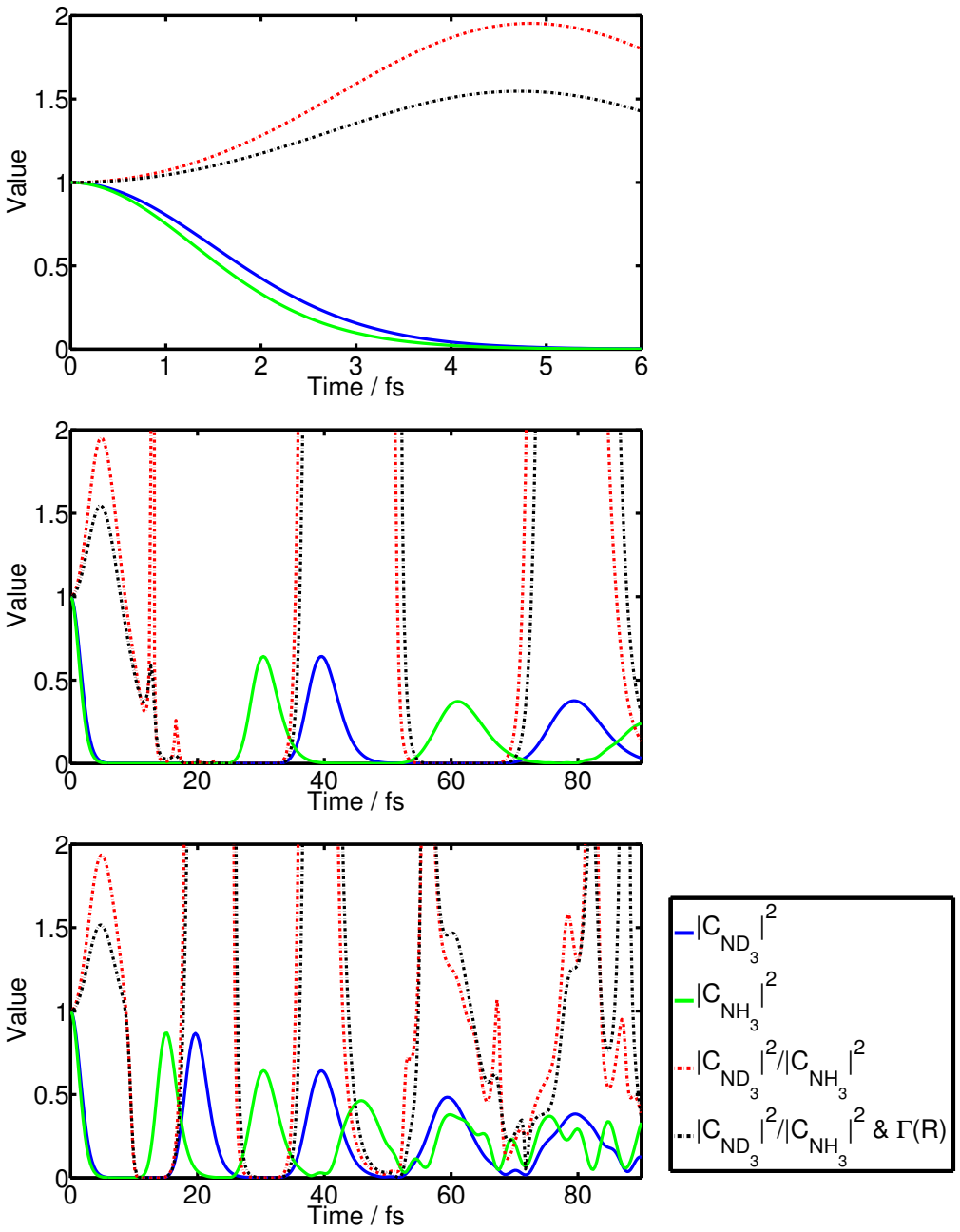

Figure 4.52: Autocorrelation functions and ratios obtained with the present method for a Franck-Condon transition. Additionally, the ratios obtained after strong-field weighting with $\Gamma = \Gamma(R)$ (Eq. (4.101)) is shown for a peak intensity of $5 \times 10^{13} \frac{\mathrm{W}}{\mathrm{cm}^2}$. The ratio obtained with $\Gamma = \Gamma(n)$ (Eq. (4.103)) is indistinguishable from the weighting with $\Gamma = \Gamma(R)$ (Eq. (4.101)) with bare eye. **Top:** Short-time behavior for the coherent superposition (Eq. (4.95)) / thermal mixture (Eq. (4.96)) as initial state. The short-time behavior of the single states (Eq. (4.97)) is very similar. **Middle:** Long-time behavior of the coherent superposition (Eq. (4.95)) / thermal mixture (Eq. (4.96)). **Bottom:** Long-time behavior for only $|0a\rangle$ as initial state (the result for $|0s\rangle$ shows qualitatively a comparable behavior). This figure is also presented in [2].

single state (Eq. (4.96)) occur at a two times larger frequency compared to the case of a coherent superposition (Eq. (4.95)) / thermal mixture (Eq. (4.96)). The doubled number of intensity recurrences can be explained considering what happens, if only the $|\,0s\,\rangle$ (or only the $|\,0a\,\rangle$) state is populated initially. In this case, only symmetric (or antisymmetric) eigenfunctions are occupied in the molecular ion and thus the energy spacing of occupied states in the wave packet is effectively doubled, leading to a doubled frequency of the signal. Additionally, a significant collapse of the NH_3^+ wave packet due to the anharmonicity of the potential can already be observed for $t > 50$ fs. Thus, if the autocorrelation function ratio could be measured for these long times, the faster dynamics of a single state could be observed.

In Ref. [21] the autocorrelation function ratio maximum around 5 fs has been observed as a novel effect. Only ratios $|\,C_{ND_3}(t)\,|^2/|\,C_{NH_3}(t)\,|^2$ which monotonously increase in time have been discussed before. Since the explanation this maximum in Ref. [21] is only based on autocorrelation functions extracted from experimental Franck-Condon factors, it provides only limited physical insight. Using the present wave-packet study a physical picture can be provided. Figure 4.53 shows snapshots of the time evolution of the ionic wave packet in addition to the autocorrelation functions for the case of a Franck-Condon transition. It remains qualitatively unchanged after correcting for a non-Franck-Condon transition. As can be seen in Figure 4.53, the NH_3^+ wave packet already reached the potential minimum at 5 fs and gets slowed down by the now rising potential. However, for ND_3^+ the potential seen by the wave packet is still strongly decreasing and thus the wave packet now catches up with the NH_3^+ wave packet. Thus, this maximum is a real-time movie of this catching-up process and specific to ammonia. Therefore, it would be very interesting to see this part of the autocorrelation function ratio measured in a future experiment. This might be possible when using a longer wavelength $\lambda > 1800$ nm.

4.5.3 Conclusions

In this section, the nuclear motion launched in the NH_3^+ and ND_3^+ cations that was recently measured in [21] was investigated. A one-dimensional model describing the inversion motion of ammonia beyond the harmonic approximation was used. The ionic wave packet was corrected for non-Franck-Condon effects in two completely different ways where only one way can be used in a purely experimental study. Surprisingly, both methods yield quantitatively almost the same result for ammonia. Three experimentally relevant initial states were considered and it was shown that while the behavior of the thermal ensemble and coherent superposition agrees due to the inversion symmetry of the problem, a single vibrational state shows a different behavior. However, in the cases considered here, this only affects the long-time dynamics which has not yet been measured. For the short-time behavior, snapshots of the time evolution of the ionic wave packet explaining the maximum in the autocorrelation function ratio (which was predicted in [21]) were presented. In conclusion, while models in reduced dimensionality may yield quantitatively wrong autocorrelation function ratios, they help to understand what is dominantly seen in a *PACER*

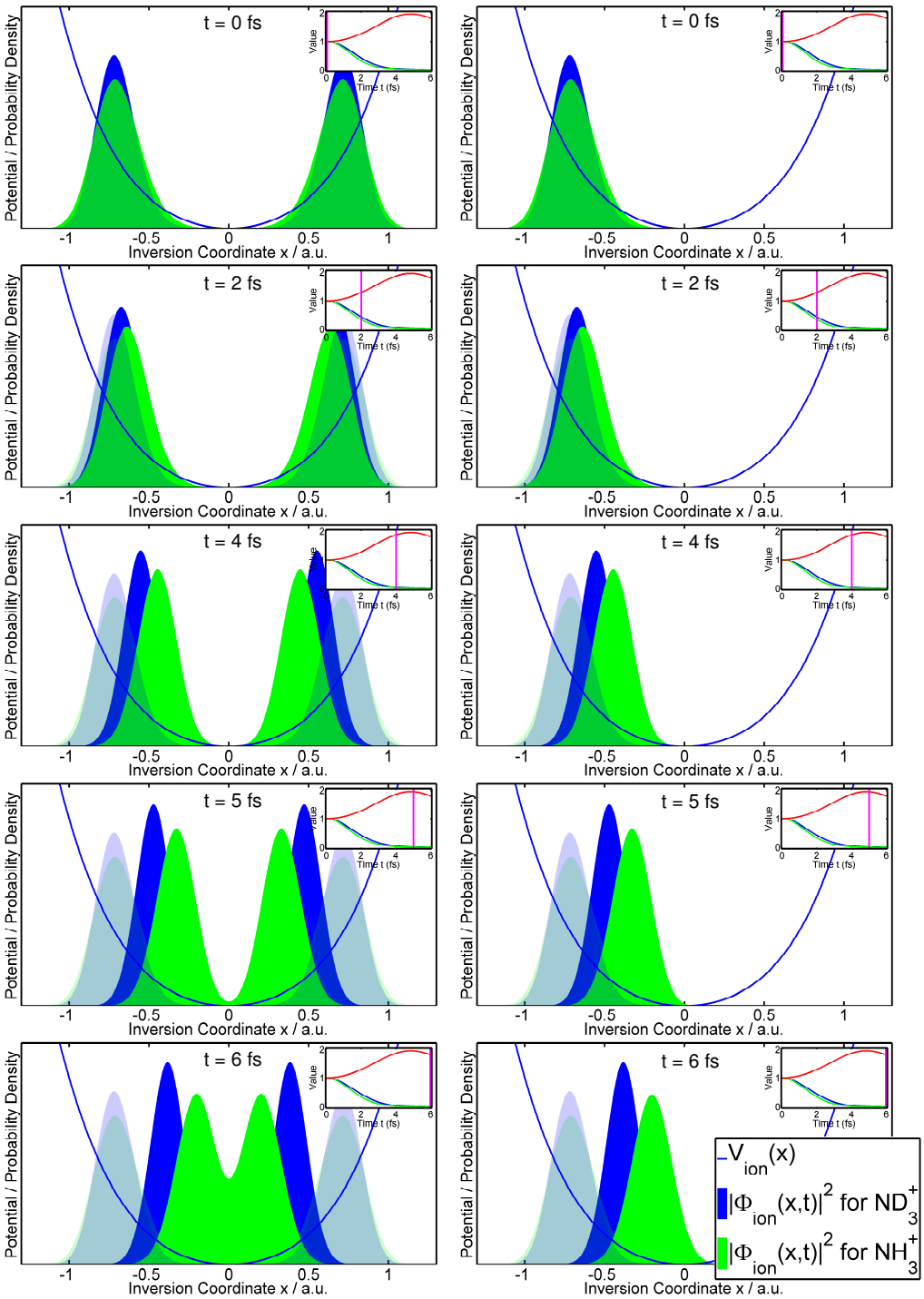

Figure 4.53: Snapshots of the time evolution of the probability density in the molecular cation. To indicate the overlap the probability density in the neutral molecule is shown shaded. The corresponding part of the autocorrelation functions is plotted at the inset where the vertical line crossing the autocorrelation functions indicates the actual time.
Left: Initial state is the thermal ensemble (Eq. (4.96)).
Right: Initial state is the coherent superposition (Eq. (4.95)) with relative phase $\varphi = 0$ between $|\,0s\,\rangle$ and $|\,0a\,\rangle$. This figure is also presented in [2].

experiment and can describe the expected behavior for a longer time-scale due to the use of more realistic potentials. The combination of reconstructing autocorrelation functions from measured Franck-Condon factors and low-dimensional modeling of the nuclear dynamics may potentially become an important tool for future investigations of other molecules. Whereas the former accurately predicts the signal expected in the experiment, the latter allows to understand and visualize the nuclear dynamics that is expected to be seen. Additionally, some implicit approximations can only be cross-checked by theory. Finally, the interesting long-time dynamics predicted for NH_3 should be a further stimulation for experimental efforts adopting longer wavelengths for generating high harmonics of molecules, despite the challenge imposed by the decreasing harmonic intensities accompanying longer wavelengths.

In the following sections the idea of imaging neutral ammonia molecules by ionization is explored. The predicted and experimentally observed geometry dependence of the ionization yield may be exploited to reach this goal. The inversion motion of neutral ammonia is especially appealing for imaging due its double-well potential which may allow for imaging the tunneling process in real time.

4.6 Imaging of Nuclear Wave Packets and Tunneling in Ammonia Molecules via Ionization

In the following the single-determinant approach described in Section 3.4 is used to obtain TDSE ionization yields for the NH_3 molecule. The electronic basis sets (energies and dipole matrices) required for the time propagations have been calculated by Etienne Plésiat and Álvaro Magaña. The ionization behavior of NH_3 is investigated and the possibility to prepare and measure nuclear inversion motion (Section 2.3) wave packets is explored. The following results have also been published in [4], except for the contribution of internuclear distances on the total ionization yield shown in Figure 4.61 (and the corresponding brief discussion).

A pronounced geometry dependence of strong-field ionization yields (wavelengths ≥ 800 nm) on the nuclear geometry for molecules undergoing an equilibrium geometry change upon ionization (like H_2 and NH_3) has been observed and discussed earlier in this thesis for H_2, Section 4.2, NH_3, Section 4.5, and also earlier in [23, 24, 28, 29]. As already mentioned in the introduction of this thesis, Chapter 1, the *Lochfraß* effect allows to exploit this effect to create and image vibrational wave packets in neutral molecules with sub-femtosecond and sub-ångström resolution. *Lochfraß* has been investigated before only for the diatomic molecules H_2 [30, 31] and I_2 [32, 33]. The NH_3 molecule is a good candidate for observing *Lochfraß* for the first time in a polyatomic molecule due to its expected strong geometry dependence of the ionization yield. Furthermore, the simplified ADK and FC-ADK ionization rates (used before to approximate H_2 ionization yields in Section 4.2) can be directly compared to the TDSE results also for NH_3 and thus their usefulness to describe geometry-dependent ionization of polyatomic molecules can be examined. Imaging NH_3 inversion motion wave packets is particularly interesting because of the double-well potential of the electronic ground state of neutral NH_3. This may allow for imaging of the quantum mechanical tunneling process in real time.

In the following section the methods and basis-set parameters used to describe the electronic response (ionization) and triggered nuclear motion in neutral ammonia are briefly discussed. In Sec. 4.6.2 the observed ionization behavior and its application to imaging based on *Lochfraß* is discussed. Sec. 4.6.3 introduces the idea to image a tunneling wave packet. This idea is further fleshed out in Sec. 4.6.4 where the observation of the tunneling process in real time and the required laser fields and ionization behavior to achieve this goal are discussed.

4.6.1 Methods

In order to study nuclear motion in neutral ammonia, first the geometry-dependent electronic response (ionization) of the molecule to the laser field is described. Thereafter, this response is included in the description of the (slower) nuclear motion. Similarly to previous works [5, 11, 54, 98], the TDSE describing the electronic re-

sponse for a fixed nuclear geometry is solved using the single-determinant approach as described Section 3.4 combined with the spectral ansatz, Section 3.5. In the case considered here in which ionization from the $3a_1$ HOMO orbital dominates the ionization yield[34], the total yield Y is calculated as the sum over the individual populations $P_n = |c_n|^2$ of the continuum orbitals (energy above the continuum threshold) similarly to Eq. (4.31).

In order to describe the inversion (or umbrella) motion of ammonia, the main nuclear coordinate considered here is the inversion coordinate x, see Section 2.3. The electronic basis is calculated for different values of this inversion coordinate using exactly the same nuclear geometries as in table 1 of Ref. [115]. A box size of $r_{\max} = 300$ a.u. and a central expansion of 449 B-spline functions (times a spherical harmonic) is used. The maximum angular momentum included is $l_{\max} = 11$. In order to check the convergence of the results, a reference calculation with a larger box of size $r_{\max} = 600$ a.u., 776 B-spline functions and maximum angular momentum $l = 8$ is performed. With this basis, the ionization yields for three different geometries, namely $x = 0$, 0.592, and 1.066 a.u. are checked and no deviations from the results obtained with the smaller box size are found (on the level of the graphs shown in the following).

The linearly polarized laser field is defined by Eq. (2.68) in Section 2.7. Unless noted otherwise, $\phi = 0$ is used in the following. The interaction potential reads $\hat{\mathrm{V}}(t) = \hat{\mathbf{p}} \cdot \vec{A}(t)$ according to Section 2.5 (dipole approximation, velocity gauge). The polarization vector $\vec{\mathcal{P}} = \vec{A}_0 \,/\left|\vec{A}_0\right|$ points along the inversion axis (and thus the static dipole moment) of ammonia. Ionization from the $3a_1$ HOMO orbital is geometrically preferred for this orientation. This orientation has been already experimentally realized and variation of the orientation did not reveal contributions to the ionization from lower lying orbitals [21].

The TDSE ionization yields are compared to the ones obtained using Ammosov-Delone-Krainov (ADK) tunneling rates Γ_{ADK} [26, 27] and the recently introduced frequency-corrected ADK (FC-ADK) model, Eq. (4.46) in Section 4.2.3, based on the Perelomov-Popov-Terent'ev (PPT) [25] theory. For consistency, the same geometry-dependent $I_p(x)$ as in the TDSE calculations is used for (FC-)ADK (from the diagonalization of the Kohn-Sham hamiltonian in the B-spline basis).

Since the magnetic-field component of the laser field is neglected in this work, the electrons occupying the same spatial orbital (but possessing different spins) respond to the laser field in an identical fashion and are thus equivalent. In the case of neutral ammonia this leads to $N_e = 2$ for the two electrons occupying initially the HOMO. However, the ionization in intense laser fields depends exponentially on the ionization potential. If the intensity and duration of the laser field leads to pronounced ionization, the initial electron density is substantially depleted. This results in an increased ionization potential and thus a decreased ionization probability. Therefore, the ionization from different orbitals is no longer independent of each other.

[34] If more than one initial orbital would contribute to the total ionization yield, the individual contributions of the orbitals are added in order to obtain the total ionization yield.

For example, if effectively one electron has been ejected, the ionization of a second (in the single-particle approximation formally independent) electron from the same spatial orbital depends not on the ionization potential of the neutral molecule, but the higher one of the molecular cation. For the H_2 molecule it was shown in [54] that the single-active-electron ionization yield matches the full two-electron solution if it is multiplied by a factor 2 ($N_e = 2$ active electrons) as long as the ionization yield is small. However, for ion yields $Y \approx 0.1$ a sharp transition was found and for higher yields the two-electron calculation agreed well with the single-active-electron result, if $N_e = 1$ was used. Assuming a comparable behavior for ammonia, i. e. that $N_e = 2$ is appropriate for ion yields below about 10 %, all ion yields obtained within the present TDSE approach and (FC-)ADK for intensities lower than $I = 10^{14}$ W/cm^2 adopt $N_e = 2$ ($N_e = 1$ otherwise).

If a significant part of the initial nuclear wave function gets depleted, as it is the case for *Lochfraß*, the effect of the ionization process on the nuclear motion in the electronic ground state of the neutral molecule is incorporated by means of a loss channel (ignoring a possible recombination) [30]. This leads to the one-dimensional time-dependent Schrödinger equation for the inversion coordinate x,

$$i\,\frac{\partial}{\partial t}\,\chi(x,t) \;=\; \left(\hat{\mathrm{H}}_0 \;-\; \frac{i\,\Gamma(x,t)}{2}\right)\,\chi(x,t) \quad , \tag{4.108}$$

where $\hat{\mathrm{H}}_0$ is the time-independent nuclear Hamiltonian and $\Gamma(x,t)$ is the geometry-dependent ionization rate. In the limit of an extremely fast ionization process compared to the time scale of nuclear motion (instantaneous ionization/vertical transition), an initial nuclear wave function $\chi_0(x)$ is transformed into

$$\sqrt{1 - Y(x)}\,\chi_0(x) \quad . \tag{4.109}$$

In the following, this limit is termed sudden ionization approximation. To obtain an ionization rate $\Gamma_{\mathrm{TDSE}}(x,t)$ for the electronic TDSE calculations, the time dependence of FC-ADK is assumed and the rate is scaled with a constant factor $q(x)$, $\Gamma_{\mathrm{TDSE}}(x,t) \;=\; q(x)\;\Gamma_{\mathrm{FC-ADK}}(x,t)$. This is done such that the time integration of $\Gamma_{\mathrm{TDSE}}(x,t)$ according to Eq. (4.43) gives the correct ionization yield $Y_{\mathrm{TDSE}}(x)$.

The inversion motion is described as previously, i.e. H_0 is given by Eq. (4.3) in Section 4.1.2, using the double-well potential and position-dependent mass model from Ref. [115]. For the matrix algorithm a box size of $x_{\max} = \pm 1.805$ a.u. and $N = 71$ points are used (converged results are obtained already with $N = 31$ points).

One may revisit Section 4.1.2 and especially Figure 4.1 which shows the six lowest-lying vibrational eigenfunctions of NH_3 obtained with the present method. The energy splitting between the first two vibrational (inversion) eigenstates is extremely small (≈ 0.8 cm^{-1}, see Section 4.1.2). Thus, if the ammonia molecule is initially in thermal equilibrium, the initial state is (as already discussed in Section 4.5) a thermal mixture consisting of 50% in the lowest symmetric state $|0s\rangle$ and 50% in the

lowest anti-symmetric state $|0a\rangle$ for a large temperature regime ($4\ \mathrm{K} < T < 300\ \mathrm{K}$). This requires a density matrix formulation for the evolution of the vibrational wave packet. The solution simplifies, however, if the inversion symmetry is not broken at any time, $\Gamma(x,t) = \Gamma(-x,t)$. In this case, one can numerically solve the Schrödinger equations 4.108 independently for $|0s\rangle$ or $|0a\rangle$ as initial state, respectively, instead of propagating the whole density matrix.

4.6.2 Ionization Behavior and Application to Imaging (Lochfraß)

The ionization yields obtained from the solution of the TDSE as well as from the ADK and FC-ADK rates are shown in Figure 4.54 for $n_c = 6 - 10$ cycle laser fields and wavelengths of $\lambda = 800, 1300$, and 1800 nm. The TDSE ionization yields are almost perfectly symmetric with respect to the inversion coordinate x, i.e. the ionization yield is unchanged whether the maximum of the electric field is oriented parallel or antiparallel to the inversion axis (see Figure 4.55). While ADK qualitatively predicts the correct geometry dependence of the ionization yield, FC-ADK also agrees quantitatively very well with the TDSE results over the whole intensity range, similar to observations for the H_2 molecule [3]. The largest differences between ADK and FC-ADK are observable at low intensities and $\lambda = 800$ nm. The differences between ADK and FC-ADK decrease with increasing wavelength and intensity due to the decreasing Keldysh parameter. Furthermore, one can observe how the TDSE ionization yields also become smoother for decreasing Keldysh parameters, i. e. multiphoton resonances get less important when going deeper into the quasistatic regime. Except for a seemingly reduced ionization yield around $x = 0$ for the TDSE at $\lambda = 800$ nm and $I = 10^{13}$ W/cm^2, all predictions show a significant increase in the ionization yield with decreasing absolute value of the inversion coordinate $|x|$. This is expected due to the decrease of the vertical binding energy $I_p(x)$ with decreasing $|x|$ which stems from the change of the equilibrium geometry from pyramidal to planar upon ionization, see also Figure 4.56. The exponential dependence of the ionization rate on the binding energy, Eq. (4.46), leads to this increase. However, the TDSE shows a less pronounced $|x|$ dependence than ADK and FC-ADK. Especially at small $|x|$ the TDSE ionization yield is much flatter than in the (FC-)ADK case.

In order to understand the already mentioned seemingly reduced ionization yield around $x = 0$ found for $\lambda = 800$ nm and there, especially, for $I = 10^{13}$ W/cm^2), it has to be reminded that these parameters indicate that the picture of multiphoton ionization becomes increasingly more adequate to describe the ionization behavior, since one finds for the Keldysh parameter $\gamma \approx 3$. One prominent signature of multiphoton ionization is the occurrence of resonance-enhanced multiphoton ionization (REMPI). As a more detailed analysis reveals, there is no suppression of the ionization yield around $x = 0$, but an increase of the ionization yield can be observed due to REMPI processes at $x \approx \pm 0.7$ a.u. and $x \approx \pm 1.3$ a.u. These maxima are

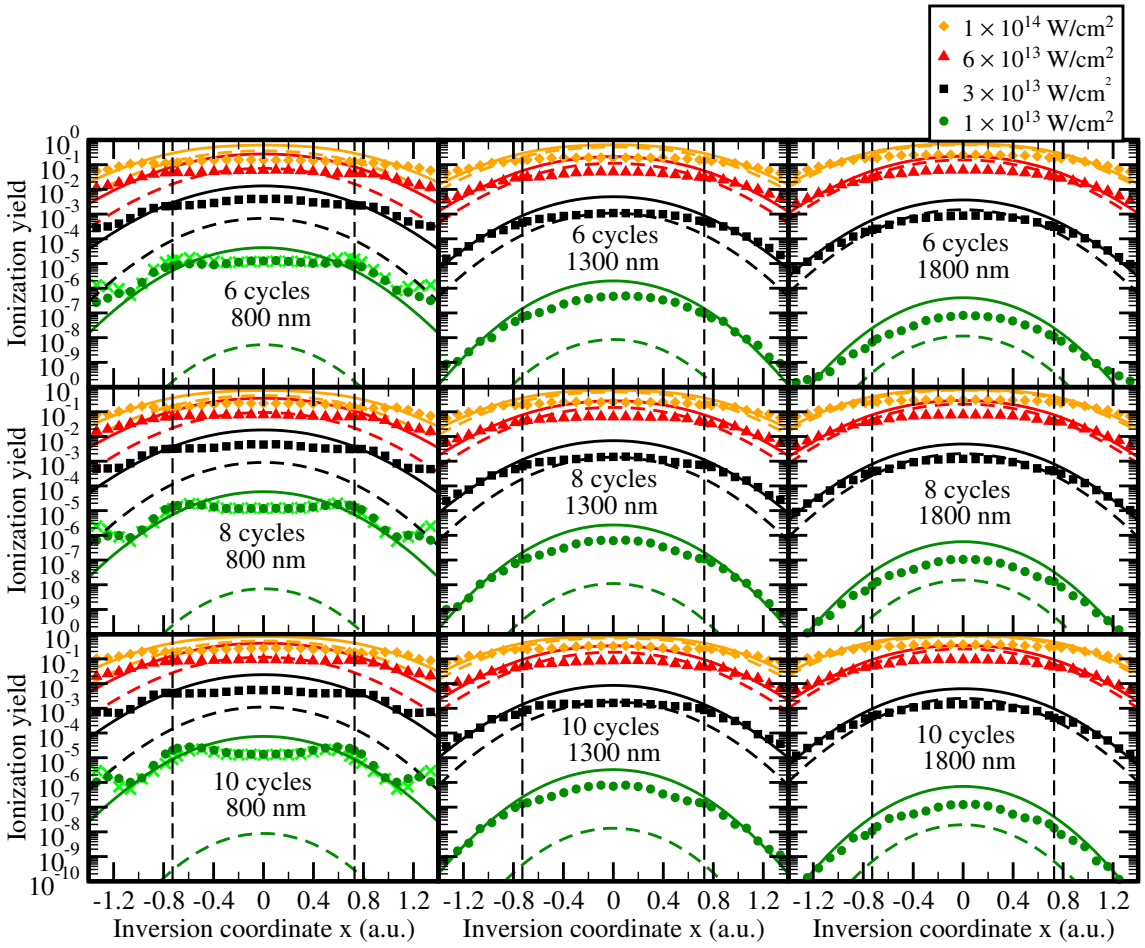

Figure 4.54: Geometry-dependent ionization yields obtained from TDSE (points), ADK (dashed lines), and FC-ADK (full lines) for different intensities, wavelengths, and number of laser cycles (values are given inside the graph). The dashed vertical lines indicate the equilibrium geometry at $x_{\mathrm{eq}} = \pm 0.728$ a.u. Furthermore, the light green crosses display the excitation yield for $\lambda = 800$ nm and peak intensity 10^{13} W/cm^2. This figure is also presented in [4].

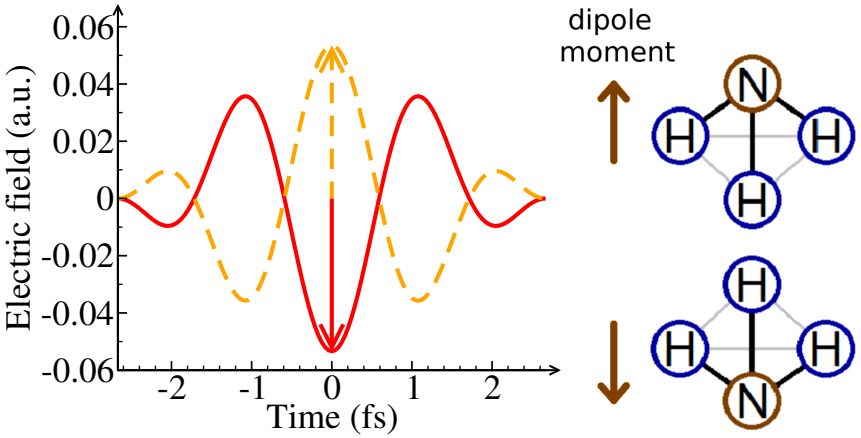

Figure 4.55: The time dependence of an electric field with $n_c = 2$ cycles total duration, wavelength $\lambda = 800$ nm, peak intensity $I = 10^{14}$ W/cm^2 and carrier-envelope phase $\phi = 0$ ($\phi = \pi$) is shown left as dashed orange (full red) line. For an electric field pointing along the inversion axis going through the nitrogen atom and the center of the triangle spanned by the hydrogen atoms, the maximum of the field may point parallel or antiparallel to the dipole moment of the molecule as indicated on the right. This figure is also presented in [4].

responsible for the local minimum at $x = 0$. This explanation is validated by considering the excitation yield (population of all initially unoccupied orbitals with an energy below the ionization threshold) that is also shown (for three laser fields) in Figure 4.54. The excitation yield behaves similar to the ionization yield and is quantitatively comparable to or, for $n_c = 6$ cycles, even exceeds the ionization yield, confirming the occurrence of REMPI processes. Furthermore, with increasing laser-field duration resonance structures become narrower and more pronounced due to the narrower frequency band width of the Fourier-limited laser field. This is in agreement with the laser-field-length dependence of the structures seen in both the ionization and the excitation yields. The maxima (and thus also the local minimum at $x = 0$) are most prominent for the longest laser fields considered in this chapter. Since REMPI processes are by definition not considered in ADK and FC-ADK, the seeming agreement of FC-ADK with the TDSE results around $|x| = 0.7$ a.u. is thus in fact accidental and due to an overall overestimation of the ion yield within FC-ADK at those laser parameters.

Lochfraß is now considered similarly to previous studies for diatomic molecules [30–33]. Starting from ammonia in its thermal equilibrium state (50% $|0s\rangle$ and 50% $|0a\rangle$), the geometry dependence of the ionization yield will create a wave packet as sketched in Figure 4.56. The wave packet created in the NH_3^+ ion (Figure 4.56 top) is shifted towards smaller values of $|x|$ due to the enhancement of the ionization yield at smaller $|x|$. This wave packet will then move towards the potential minimum of

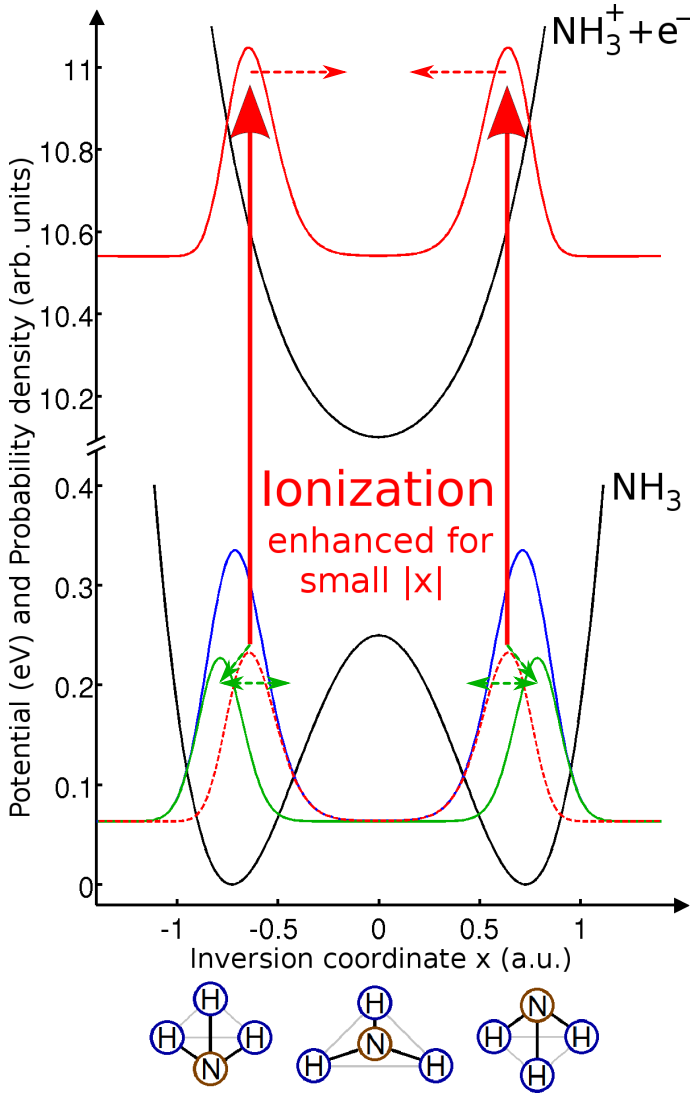

Figure 4.56: Potential energy curves of the electronic ground states of NH_3 and NH_3^+ (black lines) and probability density of the initial state (blue line). The full red line indicates the density generated in NH_3^+ due to ionization. This part of the probability density is then missing in neutral NH_3 as indicated by the dashed red line, such that the density indicated by the green line is created. This figure is also presented in [4].

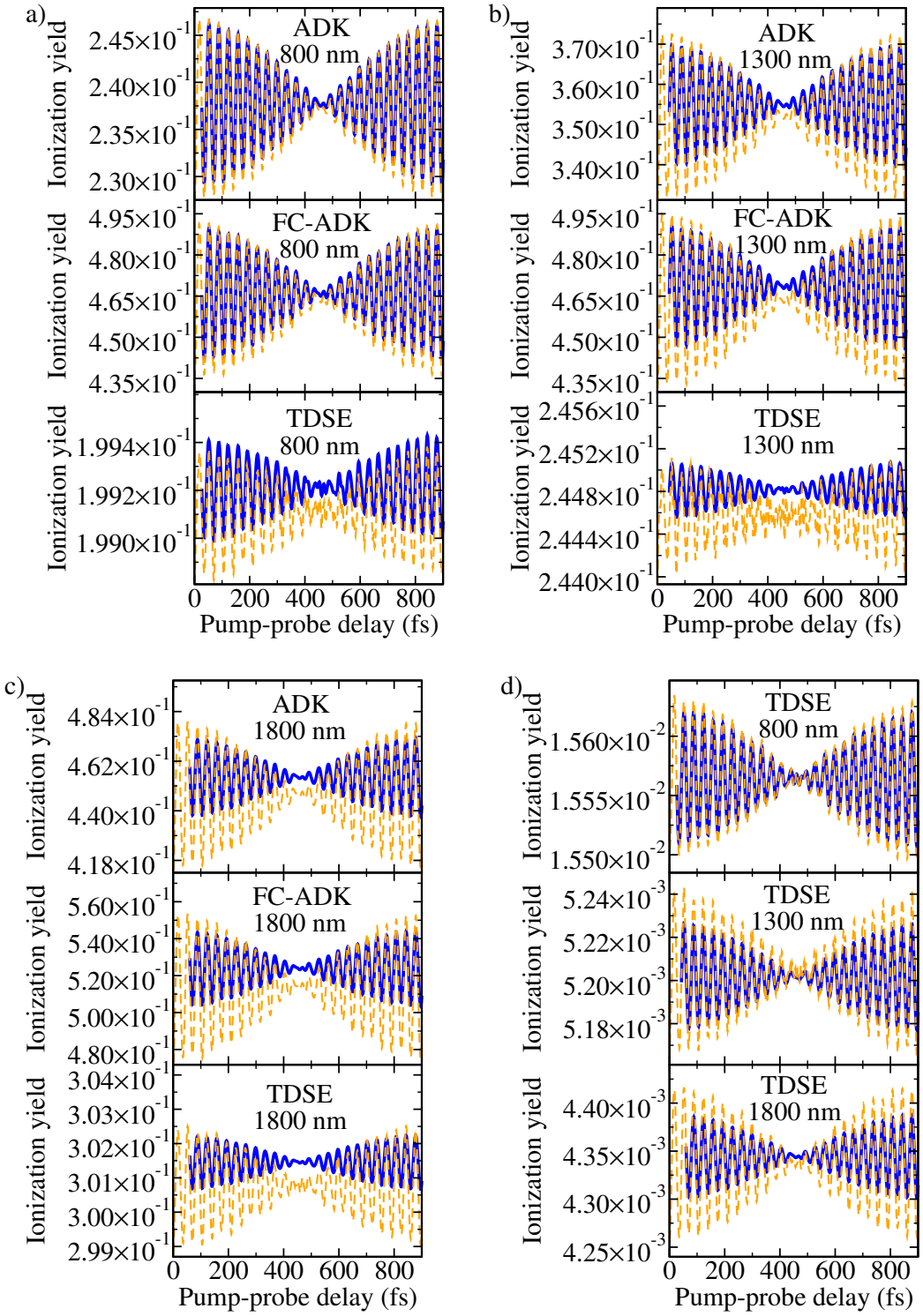

Figure 4.57: Probe field ionization yield as a function of the pump-probe delay. a-c) A 10 cycle 10^{14} W/cm^2 pump field is followed by an identical 10 cycle 10^{14} W/cm^2 probe field. Shown is the full time-dependent solution of Eq. (4.108) (full blue lines) and the sudden ionization approximation, Eq. (4.109) (dashed orange lines).
d) as a-c), but for a less intense 10-cycle 4×10^{13} W/cm^2 probe field and showing the TDSE ionization yields only.
This figure is also presented in [4].

NH_3^+, see [2] for a detailed study. Since the probability density remaining in neutral NH_3 is mostly depleted at small values of $|x|$, a wave packet shifted towards larger values of $|x|$ remains after ionization (Figure 4.56 bottom). This wave packet will then oscillate inside the minima of the double minimum potential. To probe the wave packet in neutral NH_3, one can again exploit the geometry dependence of the ionization yield. Whenever the wave packet is close to the potential barrier around $x = 0$ a.u., the total ionization probability will be enhanced compared to positions further away from the barrier. Thus, one can use a pump laser field to create the wave packet and image it with a probe laser field. The created wave packet can then be followed in real time by varying the pump-probe delay. Figure 4.57a-c shows the ionization yield of the probe field as a function of the pump-probe delay using two delayed, identical $n_c = 10$ cycle laser fields with a peak intensity of $I = 10^{14}$ W/cm^2 and wavelengths $\lambda = 800, 1300$, and 1800 nm. In all cases a similar oscillation of the ionization yield is observed. This oscillation can easily be understood considering that the symmetry with respect to x is not broken at any time and that the probability densities of $|0s\rangle$ and $|0a\rangle$ are (almost) equal. Thus, two independent oscillations with initially same amplitude and phase are launched, one for the symmetric and another one for the antisymmetric part. Similarly to H_2 [30], mainly the first excited state (but here of each symmetry) gets populated by the pump laser field. The oscillations for each symmetry have a period of

$$T_s = \frac{2\pi\hbar}{E_{1s} - E_{0s}} \approx 35.80 \text{ fs} \quad \text{and} \tag{4.110}$$

$$T_a = \frac{2\pi\hbar}{E_{1a} - E_{0a}} \approx 34.47 \text{ fs} \quad . \tag{4.111}$$

Due to this slight difference in their oscillation period (or frequency), both contributions will cancel out after

$$\frac{T_{\text{envelope}}}{2} = \frac{T_s T_a}{2\,(T_s - T_a)} \approx 462 \text{ fs} \tag{4.112}$$

and revive after T_{envelope}, as is seen in Figure 4.57 for all cases. Regarding the absolute numbers, one can see that ADK and FC-ADK predict a significantly larger contrast (oscillation height vs. average value of the ionization yield) than the TDSE. This is due to the much smaller $|x|$ dependence of the TDSE ionization yields for $I = 10^{14}$ W/cm^2, see Figure 4.54. Especially for 800 nm, the contrast $C = (Y_{\max} - Y_{\min})/Y_{\text{average}}$ is extremely small in the TDSE case, $C_{\text{TDSE}} \approx 0.0023$, compared to $C_{\text{ADK}} \approx 0.072$ and $C_{\text{FC-ADK}} \approx 0.10$. For 1800 nm, the contrast changes mainly for the TDSE and is larger, $C_{\text{TDSE}} \approx 0.0053$, but still more than an order of magnitude smaller than $C_{\text{FC-ADK}} \approx 0.078$. Even longer wavelengths could possibly improve the contrast further. The sudden ionization approximation for the nuclear motion, Eq. (4.109), which is also shown in Figure 4.57 agrees qualitatively very well (almost quantitatively) to the time-dependent solution of Eq. (4.108). Noteworthy, for the TDSE results at 800 and 1300 nm where the signal is very small, the sudden

ionization approximation shows a more "spikey" signal.

Figure 4.57d considers a similar pump-probe scheme as before, but with a lower probe field intensity of $I = 4 \times 10^{13}$ W/cm^2. Since the geometry dependence of the TDSE ionization yield is larger for smaller intensities, one would expect a higher contrast. Indeed, the contrast now reaches the percentage regime, namely $C_{\mathrm{TDSE}} \approx 0.007\,(0.01, 0.02)$ for $800\,(1300, 1800)$ nm. The contrast may be further increased using even lower probe field intensities. This would lead to even lower total ionization yields which, however, may cause practical problems due to experimental sensitivity limits. The optimal intensity is thus a compromise between contrast and sensitivity and depends on the given experimental setup.

4.6.3 Imaging of a Tunneling Wave Packet

Since the ionization yield gets larger whenever a wave packet moves closer to the barrier of the double-well potential, one may think of exploiting this behavior to directly observe a wave packet tunneling through the barrier. Considering a coherent superposition of the two lowest vibrational eigenstates,

$$|\chi(t=0)\rangle \;=\; \frac{1}{\sqrt{2}}\,(\,|0s\rangle \;+\; |0a\rangle\,) \quad , \tag{4.113}$$

a wave packet tunneling from one side to the other is achieved. This wave packet can be realized considering that the ammonia maser operates on the $|0s\rangle \leftrightarrow |0a\rangle$ transition [63]. Starting from a beam of $|0a\rangle$ states within a maser set-up, the wave packet $|\chi(t=0)\rangle$ is created after a quarter of the maser transition period and may then propagate freely. Then, after

$$\tau \;=\; \frac{\pi\hbar}{E_{0a} - E_{0s}} \;\approx\; 20 \text{ ps} \tag{4.114}$$

this wave packet will have tunneled completely to the other side. The probability density $\rho(x,t) = |\chi(x,t)|^2$ of the wave packet evolves according to

$$\rho(x,t) \;=\; \cos^2\left(\frac{\pi t}{2\tau}\right)\,\rho_{\mathrm{left}}(x) \;+\; \sin^2\left(\frac{\pi t}{2\tau}\right)\,\rho_{\mathrm{right}}(x) \tag{4.115}$$

where

$$\rho_{\mathrm{left}}(x) \;=\; \rho(x,0) \;=\; \frac{1}{2}\,\big|\,\chi_{0s}(x) \;+\; \chi_{0a}(x)\,\big|^2 \tag{4.116}$$

corresponds to the probability density localized on the left side of the double-well potential and

$$\rho_{\mathrm{right}}(x) \;=\; \rho(x,\tau) \;=\; \frac{1}{2}\,\big|\,\chi_{0s}(x) \;-\; \chi_{0a}(x)\,\big|^2 \tag{4.117}$$

to the density localized on the right side. If a single 10-cycle laser field is used to probe this wave packet, the ionization yield remains, however, almost constant during the tunneling process as is seen in the top row of Figure 4.58. Due to the symmetry of the tunneling process, the ionization yield even stays perfectly constant for an ionization yield $Y(x)$ which is symmetric in x ($\leftrightarrow -x$). This reflects the way how this wave packet tunnels according to Eq. (4.115). Figure 4.59 shows snapshots of the time evolution of this wave packet. Instead of "moving through" the barrier, the probability density rather disappears on one side of the barrier and appears on the other. Thus, even what naively seems to be the perfect detector for imaging the tunneling process, a symmetric probe where the signal is larger when the probability density is located further inside the tunneling barrier, yields only a constant signal during the tunneling process. However, observing a non-constant signal could be an experimental evidence for deviations from standard quantum mechanics.

4.6.4 Breaking the Symmetry: Imaging with an Asymmetric Ionization Yield

In order to follow the tunneling wave packet, Eq. (4.115), it is necessary to break the symmetry of the ionization yield $Y(x)$ with respect to x. This is the case if for an oriented molecule the direction of the electric field maximum with respect to the dipole moment (see Figure 4.55) leads to significantly different ionization yields for the parallel and antiparallel orientations as was demonstrated and discussed for the water molecule [98]. Figure 4.60 shows that for very short laser pulses of only $n_c = 2$ cycles, the TDSE ionization yields are indeed highly asymmetric, for example $Y(x = 0.73 \text{ a.u.})/Y(x = -0.73 \text{ a.u.}) \approx 3.7$ (4.6, 5.1) for 800 (1300, 1800) nm and $I = 10^{14}$ W/cm^2. For $n_c = 4$ cycles, the ionization yields are still notably asymmetric, e.g. $Y(x = 0.73 \text{ a.u.})/Y(x = -0.73 \text{ a.u.}) \approx 1.2$ (1.4, 1.4) for 800 (1300, 1800) nm and $I = 10^{14}$ W/cm^2. The asymmetry is superimposed to the previously discussed enhancement of the ionization yield for smaller $|x|$. Note that this asymmetry is not described within standard (FC-)ADK, Eq. (4.46), since the binding energy $I_p(x)$ is perfectly symmetric with respect to x. (A corresponding extension including dipole effects in the weak-field limit has, however, been suggested in [170, 171].)

The contributions of internuclear distances $Y_{\text{TDSE}}(x)\,|\chi(x)|^2$ to the x-integrated frozen-nuclei ionization yield Eq. (4.40) is shown in Figure 4.61 for very short ($n_c = 2$ cycles) and long ($n_c = 10$) laser pulses. Similarly to the case of the H_2 molecule in Section 4.2 the main contribution to the ionization yield is shifted away from the equilibrium geometry at $x_{\text{eq}} = \pm 0.728$ a.u. especially for lower intensities (corresponding to a large $|x|$-dependence). Of course, the strong asymmetry of $Y(x)$ for very short $n_c = 2$ cycle laser fields is directly translated to a strong asymmetry of the corresponding contribution of inversion geometries to the total ionization yield. However, due the overall smaller $|x|$-dependence of NH_3 compared to the R-dependence of H_2 the shift of the main contribution seems less pronounced in the case of NH_3. For the highest intensity $I = 10^{14}$ W/cm^2 the main contribution

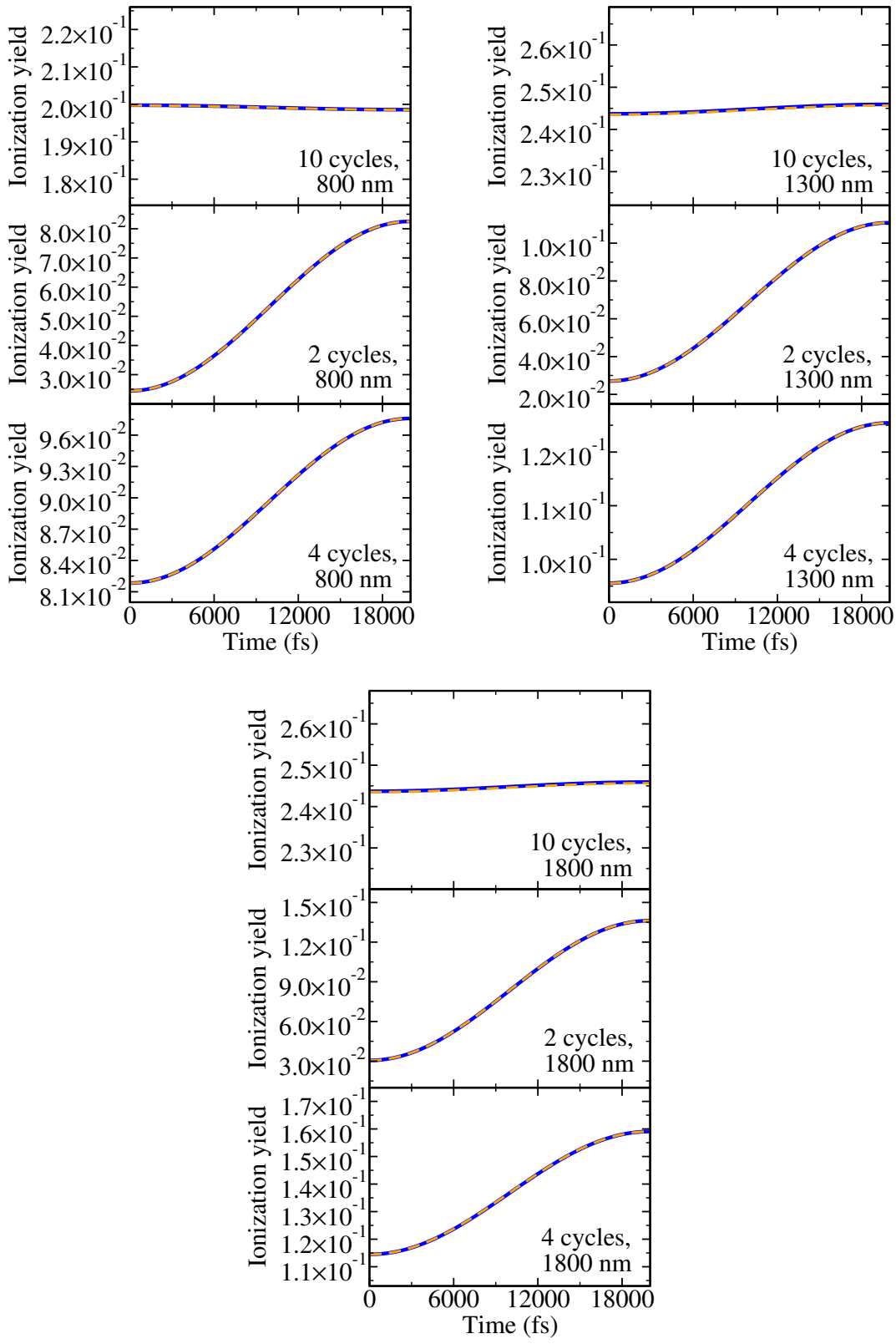

Figure 4.58: Ionization yield for $I = 10^{14}$ W/cm^2 laser fields (number of cycles and wavelength given inside the graphs) probing the tunneling wave packet. Shown are the full time-dependent solutions of Eq. (4.108) (full blue lines) and the results within the sudden ionization approximation, Eq. (4.109) (dashed orange lines). This figure is also presented in [4].

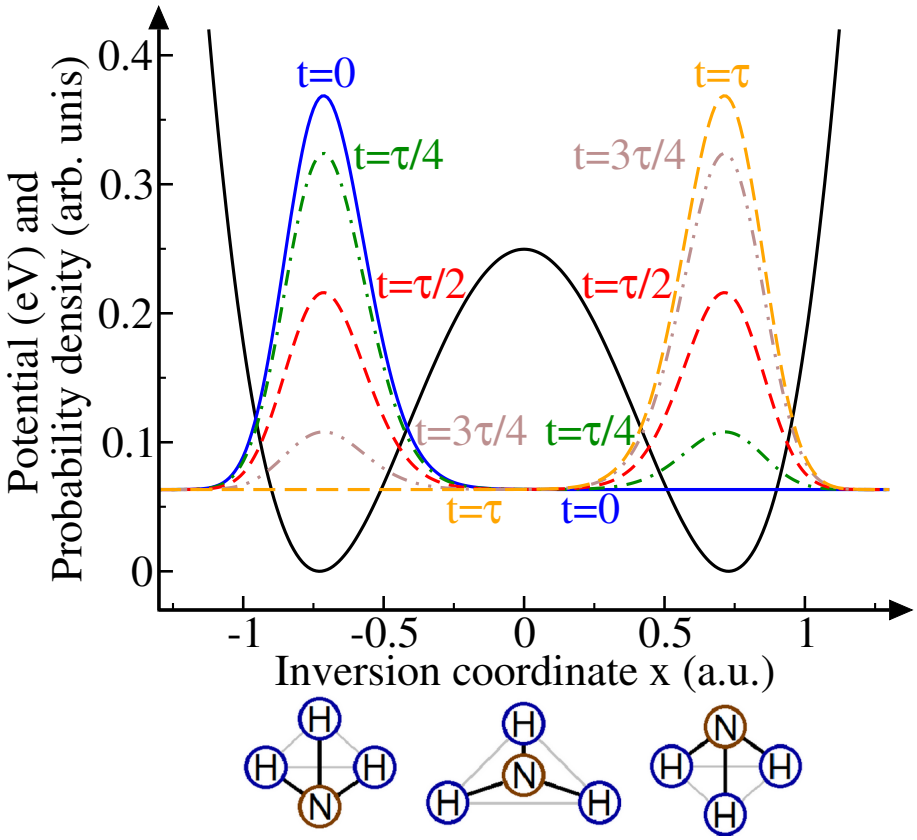

Figure 4.59: Snapshots of the time evolution of the tunneling wave packet (full blue line and dashed / chain lines) for $t = 0, \tau/4, \tau/2, 3\tau/4$, and τ in the ground state potential of NH_3 (full black line) where τ is the time required to tunnel from one well to the other completely, Eq. (4.114). This figure is also presented in [4].

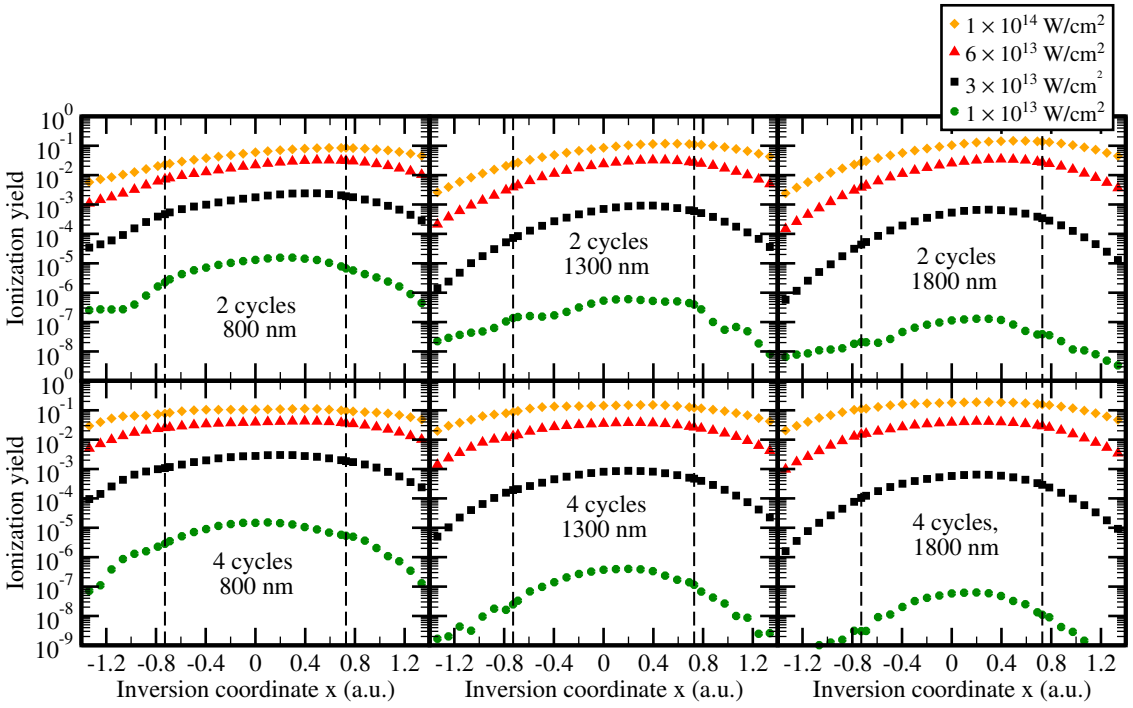

Figure 4.60: As Figure 4.54, but for shorter $n_c = 2$ and 4 cycle laser fields and using TDSE ionization yields only. This figure is also presented in [4].

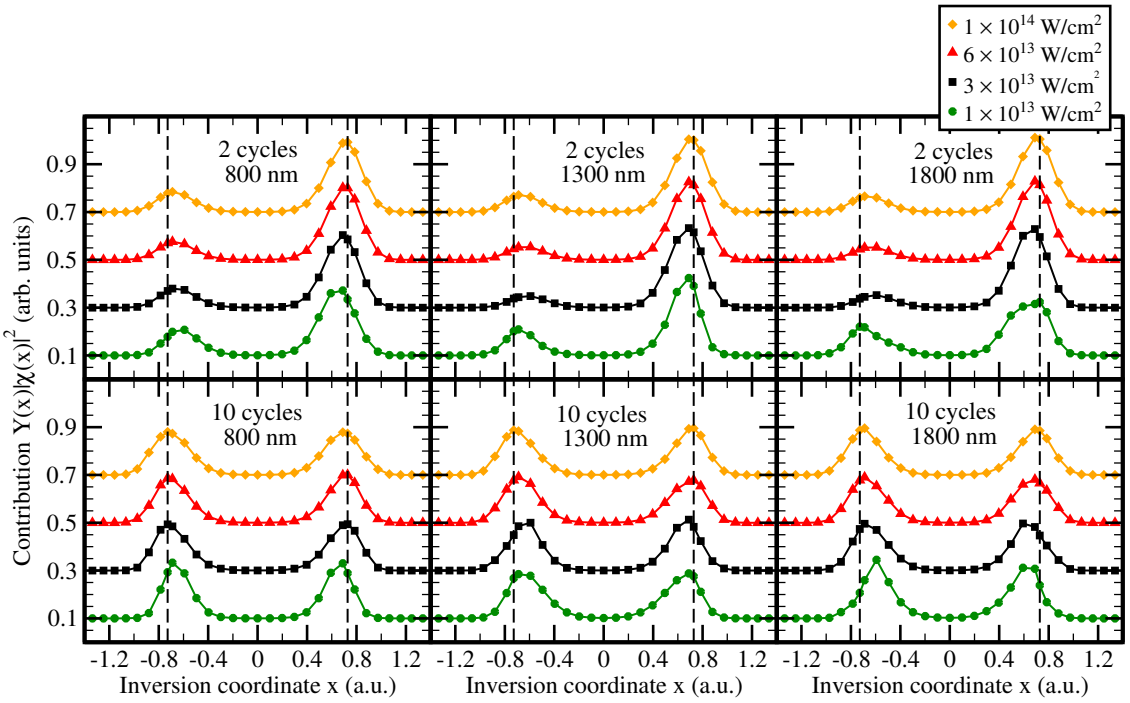

Figure 4.61: Contributions $Y_{\mathrm{TDSE}}(x)\,|\chi(x)|^2$ of internuclear distances to the (x-integrated) frozen-nuclei ionization yield Eq. (4.40) for different laser-field durations, wavelengths and intensities are given inside the graph (scaled and vertically shifted for better visibility). The dashed vertical lines indicate the equilibrium geometry at $x_{\mathrm{eq}} = \pm 0.728$ a.u.

indeed stems from the equilibrium geometry.

The second and third row of Figure 4.58 show the time dependence of the total ionization yield for the $n_c = 2-4$ cycle laser fields from Figure 4.60. As expected, the ionization yield strongly increases with time, thus these laser fields indeed allow for following the tunneling wave packet, Eq. (4.115), during the tunneling process. For these very short laser pulses, the sudden ionization approximation agrees perfectly to the full solution of Eq. (4.108).

An asymmetric wave packet in neutral NH_3 may also be created starting from the 50% $|0s\rangle$, 50% $|0a\rangle$ thermal equilibrium state by ionizing with an asymmetric ionization yield $Y(x)$, see Figure 4.62. A *Lochfraß* pump-probe scheme is now considered as previously, but now using two 2-cycle 10^{14} W/cm^2 laser fields. In this case, the density matrix describing the ensemble is propagated within the sudden ionization approximation since an independent propagation of $|0s\rangle$ and $|0a\rangle$ is not possible for an asymmetric ionization yield. However, as previously noted, the sudden ionization approximation agrees perfectly to the solution of the TDSE for these very short laser fields. Figure 4.63 shows the obtained probe field ionization yields. The behavior of the probe field ionization yield follows the expectation value $\langle x\rangle$ of the wave packet. The created asymmetry leads to a behavior similar to the tunneling wave packet in Figure 4.58, but with a significantly smaller contrast since the asymmetry created by the pump field is smaller. Superimposed to the signal from tunneling is an oscillation similar to the signal for 10-cycle laser fields, Figure 4.57, due to the $|x|$ dependence of the ionization yield, Figure 4.60. The contrast of this sub-structure depends on the $|x|$ dependence of the ionization yield on either side. For example, the very flat behavior of the ionization yield for $n_c = 2$ cycles, $\lambda = 800$ nm and $I = 10^{14}$ W/cm^2, Fig.4.60, leads to a rather small sub-oscillation of the ionization yield at the end of the tunneling process compared to its beginning, see Figure 4.63.

Note that an asymmetric ionization behavior may also be observed for longer laser pulses as an asymmetry in the emission direction of the electrons and thus if the angle-resolved photoelectron spectra are recorded. Alternatively, this asymmetry may be created by using $\omega/2\omega$ laser fields [172]. Therefore, a number of possible experimental realizations of directly observing the tunneling process in ammonia exists.

4.6.5 Conclusions

The geometry-dependent ionization behavior of ammonia has been studied by solving the TDSE within the single-determinant approximation. For 10-cycle laser fields ADK qualitatively predicts the correct ionization yield, while FC-ADK agrees to the TDSE almost quantitatively over the whole intensity range. However, both ADK and FC-ADK significantly overestimate the increase of the ionization yield with decreasing inversion coordinate $|x|$. Thus, while similar vibrational dynamics through *Lochfraß* is observable using TDSE or (FC-)ADK ionization yields, the contrast of the oscillation of the ionization yield is much smaller for the TDSE ionization yield

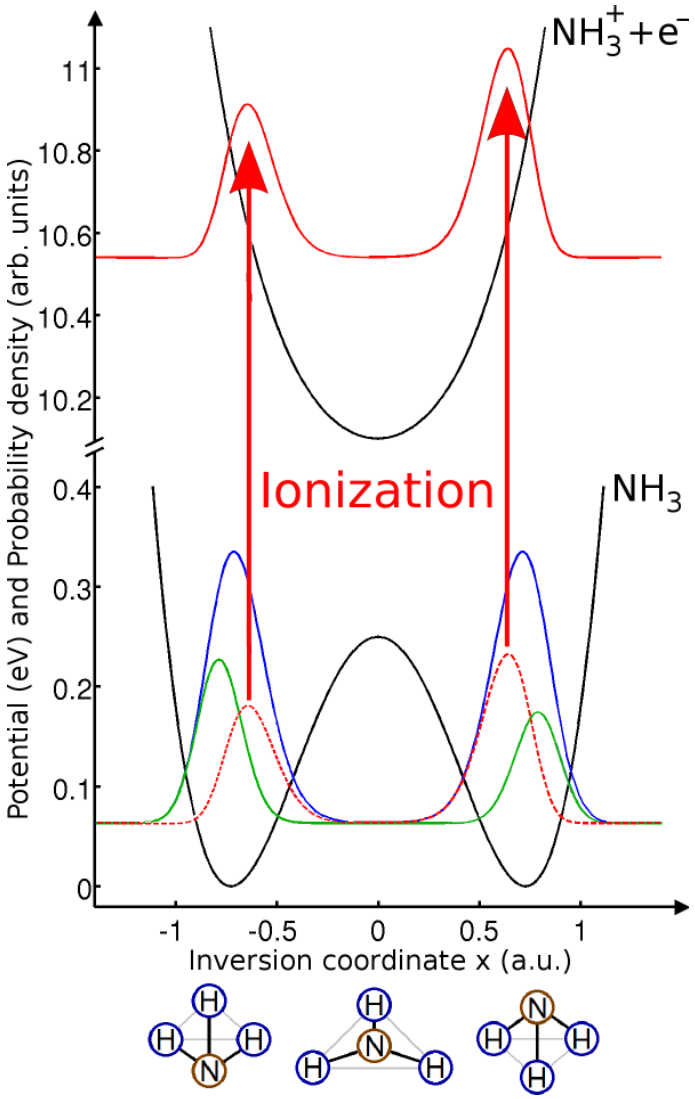

Figure 4.62: As Figure 4.56, but for an asymmetric ionization yield. This figure is also presented in [4].

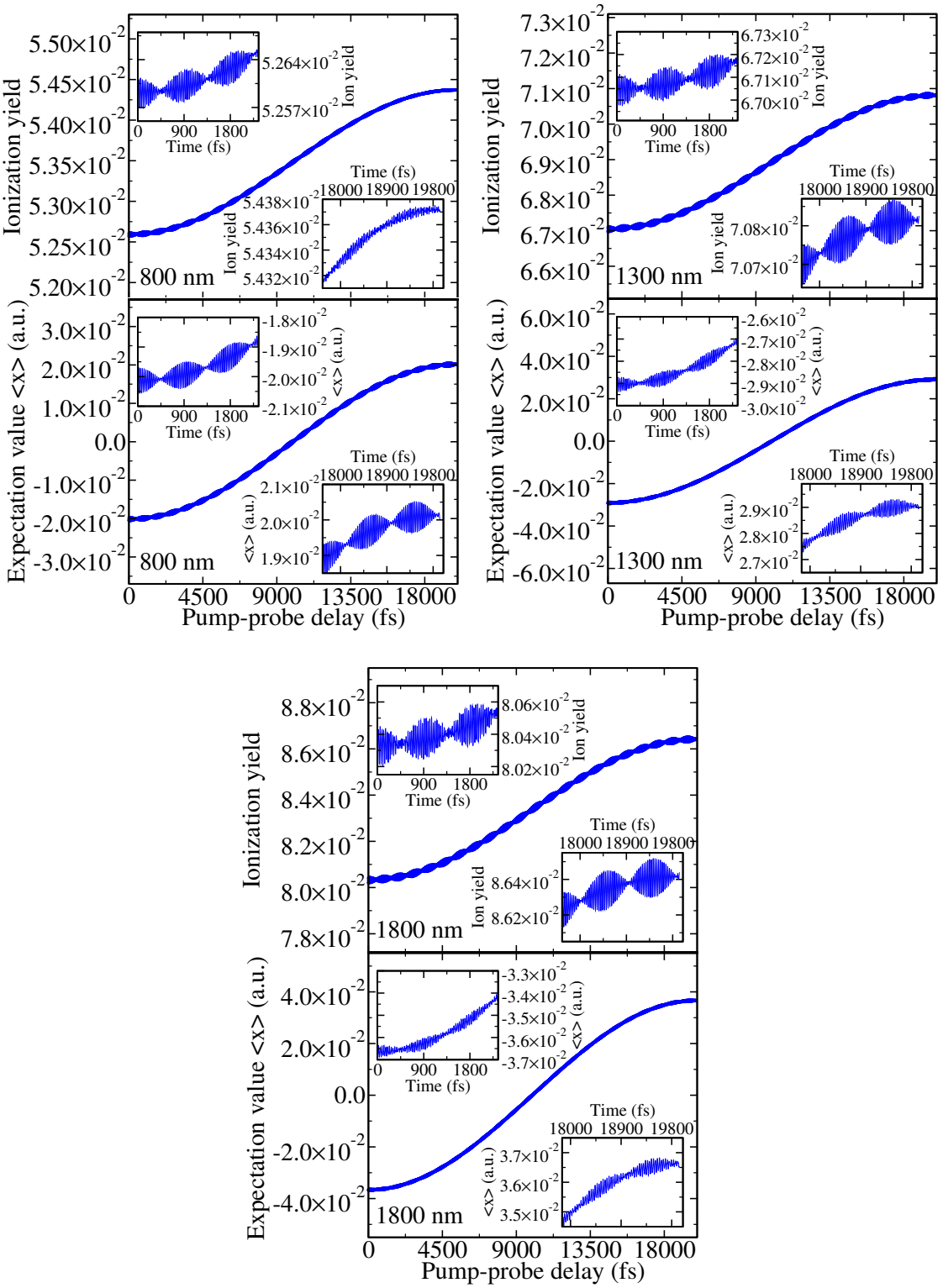

Figure 4.63: Probe field ionization yield as a function of the pump-probe delay for wavelengths 800, 1300, and 1800 nm. A 2-cycle 10^{14} W/cm^2 pump field is followed by an identical 2-cycle 10^{14} W/cm^2 probe field. Shown is the probe field ionization yield obtained from the propagation of the density matrix (upper subplots) and the expectation value $\langle x \rangle$ of the created wave packet (lower subplot). The insets enlarge the signal at the beginning and the ending of the graph. This figure is also presented in [4].

compared to (FC-)ADK. The contrast can nevertheless be improved using 1800 nm instead of 800 nm or a weaker probe field.

Furthermore, imaging of a tunneling wave packet has been discussed. While a detector leading to an increased ionization yield for wave packets close to the tunneling barrier may seem perfect to follow the tunneling process in real time, any geometry-dependent ionization yield symmetric in x leads to a perfectly constant signal. This can be understood looking at how the probability density evolves during the tunneling process. It was shown that very short 2-4 cycle laser fields break the symmetry of the geometry-dependent ionization yield with respect to x, allowing to follow the tunneling wave packet in real time. Finally, *Lochfraß* using two 2-cycle laser fields shows both the behavior of the tunneling wave packet and the faster beating oscillations previously discussed for the longer 10-cycle laser fields.

Clearly, an experimental measurement of the predictions made here would pave the way for future real-time movies of quantum-mechanical nuclear motion in polyatomic neutral molecules. The results show that FC-ADK may give a good estimate for laser parameters in order to observe *Lochfraß* also for other, especially more complex molecules which undergo an equilibrium geometry change upon ionization, though the contrast may be overestimated. For oriented molecules, asymmetries in the ionization behavior allow for even more applications such as the real-time movie of the tunneling process discussed here. One may even be able to follow proton or heavy-atom tunneling in biologically relevant molecules [173–177], provided the ionization yield of the orbital dominating the strong-field ionization process (usually the HOMO) changes sufficiently as a function of the tunneling coordinate.

All calculations performed so far have been restricted to an (anti-)parallel orientation of the laser polarization vector with respect to the inversion axis. In the next section, the orientation dependence of the NH_3 ionization yield and even elliptically polarized laser fields are investigated.

4.7 Orientation-Dependent Ionization of Ammonia Molecules and Elliptically Polarized Fields

The investigation of the ionization behavior of NH_3 studied in Section 4.6 was restricted to a parallel orientation of the laser polarization with respect to the inversion axis x. Due to the shape of the HOMO orbital, this orientation is expected to yield the largest ionization probability and thus dominates the ionization behavior which was also observed experimentally in Ref. [21]. For a possible application of ultrashort, intense laser fields for orbital imaging [10, 11], on the other hand, the full orientation dependence of the ionization yield of NH_3 remains to be investigated. Furthermore, a strongly orientation-dependent ionization yield may allow to create rotational wave packets in order to prepare NH_3 molecules with a specific orientation [34, 35] (*Lochfraß* in the rotational degree of freedom). The parallel vs. anti-parallel asymmetry of the ionization yield of NH_3 observed for 2-cycle laser pulses in Section 4.6.4 for oriented NH_3 molecules should directly translate to the orientation dependence. The duration of the laser field may thus add an additional control knob. Further insights may also be gained by considering a time-dependent change of the direction of the polarization vector, i.e. an elliptically polarized laser field.

Ionization from the $3A_1$ HOMO orbital is comparably simple to treat numerically for a parallel orientation of the polarization vector with respect to the inversion axis since only orbitals with a_1 symmetry can be populated by the laser field. The character table for the C_{3v} symmetry point group of NH_3 is given in Table 4.4. Transitions to orbitals belonging to the remaining **ir**reducible **rep**resentation**s** (irreps) A_2 and E are forbidden due to the symmetry selection rules. This greatly reduces computational costs not only because just one symmetry is involved, but also because of the number of orbitals belonging to the irrep A_1 (A_2) is small compared to the irrep E. For the basis set in Section 4.6 with energy cutoff 10 a.u. above the continuum threshold, there are 11889 orbitals of a_1 symmetry, 7123 orbitals of a_2 symmetry and 19007 orbitals of e symmetry. A dipole transition block for an $e \leftrightarrow e$ transition is thus 2.6 times as large as for an $a_1 \leftrightarrow a_1$ transition. Furthermore, a problem in the implementation of the C_{3v} symmetry group in the TP_SAE program[35] for non-parallel orientations of the laser polarization with respect to the inversion axis was identified by the author. Ionization yields from orbitals with a_1

[35] This single-determinant approach program by S. Petretti, Section 3.4, has been extended by E. Plésiat for the treatment of the C_{3v} symmetry group.

	E	$2C_3$	$3\sigma_v$
A_1	1	1	1
A_2	1	1	-1
E	2	-1	0

Table 4.4: Character table for point group C_{3v}.

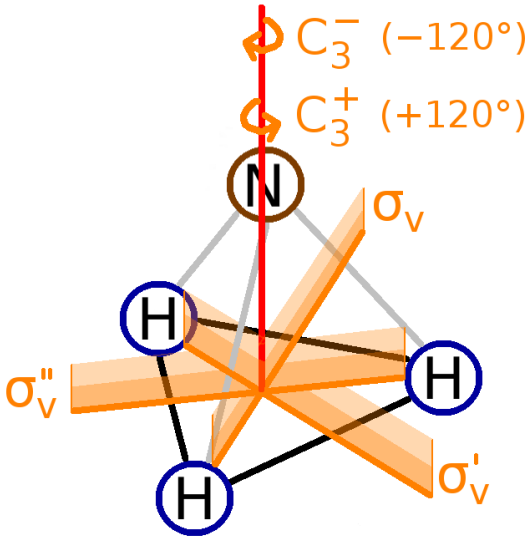

Figure 4.64: Symmetry operations relevant for the NH_3 molecule (C_{3v} point group). Sketched in orange are the three mirror planes σ_v, σ'_v, and σ''_v and the rotations C_3^+ and C_3^- ($+/-120°$ around the inversion axis, red line).

symmetry must be symmetric with respect to the symmetry operations of the C_{3v} group, Figure 4.64 (see also Table 4.4), which was not fulfilled. The results showed a large gauge dependence (except for the case of parallel orientation). The difference of the C_{3v} group compared to symmetry groups studied earlier with TP_SAE arises from the doubly-degenerate irrep E wheres only groups with non-degenerate irreps have been studied before. Within a short-term scientific mission (STSM) with P. Decleva[36] the author improved the TP_SAE program to obtain consistent results[37] and furthermore added the functionality to perform time propagations with

[36] In Trieste, Italy, January-March 2017.

[37] In the following, the steps to successfully correct the implementation of the C_{3v} group are recapitulated (this may be helpful for future students encountering problems with TP_SAE). For the degenerate irrep E there are two classes of orbitals which may be labeled as $|E_1\rangle$ and $|E_2\rangle$. Within the code, the energies and transition moments of the $|e\rangle$ orbitals are calculated from symmetry relations, e.g. $\langle E_2|x|E_2\rangle = +\langle E_1|x|E_1\rangle$ and $\langle E_2|y|E_2\rangle = -\langle E_1|y|E_1\rangle$. The problem could be narrowed down after calculating all transition matrices directly (P. Decleva) instead of using symmetry relations. By modifying the interface to read in all matrices (requiring almost twice as much storage space), the time propagation now lead to the correct behavior for the ionization yield (symmetry and gauge independence). This cross-check is thus advised when future symmetries are implemented. The implementation of the symmetry relations to calculate degenerate matrices turned out to be correct, however. By choosing a skewed orientation of the laser polarization (an orientation neither aligned to the x, y or z axis) and comparing dipole transition elements directly with the version that works correctly, it was found that the only difference was within the $\left\langle E_2\middle|\hat{\mathrm{d}}\middle|E_2\right\rangle$ transition block. For these transitions, the program tried to reuse the $\left\langle E_1\middle|\hat{\mathrm{d}}\middle|E_1\right\rangle$ transition block since it was constructed from the symmetry relation.

elliptically polarized laser fields. In the following, results obtained with this new program version, TP_SAE_v5, are presented. These orientation- and propagation-direction-dependent results are obtained at a fixed internuclear distance. Since these calculations are computationally much more expensive than only (anti-)parallel orientations, a complete variation of the nuclear geometry as in Section 4.6 is presently out of reach for the laser parameters studied here[38]. For simplicity the SAE-TDSE ionization yields are shown directly in the following without applying the factor 2 ($N_e = 2$ active electrons) for small ionization yields (or intensities).

The orientation dependence of the NH_3 molecule exposed to linearly polarized 2- and 10-cycle laser pulses is studied in the following section. The influence of the carrier-envelope phase of the laser field for specific orientations is investigated in Section 4.7.2. Finally, a new implementation to treat elliptically polarized laser fields is demonstrated in Section 4.7.3 for 2- and 10-cycle left and right circularly polarized laser pulses.

4.7.1 Orientation Dependence

In the following the polarization direction $\vec{\mathcal{P}}$ is represented by spherical coordinates as shown in Figure 4.65, i.e.

$$\vec{\mathcal{P}} = \begin{pmatrix} x \\ y \\ z \end{pmatrix} = \begin{pmatrix} \cos(\theta) \\ \sin(\theta)\cos(\varphi) \\ \sin(\theta)\sin(\varphi) \end{pmatrix} \quad . \tag{4.118}$$

For consistency, the coordinate system is chosen such that x is the inversion coordinate. For the carrier-envelope phase the values $\phi = 0$, $\theta = 0$ ($\theta = 180°$) correspond to a parallel (anti-parallel) direction of the laser field maximum $\vec{F}(t = 0)$ with respect to the unit vector $\vec{e}_x$ along the x axis (pointing from the plane spanned by the hydrogen atoms towards the nitrogen atom)[39].

Figure 4.66 shows orientation-dependent ionization yields $Y(\varphi, \theta)$ for a very short 2-cycle laser field. The variation of θ with fixed $\varphi = 30°$ shows a pronounced asymmetry for parallel vs. anti-parallel orientation ($\theta = 0$ vs. $\theta = 180°$) as observed for these very short laser fields in Section 4.6.4. The minimum of the ionization yield is located around $\theta = 90°$. This is consistent with the shape of the HOMO

However, noting the different signs for the x and y direction (see above), it is not possible to relate $\left\langle E_2 \middle| \hat{\mathrm{d}} \middle| E_2 \right\rangle$ to $\left\langle E_1 \middle| \hat{\mathrm{d}} \middle| E_1 \right\rangle$ with a single factor except for the special case that the laser polarization is aligned with only one axis. Removing the faulty reuse of transition blocks, but still using the symmetry relations, resulted in a perfect agreement with that version of the program that did not use symmetry relations at all.

[38] A calculation for a non-parallel orientation takes about 10 times longer than a parallel one. A orientation-dependent calculation exploiting symmetry and using 15° steps in θ and φ thus takes about 250 times longer than a single calculation for a parallel orientation.

[39] These relative directions have been identified by directly comparing propagated wave packet coefficients obtained using TP_SAE_v5 with the ones obtained by the time propagation method implemented very recently by P. Decleva (Krylov subspace propagator).

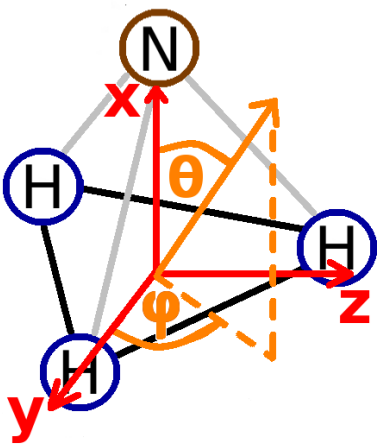

Figure 4.65: Sketch of the used coordinate systems with origin in the center of the triangle spanned by the three hydrogen atoms. The Cartesian coordinate system is shown in red. The spherical coordinates with angle θ relative to the x axis and angle φ of the projection on the y-z plane relative to the y axis are indicated in orange.

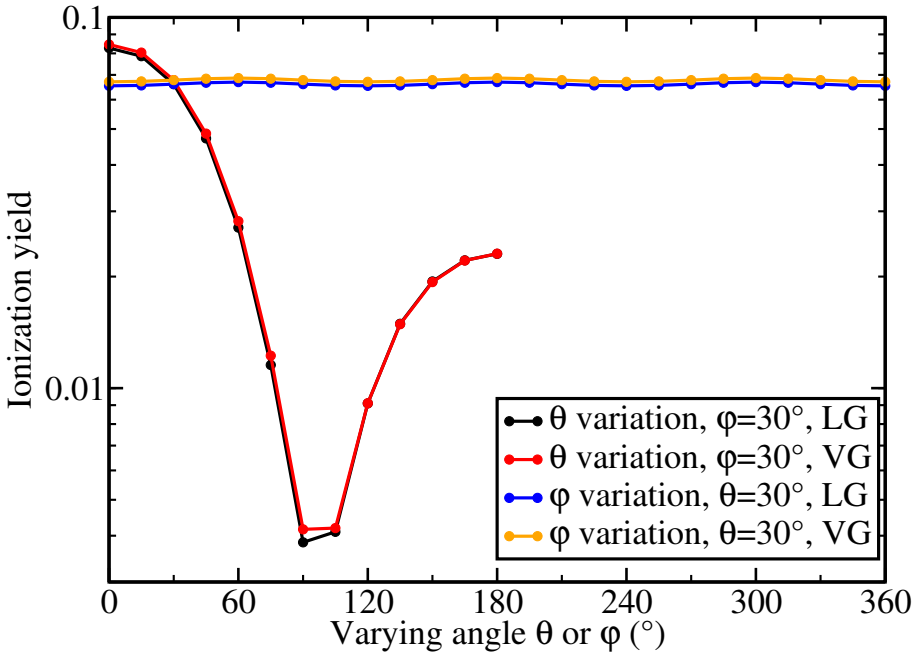

Figure 4.66: φ- and θ-dependent ionization yields for a 2-cycle 800 nm laser fields with peak intensity $I = 10^{14}$ W/cm^2 and carrier-envelope phase $\phi = 0$ obtained at the equilibrium geometry $x = 0.728$ a.u. For the correspondingly fixed angle the value 30° was chosen. Results obtained with length gauge (LG) and velocity gauge (VG) are shown.

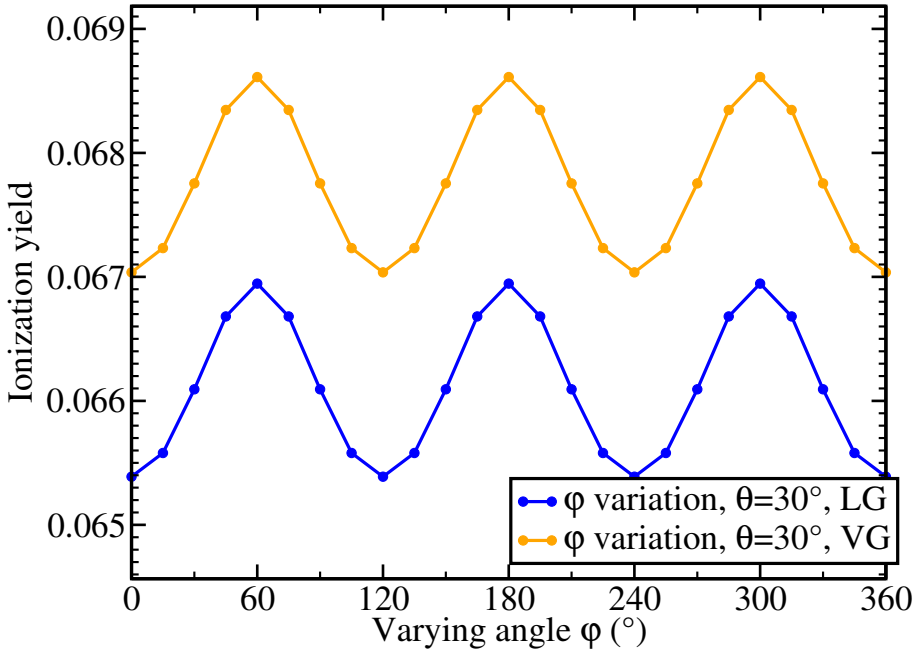

Figure 4.67: As Figure 4.66, but φ dependence only. (Note the magnification of the scale showing the ionization yield.)

orbital which has a very small probability density (almost a node) there (see, e.g., Fig. 2 in Ref. [178] for the shapes of the HOMO to HOMO-3 orbitals of NH_3). The variation of φ with fixed $\theta = 30°$ shows a very small φ dependence compared to the θ dependence. In both cases, yields obtained in length- and velocity gauge agree nicely on a similar level as in previous studies (e.g. page 66 in Ref. [96]).

Figure 4.67 shows the φ dependence only. A constant (but very small) offset between length and velocity gauges is observed. The observed oscillation as φ is varied is the simplest function (besides a constant function) which is invariant with respect to the symmetry operations of the C_{3v} group, Figure 4.64, i.e. rotations by 120° and reflections at the mirror planes at $60°, 180°$, and 300°. This invariance is expected for ionization from the HOMO orbital of NH_3 belonging to the a_1 symmetry.

In the following the full orientation dependence for 2- and 10-cycle 800 nm laser fields with peak intensities $10^{13} \ldots 10^{14}$ W/cm^2 is studied. The calculations are performed at the geometry contributing the most to the total ionization yield according to Figure 4.61 in Section 4.6.4. This corresponds to the equilibrium geometry $x = 0.728$ a.u. for 2-cycle laser fields with 10^{14} W/cm^2 peak intensity as well as 10-cycle fields with $\{3, 6, 10\} \times 10^{13}$ W/cm^2. For the remaining combinations of field intensities and durations the inversion coordinate is $x = 0.689$ a.u. The ionization yield $Y(\varphi, \theta)$ is calculated for $\varphi = 0 \ldots 360°$ and $\theta = 0 \ldots 180°$ using $\Delta\varphi = \Delta\theta = 15°$ steps and exploiting the symmetry of the ionization yield. Thus, only $\varphi = 0 \ldots 60°$ is calculated and the remaining part is constructed using symmetry relations. In order to visualize the orientation dependence in three dimensions an ionization yield

vector

$$\vec{Y}(\varphi,\theta) \equiv Y(\varphi,\theta)\,\vec{\mathcal{P}}(\varphi,\theta) \tag{4.119}$$

is defined (i.e. the length is the ionization yield $Y(\varphi,\theta)$ and the direction is the corresponding polarization direction $\vec{\mathcal{P}}(\varphi,\theta)$). Figure 4.68 shows these orientation-dependent ionization yields for very short 2-cycle laser fields. The asymmetry of the ionization yield depending on whether the polarization vector is parallel or anti-parallel to the x axis as well as the node in the x-y plane ($\theta = 90°$) is again clearly visible. The φ dependence is hardly visible as a small asymmetry when rotating around the x axis and best visible in the $x < 0$ lower part region (small ionization yields). In this lower part region, a different behavior of the φ dependence for different intensities can be observed. While for $I = 10^{13}$ W/cm^2 a maximum of the ionization yield is visible at $\varphi = 0$ and a minimum at $\varphi = 60°$, at $I = 6 \times 10^{13}$ W/cm^2 and $I = 10^{14}$ W/cm^2 the opposite is observed (minimum at 0 and maximum at 60°; for $I = 3 \times 10^{13}$ W/cm^2 the φ dependence is too small to be observed by eye).

Figure 4.69 shows these orientation-dependent ionization yields for longer 10-cycle laser fields. An asymmetry of the ionization yield depending on whether the polarization vector is parallel or anti-parallel to the x axis is not visible as expected from Section 4.6.2 for laser fields with $n_c \geq 6$ cycles duration. Again, a node in the x-y plane ($\theta = 90°$) is observed. For intensities smaller than 10^{14} W/cm^2 a relatively strong φ dependence is observed compared to the 2-cycle case. Surprisingly, the φ dependence switches its behavior between the lobe parallel to the x axis (maximum at $\varphi = 0$, minimum at $\varphi = 60°$) and the lobe anti-parallel to the x axis (minimum at $\varphi = 0$, maximum at $\varphi = 60°$).

In order to make the small φ dependence more visible, Figs. 4.70 and 4.71 show the minimum, maximum and average ionization yield for each θ (together with minimum and maximum positions) for the previously discussed 2- and 10-cycle laser fields. In most cases minima and maxima are located at either $\varphi = 0$ or $\varphi = 60°$ (red or blue horizontal bar). This corresponds to the simplest naturally occurring behavior fulfilling the symmetry properties similarly to Figure 4.67. However, since minimum and maximum locations may switch, there exist transition regions (with overall very small φ dependence) where the minimum or maximum is located at a different angle φ. The resulting φ dependence is thus more complex, see the example shown in Figure 4.72.

For the extremely short 2-cycle laser fields shown in Figure 4.70 the φ dependence seems pretty much negligible. Minimum and maximum positions of this small φ dependence switch their places $\varphi = 0 \leftrightarrow \varphi = 60°$ quite often, namely 3 times for 10^{13} and 3×10^{13} W/cm^2 and 2 times for 6×10^{13} and 10^{14} W/cm^2. These intensity pairs generally behave qualitatively very similar.

For longer 10-cycle laser fields, Figure 4.70, the φ dependence is significantly more pronounced for $I = 10^{13}$ W/cm^2 and decreases with increasing intensity. The intensities $\{1, 3, 6\} \times 10^{13}$ W/cm^2 behave qualitatively similar and switch their minimum $\leftrightarrow$ maximum position only at $\theta = 90°$. For 10^{14} W/cm^2 these positions also switch

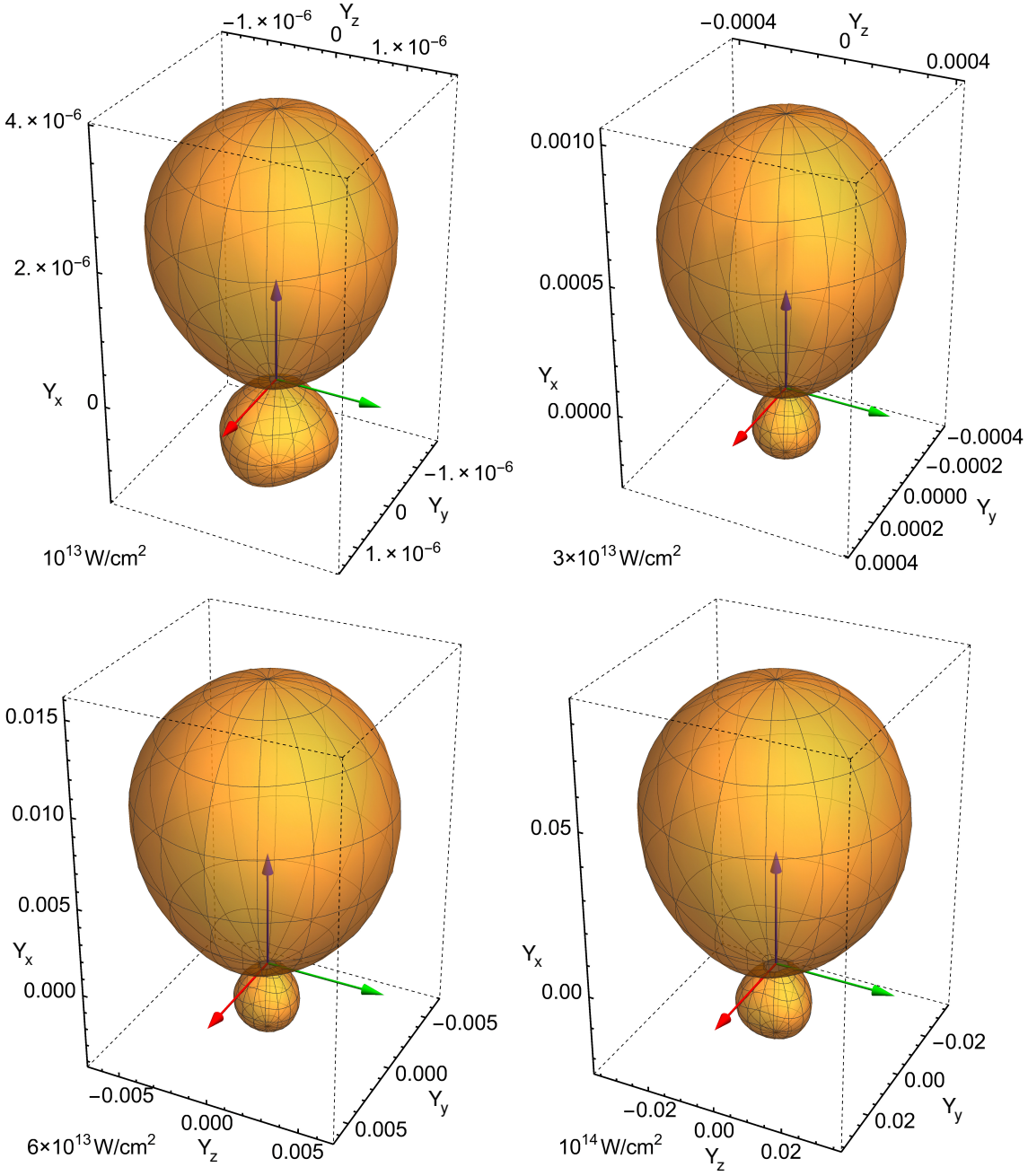

Figure 4.68: Orientation-dependent ionization yield $\vec{Y}$, Eq. (4.119) (Cartesian components Y_x, Y_y, and Y_z), for very short 2-cycle 800 nm laser fields with carrier-envelope phase $\phi = 0$ and different intensities (given inside the graph). The colored arrows point along the three Cartesian directions (x,y,z) starting from the origin (0,0,0).

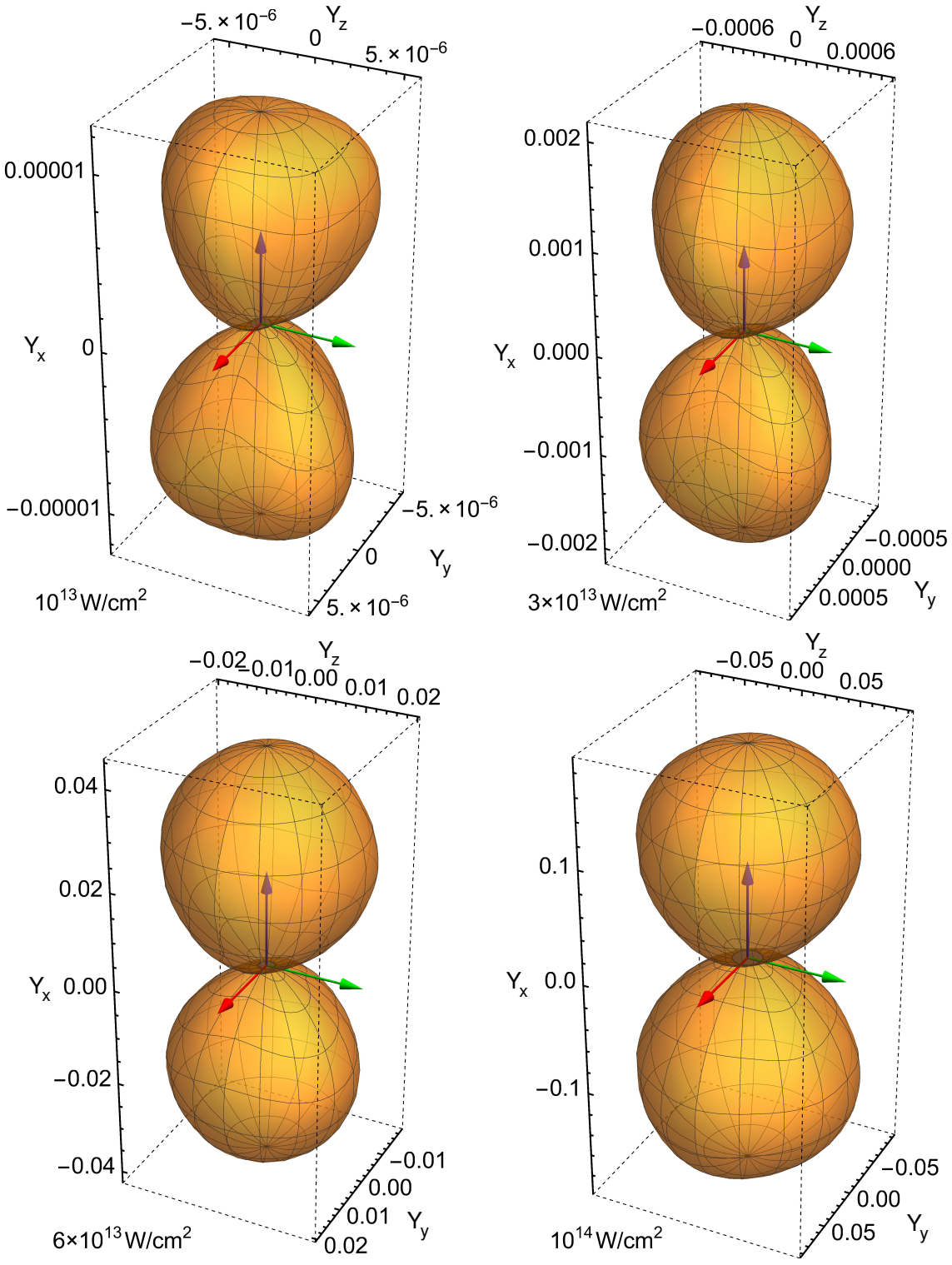

Figure 4.69: As Figure 4.68, but for longer 10-cycle laser fields.

at $\theta = 45°$ and $\theta = 135°$. When mirroring the yields at $\theta = 90°$ and exchanging minimum and maximum positions the results are almost unchanged (this includes the symmetry with respect to the inversion axis $x \leftrightarrow -x$ for these long laser fields, Section 4.6.2). This corresponds to a mirror symmetry with respect to the origin (angles after mirroring are $\tilde{\theta} = 180° - \theta$ and $\tilde{\varphi} = 180° + \varphi$).

All ionization yields discussed in this section so far were obtained using carrier-envelope phase $\phi = 0$. Figure 4.73 shows the orientation dependence for very short 2-cycle 800 nm laser fields at peak intensity 3×10^{13} W/cm^2 and carrier-envelope phase $\phi = \pi/2$ and $\phi = \pi$. For $\phi = \pi/2$ one may expect an almost symmetric ionization yield with respect to the $y - z-$plane due to the symmetry of the laser field. However, while it is significantly more symmetric than for $\varphi = 0$ it is still significantly asymmetric. Thus, the first of the two symmetric peaks of the laser field $F(t)$ (around $t = -0.55$ fs) seems to dominate the ionization behavior. For $\phi = \pi$ the orientation dependence is identical to the one for $\phi = 0$ mirrored at the origin (up to machine precision). Of course, this phase changes the sign of the electric field, $F(t, \phi = \pi) = -F(t, \phi = 0)$, and could thus also be seen as mirroring of the polarization vector at the origin $\vec{\mathcal{P}} \rightarrow -\vec{\mathcal{P}}$.

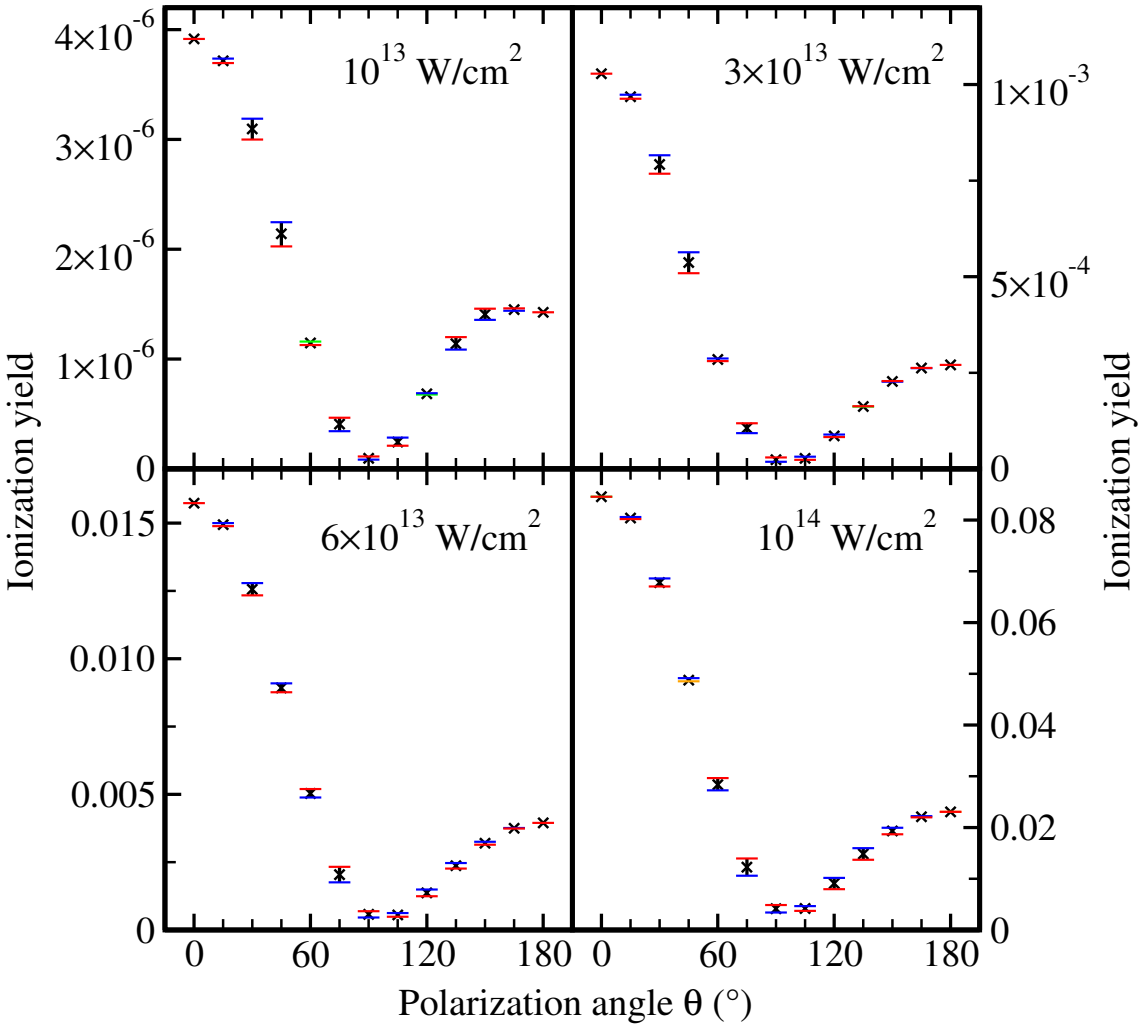

Figure 4.70: θ dependence of the ionization yield for very short 2-cycle 800 nm laser fields with carrier-envelope phase $\phi = 0$ and different intensities (given inside the graph). The black points (x) shows the ionization yield averaged over φ whereas the colored horizontal bars show the minimum and the maximum of the ionization yield for each θ. Different colors encode at which angle φ this minimum or maximum is located, i.e. $\varphi = 0$, $\varphi = 15°$, $\varphi = 30°$, $\varphi = 45°$, and $\varphi = 60°$.

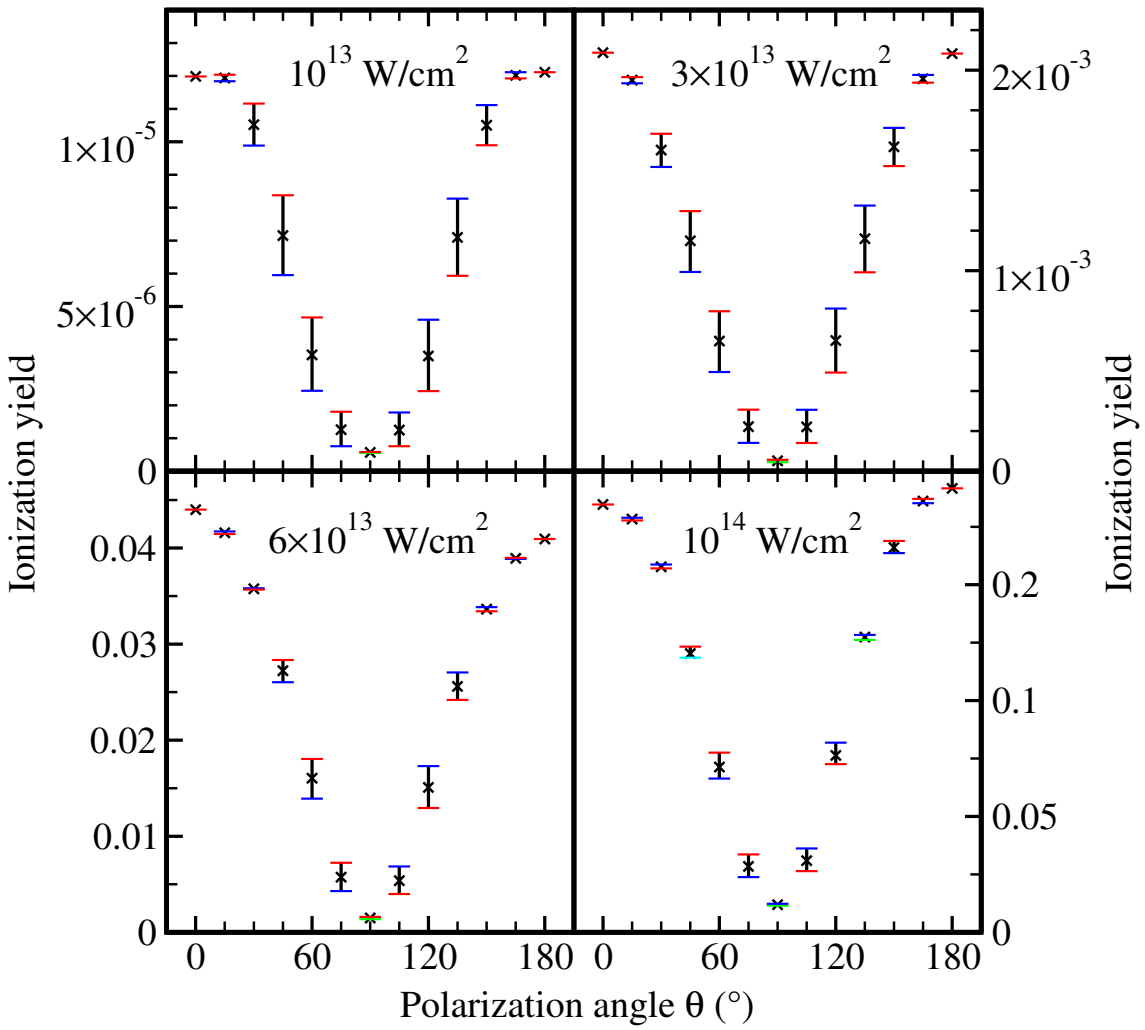

Figure 4.71: As Figure 4.70, but for longer 10-cycle laser fields (color codes: $\varphi = 0$, $\varphi = 15°$, $\varphi = 30°$, $\varphi = 45°$, and $\varphi = 60°$).

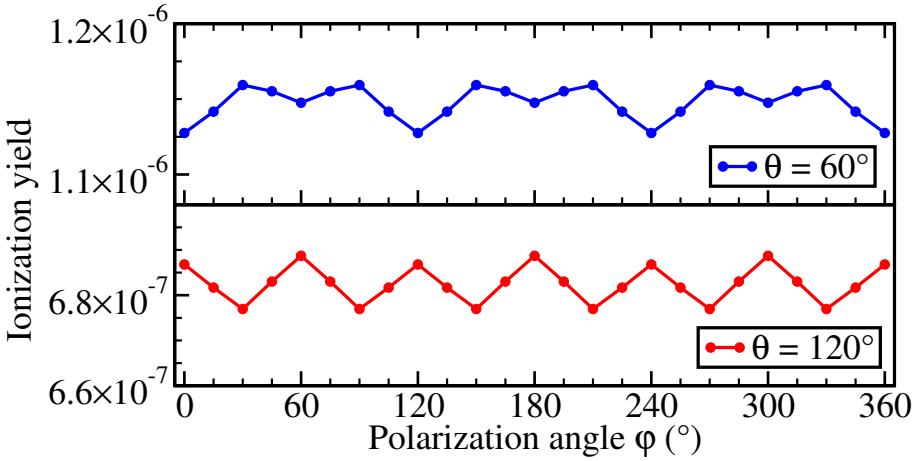

Figure 4.72: φ dependence of the ionization yield for 2-cycle 800 nm laser fields with peak intensity 10^{13} W/cm^2 at $\theta = 60°$ and 120°.

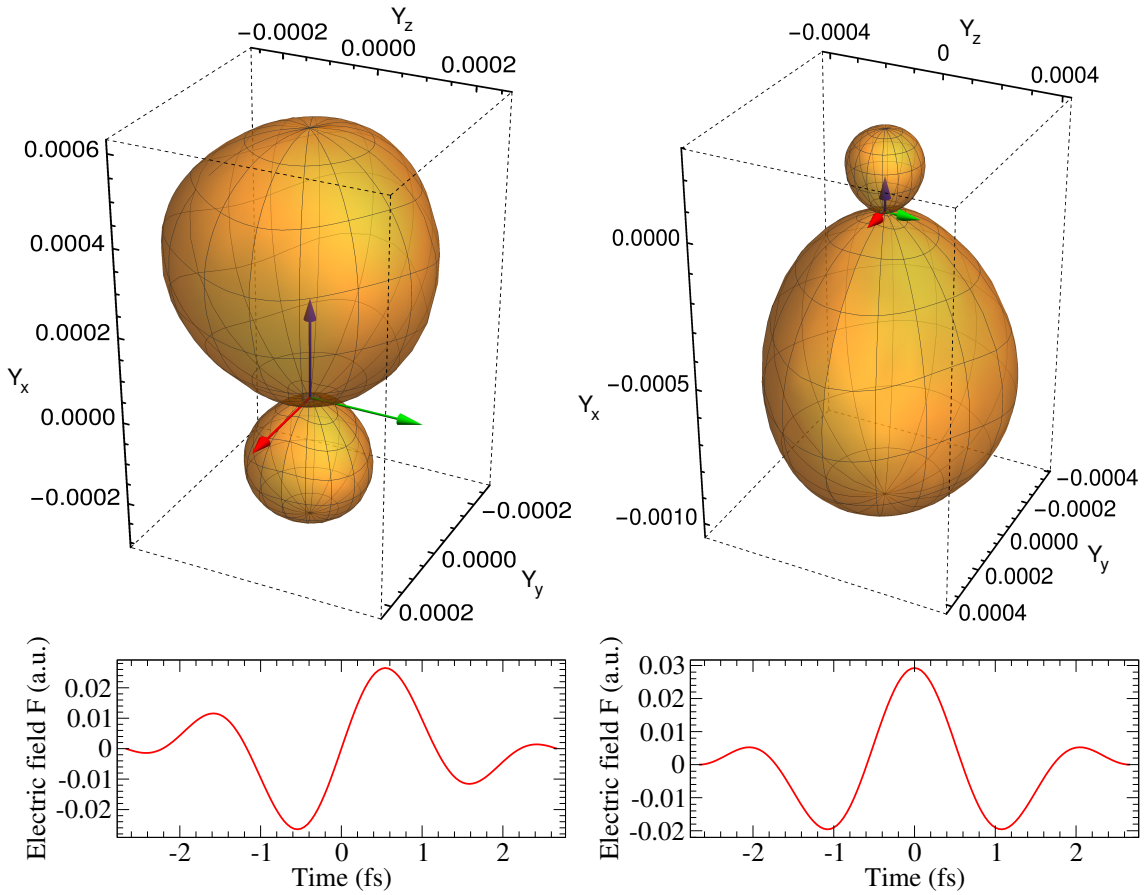

Figure 4.73: **Top:** Orientation-dependent ionization yield $\vec{Y}$, Eq. (4.119) (Cartesian components Y_x, Y_y, and Y_z), for very short 2-cycle 800 nm laser fields with peak intensity 3×10^{13} W/cm^2 and carrier-envelope phase $\phi = \pi/2$ (left) and $\phi = \pi$ (right). The colored arrows point along the three Cartesian directions (x,y,z) starting from the origin (0,0,0).
Bottom: Corresponding time-dependent electric field strength $F(t)$.

4.7.2 Dependence on the Carrier-Envelope Phase

In the following a more detailed variation of the carrier-envelope phase ϕ is performed for selected orientations and orbitals. Intense, extremely short laser fields where the parallel vs. anti-parallel asymmetry ($\phi = 0$ vs. $\phi = \pi$) was investigated before (Section 4.6.4) are studied[40]. Figure 4.74 shows the carrier-envelope phase dependence for the $3A_1$ HOMO- and the degenerate $1E$ HOMO-1 orbitals for orientations parallel to the x and y axis. It is found that ionization from the HOMO orbital exceeds ionization from the HOMO-1 orbital by at least one order of magnitude. This is the case even if the ionization from the HOMO is at a minimum while the ionization from the HOMO-1 is at maximum, $3A1 \parallel y$ vs. $1E_1 \parallel y$, even for this high peak intensity of 10^{14} W/cm^2. The contribution of the HOMO-1 is thus not observable for the wavelength and intensity regime (wavelengths $\lambda \geq 800$ nm and intensities up to 10^{14} W/cm^2) studied in this thesis. Ionization yields are symmetric when mirrored at $\phi = \pi$ except for ionization from the HOMO orbital for a polarization parallel to the x axis. While in this case the maximum of the ionization yield is indeed located at $\phi = 0$, the minimum is surprisingly slightly shifted beyond $\phi = \pi$. This shift away from $\phi = \pi$ is beyond the simple picture of ionization with parallel vs. anti-parallel polarization direction with respect to the dipole moment (Figure 4.55). The $3A_1 \parallel x$ excitation yield is also shown in Figure 4.74. It behaves very differently compared to the ionization yield. The shift of the minimum of the ionization yield is clearly linked to an increase of the excitation yield. The ϕ dependence of the excitation yield is overall very smooth. The stability of the shift of the ionization minimum due to excitation is investigated in the following.

Figure 4.75 shows the HOMO ionization yield for a variation of the peak intensity. The shift is clearly visible for the whole intensity range. In order to follow the minimum (and maximum) position of the ionization yield, the ϕ dependence is interpolated using cubic splines. The intensity dependent minimum and maximum positions obtained from the spline interpolation is shown in Figure 4.75. The minima remain very stable around $\phi = 11\pi/10$ while the maxima oscillate around $\phi = 0$. When varying the laser field duration (number of cycles n_c) instead of the intensity as shown in Figure 4.77, the minima again oscillate around $\phi = 11\pi/10$ while now also the maxima are slightly shifted, i.e. they oscillate around $\phi = \pi/20$ (in the case of $n_c = 2$ the maximum is *accidentally* located at $\phi = 0$). The shift of the minimum and maximum locations of the ionization due to excitation is surprisingly stable for a variation of the laser parameters. This is not typical for a sharp multiphoton resonance. Keep in mind that also the asymmetry in the orientation dependence for $\phi = \pi$ in Figure 4.73 indicated a non-trivial CEP dependence.

[40] $\phi = 0$ vs. $\phi = \pi$, $\varphi = 0$ vs. $\varphi = 180°$ and x vs. $-x$ all correspond to exactly the same asymmetry when all other parameters are held fixed.

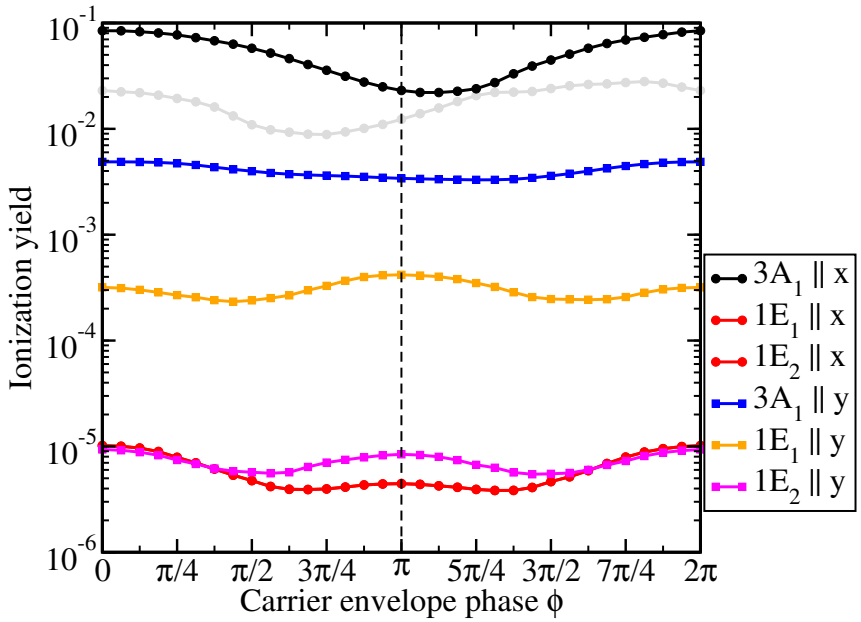

Figure 4.74: Carrier-envelope phase dependence of the ionization yield for 2-cycle 800 nm laser fields with peak intensity 10^{14} W/cm^2. Ionization from the $3A_1$ (HOMO) and $1E$ (HOMO-1) orbitals and polarization along the x and y axis (as labeled in the graph) are shown. The light grey curve which is not listed in the legend shows the $3A_1 \parallel x$ excitation yield.

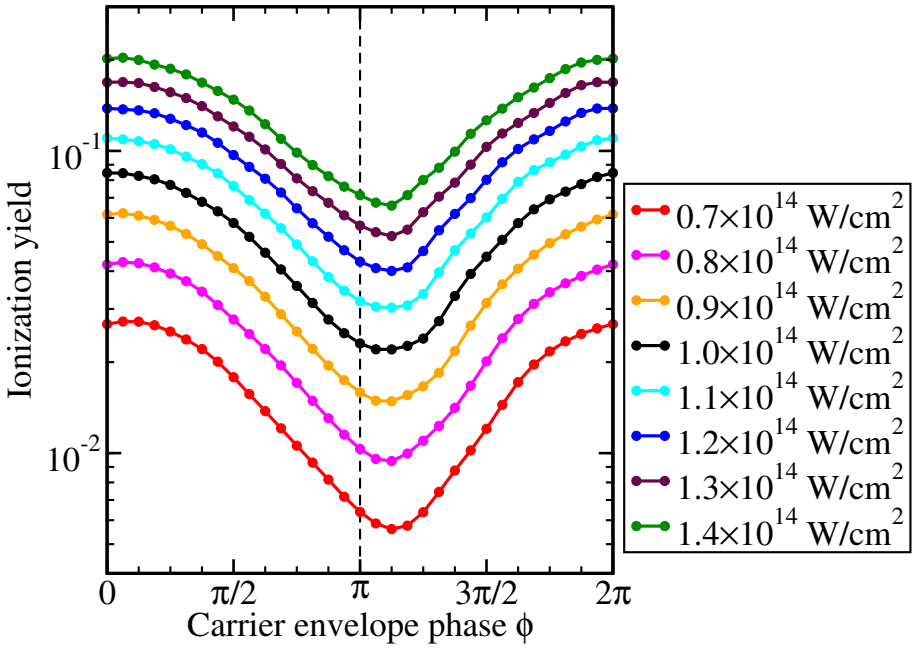

Figure 4.75: Carrier-envelope phase dependent ionization yields for the $3A_1$ (HOMO) orbital with polarization along the x axis for 2-cycle 800 nm laser fields at different peak intensities.

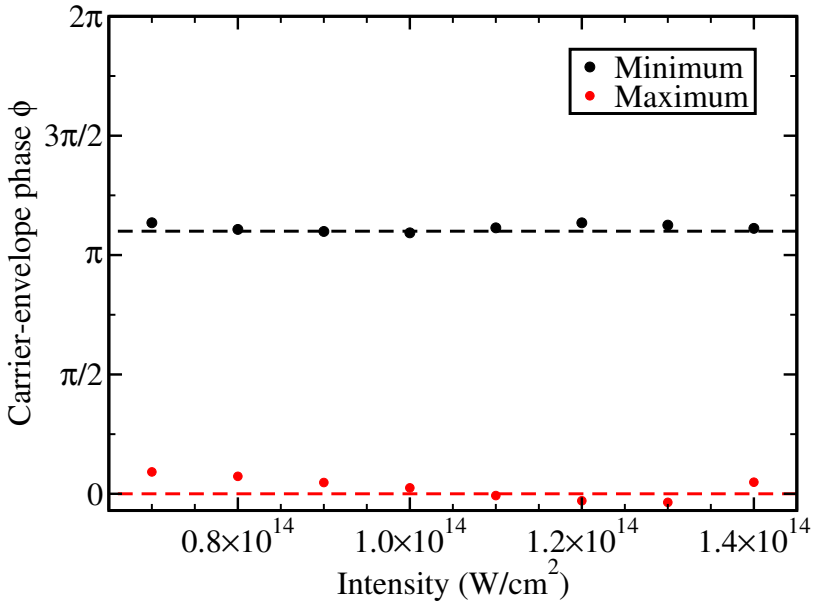

Figure 4.76: Position of the minimum and maximum of the carrier-envelope phase dependent ionization yield of the $3A_1$ orbital in 2-cycle 800 nm laser fields aligned along the x axis. The peak intensity is varied as in Figure 4.75. To guide the eye the red (black) dashed horizontal line depicts $\phi = 0$ ($\phi = 11/10\pi$), respectively.

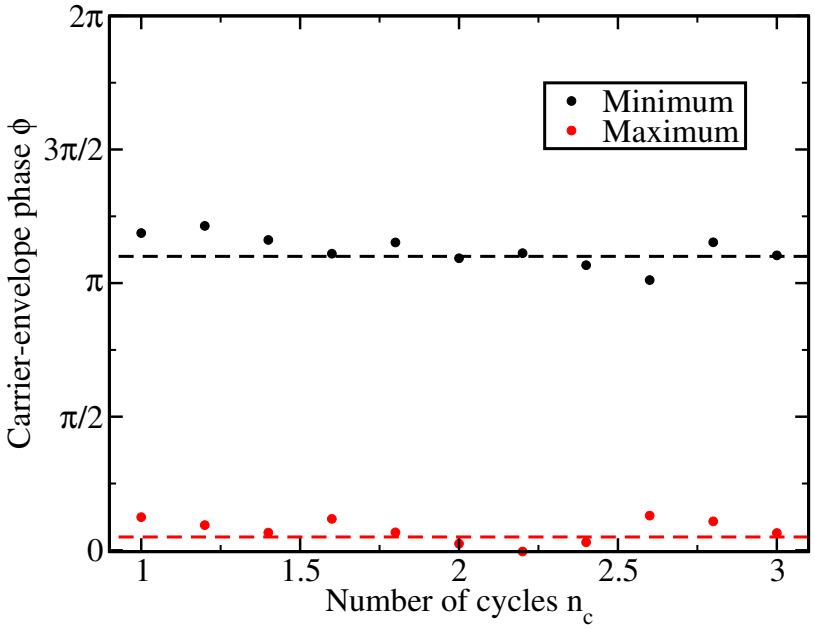

Figure 4.77: As Figure 4.75, but for fixed peak intensity 10^{14} W/cm^2 and a variation of the number of cycles n_c. The red (black) dashed line indicates $\phi = 1/20\pi$ ($\phi = 11/10\pi$), respectively.

4.7.3 Elliptical Polarization

In the following the extension of the TP_SAE code to treat elliptically polarized laser fields is discussed and ionization yields obtained with this new code are presented. The polarization direction of an elliptically polarized laser field $\vec{\mathcal{P}}$ changes with time. Thus, it seems natural to define the laser field by its propagation direction $\vec{k}$ instead. It might be interesting to understand how the orientation dependence discussed in the previous section, including the pronounced parallel vs. anti-parallel asymmetry observed for 2-cycle laser pulses, translates to the propagation-direction dependence for elliptically polarized laser fields. For propagation in free space (as assumed here) $\vec{k}$ is orthogonal to the plane in which the polarization vector $\vec{\mathcal{P}}(t)$ oscillates. Introducing spherical coordinates as in Figure 4.65 the propagation direction is written as

$$\vec{k} = \begin{pmatrix} x \\ y \\ z \end{pmatrix} = \begin{pmatrix} \cos(\theta_k) \\ \sin(\theta_k)\cos(\varphi_k) \\ \sin(\theta_k)\sin(\varphi_k) \end{pmatrix} \quad . \tag{4.120}$$

Two orthogonal vectors spanning the plane in which $\vec{\mathcal{P}}(t)$ oscillates are naturally given by the unit vectors in θ_k and φ_k direction

$$\vec{\mathcal{P}}_{\theta_k} = \begin{pmatrix} -\sin(\theta_k) \\ \cos(\theta_k)\cos(\varphi_k) \\ \cos(\theta_k)\sin(\varphi_k) \end{pmatrix} \tag{4.121}$$

$$\vec{\mathcal{P}}_{\varphi_k} = \begin{pmatrix} 0 \\ -\sin(\varphi_k) \\ \cos(\varphi_k) \end{pmatrix} \quad . \tag{4.122}$$

Clearly $\vec{k} \perp \vec{\mathcal{P}}_{\theta_k} \perp \vec{\mathcal{P}}_{\varphi_k}$. A general elliptically polarized laser field is then defined by its vector potential as

$$\vec{A}(t) = A_0\, f_{\mathrm{E}}(\,t\,)\, \left(2\cos^2(\epsilon/2)\right)^{-1/2} \left(\vec{\mathcal{P}}_{\theta_k}\, \sin(\,\omega\, t\, +\, \phi\,) \,+\, \vec{\mathcal{P}}_{\varphi_k}\, \sin(\,\omega\, t\, +\, \phi\, +\, \epsilon\,)\right) \tag{4.123}$$

with ellipticity ϵ. $\epsilon = \pi/2$ corresponds to right circular, $\epsilon = -\pi/2$ to left circular and $\epsilon = 0$ to linear polarization. The envelope $f_{\mathrm{E}}(\,t\,)$, carrier-envelope phase ϕ, and peak vector potential A_0 are similar to the case of linear polarization. The normalization factor $\left(2\cos^2(\epsilon/2)\right)^{-1/2}$ arises from the peak value of the two phase-shifted oscillations along the orthogonal vectors $\vec{\mathcal{P}}_{\theta_k}$ and $\vec{\mathcal{P}}_{\varphi_k}$[41]. In order to solve the TDSE the dipole transition matrices for the three Cartesian components of the

[41] $\max(\cos^2(u-\epsilon/2)+\cos^2(u+\epsilon/2)) = 2\cos(\epsilon/2)^2$ at $u = 0$.

dipole operator

$$\hat{\vec{\mathrm{d}}} = \begin{pmatrix} \hat{\mathrm{d}}_x \\ \hat{\mathrm{d}}_y \\ \hat{\mathrm{d}}_z \end{pmatrix} \tag{4.124}$$

are multiplied with their respective time-dependent prefactors directly following from Eq. (4.123)[42].

As a first test of the newly implemented method, the special case of linear polarization is checked. The ionization yield obtained for linear polarization with polarization direction $\theta = 75°$, $\varphi = 30°$ and for "elliptical" polarization with ellipticity $\epsilon = 0$ and the corresponding propagation direction $\theta_k \approx 133.08°$, $\varphi_k \approx 105.49°$ are compared. Indeed, the ionization yields obtained with both implementations agree within machine precision.

Ionization yields for very short 2-cycle 800 nm laser fields for a variation of the propagation angles θ_k or φ_k, respectively, are shown in Figure 4.78. A difference (vertical shift) between length and velocity gauges which seems comparable or slightly larger than for linear (Figure 4.66) is visible. However, since this difference is visible only as a vertical difference between length and velocity gauge (velocity gauge $\rightarrow$ slightly larger yields) the qualitative behavior is unchanged. On the scale of Figure 4.78 left and right circularly polarized laser fields lead to almost exactly the same ionization yields. The θ_k dependence peaks at $\theta_k = 90°$ and is minimal at $\theta_k = 0°$ and $\theta_k = 180°$. This is consistent with the behavior for linear polarization, Figure 4.66, since for $\theta_k = 90°$ the polarization vector rotates in a plane passing $\theta = 0°$ and $\theta_k = 180°$ where the ionization yield is maximal for linear polarization. For $\theta_k = 0°$ and $\theta_k = 180°$ on the other hand the polarization vector rotates in a plane at $\theta = 90°$ where the ionization yield is at the minimum. The φ_k dependence which is small compared to the θ_k dependence is enlarged in Figure 4.79. This φ_k reflects the symmetry of the molecule (Figure 4.64), i.e. ionization is symmetric within rotations by 120°. Furthermore, ionization yields are unchanged when mirroring at the planes at 60°, 180°, and 300° while at the same time exchanging left circular polarization $\leftrightarrow$ right circular polarization. This φ_k dependence is thus again the simplest naturally occurring (non constant) function fulfilling the symmetry properties of the $3A_1$ HOMO orbital.

[42] The main difference to the implementation of linear polarization is thus that the dipole transition matrices for three transition directions are kept inside the memory instead of just one (along the polarization direction $\vec{\mathcal{P}}$). Since the electric field oscillates within a plane one could alternatively also store only the dipole matrices along two transition directions ($\vec{\mathcal{P}}_{\theta_k}$ and $\vec{\mathcal{P}}_{\varphi_k}$). However, $\vec{\mathcal{P}}_{\theta_k}$ and $\vec{\mathcal{P}}_{\varphi_k}$ are in general skew directions (not parallel to any axis) and are thus likely to be represented by densely populated or full matrices while for $\hat{\mathrm{d}}_x$, $\hat{\mathrm{d}}_y$, and $\hat{\mathrm{d}}_z$ typically many transition matrix elements are zero because of symmetry selection rules. For NH_3 there are in total 11 unique non-zero transition matrices for $\hat{\mathrm{d}}_x$, $\hat{\mathrm{d}}_y$, and $\hat{\mathrm{d}}_z$ compared to 18 for $\vec{\mathcal{P}}_{\theta_k}$ and $\vec{\mathcal{P}}_{\varphi_k}$. The implemented approach storing all three Cartesian components of $\hat{\vec{\mathrm{d}}}$ is thus significantly more efficient for molecules where a significant number of transitions is zero because of symmetry selection rules while the other approach could be (slightly) better for molecules without symmetry.

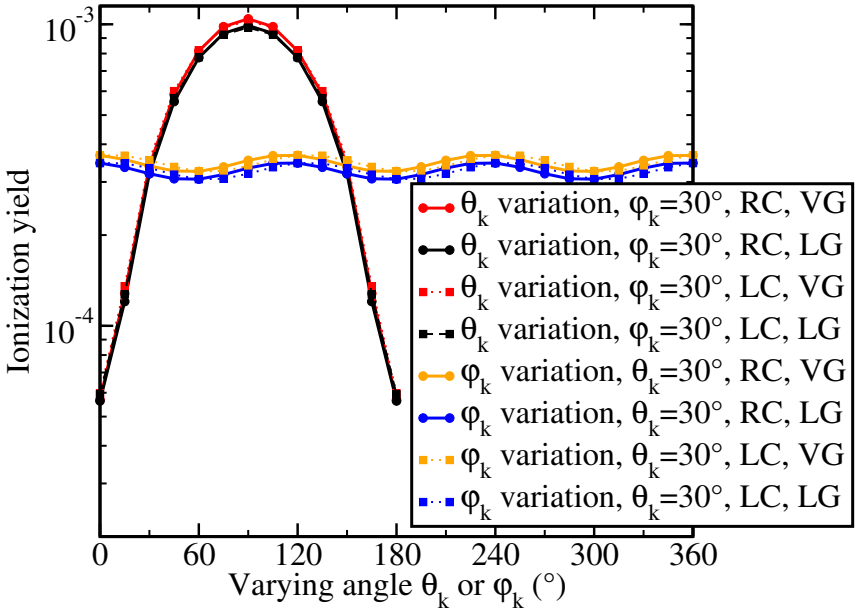

Figure 4.78: φ_k- and θ_k-dependent ionization yields for left (LC) and right-circularly (RC) polarized 2-cycle 800 nm laser fields with peak vector potential $A_0 = 0.51335$ a.u. and carrier-envelope phase $\phi = 0$ obtained at the equilibrium geometry $x = 0.5922$ a.u. For the correspondingly fixed angle the value 30° was chosen. Results obtained with length gauge (LG) and velocity gauge (VG) are shown.

Figure 4.80 shows the full propagation-direction-dependent ionization behavior for very short 2-cycle 800 nm laser fields. The obtained doughnut shape follows from the θ_k dependence explained in the paragraph before. Left and right circularly polarized fields are hardly distinguishable and can be transformed into each other by mirroring at the mirror planes (as also discussed before). The parallel vs. anti-parallel asymmetry which was prominent for 2-cycle laser fields for linear polarization is not observed by left- and right circular polarization because it is averaged out due to the rapidly changing polarization direction. For longer 10-cycle fields the propagation direction dependence, Figure 4.80, is practically identical to the 2-cycle case. Noteworthy, the φ_k dependence relative to the θ_k dependence is even smaller for 10 cycles compared to 2 cycles. This is in contrast to linear polarization where the relative φ dependence was significantly larger for 10-cycle fields. However, since the polarization direction rotates in space for circular polarization such an asymmetry can average out over time easily when the laser field duration is long enough.

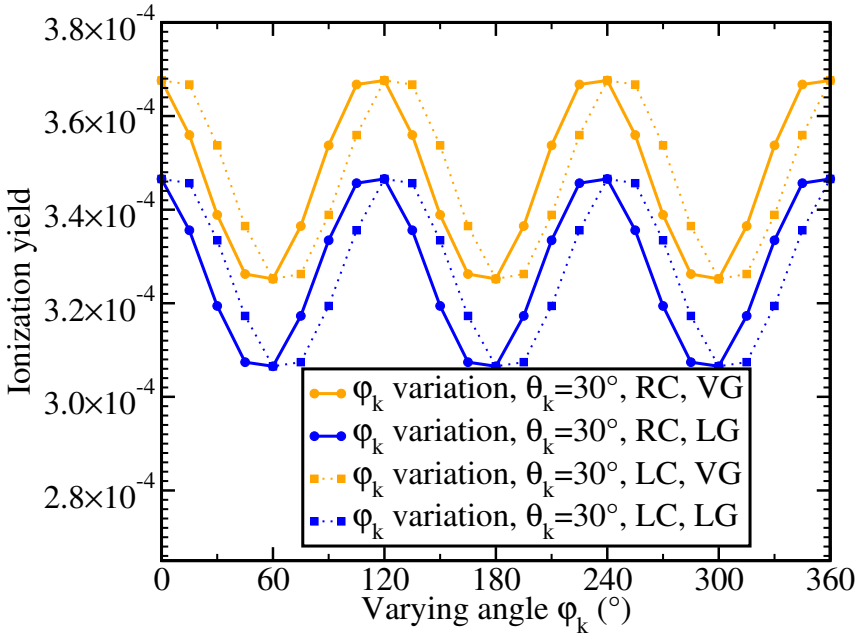

Figure 4.79: As Figure 4.78, but φ_k dependence only. (Note the magnification of the scale showing the ionization yield.)

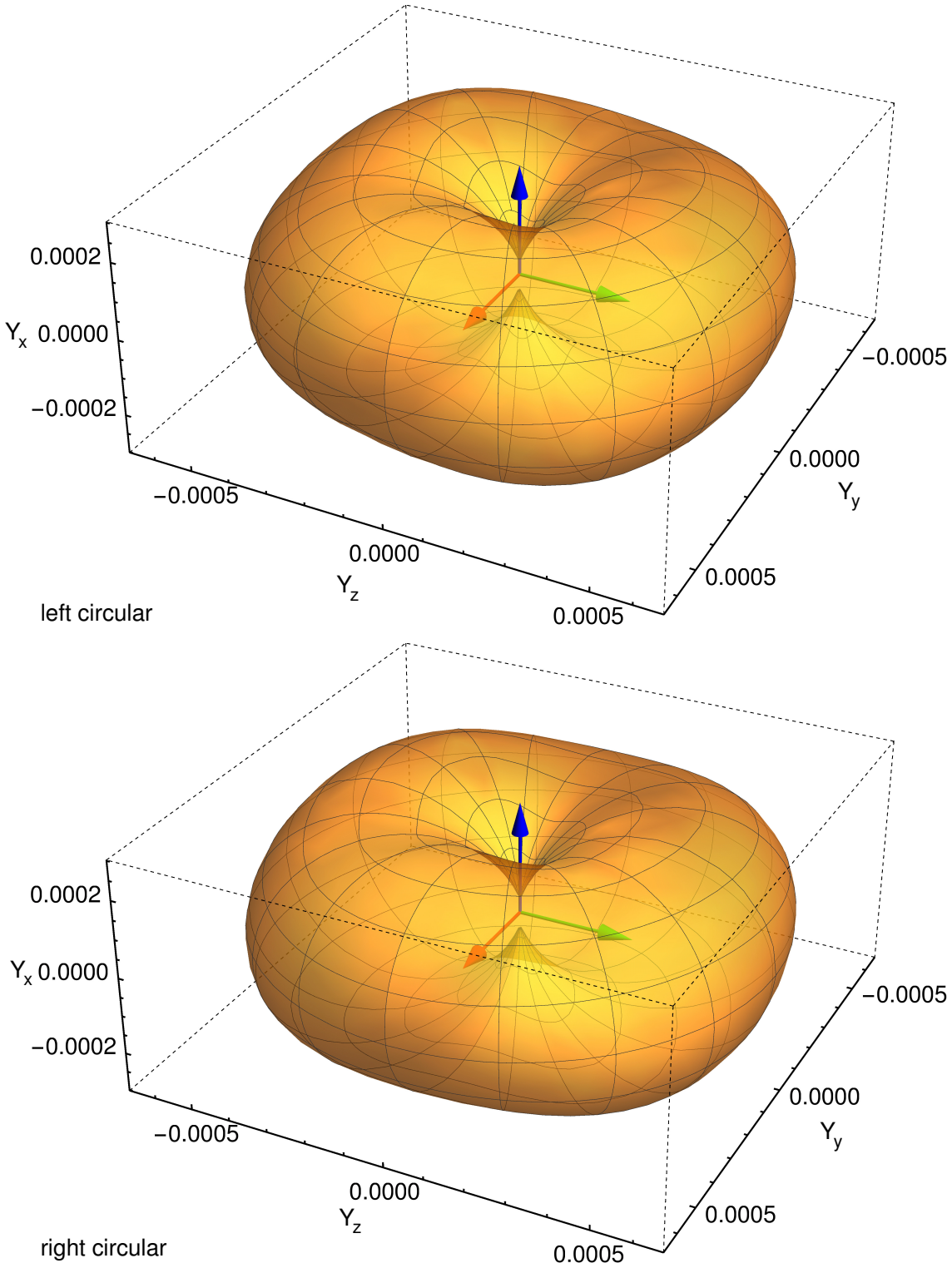

Figure 4.80: Polarization direction-dependent ionization yield $\vec{Y}$ (Cartesian components Y_x, Y_y, and Y_z) for very short 2-cycle 800 nm left and right circularly polarized laser fields with peak vector potential $A_0 = 0.51335$ a.u. The colored arrows point along the three Cartesian directions (x,y,z) starting from the origin (0,0,0).

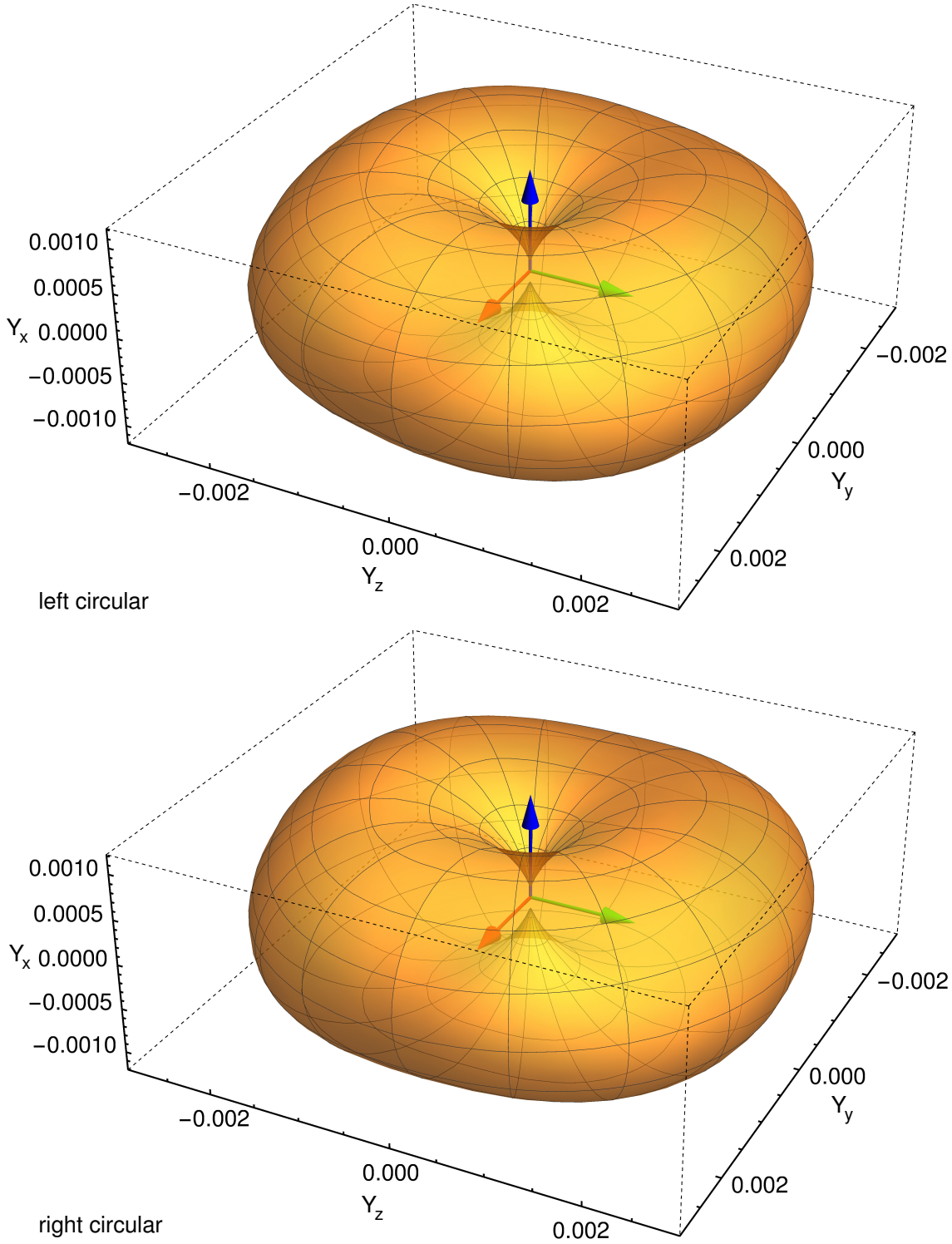

Figure 4.81: As Figure 4.80, but for longer 10-cycle laser fields.

4.7.4 Conclusions

A new program version of the TP_SAE program, TP_SAE_v5, is implemented and explored for the NH_3 molecule. It allows for the calculations of orientation-dependent ionization yields of molecules with symmetry groups containing degenerate irreps and calculations for elliptically polarized laser fields. Orientation-dependent ionization yields are practically gauge independent (on a logarithmic plot) and show that ionization indeed dominates along the inversion axis studied in Section 4.6. The parallel vs. anti-parallel ionization asymmetry for very short 2-cycle laser fields and the overall shape of the HOMO orbital are nicely seen in the orientation dependence of the ionization yield. The symmetry properties of the molecule are fulfilled by the comparably small φ dependence of the ionization yield, even though there seems to be no simple picture predicting its exact behavior. Also the carrier-envelope phase dependence of the ionization yield showed small deviations from the simple parallel vs. anti-parallel ionization picture. Those deviations are stable with respect to the laser field duration and stem from the behavior of the excitation yield. The excitation yield behavior is also very smooth, but qualitatively very different from the behavior of the ionization yield (in sharp contrast to Figure 4.54). The carrier-envelope phase dependent ionization yields also showed that the ionization from the HOMO-1 orbital is negligible for the laser parameter regime studied in this thesis.

For circularly polarized laser fields a slightly larger gauge dependence is observed compared to linear polarization. Still, the gauge dependence remains small and is visible only as a vertical offset between the length and velocity gauge ionization yields (qualitative behavior is thus unchanged). The "doughnut shape" observed for propagation direction dependent ionization follow naturally from the polarization direction dependence of linearly polarized fields. The asymmetry observed for very short 2-cycle laser fields for linear polarization are, however, averaged out due to the rapid time-dependent change of the polarization direction.

5 Summary and Outlook

The influence of nuclear motion on the ionization behavior of small molecules, particularly H_2 and NH_3, has been studied theoretically. The interaction of these molecules with intense, ultrashort laser fields has been investigated numerically by solving the corresponding time-dependent Schrödinger equation. This has been achieved on the basis of methods developed previously in the *Arbeitsgruppe Moderne Optik* and the matrix algorithm. These methods and the matrix algorithm were successfully combined and further developed in order to study the electronic and vibrational motion of H_2 and NH_3 exposed to laser fields.

The matrix algorithm is a grid approach using the discrete Fourier transformation for derivatives. It turned out to be very useful for finding eigenstates and eigenenergies of a plethora of Hamiltonians with excellent convergence properties[1]. For the investigated Hamiltonians with position-dependent mass, the PT symmetric Hamiltonian with complex potential, and the two-dimensional Henon-Heiles Hamiltonian, the obtained eigenenergies were exact within machine precision. Most importantly for the studies performed later, the matrix algorithm has proven to accurately and efficiently describe the vibration of diatomic molecules and the inversion motion of the ammonia molecule. Both bound and properly discretized continuum eigenstates of the Morse potential were found with similar or even slightly better convergence properties in direct comparison to the B-spline method. Furthermore, the NH_3 and ND_3 inversion motion energy levels obtained with the matrix algorithm using a one-dimensional position-dependent mass Hamiltonian are in excellent agreement to experimental values. Looking at the applications of the matrix algorithm later in this thesis and also other studies [6, 138–146], it will be exciting to see more studies using this method for other quantum systems with non-divergent Hamiltonians[2].

The ionization behavior of H_2 exposed to intense, ultrashort laser fields was examined. The six-dimensional time-dependent Schrödinger equation describing the electronic response to the laser field has been solved. This was done for a range of fixed internuclear distances. A method which has been previously developed in the group [28, 29, 48, 53, 76, 77] has been used. A B-spline basis in prolate spheroidal coordinates is combined with configuration interaction and the spectral ansatz. The previously reported breakdown of the fixed-nuclei approximation in the perturbative multiphoton regime [79, 81, 82] has been re-investigated. At least approximately, it turned out that this effect can be well described within the frozen-nuclei approximation, i.e. by calculating R-integrated ionization yields and just considering the

[1] Exponential convergence with respect to box size and grid spacing.

[2] For Hamiltonians where potentials with sharp edges occur, the Gibbs phenomenon (caused by the Fourier derivative) prevents an efficient convergence of the matrix algorithm.

initial spread of the vibrational wave function of the H_2 ground state. This perhaps surprising explanation does not require any vibrational dynamics during the laser field. Instead, a strong dependence of the (vertical) electronic ionization yield on the internuclear distance is observed. The cause for this strong dependence, especially well seen for the (1+1)-REMPI process, is the sensitivity of resonant electronic transitions on electronic energy differences. These energy differences change with internuclear distance such that in many cases it is not the equilibrium distance that contributes most to the total ionization yield. Instead, ionization is dominated by other internuclear distances where resonances occur. This effect changes the ionization yield by orders of magnitude. It should always play a role in the multiphoton regime, especially also for larger molecules. Luckily, considering the spread of the initial vibrational wave function and repeating fixed-nuclei calculations is a comparably small extra effort. In addition to the perturbative multiphoton regime, also the transition from the multiphoton to the quasistatic regime was investigated for short 800 nm laser pulses. The ionization yields depend only very slightly on the alignment of the molecule with respect to the internuclear axis. On the other hand, a strong dependence of the electronic ionization yield on the internuclear distance was found. The observed strong dependence further confirms the earlier prediction based on the exponential dependence of strong-field ionization rates on the vertical binding energy [23]. Interestingly, the ionization yields obtained from the numerical solution of the TDSE agree quantitatively very well with the ones obtained from FC-ADK ionization rates, a simple correction to the standard ADK formula. It extends the applicability of ADK into the multiphoton regime. FC-ADK should be very useful in the future if no TDSE solution is available as for systems more complex than H_2, e. g. for the calibration of the laser intensity in experiments.

In order to develop a method to treat the (6+1)-dimensional electronic-vibrational motion of H_2 in a fully correlated fashion, first a (1+1)-dimensional H_2^+ model was investigated. For this toy model different numerical methods and approximations have been tried and compared. The time-dependent vibrational probability densities (or absolute squares of the exact nuclear wave functions [56–58, 105]) are compared. The direct solution of the TDSE on a two-dimensional grid using the matrices from the matrix algorithm and an adaptive step size (instead of the standard split operator approach) agrees perfectly to the results previously reported in literature [56]. Interestingly, using the matrices from the matrix algorithm turned out to be significantly faster than using fast Fourier transformations if the number of points per spatial dimension is smaller than 700. It might be worth considering this method to gain numerical efficiency in brute force solutions of the TDSE on higher dimensional grids. The method may also be implemented on a supercomputer since it is highly parallelizable. Comparing different ways to solve the TDSE for (1+1)-dimensional model H_2^+, excellent agreement between length- and velocity gauge was found. Furthermore, the direct solution on a two-dimensional grid agrees very well with the TDSE solution using the spectral ansatz for the electronic motion. This is the case even within the Born-Oppenheimer approximation for which nonadiabatic couplings are neglected. Nonadiabatic corrections thus seem to play only a minor

role for the ionization process. If the nonadiabatic couplings are properly calculated and included, perfect agreement between the direct grid and the mixed grid-spectral approach was found. When restricting the number of electronic states in the mixed grid-spectral approach, it was found that the results obtained using velocity gauge are much more robust (and the error behaves much more systematic) than in the case of length gauge.

Using the grid with matrix algorithm matrices for the vibrational motion and electronic eigenstates (spectral ansatz) for the electronic motion has been generalized to treat the (6+1)-dimensional electronic-vibrational motion of the H_2 molecule. This case is significantly more challenging due to the sharp features of dipole and nonadiabatic transition matrices as a function of internuclear distance (in contrast to the very smooth behavior for one-dimensional electronic H_2^+ model eigenstates). The major challenge was following the electronic states along internuclear distance R in order to obtain continuous transition matrices between electronic states. This could finally be achieved by comparing the B-spline coefficients of the H_2 eigenstates obtained at neighboring internuclear distances while using a very fine grid of internuclear distances with spacing $\Delta R = 0.001$ a.u. Even though the observed sharp features on the $\Delta R = 0.001$ scale (even for low-lying bound states) may seem surprising, they confirm previously reported results obtained with a different computational method [158, 161]. As a first application of the newly developed approach the breakdown of the fixed-nuclei approximation in the perturbative multiphoton regime was further studied. It turned out that vibrational dynamics during the laser field indeed have a visible influence on the ionization yield especially in the region where the (1+1)-REMPI process occurs. The treatment of vibrational motion in all states resonantly excited within the $1^1\Sigma_g^+ \rightarrow 1^1\Sigma_u^+ \rightarrow H_2^+(1\sigma_g) + e^-$ REMPI process was found to be important in order to reproduce the effect quantitatively (within a more restricted calculation). This includes even the final continuum states $H_2^+(1\sigma_g) + e^-$. Nonadiabatic effects turned out to have only a negligible influence on the total ionization yield even for higher intensities (other observables can behave differently). A variation of the centrifugal barrier, on the other hand, had a clearly visible influence on the total ionization yield. It may thus be interesting to consider the rotation of the H_2 molecule in future studies. The extreme sensitivity of the two-photon REMPI process may be exploited in future studies to image vibrational dynamics in molecules, especially those containing light (and thus fast) nuclei. A further application of the newly developed approach was the calculation of a recently predicted and measured isotope effect [107, 108, 156] in the ionization H_2 vs. D_2. It was found that a good agreement to the experiment is already obtained using a simple R integration of static ionization rates. Considering 6 cycle 800 nm laser fields, however, the ionization yield ratio Y_{H_2}/Y_{D_2} decreases significantly. Good agreement is found between R integrated TDSE and FC-ADK ionization yields (as previously). Thus, the multiphoton correction significantly changes the ionization behavior especially for small field strengths of the laser field. Astonishingly, when the TDSE is solved considering the correlated (6+1)-dimensional electronic-vibrational motion of H_2, the ionization yield ratio Y_{H_2}/Y_{D_2} is significantly enhanced. It turns

out that the fast vibrational dynamics occurring in energetically surprisingly high-lying electronic continuum states is important to reproduce this effect. The motion in these electronic continuum states may efficiently suppress recombination for light nuclei. In any case, the newly implemented method to treat the correlated electronic-vibrational motion of H_2 will likely be used in many future studies of the H_2 molecule exposed to ultrashort, intense laser fields. The present method even allows to approach strong-field phenomena due to its much better scaling behavior when compared to a previous implementation [51, 79–92]. The remaining problem of the very sharp features of dipole and nonadiabatic transition matrix elements may also be reduced in the future by performing a diabatization of the electronic basis set.

In the second part of the thesis the ionization behavior of the NH_3 molecule was investigated. In a recent experiment [21] the high-harmonic spectra of the isotopes ND_3 vs. NH_3 were compared in order to image the relative nuclear motion launched in the ND_3^+ vs. NH_3^+ cations (*PACER* [19, 20]). The nuclear autocorrelation function required for the explanation of the experiment were extracted from measured photoelectron spectra in [21]. Here, these nuclear autocorrelation functions were calculated using the matrix algorithm for the simple one-dimensional position-dependent mass Hamiltonian describing the inversion motion of ammonia. The approach to extract the nuclear autocorrelation function from photoelectron spectra as well as two different approaches to correct for strong-field (i.e. non Franck-Condon) effects have been compared. It turns out that both corrections lead to identical autocorrelation functions. The autocorrelation maximum which was predicted in [21] as a novel effect could be explained by visualizing the wave packets created in ND_3^+ and NH_3^+. For this "wave packet race" the heavier isotope ND_3^+ wave packet catches up with the NH_3^+ at the position of this autocorrelation maximum. Unfortunately, this maximum occurred outside the time window observed by the *PACER* experiment. It may be observed in a future experiment. The strong-field correction which was required in order to quantitatively explain the experimental results [21] indicates a pronounced dependence of the ionization yield on the inversion coordinate (inversion geometry). It reflects the equilibrium geometry change from pyramidal to plane for the ionization of NH_3. The good agreement of the one-dimensional model with Ref. [21] (and the corresponding equilibrium geometry change) motivated the exploration of the possibility to create and image nuclear wave packets in neutral NH_3.

The ionization behavior of NH_3 has been studied by solving the electronic TDSE using the single-determinant multicentric B-spline approach previously developed in the group [5, 11, 54, 78, 95, 97, 98]. The time-dependent calculations are performed at fixed nuclear geometries which describe the inversion motion. The nuclear vibration in the electronic ground state of neutral NH_3 is then described by means of a complex absorbing potential as previously used to describe *Lochfraß* [30, 31]. Again, the vibrational calculations describing the inversion motion were performed using the matrix algorithm. The ionization yields obtained using the TDSE approach agree very well with the FC-ADK approximation for laser pulse durations of 6 cy-

cles or more. This underlines the usefulness of FC-ADK (as previously discussed for H_2) also for polyatomic molecules. The geometry dependence of the ionization yield can be used to create and measure inversion motion wave packets in neutral NH_3 via *Lochfraß*. In detail, however, the geometry dependence of the TDSE ionization yields is weaker than in the FC-ADK case. Thus, while both FC-ADK and TDSE ionization yields predict the same oscillation created and probed in neutral NH_3, the absolute amplitude of the oscillation is much smaller in the TDSE case. Still, it would be certainly interesting to experimentally measure this vibration in the future using the proposed optimal laser parameters. This would be the first observation of (vibrational) *Lochfraß* in a polyatomic molecule. This would stir interest in future examinations using this effect as an imaging technique. Note that the clear advantage of *Lochfraß* compared to *PACER* is the much larger time window which is observed. In addition to *Lochfraß* the possibility to image a wave packet tunneling through the barrier in the double-well potential of the inversion motion is investigated. Preparing the simplest possible tunneling wave packet and using the probe pulse that would be used for imaging via *Lochfraß* would lead to a constant signal in time. This is explained by the observation that this wave packet does not tunnel through the barrier by literally moving through it, but rather by disappearing on one side of the double well and reappearing on the other side. A measurement of this constant signal would thus illustrate the "magic" of the quantum-mechanical tunneling process. Additionally, it was found that an asymmetric ionization behavior for a parallel vs. anti-parallel orientation of the polarization vector with respect to the inversion axis is achieved for extremely short ($\approx$ 2 cycle) laser pulses. It was thus shown how these extremely short laser fields can be used to create a real-time movie of the tunneling process in NH_3. Hopefully, this movie of the tunneling process in NH_3 will be experimentally realized in the future.

In addition to the inversion geometry dependence, the program existing in the group has been extended to study the orientation dependence of the ionization yield. Orientation-dependent ionization yields have been shown to reflect the shape of the HOMO orbital. Furthermore, they are dependent on the orientation (parallel vs. anti-parallel asymmetry) for very short ($\approx$ 2 cycle) laser pulses. Ionization is indeed dominant for polarization along the inversion axis and ionization from the HOMO-1 is found to be negligible. Smaller wavelengths (e.g. $\lambda \leq 400$ nm) may be used in order to enhance the effect of the HOMO-1 for imaging applications (similarly to [97]). Not all features observed could be fully explained by simple pictures. For example, for a variation of the carrier-envelope phase ϕ, the maxima and minima are not exactly located at $\phi = 0$ or $\phi = \pi$ which would be naively expected for the parallel vs. anti-parallel asymmetry. This surprisingly stable effect stems from the behavior of the excitation yield. In addition to extending the program for orientation-dependent laser fields, also elliptically polarized laser fields have been newly implemented and demonstrated. The characteristic doughnut shape obtained for the propagation-direction dependence of the ionization yield for left and right circularly polarized laser fields is a direct consequence of the orientation dependence. However, the parallel vs. anti-parallel asymmetry is no longer visible for 2 cycle laser

fields. The correct implementation of orientation-dependent ionization and elliptical polarization paves the way for interesting future studies. A natural application would be to study different enantiomers of chiral molecules exposed to circular or elliptically polarized laser fields. It might be possible to distinguish those enantiomers by their (differential) ionization behavior when exposed to these laser fields.

Since for H_2 a fully correlated approach describing the electronic-vibrational motion has been successfully implemented and tested, it seems to be a natural next step to implement this approach also for the single determinant method. This method could be directly used for molecules which can be well described by an effectively one-dimensional vibration (such as NH_3). The main challenge will also be here to properly follow the electronic states along different nuclear geometries. Clearly, trying to connect the states for two extremely close nuclear geometries while using a very small electronic basis set will quickly reveal further possible practical hurdles. The possible gains of such an approach for the understanding of the influence of vibrations on the ionization behavior of small polyatomic molecules would be manifold. For the H_2 molecule a surprisingly pronounced influence of vibrational dynamics on the ionization yield was observed. While it may be argued that larger nuclei masses lead to a slower vibrational motion, this argument holds only for identical electronic potentials. A pronounced equilibrium geometry change upon ionization launches very fast vibrational dynamics in the cation also for heavier nuclei.

Bibliography

[1] J. Förster, A. Saenz, and U. Wolff. Matrix algorithm for solving Schrödinger equations with position-dependent mass or complex optical potentials. *Phys. Rev. E*, 86:016701, 2012.

[2] J. Förster and A. Saenz. Theoretical study of the inversion motion of the ammonia cation with subfemtosecond resolution for high-harmonic spectroscopy. *ChemPhysChem*, 14:1438, 2013.

[3] J. Förster, Y. V. Vanne, and A. Saenz. Ionization behavior of molecular hydrogen in intense laser fields: Influence of molecular vibration and alignment. *Phys. Rev. A*, 90:053424, 2014.

[4] J. Förster, E. Plésiat, Á. Magaña, and A. Saenz. Imaging of the umbrella motion and tunneling in ammonia molecules by strong-field ionization. *Phys. Rev. A*, 94:043405, 2016.

[5] J. P. Farrell, S. Petretti, J. Förster, B. K. McFarland, L. S. Spector, Y. V. Vanne, P. Decleva, P. H. Bucksbaum, A. Saenz, and M. Gühr. Strong field ionization to multiple electronic states in water. *Phys. Rev. Lett.*, 107:083001, 2011.

[6] S. Sala, J. Förster, and A. Saenz. Ultracold-atom quantum simulator for attosecond science. *Phys. Rev. A*, 95:011403(R), 2017.

[7] P. Agostini and L. F. DiMauro. The physics of attosecond light pulses. *Rep. Prog. Phys.*, 67:813, 2004.

[8] G. A. Mourou, T. Tajima, and S. V. Bulanov. Optics in the relativistic regime. *Rev. Mod. Phys.*, 78:309, 2006.

[9] F. Krausz and M. Ivanov. Attosecond physics. *Rev. Mod. Phys.*, 81:163, 2009.

[10] M. Meckel, D. Comtois, D. Zeidler, A. Staudte, D. Pavičić, H. C. Bandulet, H. Pépin, J. C. Kieffer, R. Dörner, D. M. Villeneuve, and P. B. Corkum. Laser-induced electron tunneling and diffraction. *Science*, 320:1478, 2008.

[11] S. Petretti, Y. V. Vanne, A. Saenz, A. Castro, and P. Decleva. Alignment-dependent ionization of N_2, O_2, and CO_2 in intense laser fields. *Phys. Rev. Lett.*, 104:223001, 2010.

[12] P. B. Corkum. Plasma perspective on strong field multiphoton ionization. *Phys. Rev. Lett.*, 71:1994, 1993.

[13] P. B. Corkum and F. Krausz. Attosecond science. *Nat. Phys.*, 3:381, 2007.

[14] J. Itatani, J. Levesque, D. Zeidler, H. Niikura, H. Pépin, J. C. Kieffer, P. B. Corkum, and D. M. Villeneuve. Tomographic imaging of molecular orbitals. *Nature*, 432:867, 2004.

[15] H. J. Wörner, J. B. Bertrand, D. V. Kartashov, P. B. Corkum, and D. M. Villeneuve. Following a chemical reaction using high-harmonic interferometry. *Nature*, 466:604, 2010.

[16] H. J. Wörner, J. B. Bertrand, B. Fabre, J. Higuet, H. Ruf, A. Dubrouil, S. Patchkovskii, M. Spanner, Y. Mairesse, V. Blanchet, E. Mével, E. Constant, P. B. Corkum, and D. M. Villeneuve. Conical intersection dynamics in NO_2 probed by homodyne high-harmonic spectroscopy. *Science*, 334:208, 2011.

[17] C. I. Blaga, J. Xu, A. D. DiChiara, E. Sistrunk, K. Zhang, P. Agostini, T. A. Miller, L. F. DiMauro, and C. D. Lin. Imaging ultrafast molecular dynamics with laser-induced electron diffraction. *Nature*, 483:194, 2012.

[18] B. Wolter, M. G. Pullen, A.-T. Le, M. Baudisch, K. Doblhoff-Dier, A. Senftleben, M. Hemmer, C. D. Schröter, J. Ullrich, T. Pfeifer, R. Moshammer, S. Gräfe, O. Vendrell, C. D. Lin, and J. Biegert. Ultrafast electron diffraction imaging of bond breaking in di-ionized acetylene. *Science*, 354:308, 2016.

[19] M. Lein. Attosecond probing of vibrational dynamics with high-harmonic generation. *Phys. Rev. Lett.*, 94:053004, 2005.

[20] S. Baker, J. S. Robinson, C. A. Haworth, H. Teng, R. A. Smith, C. C. Chirilă, M. Lein, J. W. G. Tisch, and J. P. Marangos. Probing Proton Dynamics in Molecules on an Attosecond Time Scale. *Science*, 312:424, 2006.

[21] P. Kraus and H. Wörner. Attosecond nuclear dynamics in the ammonia cation: relation between high-harmonic and photoelectron spectroscopies. *ChemPhysChem*, 14:1445, 2013.

[22] P. Lan, M. Ruhmann, L. He, C. Zhai, F. Wang, X. Zhu, Q. Zhang, Y. Zhou, M. Li, M. Lein, and P. Lu. Attosecond probing of nuclear dynamics with trajectory-resolved high-harmonic spectroscopy. *Phys. Rev. Lett.*, 119:033201, 2017.

[23] A. Saenz. On the influence of vibrational motion on strong-field ionization rates in molecules. *J. Phys. B*, 33:4365, 2000.

[24] X. Urbain, B. Fabre, E. M. Staicu-Casagrande, N. de Ruette, V. M. Andrianarijaona, J. Jureta, J. H. Posthumus, A. Saenz, E. Baldit, and C. Cornaggia. Intense-laser-field ionization of molecular hydrogen in the tunneling regime and its effect on the vibrational excitation of H_2^+. *Phys. Rev. Lett.*, 92:163004, 2004.

[25] A. M. Perelomov, V. S. Popov, and M. V. Terent'ev. Ionization of atoms in an alternating electric field. *Sov. Phys. JETP*, 23:924, 1966.

[26] M. V. Ammosov, N. B. Delone, and V. P. Krainov. Tunnel ionization of complex atoms and of atomic ions in an alternating electromagnetic field. *Sov. Phys. JETP*, 64:1191, 1986.

[27] F. A. Ilkov, J. E. Decker, and S. L. Chin. Ionization of atoms in the tunnelling regime with experimental evidence using Hg atoms. *J. Phys. B*, 25:4005, 1992.

[28] M. Awasthi and A. Saenz. Internuclear-distance dependence of ionization of H_2 in strong laser fields. *J. Phys. B*, 39:S 389, 2006.

[29] Y. V. Vanne and A. Saenz. Ionization of molecular hydrogen and deuterium by frequency-doubled Ti:sapphire laser pulses. *Phys. Rev. A*, 80:053422, 2009.

[30] E. Goll, G. Wunner, and A. Saenz. Formation of ground-state vibrational wavepackets in intense ultrashort laser pulses. *Phys. Rev. Lett.*, 97:103003, 2006.

[31] T. Ergler, B. Feuerstein, A. Rudenko, K. Zrost, C. D. Schröter, R. Moshammer, and J. Ullrich. Quantum-phase resolved mapping of ground-state vibrational D_2 wave packets via selective depletion in intense laser pulses. *Phys. Rev. Lett.*, 97:103004, 2006.

[32] L. Fang and G. N. Gibson. Strong-field induced vibrational coherence in the ground electronic state of hot I_2. *Phys. Rev. Lett.*, 100:103003, 2008.

[33] L. Fang and G. N. Gibson. Comparison of r-dependent ionization and bond softening as mechanisms for creating vibrational coherence in hot molecules. *Phys. Rev. A*, 78:051402(R), 2008.

[34] M. Spanner, S. Patchkovskii, E. Frumker, and P. Corkum. Mechanisms of two-color laser-induced field-free molecular orientation. *Phys. Rev. Lett.*, 109: 113001, 2012.

[35] E. Frumker, N. Kajumba, J. B. Bertrand, H. J. Wörner, C. T. Hebeisen, P. Hockett, M. Spanner, S. Patchkovskii, G. G. Paulus, D. M. Villeneuve, A. Naumov, and P. B. Corkum. Probing polar molecules with high harmonic spectroscopy. *Phys. Rev. Lett.*, 109:233904, 2012.

[36] J. Ullrich, R. Moshammer, A. Dorn, R. Dörner, L. P. H. Schmidt, and H. Schmidt-Böcking. Recoil-ion and electron momentum spectroscopy: reaction-microscopes. *Rep. Prog. Phys.*, 66:1463, 2003.

[37] A. T. J. B. Eppink and D. H. Parker. Velocity map imaging of ions and electrons using electrostatic lenses: Application in photoelectron and photofragment ion imaging of molecular oxygen. *Rev. Sci. Instrum.*, 68:3477, 1997.

[38] L. S. Cederbaum, J. Zobeley, and F. Tarantelli. Giant intermolecular decay and fragmentation of clusters. *Phys. Rev. Lett.*, 79:4778, 1997.

[39] T. Jahnke, A. Czasch, M. S. Schöffler, S. Schössler, A. Knapp, M. Käsz, J. Titze, C. Wimmer, K. Kreidi, R. E. Grisenti, A. Staudte, O. Jagutzki, U. Hergenhahn, H. Schmidt-Böcking, and R. Dörner. Experimental observation of interatomic coulombic decay in neon dimers. *Phys. Rev. Lett.*, 93: 163401, 2004.

[40] N. G. Kling, K. J. Betsch, M. Zohrab, S. Zeng, F. Anis, U. Ablikim, B. Jochim, Z. Wang, M. Kübel, M. F. Kling, K. D. Carnes, B. D. Esry, and I. Ben-Itzhak. Carrier-envelope phase control over pathway interference in strong-field dissociation of H_2^+. *Phys. Rev. Lett.*, 111:163004, 2013.

[41] A. Baltuška, T. Udem, M. Uiberacker, M. Hentschel, E. Goulielmakis, C. Gohle, R. Holzwarth, V. S. Yakovlev, A. Scrinzi, T. W. Hänsch, and F. Krausz. Attosecond control of electronic processes by intense light fields. *Nature*, 421:611, 2003.

[42] M. F. Kling, C. Siedschlag, A. J. Verhoef, J. I. Khan, M. Schultze, T. Uphues, Y. Ni, M. Uiberacker, M. Drescher, F. Krausz, and M. J. J. Vrakking. Control of electron localization in molecular dissociation. *Science*, 312:246, 2006.

[43] M. F. Kling, P. von den Hoff, I. Znakovskayab, and R. de Vivie-Riedle. (sub-)femtosecond control of molecular reactions via tailoring the electric field of light. *Phys. Chem. Chem. Phys.*, 15:9448, 2013.

[44] X. Xie, K. Doblhoff-Dier, S. Roither, M. S. Schöffler, D. Kartashov, H. Xu, T. Rathje, G. G. Paulus, A. Baltuška, S. Gräfe, and M. Kitzler. Attosecond-recollision-controlled selective fragmentation of polyatomic molecules. *Phys. Rev. Lett.*, 109:243001, 2012.

[45] I. Barth, J. Manz, Y. Shigeta, and K. Yagi. Unidirectional electronic ring current driven by a few cycle circularly polarized laser pulse: Quantum model simulations for mg-porphyrin. *J. Am. Chem. Soc.*, 312:424, 2006.

[46] M. Fischer, F. Grossmann, R. Schmidt, J. Handt, S. M. Krause, and J.-M. Rost. Mixed quantum-classical approach to multiphoton dissociation of the hydrogen molecular ion. *New J. Phys.*, 13:053019, 2011.

[47] M. Fischer, J. Handt, J.-M. Rost, F. Grossmann, and R. Schmidt. Molecular rotation in strong-field ionization. *Phys. Rev. A*, 86:053821, 2012.

[48] Y. V. Vanne and A. Saenz. Alignment-dependent ionization of molecular hydrogen in intense laser fields. *Phys. Rev. A*, 82:011403(R), 2010.

[49] E. Dehghanian, A. D. Bandrauk, and G. L. Kamta. Enhanced ionization of the H_2 molecule driven by intense ultrashort laser pulses. *Phys. Rev. A*, 81: 061403, 2010.

[50] G. S. J. Armstrong, J. S. Parker, and K. T. Taylor. Double-electron above-threshold ionization resonances as interference phenomena. *New J. Phys.*, 13 (1):013024, 2011.

[51] A. Palacios, J. L. Sanz-Vicario, and F. Martín. Theoretical methods for attosecond electron and nuclear dynamics: applications to the H_2 molecule. *J. Phys. B*, 48:242001, 2015.

[52] V. P. Majety, A. Zielinski, and A. Scrinzi. Photoionization of few electron systems: a hybrid coupled channels approach. *New J. Phys.*, 17:063002, 2015.

[53] M. Awasthi, Y. V. Vanne, and A. Saenz. Non-perturbative solution of the time-dependent Schrödinger equation describing H_2 in intense short laser pulses. *J. Phys. B*, 38:3973, 2005.

[54] M. Awasthi, Y. V. Vanne, A. Saenz, A. Castro, and P. Decleva. Single-active-electron approximation for describing molecules in ultrashort laser pulses and its application to molecular hydrogen. *Phys. Rev. A*, 77:063403, 2008.

[55] Y. Vanne and A. Saenz. Solution of the time-dependent dirac equation for describing multiphoton ionization of highly-charged hydrogenlike ions. *Phys. Rev. A*, 85:033411, 2012.

[56] A. Abedi, N. T. Maitra, and E. K. U. Gross. Exact factorization of the time-dependent electron-nuclear wave function. *Phys. Rev. Lett.*, 105:123002, 2010.

[57] A. Abedi, N. T. Maitra, and E. K. U. Gross. Correlated electron-nuclear dynamics: Exact factorization of the molecular wavefunction. *J. Chem. Phys.*, 137:22A530, 2012.

[58] E. Khosravi, A. Abedi, and N. T. Maitra. Exact potential driving the electron dynamics in enhanced ionization of H_2^+. *Phys. Rev. Lett.*, 115:263002, 2015.

[59] M. Born and K. Huang. *Dynamical Theory of Crystal Lattices*. Oxford University Press, 1954.

[60] M. Baer. Introduction to the theory of electronic non-adiabatic coupling terms in molecular systems. *Phys. Rep.*, 358:75, 2002.

[61] S. Jonsell, A. Saenz, and P. Froelich. Non-adiabatic couplings between the final states of tritium beta decay. *Pol. J. Chem.*, 72:1323, 1998.

[62] W. Klopper, C. Samson, G. Tarczay, and A. Csaszar. Equilibrium Inversion Barrier of NH_3 from Extrapolated Coupled-Cluster Pair Energies. *J. Comp. Chem.*, 22:1306, 2001.

[63] J. Gordon, H. Zeiger, and C. Townes. Molecular Microwave Oscillator and New Hyperfine Structure in the Microwave Spectrum of NH_3. *Phys. Rev.*, 95: 282, 1954.

[64] F. Schwabl. *Quantenmechanik (QM I)*. Springer, 2007.

[65] Y. V. Vanne. *Ionization of Molecular Hydrogen in Ultrashort Intense Laser Pulses*. PhD thesis, Humboldt-Universität zu Berlin, Germany, 2010.

[66] L. V. Keldysh. Ionization in the field of a strong electromagnetic wave. *Sov. Phys. JETP*, 20:1307, 1965.

[67] H. B. Bebb and A. Gold. Multiphoton ionization of hydrogen and rare-gas atoms. *Phys. Rev.*, 143:1, 1966.

[68] D. Gauthier, P. c. v. R. Ribič, G. De Ninno, E. Allaria, P. Cinquegrana, M. B. Danailov, A. Demidovich, E. Ferrari, L. Giannessi, B. Mahieu, and G. Penco. Spectrotemporal shaping of seeded free-electron laser pulses. *Phys. Rev. Lett.*, 115:114801, 2015.

[69] K. C. Prince, E. Allaria, C. Callegari, R. Cucini, G. D. Ninno, S. D. Mitri, B. D. E. Ferrari, P. Finetti, D. Gauthier, L. Giannessi, N. Mahne, G. Penco, O. Plekan, L. Raimondi, P. Rebernik, E. Roussel, C. Svetina, M. Trovò, M. Zangrando, M. Negro, P. Carpeggiani, M. Reduzzi, G. Sansone, A. N. Grum-Grzhimailo, E. V. Gryzlova, S. I. Strakhova, K. Bartschat, N. Douguet, J. Venzke, D. Iablonskyi, Y. Kumagai, T. Takanashi, K. Ueda, A. Fischer, M. Coreno, F. Stienkemeier, Y. Ovcharenko, T. Mazza, and M. Meyer. Coherent control with a short-wavelength free-electron laser. *Nat. Photon.*, 10: 176, 2016.

[70] T. Nakajima and G. Buica. Above-threshold ionization of Mg by linearly and circularly polarized laser fields: Origin of the subpeaks in the photoelectron energy spectra. *Phys. Rev. A*, 74:023411, 2006.

[71] C. Liu and T. Nakajima. Anomalous ionization efficiency by few-cycle pulses in the multiphoton ionization regime. *Phys. Rev. A*, 76:023416, 2007.

[72] S. D. Drell, M. Weinstein, and S. Yankielowicz. Strong Coupling Field Theories. 2. Fermions and Gauge Fields on a Lattice. *Phys. Rev.*, D14:1627, 1976.

[73] MATLAB. version R2012a (7.14.0.739), Natrick, Massachusetts: The MathWorks Inc., 2012.

[74] H. Bachau, E. Cormier, P. Decleva, J. E. Hansen, and F. Martín. Applications of B-splines in atomic and molecular physics. *Rep. Prog. Phys.*, 64:1815, 2001.

[75] J. Sapirstein and W. R. Johnson. The use of basis splines in theoretical atomic physics. *J. Phys. B*, 29:5213, 1996.

[76] Y. V. Vanne and A. Saenz. Numerical treatment of diatomic two-electron molecules using a B-spline based CI method. *J. Phys. B*, 37:4101, 2004.

[77] Y. V. Vanne and A. Saenz. Ionization of H_2 in intense ultrashort laser pulses: parallel versus perpendicular orientation. *J. Mod. Opt.*, 55:2665, 2008.

[78] M. Awasthi. *Molecules in strong laser fields: In depth study of H2 molecule.* PhD thesis, Humboldt-Universität zu Berlin, Germany, 2009.

[79] A. Palacios, H. Bachau, and F. Martín. Enhancement and control of H_2 dissociative ionization by femtosecond VUV laser pulses. *Phys. Rev. Lett.*, 96: 143001, 2006.

[80] J. L. Sanz-Vicario, H. Bachau, and F. Martín. Time-dependent theoretical description of molecular autoionization produced by femtosecond xuv laser pulses. *Phys. Rev. A*, 73:033410, 2006.

[81] A. Palacios, H. Bachau, and F. Martín. Excitation and ionization of molecular hydrogen by ultrashort vuv laser pulses. *Phys. Rev. A*, 75:013408, 2007.

[82] J. L. Sanz-Vicario, A. Palacios, J. C. Cardona, H. Bachau, and F. Martín. Ab initio time-dependent method to study the hydrogen molecule exposed to intense ultrashort laser pulses. *J. Electr. Spectros. Relat. Phenom.*, 161:182, 2007.

[83] F. Morales, J. F. Pérez-Torres, J. L. Sanz-Vicario, and F. Martín. Probing H_2 quantum autoionization dynamics with xuv atto and femtosecond laser pulses. *Chem. Phys.*, 366:58, 2009.

[84] J. F. Pérez-Torres, F. Morales, J. L. Sanz-Vicario, and F. Martín. Asymmetric electron angular distributions in resonant dissociative photoionization of H_2 with ultrashort xuv pulses. *Phys. Rev. A*, 80:011402(R), 2009.

[85] J. F. Pérez-Torres, J. L. Sanz-Vicario, H. Bachau, and F. Martín. The role of autoionizing states in two-photon dissociative ionization of H_2 by xuv ultrashort laser pulses. *J. Phys. B*, 43:015204, 2010.

[86] D. Dowek, J. F. Pérez-Torres, Y. J. Picard, P. Billaud, C. Elkharrat, J. C. Houver, J. L. Sanz-Vicario, and F. Martín. Circular dichroism in photoionization of H_2. *Phys. Rev. Lett.*, 104:233003, 2010.

[87] G. Sansone, F. Kelkensberg, J. F. Perez-Torres, F. Morales, M. F. Kling, W. Siu, O. Ghafur, P. Johnsson, M. Swoboda, E. Benedetti, F. Ferrari, F. Lepine, J. L. Sanz-Vicario, S. Zherebtsov, I. Znakovskaya, A. L'Huillier, M. Y. Ivanov, M. Nisoli, F. Martin, and M. J. J. Vrakking. Electron localization following attosecond molecular photoionization. *Nature*, 465:763, 2010.

[88] F. Kelkensberg, W. Siu, J. F. Pérez-Torres, F. Morales, G. Gaemann, A. Rouzée, P. Johnsson, M. Lucchini, F. Calegari, J. L. Sanz-Vicario, F. Martín, and M. J. J. Vrakking. Attosecond control in photoionization of hydrogen molecules. *Phys. Rev. Lett.*, 107:043002, 2011.

[89] R. E. F. Silva, P. Rivière, and F. Martín. Autoionizing decay of H_2 doubly excited states by using xuv-pump–infrared-probe schemes with trains of attosecond pulses. *Phys. Rev. A*, 85:063414, 2012.

[90] P. Rivière, R. E. F. Silva, and F. Martín. Pump-probe scheme to study the autoionization decay of optically-forbidden H_2 doubly excited states. *J. Phys. Chem. A*, 116:11304, 2012.

[91] A. Fischer, A. Sperl, P. Cörlin, M. Schönwald, H. Rietz, A. Palacios, A. González-Castrillo, F. Martín, T. Pfeifer, J. Ullrich, A. Senftleben, and R. Moshammer. Electron localization involving doubly excited states in broadband extreme ultraviolet ionization of H_2. *Phys. Rev. Lett.*, 110:213002, 2013.

[92] L. Medišauskas, R. Y. Bello, A. Palacios, A. González-Castrillo, F. Morales, L. Plimak, O. Smirnova, F. Martín, and M. Y. Ivanov. A molecular clock for autoionization decay. *J. Phys. B*, 50:144001, 2017.

[93] C. de Boor. *A Practical Guide to Splines*. Springer, New York, 1978.

[94] M. Abramowitz and I. A. Stegun. *Handbook of Mathematical Functions*. Dover, 1972.

[95] D. Toffoli, M. Stener, G. Fronzoni, and P. Decleva. Convergence of the multicenter B-spline DFT approach for the continuum. *Chem. Phys.*, 276:25, 2002.

[96] S. Petretti. *Molecules in strong laser fields: A theoretical study*. PhD thesis, Humboldt-Universität zu Berlin, Germany, 2013.

[97] S. Petretti, Á. Magaña, A. Saenz, and P. Decleva. Wavelength- and alignment-dependent photoionization of N_2 and O_2. *Phys. Rev. A*, 94:053411, 2016.

[98] S. Petretti, A. Saenz, A. Castro, and P. Decleva. Water molecules in ultrashort intense laser fields. *Chem. Phys.*, 414:45, 2013.

[99] Amsterdam density functional. https://www.scm.com.

[100] M. D. Feit, J. J. A. Fleck, and A. Steiger. Solution of the Schrödigner Equation by a Spectral Method. *J. Comp. Phys.*, 47:412, 1982.

[101] M. Lein, T. Krebich, E. K. U. Gross, and V. Engel. Strong-field ionization dynamics of a model H_2 molecule. *Phys. Rev. A*, 65:033403, 2002.

[102] M. Lein, N. Hay, R. Velotta, J. P. Marangos, and P. L. Knight. Role of the intramolecular phase in high-harmonic generation. *Phys. Rev. Lett.*, 88:183903, 2002.

[103] M. Lein, N. Hay, R. Velotta, J. P. Marangos, and P. L. Knight. Interfence effects in high-order harmonic generation with molecules. *Phys. Rev. A*, 66: 023805, 2002.

[104] E. V. van der Zwan and M. Lein. Molecular Imaging Using High-Order Harmonic Generation and Above-Threshold Ionization. *Phys. Rev. Lett.*, 108: 043004, 2012.

[105] E. Khosravi, A. Abedi, A. Rubio, and N. T. Maitra. Electronic non-adiabatic dynamics in enhanced ionization of isotopologues of hydrogen molecular ions from the exact factorization perspective. *Phys. Chem. Chem. Phys.*, 19:8269, 2017.

[106] J. W. Cooley and J. W. Tukey. An algorithm for the machine calculation of complex fourier series. *Math. Comp.*, page 297, 1965.

[107] X. Wang, H. Xu, A. Atia-Tul-Noor, B. T. Hu, D. Kielpinski, R. T. Sang, and I. V. Litvinyuk. Isotope effect in tunneling ionization of neutral hydrogen molecules. *Phys. Rev. Lett.*, 117:083003, 2016.

[108] O. I. Tolstikhin, H. J. Wörner, and T. Morishita. Effect of nuclear motion on tunneling ionization rates of molecules. *Phys. Rev. A*, 87:041401(R), 2013.

[109] G. Levai and O. Özer. An exactly solvable Schrödinger equation with finite positive position-dependent effective mass. *J. Math. Phys.*, 51:092103, 2010.

[110] G. Bastard. *Wave Mechanics Applied to Semiconductor Heterostructures*. Les Editions de Physique, Les Ulis, 1988.

[111] M. Barranco, M. Pi, S. Gatica, E. Hernandez, and J. Navarro. Structure and energetics of mixed ^{4}He-^{3}He drops. *Phys. Rev. B*, 56:8997, 1997.

[112] G. Bastard. Superlattice band structure in the envelope-function approximation. *Phys. Rev. B*, 24:5693, 1981.

[113] M. Manning. Energy Levels of a Symmetrical Double Minima Problem with Applications to the NH_3 and ND_3 Molecules. *J. Chem. Phys.*, 3:136, 1935.

[114] D. Rush and K. Wiberg. Ab Initio CBS-QCI Calculations of the Inversion Mode of Ammonia. *J. Phys. Chem. A*, 101:3143, 1997.

[115] N. Aquino, G. Campoy, and H. Yee-Madeira. The inversion potential for NH_3 using a DFT approach. *Chem. Phys. Lett.*, 296:111, 1998.

[116] J. Killingbeck. The Schrödinger equation with position-dependent mass. *J. Phys. A*, 44:285208, 2011.

[117] P. Jha, H. Eleuch, and Y. Rostovtsev. Analytical solution to position dependent mass Schrödinger equation. *J. Mod. Opt.*, 58:652, 2011.

[118] C. Bender and S. Boettcher. Real Spectra in non-Hermitian Hamiltonians Having PT Symmetry. *Phys. Rev. Lett.*, 80:5243, 1998.

[119] A. Mostafazadeh. Pseudo-Hermiticity versus PT symmetry: The necessary condition for the reality of the spectrum of a non-Hermitian Hamiltonian. *J. Math. Phys.*, 43:205, 2002.

[120] O. von Roos. Position-dependent effective masses in semiconductor theory. *Phys. Rev. B*, 27:7547, 1983.

[121] J. Cooley. An Improved Eigenvalue Corrector Formula for Solving the Schrödinger Equation for Central Fields. *Math. of Comput.*, 15:363, 1961.

[122] B. Johnson. New numerical methods applied to solving the one-dimensional eigenvalue problem. *J. Chem. Phys.*, 67:4086, 1977.

[123] J. Swalen and J. Ibers. Potential Function for the Inversion of Ammonia. *J. Chem. Phys.*, 36:1914, 1962.

[124] V. Spirko. Vibrational Anharmonicity and the Inversion Potential Function of NH_3. *J. Mol. Spectrosc.*, 101:30, 1983.

[125] W. Gordy and R. Cook. *Microwave Molecular Spectra.* Interscience, New York, 1970.

[126] S. Urban, V. Spirko, D. Papousek, J. Kauppinen, S. Belov, L. Gershtein, and A. Krupnov. A Simultaneous Analysis of the Microwave, Submillimeterwave, Far Infrared, and Infrared-Microwave Two-Photon Transitions between the Ground and ν_2 Inversion-Rotation Levels of $^{14}NH_3$. *J. Mol. Spectrosc.*, 88:274, 1981.

[127] http://physics.nist.gov/cuu/.

[128] C. Townes and A. Shalow. *Microwave Spectroscopy.* Dover, New York, 1975.

[129] W. H. Press, B. P. Flannery, S. A. Teukolsky, and W. T. Vetterling. *Numerical Recipes: The Art of Scientific Computing.* Cambridge Univ. Press, 2007.

[130] P. Morse. Diatomic molecules according to the wave mechanics. II. Vibrational levels. *Phys. Rev.*, 34:57, 1929.

[131] T. Kiel. *Relativistische Korrekturen für das Heliumatom im starken Laserfeld.* Bachelor thesis, Humboldt-Universität zu Berlin, 2012.

[132] M. Henon and C. Heiles. The applicability of the third integral of motion: Some numerical experiments. *Astronom. J.*, 69:73, 1964.

[133] J. Ehave and D. C. Clary. Potential optimized discrete variable representation. *Chem. Phys. Lett.*, 190:225, 1992.

[134] D. S. Zhang, G. W. Wei, D. J. Kouri, and D. K. Hoffman. Distributed approximating functional approach to the Fokker-Planck equation: Eigenfunction expansion. *J. Chem. Phys.*, 106:5216, 1997.

[135] B. Poirier and J. C. Light. Phase space optimization of quantum representations: Direct-product basis sets. *J. Chem. Phys.*, 111:4869, 1999.

[136] B. A. Waite and W. H. Miller. Mode specificity in unimolecular reaction dynamics: The Henon-Heiles potential energy surface. *J. Chem. Phys.*, 74: 3910, 1981.

[137] J. Rivas-Silva, G. Campoy, and A. Palma. Calculating Energy Spectrum of One-Dimensional Quantum Systems with Rational Potential P(X)/Q(X). *Int. J. Quant. Chem.*, 40:405, 1991.

[138] C. Wozar and A. Wipf. Supersymmetry Breaking in Low Dimensional Models. *Ann. of Phys.*, 237:774, 2012.

[139] J. Gienger. *Supersymmetric Matrix Quantum Mechanics.* Bachelor thesis, Humboldt-Universität zu Berlin, 2012.

[140] M. Osswald. *Korreliertes Quantentunneln in einem starken Laserfeld.* Bachelor thesis, Humboldt-Universität zu Berlin, 2012.

[141] V. Dunsing. *Investigation of a Quantum Simulator for Strong-field Methods.* Bachelor thesis, Humboldt-Universität zu Berlin, 2012.

[142] N. Sheremetyeva. *Laserfeld induziertes korreliertes Tunneln von Elektronen.* Bachelor thesis, Humboldt-Universität zu Berlin, 2013.

[143] S. Sala, G. Zürn, T. Lompe, A. Wenz, S. Murmann, F. Serwane, S. Jochim, and A. Saenz. Coherent molecule formation in anharmonic potentials near confinement-induced resonances. *Phys. Rev. Lett.*, 110:203202, 2013.

[144] A. Fischer. *Dissociative Photoionization of Molecular Hydrogen : A Joint Experimental and Theoretical Study of the Electron-Electron Correlations induced by XUV Photoionization and Nuclear Dynamics on IR-Laser Dressed Transition States.* PhD thesis, Ruprecht-Karls-Universität, Heidelberg, Germany, 2015.

[145] S. Sala. *Ultracold atoms in traps: theoretical approaches, resonances, and quantum simulations.* PhD thesis, Humboldt-Universität zu Berlin, Germany, 2016.

[146] S. Sala and A. Saenz. Theory of inelastic confinement-induced resonances due to the coupling of center-of-mass and relative motion. *Phys. Rev. A*, 94:022713, 2016.

[147] F. Martín. Ionization and dissociation using B splines: photoionization of the hydrogen molecule. *J. Phys. B*, 32:R197, 1999.

[148] A. Apalategui and A. Saenz. Multiphoton ionization of the hydrogen molecule H_2. *J. Phys. B*, 35:1909, 2002.

[149] K. Harumiya, I. Kawata, H. Kono, and Y. Fujimura. Exact two-electron wave packet dynamics of H_2 in an intense laser field: Formation of localized ionic states H^+H^-. *J. Chem. Phys.*, 113:8953, 2000.

[150] Y. V. Vanne and A. Saenz. Numerical treatment of diatomic two-electron molecules using a B-spline based CI method. *J. Phys. B*, 37:4101, 2004.

[151] G. Herzberg. *Molecular Spectra and Molecular Structure: I. Spectra of Diatomic Molecules*. D. Van Nostrand Company, Inc., 2 edition, 1963.

[152] A. Saenz. Behavior of molecular hydrogen exposed to strong dc, ac, or low-frequency laser fields: I. Bond softening and enhanced ionization. *Phys. Rev. A*, 66:063407, 2002.

[153] A. Saenz. Behavior of molecular hydrogen exposed to strong dc, ac, or low-frequency laser fields: II. Comparison of ab initio and Ammosov-Delone-Krainov (ADK) rates. *Phys. Rev. A*, 66:063408, 2002.

[154] A. Lühr, Y. V. Vanne, and A. Saenz. Parameter-free one-center model potential for an effective one-electron description of molecular hydrogen. *Phys. Rev. A*, 78:042510, 2008.

[155] A. Scrinzi, M. Geissler, and T. Brabec. Ionization above the Coulomb barrier. *Phys. Rev. Lett.*, 83:706, 1999.

[156] O. I. Tolstikhin and T. Morishita. Weak-field versus born-oppenheimer asymptotics in the theory of tunneling ionization of molecules. *Phys. Rev. A*, 95: 033410, 2017.

[157] J. von Neumann and E. P. Wigner. Über merkwürdige diskrete Eigenwerte. *Z. Phys.*, 30:465, 1929.

[158] L. Wolniewicz and G. Staszewska. $^1\Sigma_u^+ \rightarrow X\,^1\Sigma_g^+$ transition moments for the hydrogen molecule. *J. Mol. Spectrosc.*, 217:181, 2003.

[159] I. L. Cooper. On the determination of radial coupling matrix elements for non-adiabatic transitions. *J. Phys. B*, 24:1517, 1991.

[160] V. Sidis. Simple expression for the off-diagonal matrix elements of the d/dr operator between exact electronic states of a diatomic molecule. *J. Chem. Phys.*, 55:5838, 1971.

[161] P. Quadrelli, K. Dressler, and L. Wolniewicz. Nonadiabatic coupling between the EF+GK+$H^1\Sigma_g^+$, $I^1\Pi_g$, and $J^1\Delta_g$ states of the hydrogen molecule. calculation of rovibronic structures in H_2, HD and D_2. *J. Chem. Phys.*, 92:7461, 1990.

[162] S. Patchkovskii. Nuclear dynamics in polyatomic molecules and high-order harmonic generation. *Phys. Rev. Lett.*, 102:253602, 2009.

[163] P. Paul, T. Chatterbuck, C. Lyngå, P. Colosimo, L. DiMauro, P. Agostini, and K. Kulander. Enhanced high harmonic generation from an optically prepared excited medium. *Phys. Rev. Lett.*, 94:113906, 2005.

[164] M. Lewenstein, P. Balcou, M. Y. Ivanov, A. L'Huillier, and P. B. Corkum. Theory of high-harmonic generation by low-frequency laser fields. *Phys. Rev. A*, 49:2117, 1994.

[165] S. Baker, J. S. Robinson, M. Lein, C. C. Chirilă, R. Torres, H. C. Bandulet, D. Comtois, J. C. Kieffer, D. M. Villeneuve, J. W. G. Tisch, and J. P. Marangos. Dynamic two-center interference in high-order harmonic generation from molecules with attosecond nuclear motion. *Phys. Rev. Lett.*, 101:053901, 2008.

[166] W. P. Kraemer and V. Spirko. Potential energy function and rotation- vibration energy levels of NH_3^+. *J. Mol. Spectrosc.*, 153:276, 1992.

[167] J. Reutt, L. Wang, Y. Lee, and D. Shirley. Molecular beam photoelectron spectroscopy and femtosecond intramolecular dynamics of H_2O^+ and D_2O^+. *J. Chem. Phys.*, 85:6928, 1986.

[168] A. Becker, A. D. Bandrauk, and S. L. Chin. *S*-matrix analysis of non-resonant multiphoton ionisation of inner-valence electrons of the nitrogen molecule. *Chem. Phys. Lett.*, 343:345, 2001.

[169] T. K. Kjeldsen and L. B. Madsen. Strong-field ionization of diatomic molecules and companion atoms: Strong-field approximation and tunneling theory including nuclear motion. *Phys. Rev. A*, 71:023411, 2005.

[170] O. I. Tolstikhin, T. Morishita, and L. B. Madsen. Theory of tunneling ionization of molecules: Weak-field asymptotics including dipole effects. *Phys. Rev. A*, 84:053423, 2011.

[171] O. I. Tolstikhin, L. B. Madsen, and T. Morishita. Weak-field asymptotic theory of tunneling ionization in many-electron atomic and molecular systems. *Phys. Rev. A*, 89:013421, 2014.

[172] A. D. Bandrauk and S. Chelkowski. Asymmetric electron-nuclear dynamics in two-color laser fields: Laser phase directional control of photofragments in H_2^+. *Phys. Rev. Lett.*, 84:3562, 2000.

[173] P.-O. Löwdin. Proton tunneling in dna and its biological implications. *Rev. Mod. Phys.*, 35:724, 1963.

[174] L. Masgrau, A. Roujeinikova, L. O. Johannissen, P. Hothi, J. Basran, K. E. Ranaghan, A. J. Mulholland, M. J. Sutcliffe, N. S. Scrutton, and D. Leys. Atomic description of an enzyme reaction dominated by proton tunneling. *Science*, 312:237, 2006.

[175] O. M. Gonzalez-James, X. Zhang, A. Datta, D. A. Hrovat, W. T. Borden, and D. A. Singleton. Experimental evidence for heavy-atom tunneling in the ring-opening of cyclopropylcarbinyl radical from intramolecular 12C/13C kinetic isotope effects. *Journal of the American Chemical Society*, 132:12548, 2010.

[176] R. Allemann and N. Scrutton. *Quantum Tunneling in Enzyme-Catalysed Reactions*. RSC Publishing, Cambridge, UK, 2009.

[177] M. Arndt, T. Juffmann, and V. Vedral. Quantum physics meets biology. *HFSP Journal*, 3:386, 2009.

[178] S. G. Sayres, M. W. Ross, and A. W. Castleman, Jr. Influence of clustering and molecular orbital shapes on the ionization enhancement in ammonia. *Phys. Chem. Chem. Phys.*, 13:12231, 2011.

List of Figures

List of Tables

Selbständigkeitserklärung

Ich erkläre, dass ich die Dissertation selbständig und nur unter Verwendung der von mir gemäß §7 Abs. 3 der Promotionsordnung der Mathematisch-Naturwissenschaftlichen Fakultät, veröffentlicht im Amtlichen Mitteilungsblatt der Humboldt-Universität zu Berlin Nr. 126/2014 am 18.11.2014 angegebenen Hilfsmittel angefertigt habe.

Berlin, 29. August 2017 .....

Acknowledgments

First and foremost I want to thank my supervisor Alejandro Saenz. This thesis would not have been possible in its current form if he would not have given me the time and encouragement to follow my own ideas. At the same time, I profited a lot from his deep knowledge and always helpful ideas and remarks. Working together with him on the different problems of strong-field ionization during the last years has been a very enjoyable time for me.

Second, I want to thank everyone who was proof-reading parts of my thesis before its submission for their large efforts and very helpful remarks, first again Alejandro Saenz. Furthermore, I thank my colleagues Ingmar Schubert and Bruno Schulz as well as my father for proof-reading.

Of course, I thank my parents for everything. Their love, encouragement and extensive support paved me the way for my journey.

I acknowledge the "Studienstiftung des deutschen Volkes" not only for supporting my thesis financially within a PhD scholarship, but also for excellent conferences and meetings that allowed me to get to know many interesting people with which I still keep contact. I particularly thank Vera Gehlen-Baum for advertising the QualityMinds company for which she is working for. Without that, I would not have known this amazing company where I presently work in the research & development team. For the very beginning of my PhD thesis, I furthermore acknowledge financial support from the Humboldt Research Track Scholarship and the Humboldt Center for Modern Optics. Also the conference visits made possible by, e.g., the CORINF, XLIC, and QUTIF networks as well as the MPI Dresden were very enriching.

I also would like to thank all of my other colleagues with which I had a very enjoyable time. I hope to still keep contact with many of you in the future. I want to specifically thank Simon Sala with whom I have worked together with Alejandro Saenz on the ultracold-atom quantum simulator for attosecond science. It was a very great and inspiring interdisciplinary project and I still think a publication in a high-impact journal would have been deserved. I also hope to meet again some of the people I met during conferences. Thank you all for the interesting discussions and for me, it would be nice to see when someone of you becomes a professor!